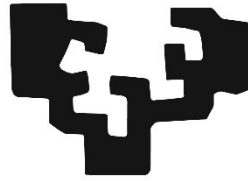eman ta zabal zazu

Universidad
del País Vasco

Euskal Herriko
Unibertsitatea

MULTIFUNCTIONAL PHOTOCURABLE ADVANCED MATERIALS FOR ELECTRONICS AND SENSING APPLICATIONS

Memoria para optar al Grado de Doctor por la Universidad del País Vasco (UPV/EHU) presentada por

Jesús Cristian Mendes Felipe

Leioa, Noviembre 2020

TESI ZUZENDARIAREN BAIMENA TESIA AURKEZTEKO	AUTORIZACIÓN DEL/LA DIRECTORA/A DE TESIS PARA SU PRESENTACIÓN

Zuzendariaren izen-abizenak /Nombre y apellidos del/la director/a: **José Luis Vilas Vilela**

IFZ /NIF: **14601692G**

Tesiaren izenburua / Título de la tesis: **Multifunctional Photocurable Advanced Materials for Electronics and Sensing Applications**

Doktorego programa / Programa de doctorado: **Ciencia y Tecnología de Materiales**
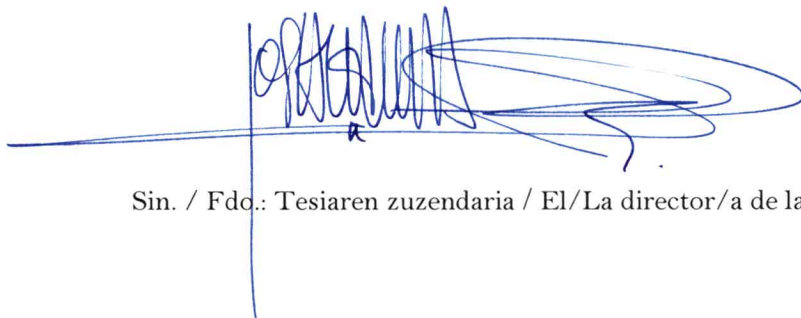
Doktoregaiaren izen-abizenak / Nombre y apellidos del/la doctorando/a: **Jesús Cristian Mendes Felipe**

Unibertsitateak horretarako jartzen duen tresnak emandako ANTZEKOTASUN TXOSTENA ikusita, baimena ematen dut goian aipatzen den tesia aurkez dadin, horretarako baldintza guztiak betetzen baititu.

Visto el INFORME DE SIMILITUD obtenido de la herramienta que a tal efecto pone a disposición la universidad, autorizo la presentación de la tesis doctoral arriba indicada, dado que reúne las condiciones necesarias para su defensa.

Tokia eta data / Lugar y fecha: Leioa, 06/11/2020

Sin. / Fdo.: Tesiaren zuzendaria / El/La director/a de la tesis

TESI ZUZENDARIAREN BAIMENA TESIA AURKEZTEKO	AUTORIZACIÓN DEL/LA DIRECTORA/A DE TESIS PARA SU PRESENTACIÓN

Zuzendariaren izen-abizenak /Nombre y apellidos del/la director/a: **Senen Lanceros Mendez**

IFZ /NIE: **30602537W**

Tesiaren izenburua / Título de la tesis: **Multifunctional Photocurable Advanced Materials for Electronics and Sensing Applications**

Doktorego programa / Programa de doctorado: **Ciencia y Tecnología de Materiales**

Doktoregaiaren izen-abizenak / Nombre y apellidos del/la doctorando/a: **Jesús Cristian Mendes Felipe**

Unibertsitateak horretarako jartzen duen tresnak emandako ANTZEKOTASUN TXOSTENA ikusita, baimena ematen dut goian aipatzen den tesia aurkez dadin, horretarako baldintza guztiak betetzen baititu.

Visto el INFORME DE SIMILITUD obtenido de la herramienta que a tal efecto pone a disposición la universidad, autorizo la presentación de la tesis doctoral arriba indicada, dado que reúne las condiciones necesarias para su defensa.

Tokia eta data / Lugar y fecha: *Leia 29/10/2020*

Sin. / Fdo.: Tesiaren zuzendaria / El/La director/a de la tesis

La Comisión Académica del Programa de Doctorado en **Ciencia y Tecnología de Materiales** en reunión celebrada el día *6* de *Noviembre* de 2020, ha acordado dar La conformidad a la presentación de la Tesis Doctoral titulada: **Multifunctional Photocurable Advanced Materials for Electronics and Sensing Applications** dirigida por las Dres. **José Luis Vilas Vilela** y **Senen Lanceros Mendez** y presentada por Don/Dña. **Jesús Cristian Mendes Felipe** adscrito o adscrita al Departamento de **Química Física**.

En Leioa a *6* de *Noviembre* de 2020

EL/LA RESPONSABLE DEL PROGRAMA DE DOCTORADO

Fdo.: _____

AUTORIZACIÓN DEL DEPARTAMENTO

El Consejo del Departamento de **Química Física** en reunión celebrada el día **06** de **noviembre** de **2020** ha acordado dar la conformidad a la admisión a trámite de presentación de la Tesis Doctoral titulada: **Multifunctional Photocurable Advanced Materials for Electronics and Sensing Applications** dirigida por los Drs. **José Luis Vilas Vilela** y **Senentxu Lanceros Mendez** y presentada por Don/Dña. **Jesús Cristian Mendes Felipe** ante este Departamento.

En Leioa a **06** de **noviembre** de 2020

VºBº DIRECTOR/A DEL DEPARTAMENTO   SECRETARIO/A   DEL DEPARTAMENTO

Fdo.: José Luis Vilas

Fdo.: Legre Pérez Álvarez

ACTA DE GRADO DE DOCTOR O DOCTORA
ACTA DE DEFENSA DE TESIS DOCTORAL

DOCTORANDO/A DON/DÑA. **Jesús Cristian Mendes Felipe**

TITULO DE LA TESIS: **Multifunctional Photocurable Advanced Materials for Electronics and Sensing Applications**

El Tribunal designado por la Comisión de Postgrado de la UPV/EHU para calificar la Tesis Doctoral arriba indicada y reunido en el día de la fecha, una vez efectuada la defensa por el/la doctorando/a y contestadas las objeciones y/o sugerencias que se le han formulado, ha otorgado por_____la calificación de:

unanimidad ó mayoría

```
┌─────────────────────────────────────────┐
│                                         │
│                                         │
└─────────────────────────────────────────┘
```

SOBRESALIENTE / NOTABLE / APROBADO / NO APTO

Idioma/s de defensa (en caso de más de un idioma, especificar porcentaje defendido en cada idioma):

Castellano _____

Euskera   _____

Otros Idiomas (especificar cuál/cuales y porcentaje) _____

En Leioa a ____ de _____de 2020

EL/LA PRESIDENTE/A,   EL/LA SECRETARIO/A,

Fdo.:   Fdo.:

Dr/a: _____   Dr/a: _____

VOCAL 1º,   VOCAL 2º,   VOCAL 3º,

Fdo.:   Fdo.:   Fdo.:

Dr/a: _____Dr/a:_____Dr/a:_____

EL/LA DOCTORANDO/A,

Fdo.: _____

Agradecimientos

Hace ocho años que comenzó mi carrera científica cuando decidí estudiar el grado de Química. Desde entonces y hasta el final de este doctorado, he conocido a muchas personas que han estado a mi lado para apoyarme, ayudarme, entenderme y, sobretodo, soportarme en mis peores momentos. Cuando comencé, jamás pensé que me llevaría tantas personas de esta gran etapa de mi vida que ahora toca terminar. Pero antes de ello, debo agradeceros a todos lo que habéis hecho por mí.

En primer lugar, me gustaría agradecer al centro BCMaterials – Basque Center for Materials, Applications and Nanostructures el apoyo económico que me ha dado durante estos tres años para realizar mi doctorado. Igualmente, agradecer a la Universidad del País Vasco / Euskal Herriko Unibertsitatea (UPV/EHU) y a los servicios generales SGIker su apoyo técnico y humano.

Me encantaría darles las gracias a mis dos directores de tesis, José Luis Vilas Vilela con el cuál comencé mi carrera como investigador realizando el trabajo fin de grado en su grupo de investigación, y Senentxu Lanceros-Mendez, pilar fundamental del centro BCMaterials y gracias al cual realicé mi primera ponencia internacional en un congreso. Gracias a los dos por darme las condiciones necesarias y los medios para realizar este doctorado. Me gustaría en especial, agradecer a Vilas todo el cariño y apoyo que me ha mostrado desde el primer día que entré en su despacho, he ganado algo más que a un "colega" científico conociéndote. A Senentxu, agradecerle todos esos cafés y reuniones juntos de las que hemos disfrutado porque me han servido para darme cuenta que detrás de esa figura de director eres una persona auténtica. Espero siempre estar en contacto con ambos.

Además, agradecerle al profesor emérito Luis Manuel León la confianza que siempre deposito en mí y todo el apoyo que me brindó para conseguir una beca en BCMaterials. Del mismo modo, agradecer a todos los profesores del Grupo de Química Macromolecular (LABQUIMAC) de la UPV/EHU con los que he tenido el placer de compartir momentos y experiencias durante la realización de mi doctorado. Muchas gracias a Leyre Perez, Leire Ruiz y José Manuel Laza, pilares indispensables del grupo, por vuestros consejos, apoyo y por todo lo que he aprendido con vosotros. Estoy seguro que todavía nos quedan trabajos por hacer.

También, agradecer a todos los compañeros que he tenido tanto en el laboratorio de LABQUIMAC como en BCMaterials, en especial a Alazne, Sheila, Julia, Jon Andrade, Ainara, Erlantz, Bruno, Nelson, Niko, Carmen, Edu, Manuel, Txema, Roberto, Arkaitz y Dani. Sin duda, habéis hecho que esta experiencia haya sido más feliz y divertida. Espero haberos ayudado y que cuando os acordéis de los momentos que vivimos lo hagáis con una sonrisa como yo lo hago. Igualmente, desearles lo mejor en el futuro a ellos y a todas las nuevas incorporaciones predoc, postdoc e Ikerbasque researchers. Creo que no me olvido de nadie, pero si es así os pido disculpas.

En especial, quiero agradecer a los amigos que me llevo para toda la vida después de estos años: Ander García, Mikel Pérez, Carlos Asensio, Lorena, Amaia, Aitor, Carlos Santiago, Estitxu, Maite, Jon Pascual, Estela, Lia y Mikel Rincón. Sois increíbles y no me cabe la menor duda de que nos faltan muchas aventuras por vivir juntos. Seguid siendo tan importantes para mí como lo habéis sido hasta ahora.

No podría faltar un agradecimiento particular para Ander Reizabal y Paula Gonzalez. Juntos empezamos esta aventura y juntos la terminaremos. Han sido tres años maravillosos en los que nos hemos reído, sufrido y desesperado juntos. No voy a olvidar todos los "marrones" que nos han caído ni tampoco todos los momentos que hemos disfrutado los tres. Espero teneros siempre ahí, ya sea para charlar científicamente o para divagar sobre el mundo.

Para finalizar, quiero darle las gracias al resto de amigos fuera de la universidad y a mi familia por todos los momentos compartidos en estos años. En especial, gracias a mi novia Alba; sabes que una parte de este doctorado te pertenece por todo el apoyo y cariño que me has dado y me sigues dando.

«Hay una fuerza motriz más poderosa que el vapor, la electricidad y la energía atómica: la voluntad»

Albert Einstein (1879 – 1955)

«Soy de las que piensan que la ciencia tiene una gran belleza. Un científico en su laboratorio no es sólo un técnico: es también un niño colocado ante fenómenos naturales que le impresionan como un cuento de hadas»

Marie Curie (1867 – 1934)

«Investigar es ver lo que todo el mundo ha visto, y pensar lo que nadie más ha pensado»

Albert Szent-Györgyi (1893 – 1986)

Resumen

En esta tesis se han obtenido y caracterizado diferentes compuestos poliméricos multifuncionales fotocurables con diferente capacidad de fotopolimerización, propiedades físico-químicas y funcionales. Se ha seleccionado el poliuretano acrilado (PUA) como matriz polimérica combinada con nanotubos de carbono de paredes múltiples (MWCNT), titanato de bario ($BaTiO_3$), óxido de indio y estaño (ITO), magnetita (Fe_3O_4), ferrita de cobalto (CFO), aleación de neodimio, hierro y boro (NdFeB) y el líquido iónico (IL) tetracloroniquelato de 1-butil-3-metilimidazolio ($[Bmim]_2NiCl_4$) para obtener diferentes respuestas funcionales y multifuncionales que incluyen piezorresistivas, dieléctricas, magnéticas y termocrómicas.

Los materiales y la tecnología experimentan una continua evolución. Actualmente, se han introducido de forma muy extendida las tecnologías de la información en el desarrollo y la utilización de nuevos materiales y han surgido nuevos conceptos como la Industria 4.0 y el Internet de las cosas (IoT). Internet juega un papel cada vez más importante en el mundo de los materiales y sus avances a nivel de ciencia y tecnología, facilitando la interconexión de información y procesos, entre otras cosas. Así, IoT se ha definido como la "red de dispositivos físicos, vehículos, electrodomésticos y otros elementos integrados con electrónica, software, sensores, actuadores y conectividad que permite que estos sistemas se conecten e intercambien datos".

De esta manera, la investigación en tecnologías de materiales se vuelve crítica y sigue existiendo la necesidad de nuevos materiales con características específicas para cada aplicación. Aquí, la combinación de nanotecnología y sistemas de materiales inteligentes y multifuncionales es uno de los aspectos clave para superar los desafíos en materiales funcionales avanzados y fabricación inteligente. Los materiales "inteligentes" se definen como materiales en los que una de sus propiedades puede modificarse de forma controlada en respuesta a un estímulo externo. Estos materiales sensibles a estímulos pueden sufrir, por ejemplo, variaciones de forma, propiedades mecánicas, transparencia, porosidad, características eléctricas o magnéticas en respuesta a estímulos externos térmicos, mecánicos o químicos, entre otros.

Muchos de estos materiales inteligentes empleados en la obtención de sensores y actuadores en el ámbito de IoT se basan en compuestos poliméricos que pueden procesarse mediante

técnicas convencionales, como disolución o fusión, pero que se producen cada vez más mediante técnicas de fabricación aditiva, como la impresión 3D. En este sentido, los composites poliméricos son ideales para estas aplicaciones, ya que aprovechan la combinación sinérgica de ventajas derivadas de sus diferentes constituyentes. La matriz polimérica ofrece ventajas de procesabilidad, así como flexibilidad y ductilidad, mientras que el relleno generalmente mejora o introduce una propiedad funcional específica, como la conductividad eléctrica o el magnetismo. Además, los polímeros ofrecen otras ventajas para las tecnologías de IoT: costo relativamente bajo, técnicas de fabricación bastante simples (sin necesidad de procesos especiales de sala limpia o de alta temperatura), se depositan fácilmente en varios sustratos y existe una amplia variedad de estructuras moleculares de polímeros como lineales o ramificados, entre otros.

Entre los diversos procesos empleados para la obtención de materiales inteligentes a emplear como sensores o actuadores, se debe destacar el curado UV o fotopolimerización. La fotopolimerización se define como un proceso de conversión rápida de composiciones especialmente formuladas, generalmente líquidas, en películas sólidas mediante irradiación con luz ultravioleta o visible. La fotopolimerización se define como una síntesis de polímeros por reacciones en cadena que se inician con la absorción de luz por un sistema polimerizable, la luz sirve como una herramienta de inicio y no interfiere con las etapas de propagación y terminación del proceso en cadena.

El extendido uso, cada vez mayor, del curado UV como técnica de obtención de materiales inteligentes se debe principalmente a sus grandes ventajas: es un método de curado rápido (en el rango de segundos o minutos), ocurre a temperatura ambiente reduciendo así el consumo total de energía y aumentando la eficiencia energética, pueden obtenerse patrones de alta resolución y emplea formulaciones sin solventes.

Los materiales a utilizar en este proceso de polimerización dependen en gran medida del proceso de fabricación y las tintas deben formularse de acuerdo con los requisitos específicos del método de impresión, incluyendo, como parámetros relevantes, las propiedades reológicas. La mayoría de las composiciones de materiales fotocurables en uso comercial consisten en mezclas de prepolímeros u oligómeros combinados con monómeros di o polifuncionales y fotoiniciadores. Dichas composiciones se pueden dividir en dos grupos: las que curan por un mecanismo radicalario y las que curan a través de un mecanismo iónico.

Entre los materiales disponibles, se debe prestar especial atención al poliuretano acrilado (PUA), un material adecuado para la preparación de composites poliméricos por sus propiedades físicas y químicas, así como por su baja viscosidad que permite una fácil dispersión del relleno. Además, este material muestra una excelente fotorreactividad, buenas propiedades mecánicas, buena adherencia, baja viscosidad de fusión, excelente resistencia a la abrasión, alta estabilidad química y resistencia a la intemperie, siendo adecuado para tecnologías de impresión sin solventes. El PUA también es de gran interés gracias a su seguridad ambiental y biocompatibilidad, bajo hinchamiento y elevada transparencia.

Todas las propiedades mencionadas hacen que el PUA sea apropiado para diferentes aplicaciones, incluidos revestimientos, adhesivos, textiles y membranas. Teniendo en cuenta sus características de curado UV, que permiten el diseño simple de patrones específicos, también es adecuado para aplicaciones biomédicas, que van desde la microfluídica hasta la ingeniería de tejidos. En este ámbito, los compuestos basados en PUA se han utilizado en recubrimientos y envases antibacterianos.

De este modo, la presente tesis se centra en el uso de una matriz polimérica de curado UV comercial basada en PUA junto con diversos aditivos o *fillers* que permitirán la obtención de composites funcionales a emplear como materiales inteligentes en el área de la sensórica.

Uno de los materiales desarrollados es el obtenido mediante la combinación de PUA con nanotubos de carbono de paredes múltiples (MWCNT). Estos composites MWCNT/PUA conteniendo entre 0,1 y 0,6 % en peso de MWCNT, permiten la obtención de materiales piezoresistivos, esto es, capaces de variar su resistencia eléctrica frente a una deformación mecánica. Tras estudiar el proceso de curado, las propiedades físico-químicas y funcionales del material, se ha observado que el contenido de MWCNT afecta de forma negativa el proceso de curado UV. Esto se ha corroborado con medidas de DSC que indican un proceso de poscurado de las muestras con altas temperaturas. Además, la estabilidad térmica y la transición vítrea (T_g) de los compuestos disminuyen al aumentar el contenido de MWCNT. Además, se ha obtenido un umbral de percolación eléctrica entre 0,1 y 0,4 % en peso de contenido de MWCNT y las propiedades mecánicas muestran valores apropiados de módulo inicial, tensión máxima y deformación máxima para aplicaciones de sensores.

Los compuestos con contenido de MWCNT de 0,3% y 0,5% en peso muestran una respuesta piezorresistiva caracterizada por valores de GF entre 0,8 y 2,6, siendo mayor para

compuestos con mayor contenido de relleno (0,5% en peso) que para compuestos alrededor del umbral de percolación (0,3% en peso). Además, se observa que el GF se estabiliza después de alrededor de 100 ciclos de tensión-deformación. Esto demuestra la idoneidad de los materiales obtenidos para el desarrollo de sensores piezorresistivos.

Cuando PUA se combinó con titanato de bario ($BaTiO_3$), se obtuvieron composites $BaTiO_3$/PUA con propiedades dieléctricas modulables adaptadas a aplicaciones electrónicas en función del contenido y tamaño de relleno. Así, se obtienen composites con contenidos de relleno de hasta 65% en peso para tamaños de relleno entre 50 nm y 200 nm. Estos materiales presentan una buena estabilidad térmica hasta 160ºC y gran flexibilidad mecánica. Además, la constante dieléctrica puede ser tan alta como 25 para las muestras con el mayor contenido de relleno, independientemente del tamaño de este. Los análisis teóricos realizados muestran cómo la respuesta dieléctrica en función de la concentración de relleno se describe adecuadamente mediante el modelo de Tinga.

Posteriormente, y con el fin de obtener materiales dieléctricos con propiedades ópticas diferentes a los obtenidos de mezclar PUA y $BaTiO_3$, se han preparado composites PUA con óxido de indio y estaño (ITO). Los materiales obtenidos presentan un contenido de relleno de hasta 25% en peso observándose que el tiempo de polimerización y la conversión del PUA dependen de la cantidad de ITO añadida. Los rellenos de ITO se dispersaron de forma correcta para todas las concentraciones de relleno (sin observarse grandes aglomerados), lo que da lugar a propiedades térmicas independientes de la cantidad de ITO y una mejora de las propiedades mecánicas con respecto al PUA puro. Por otro lado, la transmitancia óptica disminuye al aumentar la cantidad de ITO (la transparencia óptica disminuye un 20% en el rango visible para muestras que contienen 10% en peso de contenido de ITO) mientras que la constante dieléctrica aumenta al aumentar el contenido de ITO hasta un máximo de 33 para el material compuesto con 25% en peso de ITO. Esta muestra se utilizó para el desarrollo de un sensor capacitivo, que ha mostrado una alta reproducibilidad y rendimiento. De este modo, se ha demostrado la posibilidad de desarrollar compuestos poliméricos curables por UV de alta constante dieléctrica basados en ITO / PUA aplicables en electrónica impresa y recubrimientos funcionales.

Se han desarrollado materiales magnéticos fotocurables utilizando PUA y diferentes partículas como magnetita (Fe_3O_4), óxido de ferrita de cobalto (CFO) y una aleación de neodimio hierro boro (NdFeB). Para esos, las variaciones de relleno se dieron entre 1,3 y

6,3% en peso, 1,2 y 8,2% en peso, y 6,5 y 55,8% en peso para Fe_3O_4, CFO y NdFeB, respectivamente. La conversión en la fotopolimerización y el tiempo de curado disminuyen notablemente con la inclusión de magnetita y ferrita de cobalto, con una conversión total del 20% y 26% para las muestras de mayor contenido de relleno, respectivamente. Esta influencia en el proceso de curado UV se reduce agregando rellenos de NdFeB, lo que permite compuestos con hasta 55,8% en peso de contenido de relleno y una conversión de polimerización del 58%.

Las películas de compuestos magnéticos presentan una transición vítrea (T_g) independiente del tipo y contenido de relleno, mientras que el módulo de Young disminuye fuertemente para los compuestos a base de óxidos de hierro (Fe_3O_4 y CFO). Por otro lado, el módulo de Young para las muestras de NdFeB/PUA aumenta en todo el rango de contenido de relleno. La conductividad eléctrica d.c. es casi independiente del tipo y contenido de relleno, con un máximo de 1.0×10^{-9} S/m para la muestra de Fe_3O_4/PUA con un contenido de relleno de 6.3% en peso.

Las propiedades magnéticas demuestran que las partículas no sufrieron ningún proceso de degradación cuando se incluyeron en la matriz de PUA. La magnetización de saturación, la coercitividad y la remanencia pueden variarse cambiando el tipo y contenido de partículas, obteniendo materiales magnéticamente duros o débiles. Así, los materiales Fe_3O_4/PUA muestran una magnetización de saturación de hasta 3,70 emu/g, una remanencia de 0,27 emu/g y coercitividad nula; mientras que las muestras que contienen CFO muestran magnetización de saturación hasta 6,50 emu/g, remanencia de 1,69 emu/g y coercitividad de 2000 Oe. Los compuestos de NdFeB/PUA mostraron un comportamiento de material magnético duro con magnetización de saturación de hasta 63,86 emu/g, remanencia de 44,95 emu/g y coercitividad de 7000 Oe. Se concluye que es posible desarrollar materiales magnéticos procesables mediante fabricación aditiva con una respuesta magnética adaptada a los requisitos de aplicación específicos.

Finalmente, se ha desarrollado con éxito materiales para sensores de humedad flexibles activados por temperatura mezclando el PUA con el líquido iónico (IL) tetracloroniquelato de 1-butil-3-metilimidazolio ($[Bmim]_2NiCl_4$). Después de la incorporación de líquido iónico en una matriz polimérica curable por UV, se obtiene una estructura de red porosa sin cambios químicos relevantes ni en el IL ni en la matriz polimérica. Además, la incorporación del IL influye ligeramente en el proceso de curado por UV del polímero obteniendo en todos los

casos una conversión de curado del polímero superior al 84%. La inclusión del IL influye en las propiedades eléctricas y mecánicas de las muestras para los mayores contenidos de IL, obteniendo un aumento en la conductividad eléctrica y una disminución en el módulo de Young.

Se observó un efecto termocrómico de azulado a incoloro incluso con cargas bajas de IL. La humedad tiene una fuerte influencia en el efecto termocrómico hasta un 55% de humedad relativa y este proceso está influenciado térmicamente. Se comprobó que este efecto se debe a la absorción/deshidratación de agua por parte del ion $[NiCl_4]^{2-}$, que induce un cambio en el número de coordinación del Ni (II) de octaédrico a tetraédrico dependiendo de si está hidratado ($[Ni(H_2O)_6]^{2+}$ - azulado) o deshidratado ($[NiCl_4]^{2-}$ - incoloro). Por lo tanto, se demostró la idoneidad de los materiales híbridos curables por UV para recubrimientos inteligentes y multifuncionales procesables mediante tecnologías de fabricación aditiva.

Así, este trabajo demostró con éxito el desarrollo de materiales funcionales y multifuncionales curables con luz UV, compatibles con tecnologías de impresión, para aplicaciones electrónicas y de detección.

Abstract

Different photocurable multifunctional polymer composites have been obtained and characterized according to their photopolymerization capability, physico-chemical and functional properties. Polyurethane acrylate (PUA) has been selected as polymer matrix combined with multi-walled carbon nanotubes (MWCNT), barium titante ($BaTiO_3$), indium tin oxide (ITO), magnetite (Fe_3O_4), cobalt ferrite (CFO), neodymium iron boron alloy (NdFeB) and 1-buthyl-3-methylimidazolium tetracholonickelate ($[Bmim]_2NiCl_4$) ionic liquid (IL) to obtain different functional and multifunctional responses including piezoresistive, dielectric, magnetic and thermochromic.

The addition of fillers into PUA lead to a decay of the photopolymerization process whenever the filler presents UV light absorption, being higher the effect when higher filler content is added. This effect is particularly highlighted for MWCNT, Fe_3O_4 and CFO. On the other hand, filler addition does not lead to new intermolecular interactions between the fillers and the polymer within the cured materials.

Attending to the physico-chemical properties, the glass transition temperature (T_g) decreases when fillers are added, in particular for MWCNT but also for $BaTiO_3$, Fe_3O_4, CFO and NdFeB. The addition of ITO and IL, on the other hand, has not significantly affect the T_g of PUA. With respect to mechanical properties, an increase on the Young modulus (E) is obtained excepting for higher filler contents. At high filler concentration, filler agglomeration occurs and the maximum elongation (ε_b) also decreases. With respect to the electrical response, the inclusion of fillers increases d.c. electrical conductivity (MWCNT, Fe_3O_4, CFO, NdFeB and IL) and dielectric constant ($BaTiO_3$ and ITO).

Different functional and multifunctional responses have been added to the UV curable polymer, depending on the filler. The inclusion of MWCNT induce a piezoresistive response characterized by GF values between 0.8 and 2.6. $BaTiO_3$ and ITO, strongly increase the dielectric constant from 7.5 to 25 and up to 33, respectively. In the case of Fe_3O_4, CFO and NdFeB, magnetic composites with tailored magnetic properties (from hard to soft magnetic ones) are obtained. Saturation magnetization values up to 63.86 emu/g, remanence up to 44.95 emu/g and coercivity up to 7000 Oe can be obtained depending on filler type and content used. Finally, IL allows the preparation of temperature activated thermochromic

humidity sensor with a colour change from blue to colourless, depending on relative humidity.

Thus, this work successfully demonstrated the development of UV photocurable functional and multifunctional materials, compatible with printing technologies, for electronic and sensing applications.

Table of Contents

Chapter 1

Introduction

The main concepts, terms and recent developments in UV curing process and UV curable smart materials for printing technologies are presented, focusing on both materials and processes. The curing mechanisms and the main materials used in UV photocurable resins are reviewed as well as the main smart and multifunctional materials obtained based on them. Finally, the general objectives and outlook of the thesis is indicated.

1.1. Industry 4.0 and Smart Materials

Material is defined as a substance or mixture of substances that constitute an object. Materials have been always used and have to support loads, transmit or reflect light, insulate or conduct electricity or heat, resist in often-hostile surroundings, accept or reject magnetic flux, and all this without being dangerous or expensive [1]. Thus, materials have been and are so important that they have designed the ages in which history has been divided. In this sense, the Stone Age, the Bronze Age or the Iron Age are representative examples still in use in a general public context [2]. Materials science has this become one of the main research topics in the modern era and, nowadays, polymers and polymeric materials occupy a relevant role in the recent advances in science and technology [3].

Polymers are substances composed of macromolecules, long sequences of one or more species of atoms or groups of atoms linked to each other by primary, usually covalent, bonds [4]. Polymers can be classified in different ways. Based on their origin or source, they can be divided in natural and synthetic polymers; based on their polymerization structure, linear, branched and crosslinked; based on the synthesis process, step growth polymers (condensation or addition) and chain growth polymers, etc [5]. However, the most common way to classify them is attending to their behaviour against temperature, being clarified in thermoplastics, elastomers and thermosets [4]. Nowadays, polymer-related research is mostly driven by obtaining new polymeric materials with advanced characteristics or multifunctional properties, as well as on developing environmental friendlier materials. While in certain cases they do not have a defined use, the large majority are designed and synthesized for specific applications.

Related to the evolution at materials and technological level, as well as the highly extended introduction of information technologies, concepts such as Industry 4.0 and Internet of Things (IoT) have emerged [6–8]. In an ever-increasing number of advances in science and technology, Internet plays an increasing role facilitating the interconnection of information and processes, among other [9,10]. Furthermore, modern society demands energy,

infrastructures and solutions based on smart and multifunctional materials, in the scope of the Internet of Things concept [11–13]. This has been defined as the "network of physical devices, vehicles, home appliances and other items embedded with electronics, software, sensors, actuators, and connectivity which enables these things to connect and exchange data" [14,15]. In this framework, the number of IoT devices increases 31% year over year, being 8.4 billion in 2017 and estimated as many as 20.4 billion by 2020 [16]. **Figure 1.1** shows an example of the world connectivity and the IoT concept.
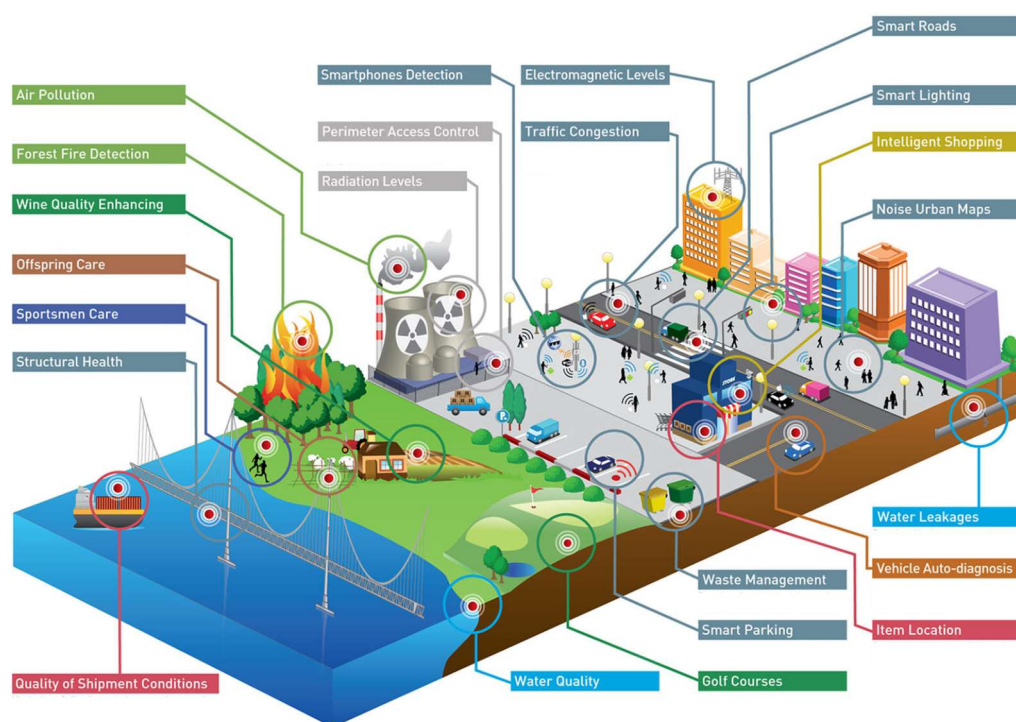
Figure 1.1 – Representation of the world connectivity and the Internet of Things (IoT) concept. Reproduced with permission *[17]*. Copyright 2015, CeDeWu Sp. z o.o.

Many sensors and actuators related with the IoT concept are based on polymer composites [11,18] that can be fabricated by conventional techniques, such as solvent-casting or extrusion, but which are increasingly being produced by additive manufacturing techniques, such as 3D printing [19,20]. In this sense, polymer composites are ideal for these applications, since they take advantage of the synergistic combination of advantages deriving from their different constituents. The polymeric matrix offers processability advantages as well as flexibility and ductility, while the filler usually enhances or introduces

a specific functional property, such as electrical conductivity or magnetism [21]. In addition, the aforementioned polymers offer other advantages for IoT technologies: relatively low cost, quite simple fabrication techniques (no need for special clean-room or high temperature processes), easily to be deposited on various substrates and a wide choice of molecular structures from linear to branched polymers, charged or neutral particles, among others [22].

In this way, investigation in material technologies becomes critical for the varied applications not just in the area of sensors and actuators for the Internet of Things, but also for cyber-physical systems (CPS) and robot-human interactions. Further, in most humidity, temperature, force or other stimuli responsive sensors one type of material is not enough and multimaterial sensors become necessary. This fact, together with the IoT and Industry 4.0 idea of shrinking volume of sensing systems, reducing costs and energy required, makes innovation on materials increasingly demanded [23,24]. There is still a need for new materials with specific characteristics for each application. Here, the combination of nanotechnology and smart and multifunctional material systems are one of the key aspects to overcome challenges in advanced functional material and smart manufacturing [18].

Over the past years, important efforts have been applied to expand the application of nanomaterials through the development of smart and multifunctional composites for their applications in areas ranging from micro devices, to sensor and actuators, as well as energy and biomedical applications [10,18,25]. "Smart" materials are defined as a material in which one of its key properties can be altered in a controlled manner in response to an external stimulus [10,25,26]. These stimuli-responsive materials can undergo, for example, variations in shape, mechanical properties, transparency, porosity, electrical or magnetic characteristics in response to thermal, mechanical or chemical external stimuli, among others [18]. **Table 1.1** summarizes the main types of smart materials [27].

Table 1.1. Main types of Smart Materials classified according to their basic physical/chemical effects.

Response / Stimulus	Electrical	Magnetic	Optical	Thermal	Mechanical	Chemical
Electrical		Magneto-electronics, spin-electronics, spintronics	Electro-chromic, electro-luminescent, electro-optic, piezo-chromic, Kerr Effect, Pockel Effect	Thermo-electric (Peltier)	Piezo-electric, electro-strictive, electro-rheological, electro-kinetic	Electrolysis, electro-chemical, bio-electric, electro-migration
Magnetic	Magneto-electronics, spin-electronics, spintronics, Hall Effect		Magneto-optic, piezo-chromic	Magneto-thermal	Magneto-strictive, magneto-rheological	Nuclear-magnetic-resonance, magneto-chemical
Optical	Photo-conductive	Opto-magnetic	Optical bi-stability	Photo-thermic	Opto-mechanical, photo-acoustic	Photo-chemical, photosynthesis, photocatalyst
Thermal		Curie point	Thermo-chromic		Shape-memory	
Mechanical	Piezoelectric, electrostrictive	Magnetostrictive			Rheopexic, auxetic, shear-thining, dialants, non-Newtonian, psuedo-plastic	
Chemical		Magneto-chemical	Colour-change, litmus, luminiscence	Exothermic, endothermic		Catalysis

One of the key implementation areas of smart materials are sensors and actuators, allowing to improve, monitoring, feedback and safety, key issues of the Internet of Things and Industry 4.0 paradigms [28]. In this way, smart materials are an intense research area in which new materials, technologies and applications will emerge in the near future [10,25]. Application areas of smart and multifunctional materials expand from consumer electronics, civil engineering, aerospace and automobile to health care and wearables applications [29,30]. The potential application of smart materials would allow solving engineering problems with improved efficiency and provides an opportunity for the development of new solutions and products [18,31].

On the other hand, strategic and technological problems are still hindering the implementation potential of smart materials, despite their important advantages and specificities [25,32].

Namely, silicon-based smart materials are manufactured using the time-consuming, expensive, and complicated fabrication processes of traditional semiconductor devices. Further, those manufacturing methods are often based on subtractive processes. In contrast, several of the recently developed smart materials can be implemented by additive manufacturing (AM) [18,33].

Additive manufacturing is rapidly expanding and modifying the way in which products are designed and manufactured. This technology allows to create complex geometries with customizable material properties, with design freedom and environmental advantage [34], by transforming designed files into fully functional products. On the other hand, the rapid spread of a wide variety of technologies associated with AM, leads to an absence of a comprehensive set of materials, design principles and manufacturing guidelines.

In this scope, UV curable polymer formulations are distinctively suitable for being implemented by AM technologies due to their rapid cure, wide range of properties, and

dimensional accuracy, being inks based on UV curable polymers increasingly used to fabricate smart materials [35].

Since its onset, the UV curing industry has become one of the most rapidly developing ones within the coatings industry [35,36]. With the introduction of photocuring of coatings as a viable industrial process well over a decade ago, the UV curing industry has followed a line of steady growth [36].

Among the various curing processes, UV-triggered radical polymerization represents an economic, fast and non-toxic method [37], especially for coatings. The advantages of UV curing compared to traditional drying techniques which rely whole or partly on the evaporation of solvents are the "rapid solidification", high solvent resistance of the cured films, reduced VOC (volatile organic compounds) emissions, high flash points of the ink and overall improved "environmental friendliness", among others. Further, for the electronics industry, in allows as improved pattern definition.

Below is presented the recent development in UV curable printing technologies with respect to technologies, materials and applications. The following sections deal with photoinitiators, monomers and oligomers characteristics of photocurable materials and as well as with the smart materials obtained by UV curable systems.

1.2. UV curing technology and materials

1.2.1. Mechanism and formulations

The use of UV-curable formulations is increasing at a fast rate [38]. The main reasons for this rapid growth are their fast curing method –in the range of seconds or minutes-, the room temperature processing reducing thus the overall energy consumption, space and energy efficiency -smaller curing units as compared with ovens for baking in thermal cure-, high resolution patterns can be obtained and the use of solvent-free formulations [39]. In this way, UV-curing is very attractive for the development of engineering applications.

The basic principle that occurs when using UV light is photopolymerization or photocuring (**Figure 1.2**). Photocuring is commonly defined as a process of rapid conversion of specially formulated, usually liquid solventless compositions into solid films by irradiation with ultraviolet or visible light [40]. Photopolymerization (Figure 1.2) is defined as a synthesis of polymers by chain reactions that are initiated upon the absorption of light by a polymerizable system, light serving only as an initiating tool and it does not interfere with the propagation and termination stages of the chain process [41].
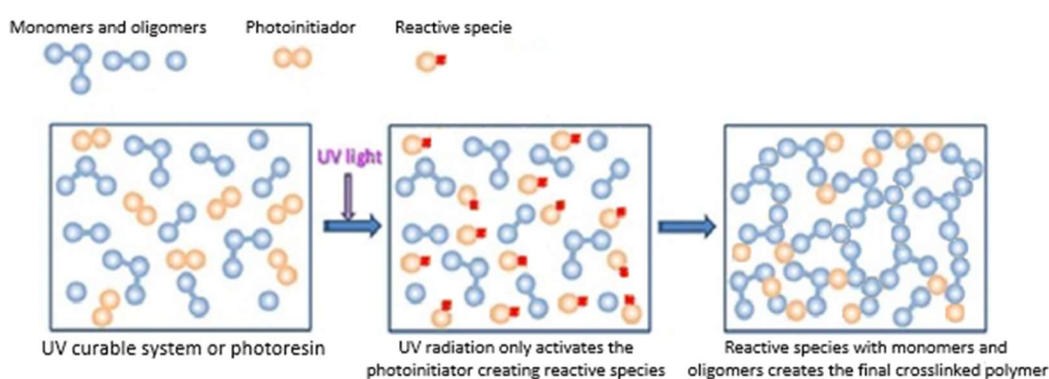
Figure 1.2 – Schematic representation of the photopolymerization process.

The materials to be used in this polymerization process strongly depend on the fabrication process, which is the scope of the present paper and the inks must be formulated in agreement with the specific printing processes requirements, including, as a relevant parameter, rheological properties [18]. The majority of the compositions of photocrosslinkable materials in commercial use consist of mixtures of prepolymers or oligomers combined with di- or polyfunctional monomers and photoinitiators [42]. Such compositions can be divided into two groups: (1) the ones that cure by free-radical mechanism and (2) the ones that cure by an ionic one.

1.2.1.1.   Free radical curing mechanism

The synthesis of macromolecules by free radical chain polymerization of monomers begins with the generation of free radicals, which are conveniently performed through photoreactions of the initiator molecules. The simplified overall mechanism is described in

Figure 1.3. The most widely used UV-curable resins are based on acrylate, which show high reactivity, i.e. short reaction times in the order of fractions of a second, and offer a large choice of monomers and oligomers. Acrylate-based resin systems typically consist of three basic components: photoinitiator (which generates free radicals when exposed to UV light), functionalized oligomers or prepolymers (which forms the backbone of the polymer network) and monomers (which acts as a reactive diluent to adjust the system viscosity) [39].

Photoinitiation

$$\text{Initiator} \xrightarrow{h\nu} \text{Initiator*} \begin{cases} \xrightarrow[\text{Type II}]{RH} R\bullet + \text{Product} \\ \xrightarrow[\text{Type I}]{RH} R_1\bullet + R_2\bullet \end{cases}$$

$$R\bullet \ (\text{or } R_1\bullet \ ; R_2\bullet) \quad + \quad M \quad \longrightarrow \quad R\,M\bullet$$

Propagation

$$R\,M\bullet \quad + \quad n\,M \quad \longrightarrow \quad R\,M_{n+1}\bullet$$

Chain-Transfer

$$R\,M_{n+1}\bullet \quad + \quad R\,H \quad \longrightarrow \quad R\,M_{n+1}H \quad + \quad R\bullet$$

Termination

$$R\,M_{n+1}\bullet \quad + \quad R\,M_{n+1}\bullet \quad \longrightarrow \quad R\,M_{n+1}M_{n+1}\,R$$

$$R\,M_{n+1}\bullet \quad + \quad R\,M_{n+1}\bullet \quad \longrightarrow \quad R\,M_{n+1} \quad + \quad M_{n+1}\,R$$
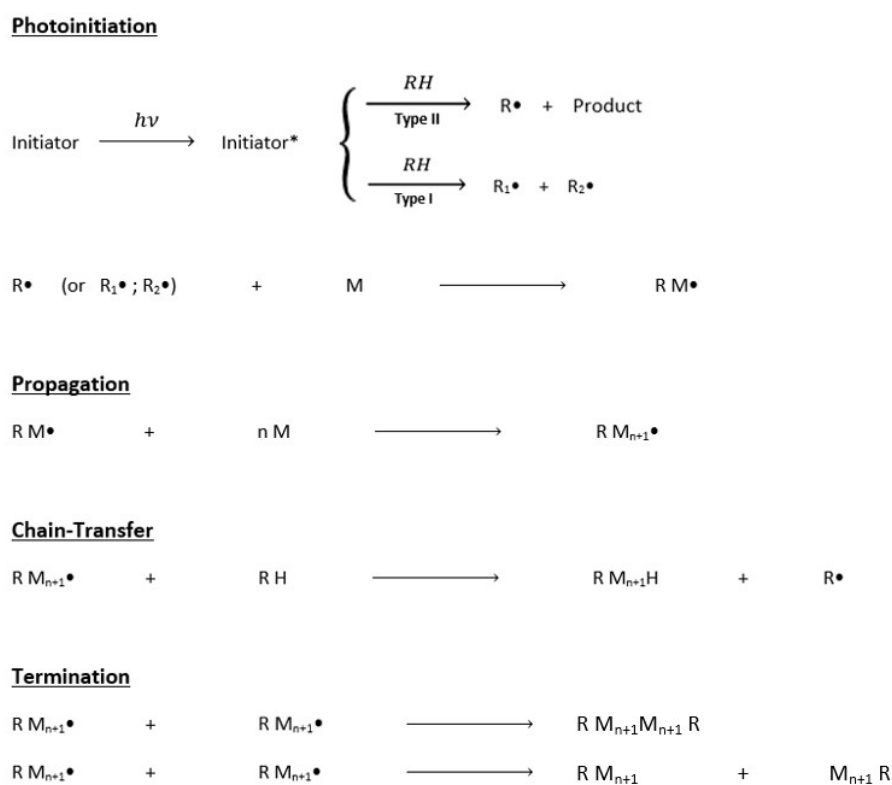
Figure 1.3 – Schematic representation of a free radical polymerization reaction of monomer M, a commonly compound with a C=C bond with photoinitiator R.

There are two types of compounds that are commonly used as photoinitiators of free radical polymerizations, which differ in their mechanism for the generation of reactive free radicals: type I or unimolecular photoiniators and type II or bimolecular photoinitiators. The type I photoinitiators are organic molecules that undergo a very rapid bond cleavage after absorption of a photon to generate two free radicals that can start the polymerization. The type II photoinitiators, organic molecules too, form relatively long lived excited triplet states

capable of undergoing hydrogen-absorption or electro-transfer reactions with co-initiator molecules that are deliberately added to the monomer containing system [39]. Typical type I and type II photoinitiators are listed in **Table 1.2**. In general, the used monomers, oligomers or prepolymers are the same for both types of photoinitiators.

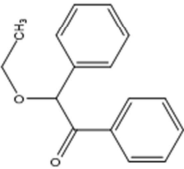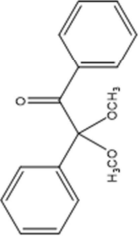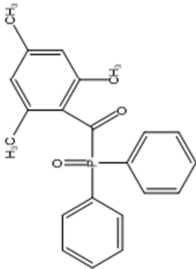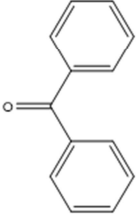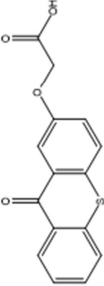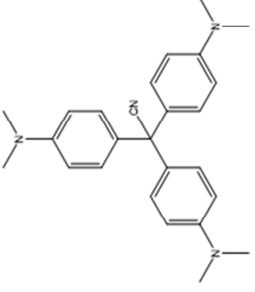Most of type I photoinitiators contain aromatic carbonyl groups since these compounds undergo rapid bond cleavage resulting in the formation of a pair of radicals. Benzoin ethers, like benzoin ethyl ether, were the first commercially used class of unimolecular photoinitiators and they cleave into benzoyl radical and benzyl ether radical by UV absorption [43]. Benzil ketals, such as 2, 2-dimethoxy-2-phenylacetophenone, is another effective photoinitiator with good package stability and which photocleavage produces benzoyl and dimethoxybenzyl radicals [44]. Acyl phosphine oxides, such as 2,4,6-trimethylbenzoyl)diphenyl-phosphine oxide, produces radicals that are much more reactive towards olefinic compounds than carbon-centred radicals [45,46].

Type II photoinitiators are organic compound that can form long-lived triplet states after absorbing a photon. These triplet species can abstract a hydrogen or an electron from co-initiator species to produce free radicals. Benzophenone, thioxanthone derivates or other ketones like 1,2-diketones are typical bimolecular photoinitiators that abstract hydrogen atoms from hydrogen donors to yield excited complexes that initiate polymerization [47]. Those compounds show the advantage of reducing the oxygen inhibition [52].

In spite of the number of available photoinitiators, the search for new initiators is ongoing with the main objective of obtain more efficient photoinitiators [53]. For example, S-(4-benzoyl)phenylthiobenzoate, BpSBz, has been found to be a type I photoinitiator. Upon exposure to UV light it is cleaved into free radicals which initiate the polymerization of methyl methacrylate [54]. Most free-radical photoinitiator structures after initiation process can be found in the references attached in the **Table 1.2**.

Table 1.2 – Chemical structures of typical photoinitiators used in photopolymerization by free radical and ionic mechanisms.

Photopolymerization mechanism	Type	Class	Example	Chemical Structure	Reference
Free radical	I	Benzoin ethers	Benzoin ethyl ether		[43]
Free radical	I	Benzil ketals	2, 2-dimethoxy-2-phenylacetophenone		[44]
Free radical	I	Acyl phosphine oxides	2,4,6-trimethylbenzoyl)diphenyl-phosphine oxide		[45,46]
Free radical	II	Benzophenone derivatives	Benzophenone		[47]
Free radical	II	Thioxanthone derivates	2-((9-oxo-9H-thioxanthen-2-yl)oxy)acetic acid		[47]

			Structure	Ref.
Free radical	II	Benzil		[47]
Ionic	Cationic	Diaryliodonium salt	(4-Methylphenyl) [4-(2-methylproyl)phenyl] iodonium hexafluorophosphate	[48]
Ionic	Cationic	Triarylsulfonium salt	Diphenyl(4-methoxyphenyl)sulfonium hexafluoroantimonate	[49]
Ionic	Cationic	Ammonium salt	N-ethoxy-2-methylpyridinium hexafluorophosphate	[50]
Ionic	Anionic	-	Crystal violet leuconitrile (CVCN)	[51]

Ionic mechanism	Anionic	-	Malachite green leucohydroxide (MGOH)	[51]

Malachite green leucohydroxide
(MGOH)
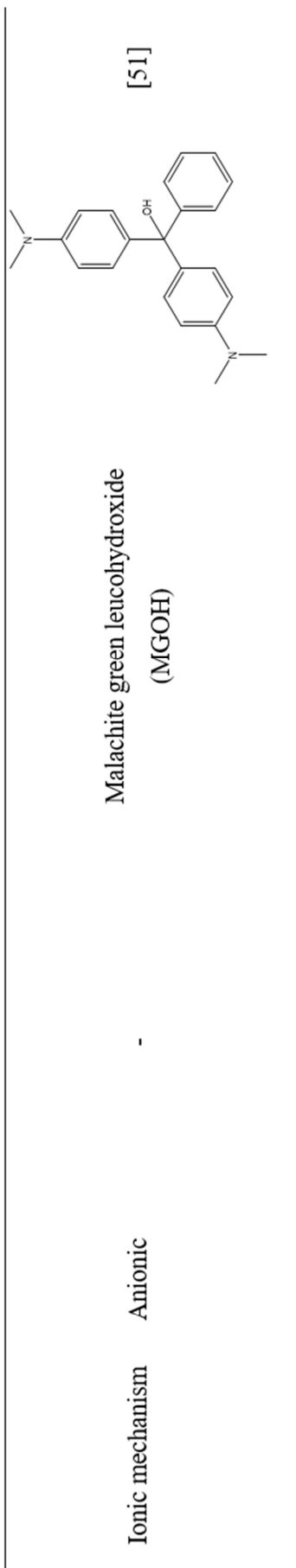
In the case of monomers, also called reactive diluents, used in photopolymerization by free radical mechanism, a large number of them are commercially available. **Table 1.3** presents some of the most used monomers. A monomer is selected for a specific application or processing technology based upon its effect on viscosity, curing speed, film properties, shrinkage during polymerization, cost, shelf life, volatility, odor, and toxicity. Acrylates are the most widely used reactive diluents [44].
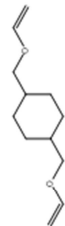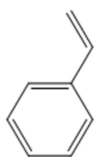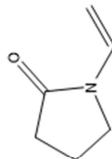
When selecting a monomer, a high functionality (number of double bonds that will be attacked and will lead to polymerization) is pursued for fast reactions. However, this can result in early gelation or vitrification of the cross-linked structure, hindering complete conversion, being mono and difunctional monomers the most widely used. In addition, the introduction of heterocyclic structures with oxygen causes a substantial acceleration of the polymerization rate [40]. 2-Ethyl hexyl acrylate (EHA) [55], n-butyl acrylates (BA) [56], 1,4-butanediol diacrylate (BDDA) [57] and diethyleneglycoldiacrylate (DEGDA) [58] are some examples of acrylate monomers.
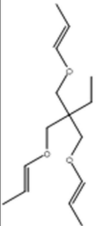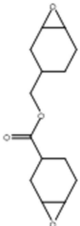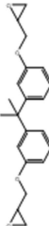
Trifunctional and tetrafunctional monomers are also used but to a lesser extent. Examples of a trifunctional monomer are acrylate or methacrylate esters of glycerol, such as pentaerythritoltriacrylate (PETA), widely used in printing inks. A tetrafunctional monomer example is pentaerythritol tetraacrylate, used in adhesives and coatings [59]. However, in most of the cases a mixture of various monomers is used.

Another type of monomers used in free radical polymerizations are the vinyl ethers. Compared to acrylates, vinyl ethers show the advantages of high diluting power and low toxicity. Diethyleneglycol divinyl ether (DEGDE), cyclohexane dimethanol divinyl ether (CHDMDE) and triethylene glycol divinyl ether (TEGDE) are some examples of this type of monomers [60]. Styrene, which is the most widely used reactive diluent for unsaturated polyester resin systems, and N-vinyl pyrrolidone are two remarkable reactive diluents. Styrene shows a good performance, with a relatively low cost and is highly flexible when cured [59,65].

Table 1.3 – Commonly used monomers in photopolymerization by free radical and ionic mechanisms.

Photopolymerization mechanism	Class	Example	Chemical Structure	Merits	Drawbacks	Reference
Free radical	Monoacrylates	2-Ethyl hexyl acrylate (EHA)		Good flexing action	Volatile, slow cure and poor solvent resistance	[55]
Free radical	Monoacrylates	n-butyl acrylates (BA)		Good viscosity reducer and flexing action	Volatile, slow cure and poor solvent resistance	[56]
Free radical	Diacrylates	1,4-butanediol diacrylate (BDDA)		Relatively good viscosiy reducer and low volatility	Suspected skin irritation sensitisers	[57]
Free radical	Diacrylates	Diethyleneglycol diacrylate (DEGDA)		Good viscosity reducer	Adverse dermatitic and toxicity properties	[58]
Free radical	Triacrylates	Pentaerythritol triacrylate (PETA)		Rapid cure	Eye irritant and suspect to be carcinogenic	[59]
Free radical	Tetracrylates	Pentaerythritol tetraacrylate		Low volatility	Eye irritant and suspect to be carcinogenic	[59]

Polymerization	Class	Diluent	Advantages	Disadvantages	Ref.
Free radical	Vinyl ethers	Diethyleneglycol divinyl ether (DEGDE)	High diluting power and low toxicity	Eye irritant	[60]
Free radical	Vinyl ethers	1,4-Cyclohexanedimethanol divinyl ether (CHDMDE)	High diluting power and low toxicity	Eye irritant and toxicity properties	[60]
Free radical	Vinyl ethers	Triethylene glycol divinyl ether (TEGDE)	High diluting power and low toxicity	-	[60]
Free radical	-	Styrene	Low cost and high flexibility when cured	Volatile and hazardous	[44]
Free radical	-	N-vinyl pyrrolidone	Low toxicity and high flexibility when cured	-	[44]
Ionic	Vinyl ethers	Diethyleneglycol divinyl ether	Fast photopolymerization	Inconvenient and expensive synthesis	[61]

Ionic	Propenyl ethers	Trimethylolpropane tripropenyl ether		Good reactivity	-	[62]
Ionic	Propenyl ethers	Trimethylolpropane dipropenyl ether		Good reactivity	-	[62]
Ionic	Epoxides	3,4-Epoxycyclohexylmethyl-3',4'-epoxycyclohexane carboxylate		Low shrinkage and chemical and thermal resistance	Fragility and low toughness	[63]
Ionic	Epoxides	Diclycidylether derivative of bisphenol A (ADE)		Low shrinkage and chemical and thermal resistance	Fragility and low toughness	[64]
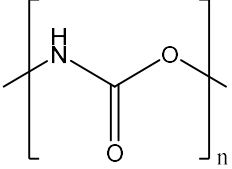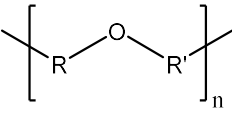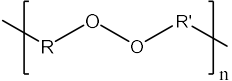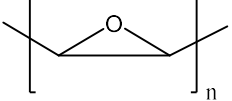
For oligomers, also called prepolymers, and in the same way as with monomers, acrylated ones are most frequently used for photopolymerization by free radical mechanism due to their higher reactivity, lower volatility, environmental degradation resistance, low color and chemical resistance in comparison with other oligomers [66]. The chemical structure of the oligomers has influence on the viscosity of the reaction mixture, which affects both the propagation and the termination polymerization steps. Thus, the final properties of the obtained material depend on the oligomer structures.

There are four basic structures for acrylated oligomers employed in photopolymerization that contains the following chemical groups: polyurethane, polyethers, polyesters and epoxy resins. **Table 1.4** shows the structures of these chemical groups and the merits and drawbacks for all of them. The typically used oligomers are composed by these mentioned chemical groups and acrylated groups on the extremes of the structures. The functionality (number of acrylated groups) can be two, three, four or higher and the basic chemical structures can be more complex [44].

Particular attention has to be paid to polyurethane acrylate (PUA), a suitable material for the preparation of polymer composites due to its physical and chemical properties, as well as their low viscosity that allows easy filler dispersion [67]. In addition, this material shows excellent photoreactivity, mechanical properties, good adhesion, low melting viscosity, excellent abrasion resistance, high chemical stability and weatherability, being suitable for solvent-free printing technologies [68,69]. PUA is also of large interest due to its environmental safety and biocompatibility, low swelling and high transparency [70].

All mentioned properties make PUA appropriate for different applications, including coatings, adhesives, textiles and membranes [71]. Taking into account its UV curable characteristics, allowing the simple design of specific patterns, it is also suitable for biomedical applications, ranging from microfluidics to tissue engineering [70]. In this scope, composites based on PUA have been used in antibacterial coatings and packaging [71].

Table 1.4 – Commonly used oligomers for photopolymerization by free radical mechanism.

Type	Chemical Structure	Merits	Drawbacks
Polyurethane		Versatility, best combination of hardness and elasticity, weatherability and adequate H_2O resistance	Aromatic yellow, aliphatics costly, aliphatics toxic and plasticized by H_2O
Polyether		Fairly good adhesion, flexibility, elasticity and UV-resistance	Low glass transition
Polyester		Fairly good adhesion, versatility and hardness	Poor UV-resistance and hydrolytic stability
Epoxy		Adhesion, hydrolytic stability, hardness and acid resistance	Poor UV-resistance and high viscosity

1.2.1.2. Ionic curing mechanism

UV-induced free-radical polymerization has enjoyed commercial success over ionic polymerization. However, the UV-induced ionic curing systems are finding increasing application in several specialized fields due to their advantages compared to free radicals: no oxygen inhibition, minimal sensitivity to water and the ability to polymerize vinyl ethers, oxiranes (epoxides) and other heterocyclic monomers that do not polymerize by a free radical mechanism [72]. In addition, ionic photopolymerization has the ability for dark cure, cation-initiated polymerization can continue after exposure to the radiation source until the reactive cations become immobilized. Moreover, the shrinkage of the polymers during ionic photocuring is lower than in free radical photocuring, showing cured material, in general,

high mechanical properties and good adhesion to various substrates [73]. **Table 1.5** shows a comparison of different material properties related to free radical and ionic curing.

Table 1.5 – Comparison of some relevant materials characteristics obtained after free radical or ionic curing.

Property	Free-radical curing	Cationic curing
Cure speed	Faster	Slower
Oxygen inhibition	Yes	No
Adhesion	"Problems"	Excellent
Toxicity	Skin irritation	Acceptable
Moisture inhibition	No	Yes
Post-irradiation cure	No	Yes
Formulation latitude	Good	Limited
Through cure	Fair	Good
Viscosity	Higher	Lower
Cost	Moderate	Higher

In the same way as free-radical polymerization systems, two types of compositions curing by ionic mechanism can be obtained: cationic and anionic photopolymerization systems. It is worth to mention that the possibility that photoinitiated polymerization can occur through an anionic mechanism has long been overlooked and, even today, literature reports on anionic photopolymerization are rare [41].

Cationic photopolymerization was discovered by Prof. Crivello [74–76] in the late 70s. This mechanism is initiated with photoinitiators that can absorb UV light to create reactive cations that initiate the polymerization reaction. Onium salt-type photoinitiators were first used. They have general structure that consists of an organic cationic moiety with a positive charge on a heteroatom and a counter anion in the structure. This category includes aryldiazonium, diaryliodonium, triarylsulfonium, alkyl-arylsulfonium, phenacylsulfonium, phosphonium, ammonium and addition-fragmentation-type onium salts, among others [77]. Some examples such as (4-Methylphenyl) [4-(2-methylpropyl)phenyl] iodonium

hexafluorophosphate [48], diphenyl(4-methoxypheny1)sulfonium hexafluoroantimonate [49] or N-ethoxy-2-methylpyridinium hexafluorophosphate [50] are shown in **Table 1.2**.

The difference between anionic and cationic photopolymerization only lies in the photoinitiator, anionic photopolymerization working in the same way as cationic photopolymerization. The initiation mechanism is the photoinduced release of a reactive anion, which is added to the monomer. The polymer is then formed through the repetitive addition of monomers to the growing anionic chain. This mechanism has been found to photoinitiate the polymerization of methyl 2-cyanoacrylate (CA) using crystal violet leuconitrile (CVCN) and of malachite green leucohydroxide (MGOH) [51] (**Table 1.2**). More recent studies have revealed other compounds such as ketoprofen [78] or more complex compounds such tertiary-amine-releasing systems, aromatic formamides, cobalt-amine complexes, amine–imides and aminoketones [43]. Most ionic photoinitiator structures after initiation process can be found in the references attached in the **Table 1.2**.

In the case of monomers used in cationic photopolymerization, different types have been proposed and reported in literature, mainly epoxides, vinyl ethers and propenyl ethers [72]. Vinyl ethers are really attractive since their photopolymerization is rather fast and photocuring rates are in many cases faster than for the corresponding free-radical photopolymerization of acrylic monomers. However, their synthesis is expensive. A good alternative is the use of propenyl ethers, which show good reactivity. Some examples of vinyl and propenyl ethers typically used are diethyleneglycol divinyl ether, trimethylolpropane tripropenyl ether and trimethylolpropane dipropenyl ether [61,62], which are shown in **Table 1.3**.

Epoxides are another type of monomers employed in cationic photopolymerization due to their high mechanical properties, relatively low shrinkage, and chemical and thermal resistance. Nevertheless, epoxy matrix suffers from fragility and low toughness. 3,4-epoxycyclohexylmethyl-3',4'-epoxycyclohexane carboxylate and diclycidylether derivative of bisphenol A (ADE) are some examples [63,64] shown in **Table 1.3**.

It should be noted that the oligomers employed in ionic photopolymerization, both cationic and anionic, show similar structures to the mentioned monomers but with a large chain structure, high functionality and more voluminous groups leading to higher viscosity [55].

1.2.2. Cure extent evaluation

Control the UV curing process is as important as the choice of the photoinitiator and the monomers and oligomers to be used. Photopolymerization typically occurs within seconds or minutes, being an important issue to study the kinetics of photopolymerization both quantitatively and qualitatively. In that, the most used methods to evaluate the cure extent are Differential Scanning Photocalorimetry (photo-DSC), Real Time Infrared Spectroscopy (RT-IR) and Confocal Raman Microscopy.

Differential scanning photocalorimetry measures the heat flux evolved by the photo-initiated exothermal reaction as a function of time at a given temperature. It is very well suited for the determination of kinetic parameters, such as enthalpy, degree of conversion, rate constants, and Arrhenius parameters, among other relevant parameters [44]. This technique measures the heat flux evolved by the photo-initiated (i.e. UV initiated) exothermal reaction as a function of time at a given temperature. The main advantage of photocalorimetry resides in a good temperature control for reactions having a $t_{1/2}$ value (time to reach 50 % conversion) higher than 15 s. However, this technique provides only a measure of the global heat flow without any information about the specific chemical reaction. Moreover, because of the low thermal conductivity of the material, the increase in sample temperature due to the exothermicity of the photopolymerization reaction is high, preventing the study of very fast photopolymerization kinetics with $t_{1/2} < 15$ s [79]. An instrument setup of photo-DSC is presented in **Figure 1.4** [44].
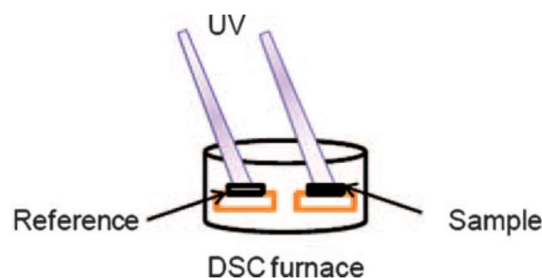
Figure 1.4 – Schematic representation of the Differential Scanning Photocalorimetry (Photo-DSC) setup.

There are several cases where the extent of the cure has been evaluated by this technique. Photo-DSC has been used to study the cure kinetics of UV-initiated cationic photo-polymerization of epoxy resin monomers in presence of different photoinitiators and to investigate the photo-reactivity with respect to their chemical structure [80]. The effect of the presence of a hyperbranched OH-functionalized polymer (HBP) on the kinetics of cationic photopolymerization of an epoxy system was also investigated using Photo-DSC and RT-IR [81]. Similarly, Photo-DSC was applied to study the gelation and photopolymerization of some multifunctional acrylates [82].

The development of the Real-Time Infrared Spectroscopy technique has improved the ability to monitor UV-curing processes. RT-IR, with its milliseconds resolution time, has been successfully used to monitor photopolymerizations occurring within a fraction of a second. RT-IR spectroscopy involves the exposure of a photopolymerizable sample simultaneously to IR and UV radiations, as represented in **Figure 1.5**. Therefore, this technique enables to monitor the specific changes in chemistry during UV-curing by following the decay of the stretching vibrations of the reactive functional groups. Thus, from the recorded profile the degree of conversion can be evaluated, i.e. the amount of unreacted functional groups that remain in the UV-cured polymer [44,79].
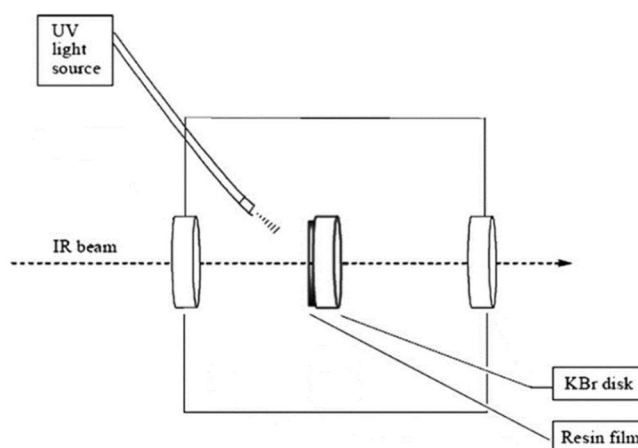
Figure 1.5 – Schematic representation of a Real-Time Infrared Spectroscopy (RT-IR) setup.

RT-IR spectroscopy is being used for several years, for example, for the characterization of the UV curing kinetics of a thiol-ene system containing trimethylolpropane tris(2-mercaptoacetate) and trimethylolpropane diallyl ether [83]. Real-Time FTIR-ATR spectroscopy has been also used to study the kinetics of photopolymerization reactions induced by monochromatic UV light testing various photoinitiator systems [84]. The evaluation of the photopolymerization kinetics obtained by Photo-DSC and RT-IR techniques does not necessarily provide comparable results due to the absence of temperature control during RT-IR analysis or the different amounts of material employed [85].

RT-IR and photo-DSC techniques do not provide information about the cure extent throughout the film thickness. Thus, another technique has been developed, which allows the measurement of chemical bonds throughout the film thickness, confocal Raman microscopy. This technique combines the chemical information from vibrational spectroscopy with the spatial resolution of confocal microscopy [86]. Further, it is able to provide a detailed representation on the spatial distribution of residual chemical bonds within the material depth as well as a surface mapping. The spatial resolution of Confocal Raman microscopy is in the range of 1 μm^3. **Figure 1.6** shows a schematic layout of confocal Raman spectrometer [86].
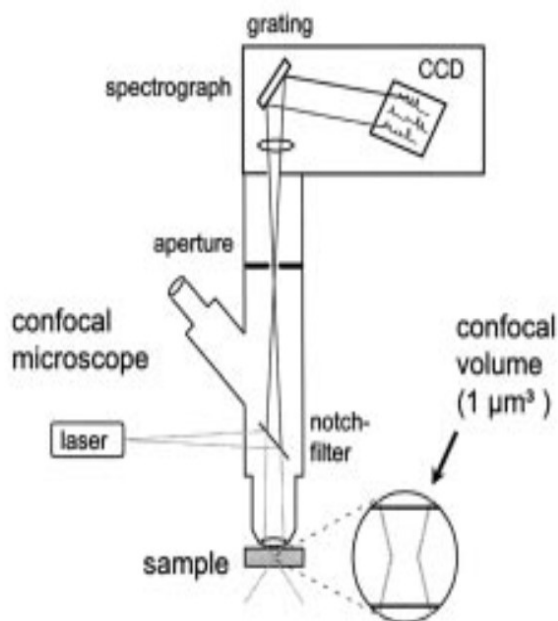
Figure 1.6 – Schematic layout of a confocal Raman spectrometer.

In this way, Confocal Raman microscopy has been used to characterize UV cured coatings, in one case, depth profiles of acrylate curing conversion were recorded in order to elucidate the interaction of photoinitiator, photostabilizer and irradiation source [86] and, in other case, to investigate the aluminium flakes in metallic coatings [87].

1.2.3. Printing technologies for UV curable polymers

Among the several existing 2D and 3D printing technologies, just few of them have been consolidated in industry as potentially useful techniques such as offset lithography, flexography, inkjet printing, xerography or rotogravure. Printing processes can be divided into two different groups: the ones that use a master image carrier or a printing plate (e.g. screen printing and spray coating) and the ones that use computers digital files to create the pattern (e.g. inkjet printing or stereolithography, among others) [88–90].

In 2D printing, the layers are cured right after the complete image is printed. The curing is carried out in a different way depending on the nature of the ink, focusing the present review on the ones cured by UV light. In 3D printing technologies instead, the curing of the resin is performed layer by layer until the whole 3D object is created. In this case there are specific

UV curing techniques, such as stereolithography (SLA) or digital light processing (DLP), based on the spatially controlled solidification of a liquid resin layer by layer using UV laser and a UV DLP-based projector, respectively [91].

Inkjet, spray and screen printing (**Figure 1.7**) are widely used 2D printing techniques that enable the usage of different type of inks. Inkjet printing (Figure 1.7a) is a non-direct contact deposition technique since drops are deposited from a certain distance with respect to the substrate. A pattern is designed in the computer and the cartridge is moved all over the substrate following the pattern and depositing drops in the required places. This method allows the design of complex patterns with high resolution customizing the material deposition volume and location, i.e. it provides the droplet-on-demand option (DOD). The material is deposited drop by drop, hence, for a continuous path drops need to overlap or touch each other. Multilayers can also be printed and the thickness of the layer can be controlled either in this way or changing the amount of the material in the drop [92]. The inkjet printing process has the advantage of quite high resolution, which is easily 300dpi and up to as a much as 1200 dpi without too great difficulty. In addition, the inks are required to be of low viscosity (4–30 cP) and require to be electrostatically charged [93].
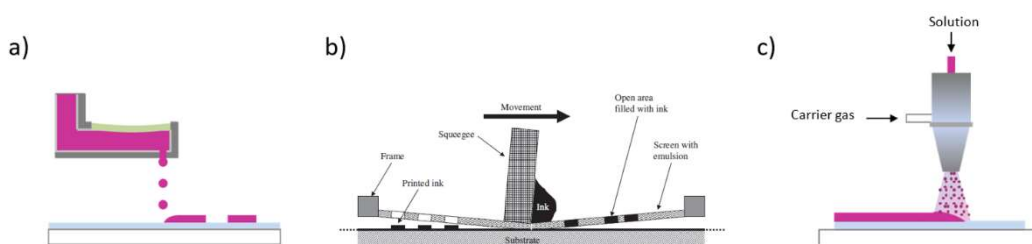
Figure 1.7 – Graphical representation of a) inkjet printing, b) screen printing and c) spray coating techniques. Figure 1.7b reproduced with permission *[93]*. Copyright 2009, Elsevier.

Screen printing (Figure 1.7b) is a printing technique where a mesh is used in order to transfer the pattern to the substrate. A squeegee is moved all over the substrate along the mesh, transferring the ink to the substrate. This technique allows the printing of complex patterns with a resolution of about 100 µm. Its main distinction from all other printing and coating

techniques is a large wet film thickness and a requirement for a relatively high viscosity (100 – 100000 cP) and a low volatility of the coating solution [93].

Similar to inkjet printing, spray coating (Figure 1.7c) is not a direct contact deposition technique and the material is deposited in micron size droplets. The liquid coming out from a nozzle is atomized by ultrasonic vibrations or pressure and the droplets are deposited randomly. An inert gas, such as nitrogen is used as a carrier gas. The nozzle is moved all over the substrate in order to cover the full surface. Depending on the solution flow rate and the moving speed of the nozzle, the thickness of the layer can be controlled. This deposition method does not allow complex patterns unless a mask with the desired pattern is used. However, this technique allows the use of inks in a large viscosity range (10 – 1000 cP) [93].

Stereolithography (SLA), digital light processing (DLP), continuous liquid interface production (CLIP) and PolyJet (**Figure 1.8**) are 3D printing techniques based on UV curing processes for the fabrication of an object [94].

In stereolithography (Figure 1.8a) specific surface regions of photosensitive liquid resin undergo localized polymerization by exposure to a UV laser [95,96]. The 3D object is fabricated by the photopolymerization of each layer on a platform. A UV laser beam scans the surface of the resin and selectively hardens the material corresponding to a cross section of the 3D product, which is fabricated from the bottom to the top. The required supports for overhangs and cavities are automatically generated and later manually removed. Once the object is completed, the excess resin is drained to be reused. The main advantages of SLA are the accuracy and the resolution, where stereolithography is better than all other solid free-form fabrication (SFF) techniques (in most SFF techniques 50-200 mm in size are the smallest details printed, versus 20 mm in many commercially available stereolithography set ups) [91]. The main disadvantage instead is the cost.
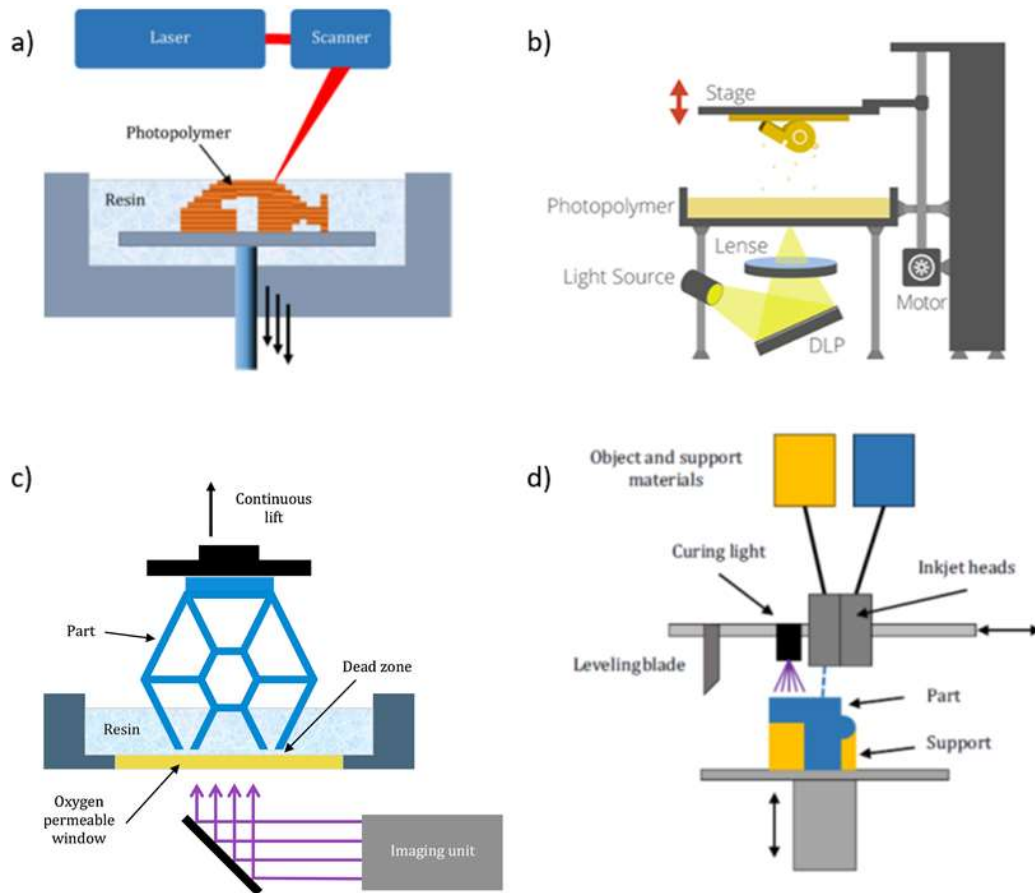
Figure 1.8 – Schematic representation of a) stereolithography, b) digital light processing, c) continuous liquid interface production and d) Polyjet. Reproduced with permission *[94]*. Copyright 2016, Elsevier.

Digital light processing (Figure 1.8b) is similar to stereolithography, being the light source the main difference. DLP uses a more conventional light source and it is applied to the whole photopolymer resin in a single pass, leading to a faster process than SLA. The DLP projector displays the image of the 3D model onto the liquid polymer. The exposed liquid polymer hardens, built plate moves down and the liquid polymer is once more exposed to light. The process is repeated until the 3D model is complete and the vat is drained of liquid, revealing the solidified model. As for SLA, in DLP support structures are required and parts with high resolution are fabricated [97]. DLP and SLA printing techniques allow the use of resins in a large viscosity range (100 – 10000 cP) [94]. However, expensive and limited materials are some drawback of this techniques compared with thermal-based 3D printing techniques such as FDS, which has the advantages of low cost, good strength and multi-material capability

[98]. The SLA or DLP techniques can be used with a wide variety of monomers and resin systems [99].

Continuous liquid interface production (Figure 1.8c) is another UV curing based 3D printing technique. It is a bottom-up continuous process where the UV light beam passes through a window at the bottom part of the vat with the resin iluminating a cross section of the object. In order to avoid the attachment of the solidified resin to the window, there is a oxygen inhibited dead zone. This process allows the fabrication of smooth surfaces [100].

PolyJet (Figure 1.8d) is an additive manufacturing printing technique. The photopolymer is deposited and subsequently the UV light cures the material until the 3D object is completed layer by layer. A roller embedded into the printhead smooths the deposited droplets into a flat layer. UV lamps, which are also mounted in the printhead, fully cures the jetted photopolymer droplets. PolyJet support material is a separate composition formulated to release from the part when jetted off or dissolved with water [101–103]. In the same way that happens in thermal-based 3D printing techniques, the build orientation can significantly affect elastic modulus and fracture stress but tensile strength is relatively insensitive to print direction [94].

During these mentioned printing processes, some problems can be occur: bad adhesion of the resin/ink to the substrate (or between layers in the case of UV-based 3D printing techniques), deformations, cracks or porous appearance in the printed pieces or even incomplete cured materials. Almost all of them can be solved by changing the printing parameters. In the rest, possible solutions could be change the design of the piece to print, the conditions of the printing process (temperature, humidity, etc.), addecuate surface treatments or make a postcure process.

1.3. UV curable Smart Materials

Chromic, self-healing, shape-memory, piezoresistive and piezoelectric materials (**Table 1.6**) are some examples of UV curable smart materials that are described in the following.

The piezoresistive effect represents the variation of the electrical resistivity of a material when mechanical strain is applied. In UV curable materials, typically polymer based materials, this smart behavior is obtained by the addition of a filler into the polymeric matrix, which is the main responsible by a larger piezoresistive response. Further, the filler also improves or changes some properties such as mechanical or thermal properties of the polymeric UV curable material. Commonly used materials for piezoresistive responsive composites are carbon based materials such as carbon nanotubes (CNTs), graphene or carbon fillers (CFs). Silver fillers, microcrystalline silicon or 3, 4-polyethylenedioxythiopene-polystyrene sulfonic acid (PEDOT/PSS) are some other alternatives [18].

CNTs are the most widely used fillers for piezoresistive composites, improving mechanical properties, electrical and thermal conductivities [121]. Thus, multi-walled carbon nanotubes (MWCNTs) and a commercial available UV curable epoxy photoresin (SU-8) were used to create a flexible organic piezoresistive micro-electro-mechanical system (MEMS) strain sensor with enhanced sensitivity [104] (**Figure 1.9**). The electrical resistance changes versus strain of these CNT/SU-8 piezoresistive materials shows linear and non-linear regions at low and high strain, respectively. It is also highlighted the role of the MEMS design in the enhancement of the final sensing performance of the devices, reaching the gauge factor at 200 for optimized sensor geometries, that means a highly sensibility for flexible electronic applications.
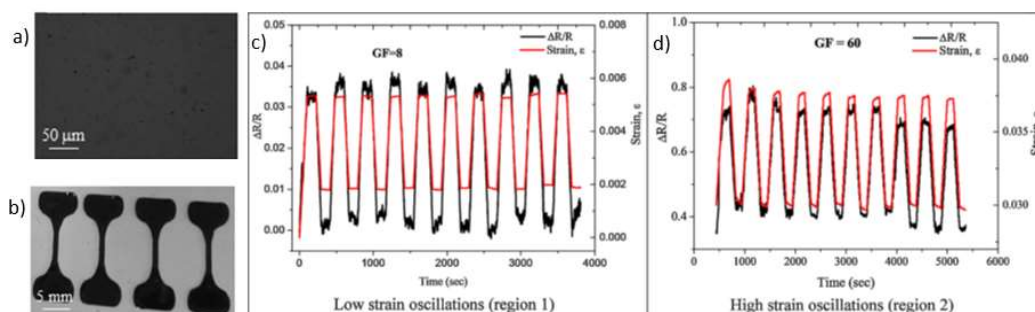
Figure 1.9 – The 1 wt.% CNT/SU-8 thin film sample (a), the dog-bone shaped specimens of the same sample (b) and the ΔR/R response of a 0.8 wt.% CNT/SU-8 thin film for tensile/compressive strain oscillations between 0.2–0.55 % (c) and 3–3.7 % (d). Reproduced with permission *[104]*. Copyright 2014, Elsevier.

Table 1.6 – Summary of the most relevant UV-curable smart materials presented in the literature.

Classification	Shape	Polymer	Filler	Description	Reference
Piezoresistive	Film	Commercial Epoxy Resin (SU-8)	MWCNTs	MWCNTs and SU-8 are used to fabricate a flexible organic piezoresistive micro-electro-mechanical system (MEMS) strain sensor with enhanced sensitivity.	[104]
Piezoresistive	Film	UDMA and HDDMA	SWCNTs	UDMA and HDDMA in combination with SWCNTs are used to obtain piezoresistive nanocomposites, aligned (better properties) and randomly oriented filler.	[105]
Piezoresistive	Sandwich Structure	Commercial Acrylic Resin (TangoPlus)	MWCNTs	MWCNTs/TangoPlus composites for the electrodes and a Ionic Liquid/polymer composite for the internal layer that are between the two electrodes are used to fabricate a new piezoresistive sensor with sandwich type structure.	[106]
Piezoelectric	Film	Commercial Acrylic Resin (Ebecryl 150)	ZnO Nanostructures	Ebecryl 150 and four different morphologies of ZnO filler is used to develop piezoelectric films that, despite the low ZnO content, show interesting piezoelectric properties (in particular, the devices containing flower-like nano-structures).	[107]
Piezoelectric	Film	HDDA	PVDF	HDDA and PVDF are used to obtain a photocurable ink (35 wt.% of PVDF particles) employed to create 3D printed piezoelectrically-active thick film with an optimized piezoelectric voltage coefficient (g_{33}).	[108]
Shape-Memory	Film	DGEBA	PCL fibers	DGEBA and PCL fibers are used to obtain shape memory films with shape recovery ratios between 88 and 100% by electrospinning and UV curing.	[109]

Type	Structure	Material		Description	Reference
Shape-Memory	Helical Thread Structure	Epoxy polymers		Different epoxy polymers are used to develop a helical thread structure with functional graded shape memory parts that have spontaneous and sequential shape recovery abilities at 100°C in 6.5 seconds.	[110]
Shape-Memory	3D structure	PEO-PU, BIS, HEMA and NIPAM		3D printed structures based on a series of hydrogel inks capable of reversible shape variations in response to hydration and temperature.	[111]
Shape-Memory	3D structures	Poly(lactic acid)	Iron oxide	4D active shape-changing architectures in custom-defined geometries exhibiting thermally and remotely actuated responses.	[112]
Self-Healing	Film	Complex Polyol		Complex polyol structure polymer is used to obtain films with self-healing properties, they could be repaired in a short time by hot air gun and maintained high repair efficiency.	[113]
Self-Healing	Film	Polyimide sheets and Epoxy polymer		Polyimide sheets and epoxy photocurable resin are used to obtain self-healing films using a layer-by-layer technique.	[114]
Self-Healing	3D structures	ABS-like resin		3D self-healing structures printed by stereolithography where unit cells embedded in the structure are filled with a UV-curable resin and act as reservoirs for the self-healing agent making possible a repeated healing of mechanical damage.	[115]

Self-Healing	3D structures	Methacrylated resin (Hard Clear Photocentric) modified with anisole	PMMA-filled microcapsules	Stereolithographic 3D printing of self-healing composites using a photocurable resin modified with anisole and PMMA-filled microcapsules. The composites demonstrate solvent-welding based autonomous self-healing to afford 87% recovery of the initial critical toughness.	[116]
Self-Healing and Shape Memory	3D structures	Benzyl methacrylate (BMA) and poly(ethylene glycol)-dimethacrylate (PEGDMA) 3:1 mixture	Semicrystalline linear PCL	Semicrystalline linear PCL polymer incorporated into a methacrylate-based system 3D printed by DLP technology allowing the preparation of complex 4D printing structures with resolution up to 30μm, shape memory behaviour and recovery ability to more than 90% of the mechanical properties.	[117]
Self-Healing and Shape Memory	3D structures	PCL and UPy		4D printed thermally activated self-healing and shape memory samples based on co-crosslinked PCL chains and 2-ureido-4[1H]-pyrimidinone (UPy) units.	[118]
Self-Healing and Shape Memory	3D structures	Urethane diacrylate and a linear semicrystalline PCL		UV-light-assisted direct-ink-write printing of highly stretchable, shape memory, and self-healing elastomer that can be stretched up to 600%. It was 3D printed in complex structures and used for vascular repair.	[119]

Photochromic	Film	ACV^{2+}	ACV^{2+} in PEUDA matrix are used to obtain by UV curing a cross-linked polyviologen film that after UV illumination for 60 s it can swiftly change its color from pale yellow to deep blue.	[120]
Electrochromic	Sandwich Structure	ACV^{2+} and electrolyte gel	PEUDA	ACV^{2+} in PEUDA matrix in addition to gel electrolyte film are used to obtain electrochromic sandwich structure that can undergo reversible color change in response to the external voltages of −2.0 V and 2.0 V.	[120]

Piezoresistive nanocomposites were also obtained by dispersing and aligning simple-walled carbon nanotubes (SWCNTs) in a blend of two different photopolymerizable monomers which consisted of urethane dimethacrylate (UDMA) and 1,6-hecadienol dimethacrylate (HDDMA) [105]. Dielectrophoresis technique was used under the application of AC electric fields obtaining aligned CNTs/polymer nanocomposites. The influence of the degree of alignment of CNTs on the electrical conductivity and piezoresistive response in both the aligned and transverse to alignment directions were be assessed, being obtained the best piezoresistive sensitivity for aligned specimens.

More complex piezoresistive structures were also developed by UV curing and using CNTs. A piezoresistive sandwich type sensor that include three different layered materials a TangoPlus FLX930 photoresin for the top and bottom of the structure, a MWCNTs/TangoPlus composite for the electrodes and an Ionic Liquid/polymer composite for the internal layer that are between the two electrodes was fabricated [106]. All materials used in that study are UV-curable. (1-ethyl-3-methyl-imidazolium tetrafluoroborate (EMIMBF$_4$) is the ionic liquid (IL) employed and 2-[[(butylamino)carbonyl]oxy]ethyl acrylate (BACOEA) is the used polymer. The performance of the piezoresistive sensors was investigated as a function of the degree of crosslinking and polymerization of the IL/polymer composites. As the compressive strain was increased, the distance between the two electrodes decreased, the variations in polymer chains and IL resulting in a decrease of the electrical resistance of the sensors. It is confirmed that the sensitivity of the sensors is affected by the degree of crosslinking and polymerization of the IL/polymer composites.

Piezoelectric materials have been also investigated in UV curable smart materials. The piezoelectric effect is the ability of certain materials to generate voltage when subjected to a mechanical stress, or to generate a mechanical strain when subjected to an electric field [122]. The piezoelectric effect in photocurable materials is achieved using piezoelectric fillers such as polycrystalline ceramics (lead zirconium titanate, lead lanthanum zirconium

titanate, and barium titanate), single crystals (quartz, and zinc oxide) or some polymers (polyvinylidene fluoride) [108].

An UV-cured composite films containing zinc oxide (ZnO) nanostructures with different morphologies was presented by Malucelli *et al.* [107]. The UV curable material is a commercially available acrylic resin, namely bis-phenol A ethoxylate diacrylate (Ebecryl 150), and the studied morphologies of ZnO fillers included nanoparticles (ZNP), bipyramidal structures (ZBP), flower-like structures (ZNF) and long needles (ZLN) (**Figure 1.10**). The different morphologies of the ZnO nanostructures were found to significantly affect the thermo-oxidative stability and the glass transition temperature of the UV-cured films. All the UV-cured nanocomposite films, despite the low ZnO content, showed interesting piezoelectric properties. In particular, the devices containing flower-like nano-structures exhibited the highest root mean square voltage both at 150 Hz and at the resonance frequency (about 0.176 ± 0.001 and 0.914 ± 0.001 mV, respectively).
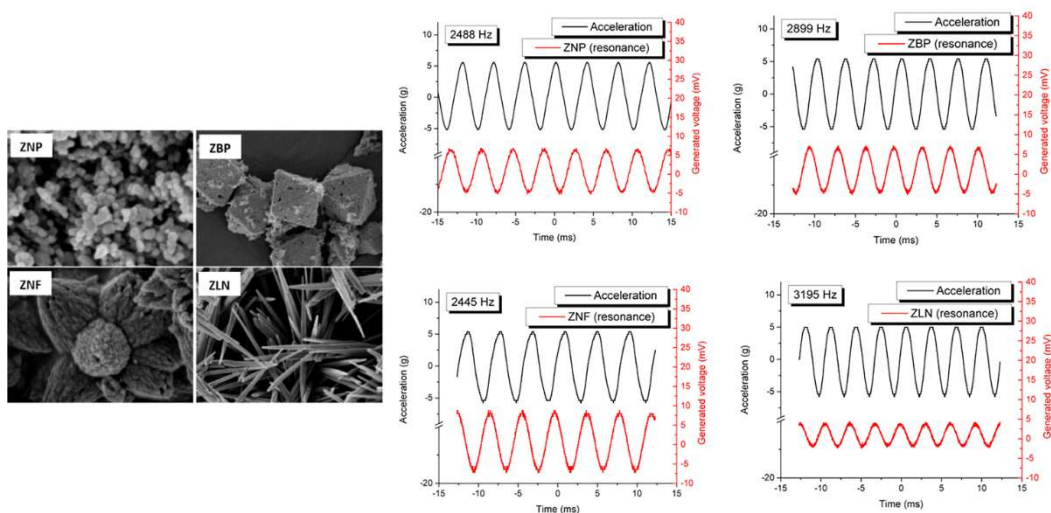
Figure 1.10 – Micrographs of ZnO nanostructures used for the development of piezoelectric UV curable composites and their generators output voltage at resonance frequency. Reproduced with permission *[107]*. Copyright 2017, Elsevier.

A better integration between the UV curable polymer matrix and the filler can be achieved, if the filler is a polymeric material such as polyvinylidene fluoride (PVDF). PVDF has been widely applied due to its stable and high piezoelectric coefficient [30]. PVDF also presents

a unique combination of properties in comparison to other piezoelectric materials, such as excellent mechanical flexibility, chemical stability, biocompatibility and solution based processability. Therefore, an all-polymer-based piezoelectric photocurable resin (V-Ink) based on 1,6-hexanediol diacrylate (HDDA) and PVDF was developed [108], being suitable for additive manufacturing processes. The optimized V-Ink contains 35 wt.% of polyvinylidene fluoride particles suspended in the photocurable resin. A 3D printed piezoelectrically-active thick film was demonstrated with an optimized piezoelectric voltage coefficient (g_{33}) of 105.12×10^{-3} V·m/N.

Shape-memory polymers (SMP) are other smart materials that can be obtained by UV curing but are not electrically active. Shape-memory polymers are materials capable of reacting to external stimuli such as temperature, magnetic or electric fields and solvents, to return from a pre-programmed shape to their original form [123]. Temperature is the most studied one.

Poly (ε-caprolactone) (PCL) based shape memory polymer blends have been the focus of recent research. These materials show sharp and rapid shape memory-recovery response as a consequence of the melting/recrystallization of the PCL component as switching transition. For that, PCL has been used as a shape memory material and diglycidyl ether of bisphenol A (DGEBA) as an epoxy UV curable matrix to obtain shape-memory polymeric composites [109]. Electrospinning technique was used to create PCL fibbers into an epoxy DGEBA matrix that was then UV cured. In this way, a film was obtained with a mat of fibbers with shape memory response (at 60°C). Shape fixity ratios range from 95 to 99% and shape recovery ratios between 88 and 100%, respectively. This shape memory behavior can be observed in **Figure 1.11**.

Figure 1.11 – Photographs of initial shape (a), fixed shape after folding the mat three times in half at 60 °C (b) and recovery shape after heating again to 60 °C (c). Reproduced with permission *[109]*. Copyright 2017, Elsevier.

Some other investigations are based on materials that do not use any filler and the shape memory effect is achieved only by the polymer. This is the case of [110], where seven epoxy polymers with different glass transition temperatures were used to create a functional gradient shape memory "helical thread" structure, where shape recovery is thermally triggered. It was demonstrated the feasibility of using 3D printing technique to fabricate functional graded shape memory polymers (SMPs) with both spontaneous and sequential shape recovery abilities. The SMP components, with properly assigned spatial variation of the thermodynamical property distribution, react rapidly to a thermal stimulus (at around 100°C), and return to a specified configuration in a precisely controlled shape changing sequence in around 6.5 seconds. The sequential shape recovery process can be observed in **Figure 1.12**.
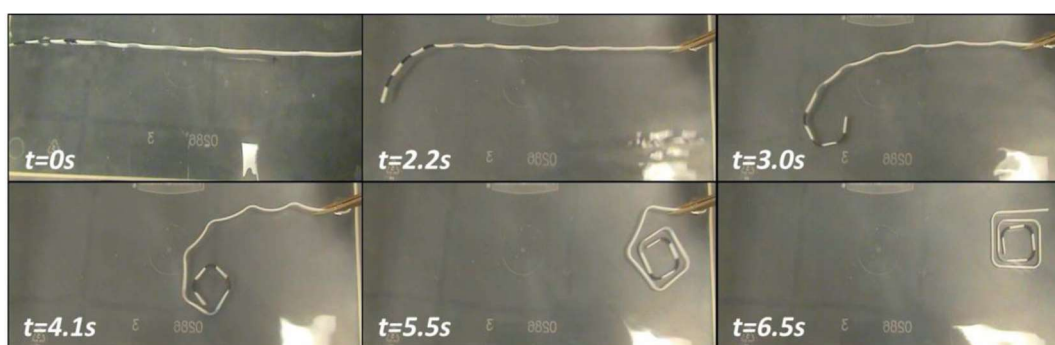

Figure 1.12 – Series of photographs showing the spontaneous and sequential shape recovery process of the helical SMP component. Reproduced with permission *[110]*. Copyright 2015, Elsevier.

Shape memory materials by UV curing have been obtained not only in film or thread form but also in 3D structures. Naficy *et al.* [111] developed 3D printed structures based on a

series of hydrogel inks capable of reversible shape deformation in response to hydration and temperature. This hydrogels are composed mainly by polyether-based polyurethane (PEO-PU) with varying molecular weight, α-ketoglutaric acid as initiator, N,N′-methylenebisacrylamide (BIS) as crosslinking agent and 2-hydroxyethyl methacrylate (HEMA) and Poly(N-isopropylacrylamide) (NIPAM) as monomers. Obtained hydrogels present robust mechanical performance and their mechanical properties can be adapted by changing the nature of the long polymer chains within their networks. 3D SMP structures, both temperature and hydration responsive, can be prepared incorporating near PEO-PU polymers into UV curable monomer solutions by using a dual ink extrusion 3D printer.

Also, shape memory polymers (SMPs) and shape memory nanocomposites (SMNCs) can be obtained by 4D printing through UV curing process [112]. Here, 4D active shape-changing architectures in custom-defined geometries exhibiting thermally and remotely actuated behaviours are achieved by direct-write printing of ultraviolet (UV) cross-linkable poly(lactic acid)-based inks. The addition of iron oxide integrates 4D shape-changing objects with fast remotely actuated and magnetically guidable properties.

Self-heling materials effectively expand the lifetime of the product and have desirable economic and human safety attributes. Self-healing materials are polymers, metals, ceramics and their composites that when damaged through thermal, mechanical, ballistic or by other means, have the ability to heal and restore the material to its original set of properties [124].

Combining self-healing characteristics with the UV-curing advantages (an environmental friendly, energy saving and efficient technology), self-healing UV curable materials become in an interesting research area. In this way, a novel UV-curable self-healing oligomer was designed on the basis of a quadrupolar hydrogen bonds system [113]. The oligomer is formed by reacting a mixture of a hydrogen bonding group and a photosensitive monomer with three-arm polyols. The oligomer coating could be repaired in a short time by hot air gun and maintained high repair efficiency (**Figure 1.13**). The coating could self-heal remarkably at a depth range from 3 µm to 4 µm. The polymer exhibited excellent thermal stability and

significant weight loss occurred at a temperature of 270°C, indicating that the healing process at 170°C was safe for the material.
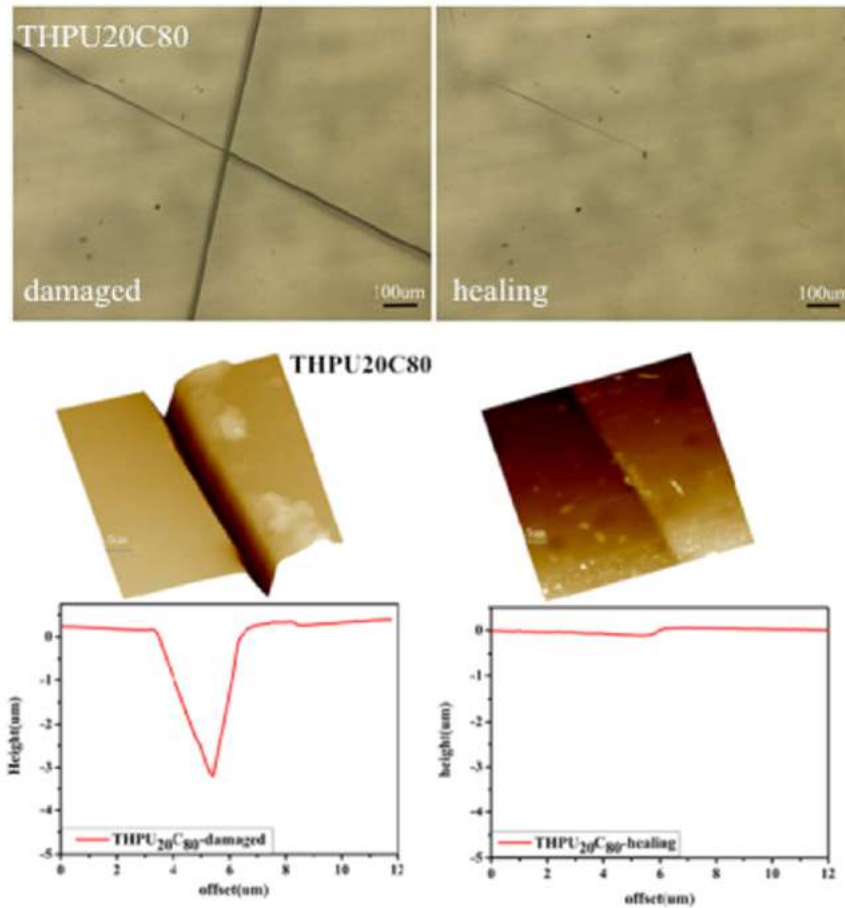
Figure 1.13 – Optical and atomic force micrographs of the oligomer THPU20C80 damaged and after healing. Reproduced with permission *[113]*. Copyright 2016, Elsevier.

A skin structure exhibiting flexibility, self-healing and damage sensing was designed, fabricated and tested by Carlson *et al.* [114]. This coating is fabricated on a substrate of copper-clad polyimide sheets by a layer-by-layer technique using polyimide sheets and an UV curable epoxy polymer (used as both a structural adhesive and as the self-healing fill material). In addition, this skin structure is integrated with an array of LC circuits and an integrated antenna coil that is used to detect and locate the damaged portion of the skin. If the skin is damaged, the UV-curable epoxy is released and is cured by sunlight.

In addition, self-healing materials with the ability to partially or completely restore their mechanical properties by healing the damage inflicted on them can be prepared by UV curing. Davami *et at.* [115] designed and printed 3D self-healing structures by stereolithography where unit cells embedded in the structure are filled with a UV-curable resin acting as reservoirs for the self-healing agent making possible a repeated healing of mechanical damage. An ABS-like UV curable photopolymer resin has been used and when a crack propagates and reaches one reservoir, the healing agent is released into the crack plane through capillary action, and the use of UV radiation allows to bond the crack faces.

Stereolithographic 3D printed self-healing structures were also prepared by Sanders *et al.* [116]. In this case, commercial photocurable resin modified with anisole and PMMA-filled microcapsules were employed and the obtained composites demonstrated solvent-welding based autonomous self-healing to afford 87% recovery of the initial critical toughness.

Special attention has to be paid to a new generation of 4D printed materials that present not only self-healing behavior also shape memory properties. These materials combine the ability of be transformed from one shape to another by a thermo-mechanical programming process with the durability and the mimicking of natural tissues provided by their self-healing ability, making them as attractive materials to produce actuators for soft robotics [118]. In this sense, a double-network self-healing SMP (SH-SMP) system for high-resolution self-healing 4D printing was reported [117]. Here, semicrystalline linear PCL polymer imparted the self-healing ability and it was incorporated into a methacrylate-based SMP with a good compatibility with the DLP 3D printing technology, allowing the preparation of complex 4D printing structures with high resolution (up to 30μm) (**Figure 1.14)**. The obtained material presented a recovery ability and the mechanical properties of a damaged structure can be recovered above 90% after adding more than 20 wt.% of PCL into the SH-SMP system.
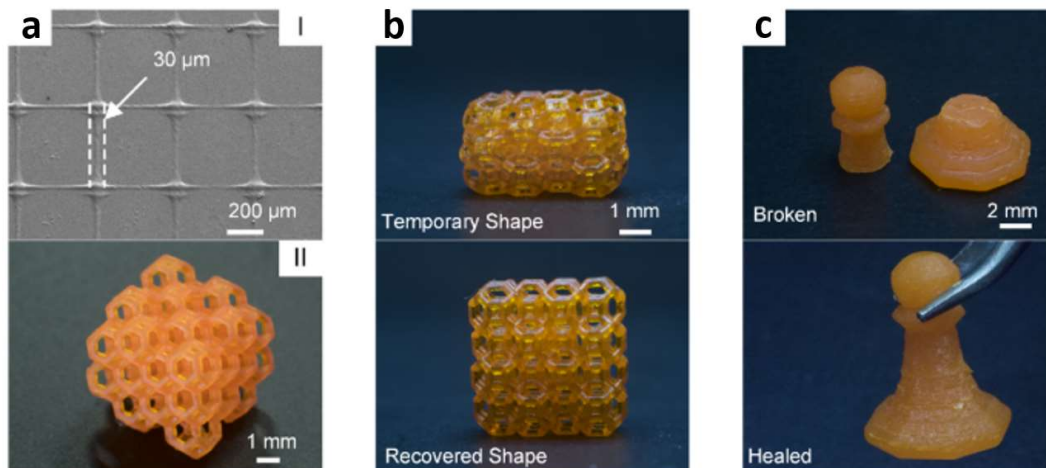
Figure 1.14 – High-resolution complex 3D structures printed using SH-SMP solution (a): 3D printed high-resolution grid (I); 3D printed Kelvin foam (II). Demonstration of 4D printing: temporary shape (top) and permanent shape (down) of 3D printed Kelvin foam (b). Demonstration of the self-healing ability of the printed 3D structure: the broken chess piece (top) can be healed together (down) by heating at 80 °C for 5 min (c). Reproduced with permission *[117]*. Copyright 2019, ACS Publications.

Invernizzi *et al.* [118] also presented 4D printed thermally activated self-healing and shape memory PCL-based polymers. Using DLP 3D printing technology, samples based on PCL chains and 2-ureido-4[1H]-pyrimidinone (UPy) units co-crosslinked can be prepared with a stiffness similar to PCL and a higher elongation at break. The shape memory behavior was demonstrated with the printing of an opposing thumb capable of being moved forward to the tip of a forefinger and then backward, preserving it after healing.

Furthermore, enhanced properties such as high stretching can be obtained together with a self-healing and shape memory effect [119]. Thus, an ink containing urethane diacrylate and a linear semicrystalline PCL polymer was developed for the 3D printing of a semi-interpenetrating polymer network elastomer that can be stretched up to 600%. 3D-printed complex structures with interesting functional properties, such as high strain shape memory and shape memory assisted self-healing capability were obtained via UV-light-assisted direct-ink-write printing. Further, the demonstration of the 3D-printed material as a vascular repair was achieved.

Chromic materials are a type of materials capable of undergoing a change, often reversible, in the color due to a transformation between two forms [125]. If this change in color occurs by the absorption of electromagnetic radiation, they are called photochromic material. If this change in color occurs by the application of an electric charge, they are called electrochromic material. These two type of smart materials are based on organic compounds with extended π-conjugation. The most investigated ones are the viologens (1,1'-disubstituted-4, 4'-bipyridine salts) that are functional in their crystalline states, dispersed in appropriate matrixes or incorporated polymers by copolymerization or graft-modified reactions [120].

Acrylate-functional viologen (ACV^{2+}) in polyether urethane diacrylate matrix (PEUDA) were used to obtain by UV curing a cross-linked polyviologen film with excellent photochromic and electrochromic performances [120]. The photochromic effect appears after UV illumination for 60 s, when the cross-linked $PACV^{2+}$ film can swiftly change its color from pale yellow to deep blue. In addition, the optical transmission of cross-linked $PACV^{2+}$ film at 610 nm did not change significantly and still retained about 63.6% after 30 cycles. The cyclic voltammetry experiment showed that the film can undergo repetitively electrochemical redox reactions with good reversibility beyond the 10th scan.

Furthermore, when a gel electrolyte film was added to the $PACV^{2+}$ film, an electrochromic sandwich structure film was obtained (**Figure 1.15**). The gel electrolyte film is a mixture of acetonitrile (MeCN), polymethyl methacrylate (PMMA), propylene carbonate (PC) and $LiClO_4$. The electrochromic device composed of the $PACV^{2+}$ film and gel electrolyte film undergoes reversible color change in response to the external voltages of −2.0 V and 2.0 V, respectively, while the contrast of EC device at 610 nm did not change significantly and still retained about 39.5% after 10 cycles.
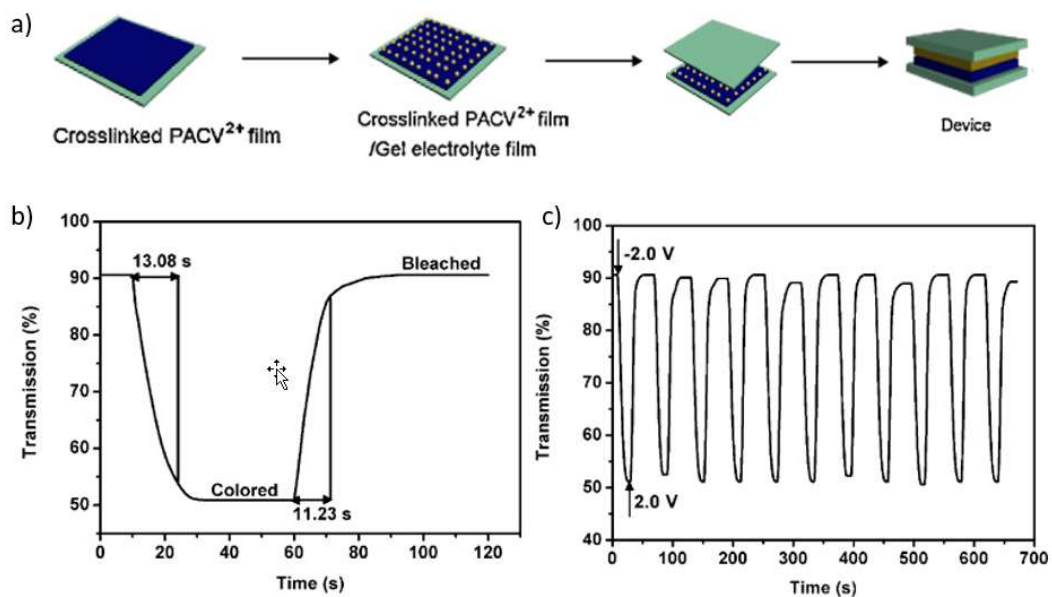
Figure 1.15 – Schematic illustration for the construction of the electrochromic device (a), its coloring and bleaching response times (b) and the cyclic changes in optical transmissions at 610 nm obtained by cyclic application of the external voltages of −2.0 V and 2.0 V (c). Reproduced with permission *[120]*. Copyright 2011, Elsevier.

A summary of the most relevant UV-curable smart materials presented in the literature is presented in **Table 1.6**. As it can be observed, UV curable smart materials, such as other smart materials, are composed by a polymeric matrix and an active filler that provides this smart behavior (filler can be also a polymer). There is no unique method for designing these UV curable materials, depending on the filler and the polymer matrix, the synthesis methods are different (different ways to disperse the filler, different conditions, curing characteristics, etc.).

1.4. General objectives and work plan

Smart materials are attracting increasing interest based on the used for the Industry 4.0 and the Internet of Things concepts. Their properties allow them to be very suitable for sensor applications in several fields like aerospace, civil engineering and different industrial applications, with improved performance and integration. Further, in order to improve integration, additive manufacturing technologies are being implemented being therefore important the parallel development of suitable inks.

Depending on the composition of the ink, the curing process is achieved in a different way (thermal treatments, cross-linking methods, etc.), being UV-curable materials among the most suitable ones for smart materials applications. UV curable materials are based on photopolymers that are cross-linked when exposed to UV light. In contrast with solvent based materials, they present advantages like fast curing processes at room temperature with reduced VOC emissions, making then environmentally friendlier and really attractive for thin film processing in electronics and engineering.

Considering the mentioned advantages, UV curable smart materials are becoming in a general research and implementation interest. Chromic, self-healing, shape memory, piezoresistive, or piezoelectric materials are some examples of it.

Despite UV curable smart materials are a key technology for advance technologies, the number of those materials is still small. This fact is mainly due to the difficulty in reaching proper combination of UV-curable resin and nano-fillers, with both suitable smart and multifunctional performance and processability; being this the key future challenge in this research field and the main objective of this thesis. In addition, each photocurable material has to be adapted to the specific functional filler to be used and vice versa.

Viscosity, density, surface tension and contact angle on different substrates are the parameters that are most affected when these smart and multifunctional UV-curable materials are prepared. In addition, depending on the nano-filler employed, the absorption of the UV light can be also affected. Thus, obtain the best material, in terms of functionality/smart response, is really complicated. In this way, the potential solutions or new approaches that are being investigated nowadays, are the use of polymer coated fillers, new filler dispersion techniques or new fillers more compatible with the UV-curable resin (that not affect the UV curing process).

In this scope, the main objective of the present thesis is the development of a set of UV curable smart and multifunctional materials suitable for sensing and printable electronic

applications. Thus, UV curable materials with tailored electric, dielectric, magnetic and chromic properties have been developed.

The structure of this document follows the sequential development of the different materials developed in the present thesis. Thus, chapter 1 has been focused on the main concepts and a general overview of the state of the art in the area, as the specific state of the art on the developed materials in this work are presented in each chapter.

Chapter 2 presents the synthesis, characterization and optimization of stimuli responsive UV cured polyurethane acrylated/carbon nanotube (PUA/MWCNT) composites for piezoresistive sensing. Here, the influence of carbon nanotubes in the photopolymerization process of the polyurethane acrylated is presented, as well as the changes on chemical, thermal, electrical and mechanical properties together with the influence of filler dispersion within the polymer matrix on the same properties. Further, the applicability of this material for use in piezoresistive sensing is demonstrated.

In addition to smart materials, multifunctional composites are increasingly relevant for flexible printed electronics, sensors, actuators or smart coatings. UV curable polymeric materials being increasingly needed in those areas. In this sense, chapter 3 present the development of UV curable barium titanate/polyurethane acrylate ($BaTiO_3$/PUA) composites with varying ceramic type and contents allowing to tailor the dielectric response of the material. The filler dispersion and amount influences on the composite properties was studied. Moreover, in this case, a theoretical study was carried out to determine the best model that predict the dielectric properties taking into account different parameters such as the filler size, shape or the interaction between filler and polymer, among other.

Further, and following with dielectric materials, high dielectric constant UV curable composites based on polyurethane acrylate and indium tin oxide (ITO) were prepared in order to develop materials suitable for capacitive sensing. In this work, presented in the chapter 4 of the thesis, not just increased dielectric response, but also materials with

improved transparency or translucent properties are developed. For that, composites with different ITO content were prepared and the thermal, mechanical, electrical and optical properties evaluated. Also, their functionality as capacitive sensor was demonstrated.

In chapter 5, one of the main problems associated with the UV curing process will be studied. The presence of magnetic fillers inhibits the polymerization process of UV curable materials. Therefore, different magnetic particles such as cobalt ferrite (COF), magnetite (Fe_3O_4) or neodymium iron boron alloy (NdFeB) have been used for the study of their influence in the UV curing process of polyurethane acrylated. Further, the thermal, electrical, mechanical and magnetic properties for the different filler types and contents are presented.

Finally, chapter 6 focusses on UV vurable polymer composites with ionic liquids. Polyurethane acrylated/magnetic ionic liquid (PUA/MIL) composites were developed for thermochromic and humidity sensing applications. The influence of ionic liquid content and dispersion, as well as their hydration/dehydration state on the thermal, electrical and mechanical properties was evaluated. Furthermore, their applicability for humidity sensing is demonstrated.

The final chapter of this thesis is devoted to the presentation of the conclusions of the developed work and some final remarks on future works.

1.5. References

[1]   M. Ashby, H. Shercliff, D. Cebon, Materials: engineering, science, processing and design, 2010. doi:10.1016/s1369-7021(10)70042-0.

[2]   M.A. Morse, Craniology and the Adoption of the Three-Age System in Britain, Proc. Prehist. Soc. 65 (1999) 1–16. doi:10.1017/s0079497x00001924.

[3]   J. Charles E. Carraher, Polymer Chemistry, Eight Edit, CRC Press, Massachusetts, USA, 2011.

[4]   R.J. Young, P.A. Lovell, Introduction to polymers, Third Edit, Taylor & Francis Group, New York, 2011.

[5]   R.O. Ebewele, Polymer science and technology, 2000. doi:10.1016/0261-3069(95)90127-2.

[6]   M. Aazam, S. Zeadally, K.A. Harras, Deploying Fog Computing in Industrial Internet of Things and Industry 4.0, IEEE Trans. Ind. Informatics. 14 (2018) 4674–4682. doi:10.1109/TII.2018.2855198.

[7]   P.F. Drucker, The Future of Industrial Man, Futur. Ind. Man. (2017). doi:10.4324/9781315132143.

[8]   F. Shrouf, J. Ordieres, G. Miragliotta, Smart factories in Industry 4.0: A review of the concept and of energy management approached in production based on the Internet of Things paradigm, IEEE Int. Conf. Ind. Eng. Eng. Manag. 2015-Janua (2014) 697–701. doi:10.1109/IEEM.2014.7058728.

[9]   N. Bari, G. Mani, S. Berkovich, Internet of things as a methodological concept, Proc. - 2013 4th Int. Conf. Comput. Geospatial Res. Appl. COM.Geo 2013. (2013) 48–55. doi:10.1109/COMGEO.2013.8.

[10] E.B. Murphy, F. Wudl, The world of smart healable materials, Prog. Polym. Sci. 35 (2010) 223–251. doi:10.1016/j.progpolymsci.2009.10.006.

[11] J. Gubbi, R. Buyya, S. Marusic, M. Palaniswami, Internet of Things (IoT): A vision, architectural elements, and future directions, Futur. Gener. Comput. Syst. 29 (2013) 1645–1660. doi:10.1016/j.future.2013.01.010.

[12] I. Lee, K. Lee, The Internet of Things (IoT): Applications, investments, and challenges for enterprises, Bus. Horiz. 58 (2015) 431–440. doi:10.1016/j.bushor.2015.03.008.

[13] S.H. Shah, I. Yaqoob, A survey: Internet of Things (IOT) technologies, applications and challenges, 2016 4th IEEE Int. Conf. Smart Energy Grid Eng. SEGE 2016. i (2016) 381–385. doi:10.1109/SEGE.2016.7589556.

[14] K. Witkowski, Internet of Things, Big Data, Industry 4.0 - Innovative Solutions in Logistics and Supply Chains Management, Procedia Eng. 182 (2017) 763–769.

doi:10.1016/j.proeng.2017.03.197.

[15]   J. Wan, S. Tang, Z. Shu, D. Li, S. Wang, M. Imran, A. V. Vasilakos, Software-Defined Industrial Internet of Things in the Context of Industry 4.0, IEEE Sens. J. 16 (2016) 7373–7380. doi:10.1109/JSEN.2016.2565621.

[16]   Gartner, Gartner Says 8.4 Billion Connected "Things" Will Be in Use in 2017, Up 31 Percent From 2016, (2018). https://www.gartner.com/en/newsroom/press-releases/2017-02-07-gartner-says-8-%0Abillion-connected-things-will-be-in-use-in-2017-up-31-percent-from-2016.

[17]   D. Brodowicz, Eco-cities : Challenges , Trends and Solutions, 2017.

[18]   J. Oliveira, V. Correia, H. Castro, P. Martins, S. Lanceros-Mendez, Polymer-based smart materials by printing technologies: Improving application and integration, Addit. Manuf. 21 (2018) 269–283. doi:10.1016/j.addma.2018.03.012.

[19]   H. Liu, Q. Li, S. Zhang, R. Yin, X. Liu, Y. He, K. Dai, C. Shan, J. Guo, C. Liu, C. Shen, X. Wang, N. Wang, Z. Wang, R. Wei, Z. Guo, Electrically conductive polymer composites for smart flexible strain sensors: a critical review, J. Mater. Chem. C. 6 (2018) 12121–12141. doi:10.1039/C8TC04079F.

[20]   X. Wang, M. Jiang, Z. Zhou, J. Gou, D. Hui, 3D printing of polymer matrix composites: A review and prospective, Compos. Part B Eng. 110 (2017) 442–458. doi:10.1016/j.compositesb.2016.11.034.

[21]   T. Nardi, M. Sangermano, Y. Leterrier, P. Allia, P. Tiberto, J.A.E. Månson, UV-cured transparent magnetic polymer nanocomposites, Polymer (Guildf). 54 (2013) 4472–4479. doi:10.1016/j.polymer.2013.06.052.

[22]   G. Harsanyi, Polymer films in sensor applications: a review of present uses and future possibilities, Sens. Rev. 20 (2000) 98. papers2://publication/uuid/0E43115E-F45F-4F7A-B96C-3FE95D85D9B4.

[23]   A. Kumar, Methods and Materials for Smart Manufacturing: Additive Manufacturing, Internet of Things, Flexible Sensors and Soft Robotics, Manuf. Lett. 15 (2018) 122–125. doi:10.1016/j.mfglet.2017.12.014.

[24]   Y. Zhan, Y. Mei, L. Zheng, Materials capability and device performance in flexible electronics for the Internet of Things, J. Mater. Chem. C. 2 (2014) 1220–1232. doi:10.1039/c3tc31765j.

[25]   R. Bogue, Smart materials: A review of capabilities and applications, Assem. Autom. 34 (2014) 16–22. doi:10.1108/AA-10-2013-094.

[26]   R. Bogue, Smart materials: A review of recent developments, Assem. Autom. 32 (2012) 3–7. doi:10.1108/01445151211198674.

[27]   A. Maceiras, Polyimides for Piezoelectric Materials, Magnetoelectric Nanocomposites and Battery Separators: Synthesis and, 2016.

[28]   M. Wollschlaeger, T. Sauter, J. Jasperneite, The future of industrial communication: Automation networks in the era of the internet of things and industry 4.0, IEEE Ind. Electron. Mag. 11 (2017) 17–27. doi:10.1109/MIE.2017.2649104.

[29]   X. Qiu, S. Hu, "Smart" materials based on cellulose: A review of the preparations, properties, and applications, Materials (Basel). 6 (2013) 738–781. doi:10.3390/ma6030738.

[30]   P. Martins, A.C. Lopes, S. Lanceros-Mendez, Electroactive phases of poly(vinylidene fluoride): Determination, processing and applications, Prog. Polym. Sci. 39 (2014) 683–706. doi:10.1016/j.progpolymsci.2013.07.006.

[31]   A. Benjeddou, Smart structures , materials and nano technology in engineering, Int. J. Smart Nano Mater. 9 (2018) 85–87. doi:10.1080/19475411.2018.1463938.

[32]   G. Grau, R. Kitsomboonloha, S.L. Swisher, H. Kang, Printed Transistors on Paper : Towards Smart Consumer Product Packaging, (2014) 5067–5074. doi:10.1002/adfm.201400129.

[33]   G. Sossou, F. Demoly, G. Montavon, S. Gomes, An additive manufacturing oriented design approach to mechanical assemblies, J. Comput. Des. Eng. 5 (2018) 3–18. doi:10.1016/j.jcde.2017.11.005.

[34]   E.A. Clark, M.R. Alexander, D.J. Irvine, C.J. Roberts, M.J. Wallace, S. Sharpe, J. Yoo, R.J.M. Hague, C.J. Tuck, R.D. Wildman, 3D printing of tablets using inkjet with UV photoinitiation, Int. J. Pharm. 529 (2017) 523–530. doi:10.1016/j.ijpharm.2017.06.085.

[35]   E. Saleh, P. Woolliams, B. Clarke, A. Gregory, S. Greedy, C. Smartt, R. Wildman, I. Ashcroft, R. Hague, P. Dickens, C. Tuck, 3D inkjet-printed UV-curable inks for multi-functional electromagnetic applications, Addit. Manuf. 13 (2017) 143–148. doi:10.1016/j.addma.2016.10.002.

[36]   M. Sangermano, A. Chiolerio, G. Marti, P. Martino, P. Martino, UV-Cured Acrylic Conductive Inks for Microelectronic Devices, Macromol. Mater. Eng. 298 (2013) 607–611. doi:10.1002/mame.201200072.

[37]   C. Decker, The Use of UV Irradiation in Polymerization, Polym. Int. 45 (1998) 133–141.

[38]   G. Mashouf, M. Ebrahimi, S. Bastani, UV curable urethane acrylate coatings formulation: Experimental design approach, Pigment Resin Technol. 43 (2014) 61–68. doi:10.1108/PRT-10-2012-0072.

[39]   A. Endruweit, M.S. Johnson, A.C. Long, Curing of Composite Components by Ultraviolet Radiation: A Review, Polym. Compos. 27 (2006) 119–128. doi:10.1002/pc.20166.

[40]   A. Ravve, Light-Associated Reactions of Synthetic Polymers, First Edit, Springer, New York, USA, 2006. doi:10.1007/0-387-36414-5_2.

[41]   W. Schnabel, Polymers and Light. Fundamentals and Technical Applicaions, First Edit, Berlin (Alemania), 2004. doi:10.1007/b12437.

[42]   J.P. Fouassier, Photoinitiation, photopolymerization, and photocuring (fundamentals and applications), IEEE Electr. Insul. Mag. 12 (1996) 36. doi:10.1109/MEI.1996.546285.

[43]   J.P. Fouassier, J. Lalevée, Photoinitiators for Polymer Synthesis: Scope, Reactivity and Efficiency, 2012. doi:10.1002/9783527648245.

[44]   A. Tiwari, A. Polykarpov, Photocured Materials, First, Royal Society of Chemistry, Cambridge, UK, 2014.

[45]   T. Sumiyoshi, W. Schnabel, A. Henne, P. Lechtken, On the photolysis of acylphosphine oxides: 1. Laser flash photolysis studies with 2,4,6-trimethylbenzoyldiphenylphosphine oxide, Polymer (Guildf). 26 (1985) 141–146. doi:10.1016/0032-3861(85)90069-2.

[46]   A. Kajiwara, Y. Konishi, Y. Morishima, W. Schnabel, K. Kuwata, M. Kamachi, Time-Resolved Electron-Spin-Resonance Study on Radical Polymerization with (2,4,6-Trimethylbenzoyl)Diphenylphosphine Oxide - Direct Estimation of Rate Constants for Addition-Reactions of Diphenylphosphonyl Radicals to Vinyl Monomers, Macromolecules. 26 (1993) 1656–1658. doi:Doi 10.1021/Ma00059a025.

[47]   N. Arsu, M. Aydin, Y. Yagci, S. Jockusch, N.J. Turro, One component thioxanthone based Type II photoinitiators, Photochem. UV Curing New Trends. 661 (2006) 1–13.

[48]   B. Golaz, V. Michaud, Y. Leterrier, J.A.E. Mnson, UV intensity, temperature and dark-curing effects in cationic photo-polymerization of a cycloalphatic epoxy resin, Polymer (Guildf). 53 (2012) 2038–2048. doi:10.1016/j.polymer.2012.03.025.

[49]   S.R. Akhtar, J. V. Crivello, M.L. Schmitt, J.L. Lee, New Synthesis of Aryl-Substituted Sulfonium Salts and Their Applications in Photoinitiated Cationic Polymerization, Chem. Mater. 2 (1990) 732–737. doi:10.1021/cm00012a027.

[50]   Y. Yağci, A. Kornowski, W. Schnabel, N-alkoxy-pyridinium and N-alkoxy-quinolinium salts as initiators for cationic photopolymerizations, J. Polym. Sci. Part A Polym. Chem. 30 (1992) 1987–1991. doi:10.1002/pola.1992.080300922.

[51]   V. V. Jarikov, D.C. Neckers, Anionic photopolymerization of methyl 2-cyanoacrylate and simultaneous color formation, Macromolecules. 33 (2000) 7761–7764. doi:10.1021/ma0012090.

[52]   Z.W. Wicks, J.F.N. Jones, S.P. Pappas, D.A. Wicks, Organic Coatings: Science and Technology, 3rd edn, John Wiley & Sons, Inc., New York, 2007. doi:10.1016/0033-0655(85)80003-0.

[53]   M. Sangermano, I. Roppolo, A. Chiappone, New horizons in cationic photopolymerization, Polymers (Basel). 10 (2018). doi:10.3390/polym10020136.

[54]   A. Wrzyszczynski, J. Bartoszewicz, G.L. Hug, B. Marciniak, J. Paczkowski,

Photochemical studies of a photodissociative initiator based on a benzophenone derivative possessing a thioether moiety, J. Photochem. Photobiol. A Chem. 155 (2003) 253–259. doi:10.1016/S1010-6030(02)00391-X.

[55] H. Itoh, A. Kameyama, T. Nishikubo, Synthesis of new hybrid monomers and oligomers containing cationic and radical polymerizable vinyl groups and their photoinitiated polymerization, J. Polym. Sci. Part A Polym. Chem. 34 (1996) 217–225. doi:10.1002/(SICI)1099-0518(19960130)34:2<217::AID-POLA8>3.0.CO;2-Q.

[56] J. Xu, Y. Jiang, T. Zhang, Y. Dai, D. Yang, F. Qiu, Z. Yu, P. Yang, Synthesis of UV-curing waterborne polyurethane-acrylate coating and its photopolymerization kinetics using FT-IR and photo-DSC methods, Prog. Org. Coatings. 122 (2018) 10–18. doi:10.1016/j.porgcoat.2018.05.008.

[57] T. Scherzer, W. Knolle, S. Naumov, R. Mehnert, Direct initiation of the photopolymerization of acrylates by short-wavelength excimer UV radiation, Nucl. Instruments Methods Phys. Res. Sect. B Beam Interact. with Mater. Atoms. 208 (2003) 271–276. doi:10.1016/S0168-583X(03)00620-7.

[58] C. Check, R. Chartoff, S. Chang, Inkjet printing of 3D nano-composites formed by photopolymerization of an acrylate monomer, React. Funct. Polym. 97 (2015) 116–122. doi:10.1016/j.reactfunctpolym.2015.09.009.

[59] V. Shukla, M. Bajpai, D.K. Singh, M. Singh, R. Shukla, Review of basic chemistry of UV-curing technology, Pigment Resin Technol. 33 (2004) 272–279. doi:10.1108/03699420410560461.

[60] J. Chen, M.D. Soucek, W.J. Simonsick, R.W. Celikay, Synthesis and photopolymerization of norbornyl epoxidized linseed oil, Polymer (Guildf). 43 (2002) 5379–5389. doi:10.1016/S0032-3861(02)00404-4.

[61] M. Sangermano, Advances in cationic photopolymerization, Pure Appl. Chem. 84 (2012) 2089–2101. doi:10.1351/PAC-CON-12-04-11.

[62] M. Sangermano, G. Malucelli, R. Bongiovanni, A. Priola, U. Annby, N. Rehnberg, Cationic photopolymerization of polyfunctional 1-propenyl ether systems, Polym. Int. 50 (2001) 998–1003. doi:10.1002/pi.733.

[63] C. Decker, K. Moussa, Kinetic study of the cationic photopolymerization of epoxy monomers, J. Polym. Sci. Part A Polym. Chem. 28 (1990) 3429–3443. doi:10.1002/pola.1990.080281220.

[64] J.L. Stanford, A.J. Ryan, Y. Yang, Photoinitiated cationic polymerization of epoxides, Polym. Int. 50 (2001) 986–997. doi:10.1002/pi.730.

[65] A.B. Strong, Fundamentals of Composites Manufacturing. Materials, Methods, and Applications, 2nd ed., Dearborn, Michigan, 2008. doi:10.1016/0956-7143(92)90210-L.

[66] R. Schwalm, UV coatings. Basics, Recent Developments and New Applications, First Edit, Elsevier, Amsterdam, The Netherlands, 2006.

[67] H. Xiang, X. Wang, G. Lin, L. Xi, Y. Yang, D. Lei, H. Dong, J. Su, Y. Cui, X. Liu, Preparation, characterization and application of UV-curable flexible hyperbranched polyurethane acrylate, Polymers (Basel). 9 (2017). doi:10.3390/polym9110552.

[68] H. Xu, F. Qiu, Y. Wang, W. Wu, D. Yang, Q. Guo, UV-curable waterborne polyurethane-acrylate: Preparation, characterization and properties, Prog. Org. Coatings. 73 (2012) 47–53. doi:10.1016/j.porgcoat.2011.08.019.

[69] F. Wang, J.Q. Hu, W.P. Tu, Study on microstructure of UV-curable polyurethane acrylate films, Prog. Org. Coatings. 62 (2008) 245–250. doi:10.1016/j.porgcoat.2007.12.005.

[70] S.J. Choi, H.N. Kim, W.G. Bae, K.Y. Suh, Modulus- and surface energy-tunable ultraviolet-curable polyurethane acrylate: Properties and applications, J. Mater. Chem. 21 (2011) 14325–14335. doi:10.1039/c1jm12201k.

[71] J.H. Li, R.Y. Hong, M.Y. Li, H.Z. Li, Y. Zheng, J. Ding, Effects of ZnO nanoparticles on the mechanical and antibacterial properties of polyurethane coatings, Prog. Org. Coatings. 64 (2009) 504–509. doi:10.1016/j.porgcoat.2008.08.013.

[72] J. Ortyl, R. Popielarz, New photoinitiators for cationic polymerization, Polimery/Polymers. 57 (2012) 510–517. doi:10.14314/polimery.2012.510.

[73] V.K. Varadan, K.J. Vinoy, S. Gopalakrishnan, Smart Material Systems and MEMS: Design and Development Methodologies, 2006. doi:10.1002/0470093633.

[74] L. Racicot, T. Kasahara, M.A. Ciufolini, Arylation of diorganochalcogen compounds with diaryliodonium triflates: Metal catalysts are unnecessary, Org. Lett. 16 (2014) 6382–6385. doi:10.1021/ol503177q.

[75] J. V. Crivello, Cationic polymerization - Iodonium and sulfonium salt photoinitiators, in: Adv. Polym. Sci., 1984: pp. 1–48. doi:10.1007/BFb0024033.

[76] J. V. Crivello, The Discovery and Development of Onium Salt Cationic Photoinitiators, J. Polym. Sci. Part A Polym. Chem. 37 (1999) 4241–4254.

[77] S. Shi, C. Croutxé-Barghorn, X. Allonas, Photoinitiating systems for cationic photopolymerization: Ongoing push toward long wavelengths and low light intensities, Prog. Polym. Sci. 65 (2017) 1–41. doi:10.1016/j.progpolymsci.2016.09.007.

[78] Y.-H. Wang, P. Wan, Ketoprofen as a photoinitiator for anionic polymerization., Photochem. Photobiol. Sci. 14 (2015) 1120–6. doi:10.1039/c4pp00454j.

[79] C. Esposito Corcione, M. Frigione, A. Maffezzoli, G. Malucelli, Photo - DSC and real time - FT-IR kinetic study of a UV curable epoxy resin containing o-Boehmites, Eur. Polym. J. 44 (2008) 2010–2023. doi:10.1016/j.eurpolymj.2008.04.030.

[80] V.Y. Voytekunas, F.L. Ng, M.J.M. Abadie, Kinetics study of the UV-initiated cationic polymerization of cycloaliphatic diepoxide resins, Eur. Polym. J. 44 (2008) 3640–3649. doi:10.1016/j.eurpolymj.2008.08.043.

[81] C. Esposito Corcione, G. Malucelli, M. Frigione, A. Maffezzoli, UV-curable epoxy systems containing hyperbranched polymers: Kinetics investigation by photo-DSC and real-time FT-IR experiments, Polym. Test. 28 (2009) 157–164. doi:10.1016/j.polymertesting.2008.11.002.

[82] D.S. Esen, F. Karasu, N. Arsu, The investigation of photoinitiated polymerization of multifunctional acrylates with TX-BT by Photo-DSC and RT-FTIR, Prog. Org. Coatings. 70 (2011) 102–107. doi:10.1016/j.porgcoat.2010.10.010.

[83] B. Chiou, S.A. Khan, Real-Time FTIR and in Situ Rheological Studies on the UV Curing Kinetics of Thiol-ene Polymers, Macromolecules. 9297 (1997) 7322–7328. doi:10.1021/ma9708656.

[84] T. Scherzer, U. Decker, Real-time FTIR-ATR spectroscopy to study the kinetics of ultrafast photopolymerization reactions induced by monochromatic UV light, Vib. Spectrosc. 19 (1999) 385–398. doi:10.1016/S0924-2031(98)00070-8.

[85] P. Kerbouc'h, P. Lebaudy, L. Lecamp, C. Bunel, Numerical simulation to correlate photopolymerization kinetics monitoring by RT-NIR spectroscopy and photocalorimetry, Thermochim. Acta. 410 (2004) 73–78. doi:10.1016/S0040-6031(03)00394-0.

[86] W. Schrof, E. Beck, R. Königer, W. Reich, R. Schwalm, Depth profiling of UV cured coatings containing photostabilizers by confocal Raman microscopy, Prog. Org. Coatings. 35 (1999) 197–204. doi:10.1016/S0300-9440(99)00026-0.

[87] W. Schrof, E. Beck, G. Etzrodt, H. Hintze-Brüning, U. Meisenburg, R. Schwalm, J. Warming, Depth-resolved characterization of UV cured coatings by confocal Raman and two-photon microscopy, Prog. Org. Coatings. 43 (2001) 1–9. doi:10.1016/S0300-9440(01)00245-4.

[88] H. Kipphan, Handbook of Print Media, Springe, Berlin, Germany, 2001. doi:10.1007/978-3-540-29900-4.

[89] A.J. Bard, L.R. Faulkner, Fundamentals and Applications, 1980. doi:10.1146/annurev.matsci.30.1.117.

[90] N. Saengchairat, T. Tran, C.K. Chua, A review: additive manufacturing for active electronic components, Virtual Phys. Prototyp. 12 (2017) 31–46. doi:10.1080/17452759.2016.1253181.

[91] F.P.W. Melchels, J. Feijen, D.W. Grijpma, A review on stereolithography and its applications in biomedical engineering., Biomaterials. 31 (2010) 6121–30. doi:10.1016/j.biomaterials.2010.04.050.

[92] E.M. Hamad, S.E.R. Bilatto, N.Y. Adly, D.S. Correa, B. Wolfrum, M.J. Schöning, A. Offenhäusser, A. Yakushenko, Inkjet printing of UV-curable adhesive and dielectric inks for microfluidic devices, Lab Chip. 16 (2016) 70–74. doi:10.1039/c5lc01195g.

[93] F.C. Krebs, Fabrication and processing of polymer solar cells: A review of printing and coating techniques, Sol. Energy Mater. Sol. Cells. 93 (2009) 394–412.

doi:10.1016/j.solmat.2008.10.004.

[94]   J.W. Stansbury, M.J. Idacavage, 3D printing with polymers: Challenges among expanding options and opportunities, Dent. Mater. 32 (2016) 54–64. doi:10.1016/j.dental.2015.09.018.

[95]   P.F. Jacobs, Rapid Prototyping & Manufacturing. Fundamentals of Stereolithography, First Edit, Society of Manufacturing Engineers, United States of America, 1992.

[96]   P.J. Bartolo, Stereolithography: Materials, Processes and Application, Springer, New York, 2011. doi:0.1007/978-0-387-92904-0.

[97]   Think 3D, Digital light processing (DLP) 3D printing technology overview, (2019). https://www.think3d.in/digital-light-processing-dlp-3d-printing-technology-overview/.

[98]   X. Wang, M. Jiang, Z. Zhou, J. Gou, D. Hui, 3D printing of polymer matrix composites: A review and prospective, Compos. Part B Eng. 110 (2017) 442–458. doi:10.1016/j.compositesb.2016.11.034.

[99]   C. Yan, Y. Shi, J. Yang, J. Liu, Multiphase polymeric materials for rapid prototyping and tooling technologies and their applications, Compos. Interfaces. 17 (2010) 257–271. doi:10.1163/092764410X490680.

[100]   D. Dendukuri, D.C. Pregibon, J. Collins, T.A. Hatton, P.S. Doyle, Continuous-flow lithography for high-throughput microparticle synthesis, Nat. Mater. 5 (2006) 365–369. doi:10.1038/nmat1617.

[101]   A. Cazón, P. Morer, L. Matey, PolyJet technology for product prototyping: Tensile strength and surface roughness properties, Proc. Inst. Mech. Eng. Part B J. Eng. Manuf. 228 (2014) 1664–1675. doi:10.1177/0954405413518515.

[102]   M. Fahad, P. Dickens, M. Gilbert, Novel polymeric support materials for jetting based additive manufacturing processes, Rapid Prototyp. J. 19 (2013) 230–239. doi:10.1108/13552541311323245.

[103]   O. Ivanova, A. Elliott, T. Campbell, C.B. Williams, Unclonable security features for additive manufacturing, Addit. Manuf. 1 (2014) 24–31. doi:10.1016/j.addma.2014.07.001.

[104]   D. Thuau, C. Ayela, P. Poulin, I. Dufour, Highly piezoresistive hybrid MEMS sensors, Sensors Actuators, A Phys. 209 (2014) 161–168. doi:10.1016/j.sna.2014.01.037.

[105]   E.C. Sengezer, G.D. Seidel, R.J. Bodnar, Anisotropic piezoresistivity characteristics of aligned carbon nanotube-polymer nanocomposites, Smart Mater. Struct. 26 (2017). doi:10.1088/1361-665X/aa78c3.

[106]   J. Lee, M.O. Faruk Emon, M. Vatani, J.W. Choi, Effect of degree of crosslinking and polymerization of 3D printable polymer/ionic liquid composites on performance of

stretchable piezoresistive sensors, Smart Mater. Struct. 26 (2017). doi:10.1088/1361-665X/aa5c70.

[107] G. Malucelli, A. Fioravanti, L. Francioso, C. De Pascali, M.A. Signore, M.C. Carotta, A. Bonanno, D. Duraccio, Preparation and characterization of UV-cured composite films containing ZnO nanostructures: Effect of filler geometric features on piezoelectric response, Prog. Org. Coatings. 109 (2017) 45–54. doi:10.1016/j.porgcoat.2017.04.020.

[108] X. Chen, H.O.T. Ware, E. Baker, W. Chu, J. Hu, C. Sun, The Development of an All-polymer-based Piezoelectric Photocurable Resin for Additive Manufacturing, Procedia CIRP. 65 (2017) 157–162. doi:10.1016/j.procir.2017.04.025.

[109] A. Iregui, L. Irusta, O. Llorente, L. Martin, T. Calvo-Correas, A. Eceiza, A. González, Electrospinning of cationically polymerized epoxy/polycaprolactone blends to obtain shape memory fibers (SMF), Eur. Polym. J. 94 (2017) 376–383. doi:10.1016/j.eurpolymj.2017.07.026.

[110] K. Yu, A. Ritchie, Y. Mao, M.L. Dunn, H.J. Qi, Controlled Sequential Shape Changing Components by 3D Printing of Shape Memory Polymer Multimaterials, Procedia IUTAM. 12 (2015) 193–203. doi:10.1016/j.piutam.2014.12.021.

[111] S. Naficy, R. Gately, R. Gorkin, H. Xin, G.M. Spinks, 4D Printing of Reversible Shape Morphing Hydrogel Structures, Macromol. Mater. Eng. 302 (2017) 1–9. doi:10.1002/mame.201600212.

[112] H. Wei, Q. Zhang, Y. Yao, L. Liu, Y. Liu, J. Leng, Direct-write fabrication of 4D active shape-changing structures based on a shape memory polymer and its nanocomposite, ACS Appl. Mater. Interfaces. 9 (2017) 876–883. doi:10.1021/acsami.6b12824.

[113] R. Liu, X. Yang, Y. Yuan, J. Liu, X. Liu, Synthesis and properties of UV-curable self-healing oligomer, Prog. Org. Coatings. 101 (2016) 122–129. doi:10.1016/j.porgcoat.2016.08.006.

[114] J.A. Carlson, J.M. English, D.J. Coe, A flexible, self-healing sensor skin, Smart Mater. Struct. 15 (2006). doi:10.1088/0964-1726/15/5/N05.

[115] K. Davami, M. Mohsenizadeh, M. Mitcham, P. Damasus, Q. Williams, M. Munther, Additively Manufactured Self-Healing Structures with Embedded Healing Agent Reservoirs, Sci. Rep. 9 (2019) 1–8. doi:10.1038/s41598-019-43883-3.

[116] P. Sanders, A.J. Young, Y. Qin, K.S. Fancey, M.R. Reithofer, R. Guillet-Nicolas, F. Kleitz, N. Pamme, J.M. Chin, Stereolithographic 3D printing of extrinsically self-healing composites, Sci. Rep. 9 (2019) 1–6. doi:10.1038/s41598-018-36828-9.

[117] B. Zhang, W. Zhang, Z. Zhang, Y.F. Zhang, H. Hingorani, Z. Liu, J. Liu, Q. Ge, Self-Healing Four-Dimensional Printing with an Ultraviolet Curable Double-Network Shape Memory Polymer System, ACS Appl. Mater. Interfaces. 11 (2019) 10328–10336. doi:10.1021/acsami.9b00359.

[118] M. Invernizzi, S. Turri, M. Levi, R. Suriano, 4D printed thermally activated self-healing and shape memory polycaprolactone-based polymers, Eur. Polym. J. 101 (2018) 169–176. doi:10.1016/j.eurpolymj.2018.02.023.

[119] X. Kuang, K. Chen, C.K. Dunn, J. Wu, V.C.F. Li, H.J. Qi, 3D Printing of Highly Stretchable, Shape-Memory, and Self-Healing Elastomer toward Novel 4D Printing, ACS Appl. Mater. Interfaces. 10 (2018) 7381–7388. doi:10.1021/acsami.7b18265.

[120] L.P. Gao, G.J. Ding, Y.C. Wang, Y.L. Yang, Preparation of UV curing crosslinked polyviologen film and its photochromic and electrochromic performances, Appl. Surf. Sci. 258 (2011) 1184–1191. doi:10.1016/j.apsusc.2011.09.068.

[121] P.C. Ma, N.A. Siddiqui, G. Marom, J.K. Kim, Dispersion and functionalization of carbon nanotubes for polymer-based nanocomposites: A review, Compos. Part A Appl. Sci. Manuf. 41 (2010) 1345–1367. doi:10.1016/j.compositesa.2010.07.003.

[122] V.F. Cardoso, C. Ribeiro, S. Lanceros-Mendez, Advanced Piezoelectric Materials: Science and Technology. Chapter 8: Electroactive Polymers as Actuators, Second Edi, Duxford, United Kingdom, 2017.

[123] C. Liu, H. Qin, P.T. Mather, Review of progress in shape-memory polymers, J. Mater. Chem. 17 (2007) 1543–1558. doi:10.1039/b615954k.

[124] R.P. Wool, Self-healing materials: a review, Soft Matter. 4 (2008) 400. doi:10.1039/b711716g.

[125] R.J. Mortimer, A.L. Dyer, J.R. Reynolds, Electrochromic organic and polymeric materials for display applications, Displays. 27 (2006) 2–18. doi:10.1016/j.displa.2005.03.003.

Chapter 2

Photocurable piezoresistive materials

The development of composites based on polyurethane acrylate (PUA) UV-curable resins and multi-walled carbon nanotubes (MWCNT) is explained. Their UV curing capability, morphological, thermal, mechanical, electrical and piezoresistive properties are analyzed. The suitability of the materials for force and deformation sensing applications is demonstrated.

2.1. Introduction

As indicated Chapter 1, in an ever-increasing number of advances in science and technology, Internet plays a dominant role facilitating the interconnection of information and processes [1,2]. Smart materials are considered as key materials for the development of wireless, interconnected and sustainable systems and in this sense, they are directly related to the evolution of Internet of Things (IoT) concept [3]. Among the different smart materials and particularly electroactive ones, piezoresistive materials have arisen as highly demanded materials for device components on industrial and consumer products [4–6]. The piezoresistive effect is defined as the variation of electrical resistivity of a material in response to a mechanical stress or strain. This variation of the electrical resistance shows geometrical (variation of the electrodes distance) and intrinsic (mechanically induced variation in the mobility of the electrons) contributions [7]. Metallic strain gauges or semiconductors have been traditionally used as piezoresistive sensors, being characterized by low and high piezoresistive sensitivity, respectively [8]. However, the poor mechanical properties of these materials (lack of ductility and flexibility) limited their use [9,10].

The composite materials could represent an effective alternative to overcome these limitations, thus obtaining materials with improved properties, ie, piezoresistive materials with large flexibility, ease to process and with a cost-effective production [8]. One of the most successful methods to obtain these composites is by the combination of polymeric matrices with a carbon based piezoresistive materials, such as carbon nanofibers (CNF), carbon nanotubes (CNT) or graphene [11–13]. The wide formulations available by the combination of polymers and nanofillers allow the obtaining of a toolbox of materials capable to adapt their properties by adapting their formulation in order to reach the requirements of specific applications [4]. The main advantages of polymers over metals and ceramics include the tailorable mechanical, electrical and thermal properties, as well as the versatile manufacturing techniques, often allowing to process the material in a variety of shapes and easy integration into devices [14]. Similarly to the polymers, there is important variety of carbon-based nanofillers (different aspect, size or surface area) accessible, so from an adequate formulation of these components a wide range of tailor made composites could be design and fabricated. That is, advanced piezoresistive composites could be obtained with specific electrical, mechanical, thermal and electromechanical properties.

Multi-walled carbon nanotubes (MWCNT) are among the most used carbon-based nanofillers for the development of polymer composites due to their large aspect ratio, high electrical conductivity and mechanical reinforcing properties within polymers [15]. In particular, the high aspect ratio of MWCNT [11,16] allows to obtain polymer composites with the lowest electrical percolation thresholds [17], thus leading to high electrical conductivity values while still maintaining the mechanical properties of the polymers matrix, including, in some cases, flexibility and even stretchability [18]. It is to notice that the percolation threshold concentration is critical not just for strongly increasing the electrical conductivity of the composite [4], but also for maximizing the piezoresistive sensitivity [19].

Thus, high temperature methods (extrusion) or solvent casting have been used for the development of the piezoresistive polymer composites. For solvent casting methods, most of the studies used highly toxic organic solvents such as chloroform [20], dimethylformamide [21], or toluene [16], leading to product waste managing problems and increased VOCs emissions. Therefore, environmentally friendlier approaches are being investigated, such as, the use of cyclopentyl methyl ether (CPME) or water as a solvent for the fabrication of printable piezoresistive sensors [4,12]. In this sense, a solvent free ultraviolet curing based method can be considered as an excellent alternative to solve this problem and therefore, it will be the main objective of this chapter. This method, as explained before, is a fast curing method (seconds or minutes), it can be performed at room temperature in a reduced space and high resolution patterns can be obtained [22].

With respect to UV curable piezoresistive composites, a few works have been presented. A flexible organic piezoresistive micro-electro-mechanical system (MEMS) was obtained combining MWCNT and a commercial available UV curable epoxy photoresin (SU-8). The prepared strain sensor shows a gauge factor of 200 for optimized sensor geometries [23]. In addition, single-walled carbon nanotubes (SWCNT) can be used to obtain a UV curable piezoresistive material in combination with urethane dimethacrylate (UDMA) and 1,6-hecadienol dimethacrylate (HDDMA) [24]. In this case, randomly oriented and aligned SWCNT/polymer nanocomposites were studied. The piezoresistive behavior with 0.03 wt.% SWCNT content for aligned composites shows a GF between 2 and 10 depending on the strain direction (axial and transverse, respectively). Also, UV curable piezoresistive tactile sensors were developed using ionic liquid as nanofiller. (1-ethyl-3-methyl-imidazolium tetrafluoroborate (EMIMBF$_4$) as an ionic liquid and the 2-[[(butylamino)carbonyl]oxy]ethyl

acrylate (BACOEA) as acrylate polymer were used to obtain piezoresistive tactile sensors characterized by GF of about 0.6 under uniaxial pressure [25].

In addition, different UV curable piezoresistive materials applicable for 3D printing techniques have been developed. Liu *et al.* [26] proposed a novel approach to fabricate a fully 3D printed sensor. The 3D printed force sensor was obtained by printing a substrate using digital light processing (DLP) based 3D printer and high temperature resin, and a strain gauge was made by inkjet printing and poly(3,4-ethylenedioxythiophene) polystyrene sulfonate (PEDOT/PSS) ink. The obtained sensor was characterized within the range from 0 mN to 600 mN, with a linearity error of 3.8% FS, a sensitivity of 0.97% N^{-1}, a repeatability of 1.9% FS, a hysteresis of 3.1% FS and overall accuracy of 5.3% FS.

Emon *et al.* [27] showed the fabrication process of a 3D printed smart insoles with stretchable piezoresistive sensors for plantar pressure monitoring. These soft pressure sensors were located on the heel, midfoot and forefoot to detect the force, the timing and the location of the strike while walking. The insole was 3D printed using a soft and flexible UV curable material and presented multiple open channels on it to attach the subsequently fabricated piezoresistive sensors. These flexible, stretchable and multi-layered piezoresistive sensors were fabricated via screen printing and moulding processes, and comprises an ionic liquid (IL) based piezoresistive layer sandwiched between two multi-walled carbon nanotube (MWCNT) based stretchable electrodes and finally, top and bottom insulation layers. All layers were UV cured with the exception of the stretchable electrode. Further, the fabrication of flexible piezoresistive sensor embedded in 3D printed tires was also demonstrated [28]. The fabrication of the piezoresistive pressure sensor as their performance were reported.

Piezoresistive UV curable materials have been presented by Davoodi *et al.* [29] who developed a new UV curable ink based on a composite of milled carbon fibber (MCF) and silicon rubber (SR) in a total 30 wt.% fibber content. Flexible piezoresistive sensors were printed using a novel high-speed material jetting (MJ) 3D printer of high-viscosity conductive inks. The sensor shows high flexibility and foldability as well as a high resistance sensitivity to severe bending tests. The stretchability of the 3D printed materials was improved by sandwiching the MCF/SR active layer between two SR layers. The evaluation of electromechanical properties of these sandwiched MCF/SR sensors demonstrated high piezoresistive sensitivity with a gauge factor around 400.

In this context, the present work reports on the development of stimuli responsive and environmental friendly materials for sensing applications based on UV cured MWCNT/polyurethane acrylate resin (MWCNT/PUA) composites with optimized piezoresistive response, which is in turn related to the morphological, thermal, mechanical, and electrical properties of the material as a function of MWCNT content.

2.2. Experimental

2.2.1. Materials and Sample preparation

Multi-walled carbon nanotubes (MWCNT) with reference NC7000TM were provided by Nanocyl, S.A, Belgium. They were manufactured by chemical vapour deposition and show a carbon purity of $\approx 90\%$, average diameter ≈ 9.5 nm, and average length ≈ 1.5 µm. Commercial polyurethane acrylate photoresin SPOT-ETM was supplied by SPOT-A Materials® (Spain). All composites samples were processed using the MWCNT and the photoresin as received.

The samples were prepared mixing different amounts of the nanocarbonaceous filler (0; 0.1; 0.2; 0.3; 0.4; 0.5; 0.6 wt.%) with the corresponding volume of the SPOT-ETM resin by magnetic stirring for 30 min. To promote a good dispersion and disentanglement of the MWCNT bundles, the samples were sonicated using an ultrasonic probe (Bioblock Scientific, model Vibracell 75115) for 5 minutes at 500W and 20kHz with 7 seconds of pulse and 3 seconds of pause. Then, samples were placed in an ultrasound bath (J. P. SELECTA Model 3000865) during 1 h. After complete dissolution, flexible films were obtained using doctor blade technique on a clean glass substrate. The samples were cured at room temperature for 20 minutes with a UV-LEDs lamp that works at 395 nm wavelength and 19 mW/cm^2 of irradiance. All process is illustrated in **Figure 2.1**. The resulting highly flexible composite films showed thicknesses between 150–300 µm, measured using a coater measurement gauge Fisher DualScope MPOR.
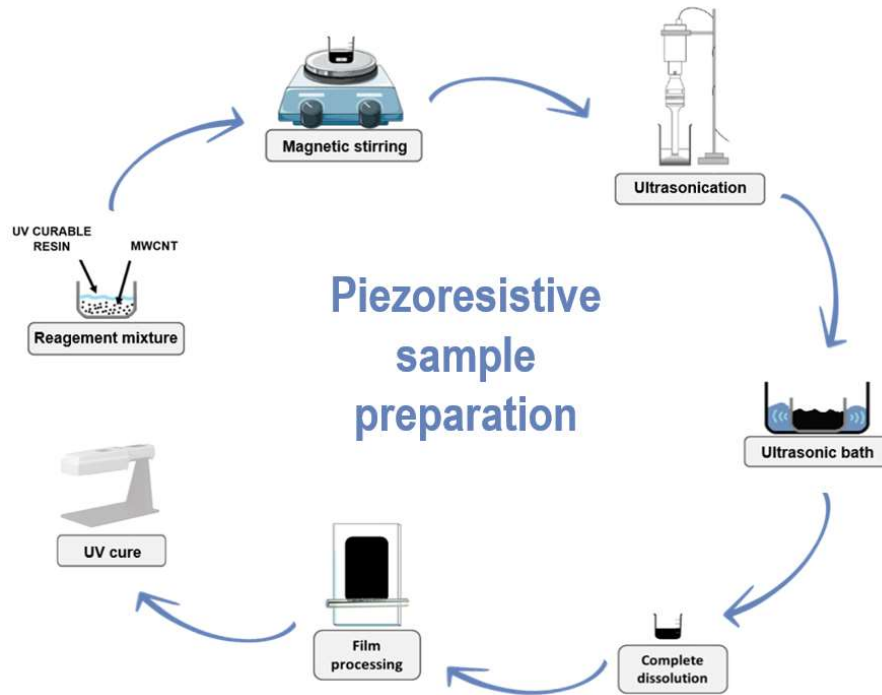
Figure 2.1 – Schematic diagram showing the preparation of MWCNT/PUA composite films through a Doctor Blade method.

2.2.2. Samples characterization

The UV curing process was studied by photo-DSC, using a DSC (TAInstruments Q2000) equipped with a photocalorimetric accessory (Omnicure S2000) with a 200 W mercury lamp, with an optical range from 320 to 500 nm and an intensity between 1 and 2 mW/cm^2. The sample area was 0.2 cm^2.

The conversion degree (α) of double bonds (C=C) has been obtained considering the area of the exothermic peak and using Equation (2.1).

$$\alpha = \frac{\Delta H_t}{\Delta H_0^{theor}} \tag{2.1}$$

where ΔH_t is the reaction enthalpy at time t, and ΔH_0^{theor} is the theoretical value of the enthalpy for the complete conversion [30]. In this case, due to the use of a commercial resin with an unknown double bond group, functionality and molecular weight, the final value of the enthalpy after the complete UV curing process of the pure resin was considered as the theoretical enthalpy.

The polymerization rate (R_p) has been obtained after Equation (2.2).

$$R_p = \frac{d\alpha}{dt} = \frac{dH/dt}{\Delta H_0^{theor}} \tag{2.2}$$

Composite morphology was evaluated using Scanning Electron Microscopy (SEM). The images were obtained using a Hitachi S-4800 scanning electron microscope at an accelerating voltage of 10 kV with magnification of 20000×.

Fourier transform infrared spectroscopy in the total attenuated reflection (FTIR-ATR) mode was performed in a Nexus FTIR Nicolet spectrophotometer in the spectral range 4000 to 600 cm^{-1} with a spectral resolution of 4 cm^{-1} and 32 scans.

The thermal behaviour of the samples was evaluated by thermogravimetric analysis (TGA) using a Mettler Toledo TGA/SDTA851 instrument. The tests were carried out under nitrogen atmosphere from 25 °C to 700 °C at a rate of 10 °C·min^{-1}. For each sample, the degradation temperature (T_{onset}), calculated as the extrapolated onset temperature in the TGA curve, and the temperature of the maximum degradation rate (T_{max}), measured as the first derivative peak temperature, were recorded. In addition, the glass transition temperature (T_g) of the samples was evaluated by differential scanning calorimetry (DSC), performed from - 50 to 250 ºC at a rate of 20 ºC·min^{-1} using a DSC 822e from Mettler Toledo under nitrogen atmosphere in two successive scans. The glass transition temperature was calculated as the extrapolated onset of the baseline shift.

Analysis of the mechanical properties were performed using a universal testing machine Shimadzu model AG-IS with a load cell of 1 kN. Measurements were carried out in tensile mode at room temperature on rectangular composites with dimensions of approximately ≈ 10 mm x 4 mm x 250 µm at a test velocity of 1 mm·min^{-1}.

The electrical conductivity of the samples was measured with a Keithley 487 picoammeter/voltage source. The current-voltage characteristic response was obtained in direct current (DC) mode with an applied voltage ranging between -10 V to +10 V, at room temperature.

On each sample, two gold electrodes with diameter of 5 mm were deposited by magnetron sputtering on both sides of the samples. The coating was performed by using a Quorum Q150T S sputter coater.

The electrical conductivity (σ) is obtained as the inverse of the electrical resistivity (ρ) by applying Equation (2.3):

$$\sigma = \frac{1}{\rho} = \frac{1}{R}\frac{t}{A}$$

(2.3)

where R is the electrical resistance of the sample, A is the area of the electrodes and t represents the thickness of the samples.

The piezoresistive response of the composites has been obtained after electro-mechanical test carried out in the following way: uniaxial strain tests were performed with a Shimadzu model AG-IS universal testing machine (load cell of 500 N) while simultaneously measuring the resistance of the samples during uniaxial mechanical deformation with an Agilent 34401A multimeter. The dimensions and geometry of the samples where similar to the ones used for mechanical testing and deformations up to 4% of strain were applied to the samples at a deformation rate of 5 mm·min^{-1}. The electrodes in the composites were placed in contact with the clamps of the universal testing machine so that no deformation is applied to them. The experimental conditions are schematically represented in **Figure 2.2** [31].
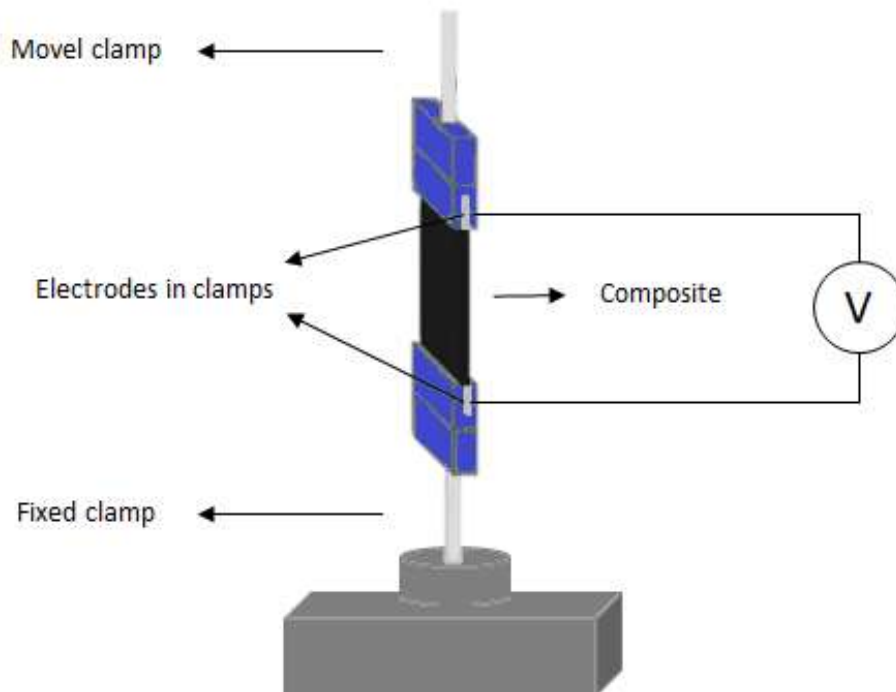

Figure 2.2 – Schematic representations of the electro-mechanical measurements in the composites.

The electro-mechanical sensibility of the samples, quantified by the gauge factor (*GF*), was calculated after Equation (2.4) [32,33].

$$GF = \frac{dR/R_0}{dl/l_0} = \frac{d\rho/\rho_0}{dl/l_0} + (1 + 2\nu) \tag{2.4}$$

where R_0 is the steady-state electrical resistance of the material without deformation and *dR* is the resistance variation due to the deformation dl [37,38]. Further, *v* represents the Poisson ratio and ρ represents the electrical resistivity. It is notice that two different factors contribute to the GF (Equation 2.4): an intrinsic variation of the electrical resistivity, related to the variation of the conductive network ($\frac{d\rho/\rho_0}{dl/l_0}$), and a geometrical contribution, related to dimensional variations of the samples upon deformation (1 + 2 v) [32,33].

2.3. Results and discussion

2.3.1. Photopolymerization process

Figure 2.3a shows the conversion (α) of the curing reaction as a function of the reaction time for MWCNT/PUA composites with different nanofiller contents. It is observed that an increase in the MWCNT induce an important decrease on both acrylic double bond conversion and photopolymerization rate. Similarly, Sandoval *et al*. [34] described this phenomenon where the strong absorption of light by the MWCNT strongly competes with the light adsorption by the photoinitiator.

The polymerization rate (R_P) versus time is presented in **Figure 2.3b** for the same samples. The maximum polymerization rate is reached in the first seconds for all samples. However, a decrease on the polymerization rate owning to the carbon filler content could be observed, since at higher conversions an immobilization of the polymer chains occurs caused by the curing reaction [35]. In addition, the R_P maximum is not significantly affected by the MWCNT filler content.
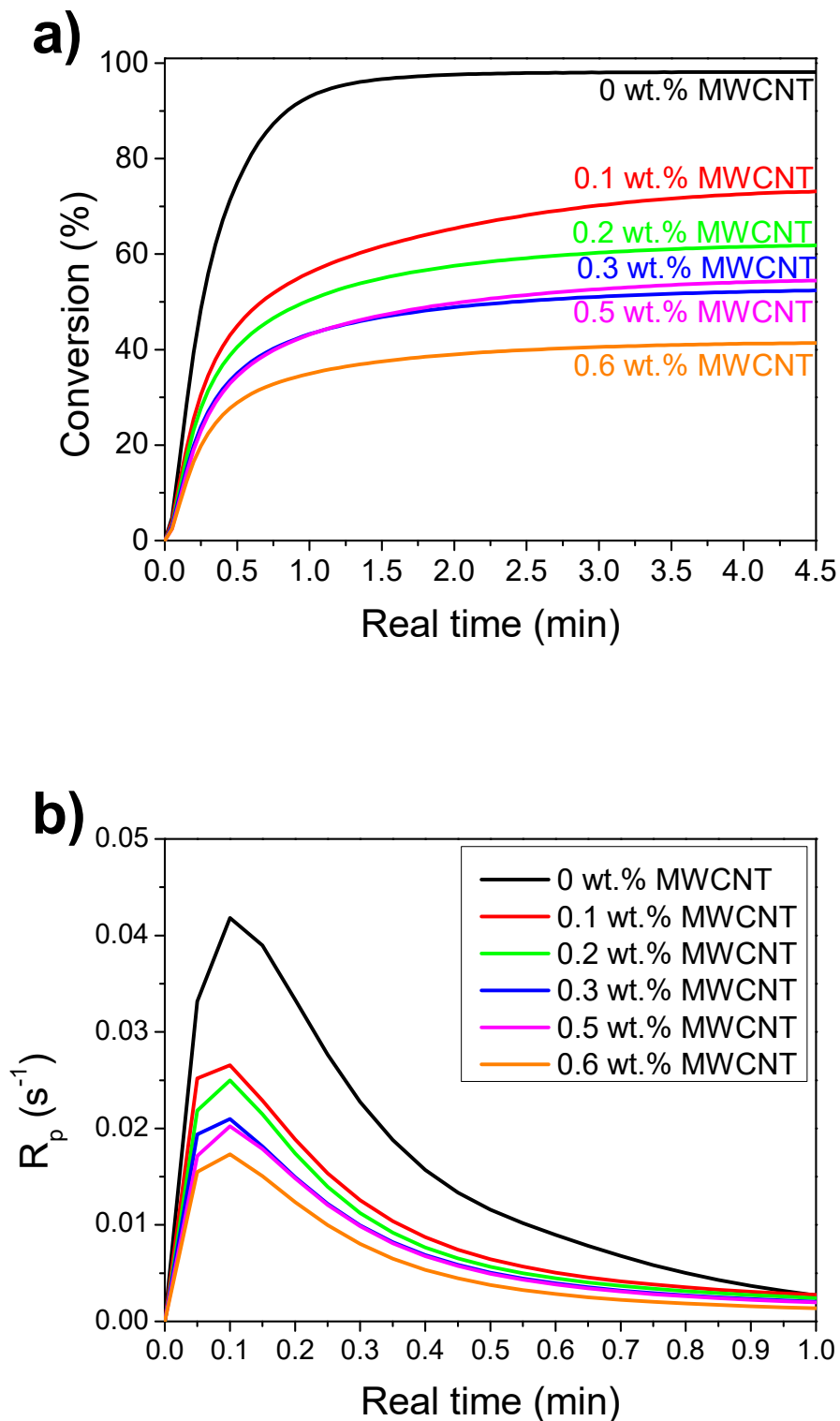
Figure 2.3 – Curing conversion of PUA and composites samples for 0, 0.1, 0.2, 0.3, 0.5 and 0.6 wt.% MWCNT content (a) and photopolymerization rate (R_p) for the same samples (b).

The maximum conversion for each composition is obtained in less than 1 minute for both PUA resin and composites, with the maximum conversion close to 100% for PUA and

decreasing to 35% for MWCNT/PUA composite with 0.6 wt.% MWCNT content. The behaviour of R_p is similar for the resin and the composites with different nanofiller content. It can be observed that minimum degree of R_p is achieved with the highest MWCNT content, being for the 0.6 wt.% MWCNT/PUA sample less than half of the PUA resin sample due to the UV radiation absorption by the MWCNT [35,36]. Therefore, the increase of the amount of MWCNT reduces the light penetration and, consequently, the probability of producing initiating radicals, which is reflected in the final conversion values [37].

2.3.2. Morphological and chemical properties

Dispersion and wettability between the MWCNT and the photoresin matrix could be evaluated by the analysis of the SEM images of the samples with different nanofiller contents (from 0.1 to 0.6 wt.% MWCNT) in **Figure 2.4**.

SEM images demonstrate that composites samples present good dispersion of the MWCNT within the polymer matrix, which fully surrounds the fillers, not showing any voids or loose interfaces between fillers and the polymer matrix. Further, just a few small aggregates of several micrometers in diameter are observed for the samples with larger MWCNT content. These aggregates are homogeneously distributed along the samples, as it could be observed in the SEM images of the composite with 0.6 wt.% MWCNT. Alishiri and co-workers have reported similar results for composites of biocompatible acrylate-terminated polyurethane containing chemically modified MWCNT [38].

A suitable dispersion of the fillers is desirable as it has been demonstrated that the electrical conductivity (see later) of composites depends on MWCNT distribution within the polymer matrix. Thus, well distribution of small agglomerates or clusters is more important for achieving higher electrical conductivity [39,40] than a good dispersion of individual fillers. However, agglomerate distribution could affect other properties of composites, as the case of the mechanical properties [40]. Different parameters such as dispersion method, dispersion agent or structural quality of carbon nanofillers [41] have a direct influence in electrical properties of polymer/carbonaceous filler composites.
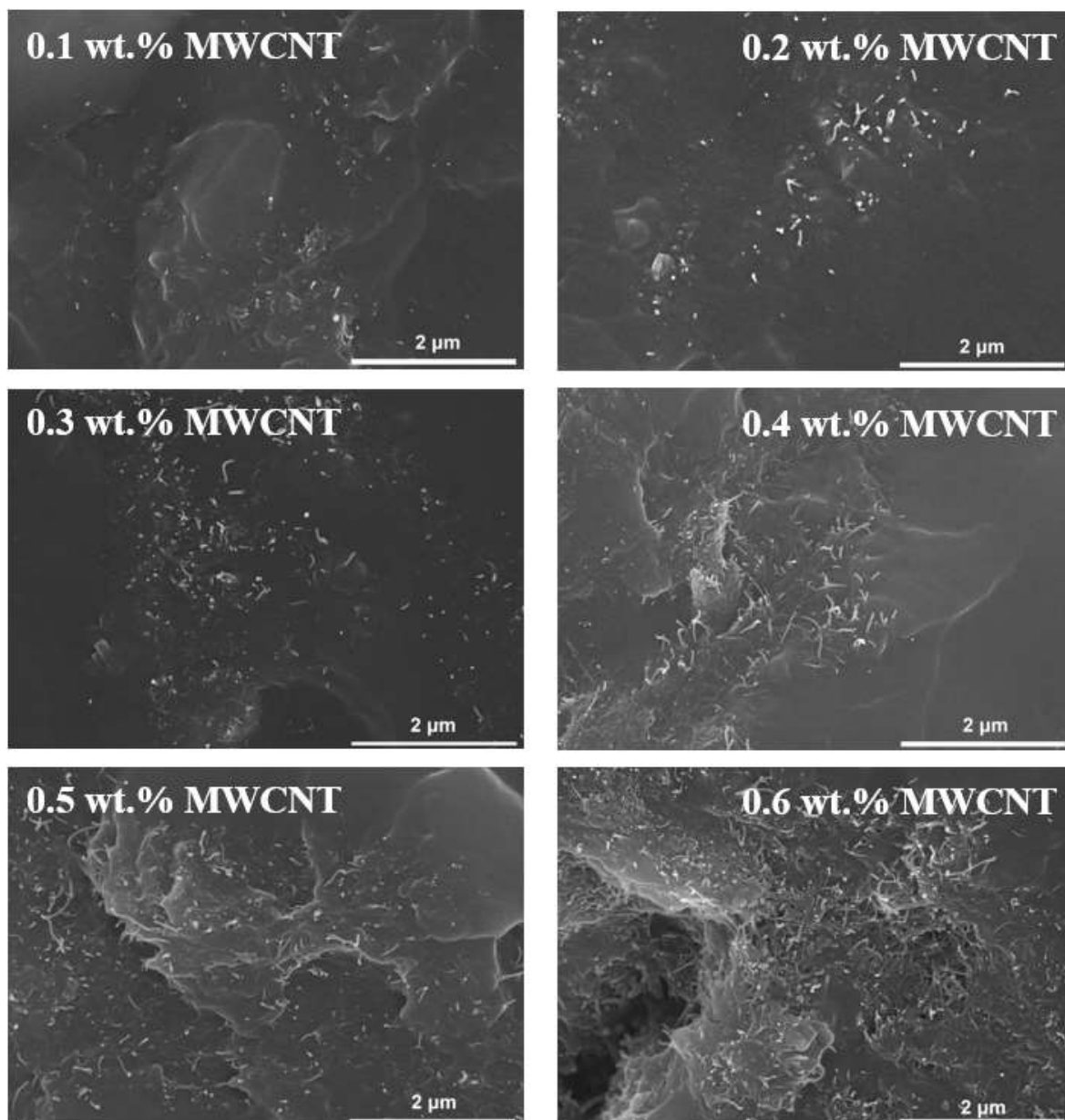
Figure 2.4 – Representative SEM images of the MWCNT/PUA for 0.1 to 0.6 wt.% MWCNT at magnifications of 20000x.

FTIR spectroscopy (**Figure 2.5**) allows to identify the characteristic absorption bands of SPOT-E^{TM} photoresin, a polyurethane acrylate resin [42]. The resulting polymer obtained after the UV curing process presents characteristics peaks on the FTIR spectra typical for polyurethane acrylate polymeric vibrations, 3330-3400 cm^{-1} (N-H stretching), 2855-2955 cm^{-1} (CH$_2$ and CH$_3$ stretching), 1725 cm^{-1} (C=O stretching), 1550 cm^{-1} (C-N and N-H combined stretching), 1360 cm^{-1} (C-N stretching) and 1110 cm^{-1} (C-O-C stretching) [43]. The addition of different MWCNT contents leads to no significant changes in the photoresin spectra, indicating no chemical bonding between the polymer and the MWCNT.

In addition, the absence (or a small band) of the C=C bond at 1650 cm^{-1} imply the complete curing reaction after the UV curing process [44,45].
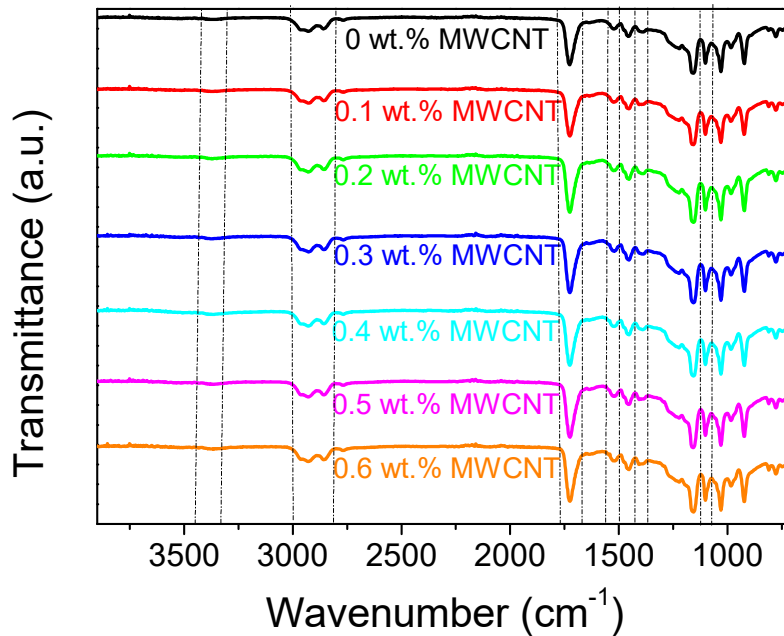
Figure 2.5 – Fourier Transformed Infrared (FTIR) spectra for PUA resin and MWCNT/PUA composites for 0.1 to 0.6 wt.% MWCNT content.

2.3.3. Thermal properties

The thermal properties of the composites are characterized using TGA and DSC in order to analyse the variations of the thermal degradation and transition, respectively, temperatures, due to the presence of the carbon nanofillers on the composites.

The thermogravimetric (TG) and the differential thermal gravimetry (DTG) curves of the MWCNT/PUA composites for the different amounts of nanofiller (up to 0.6 wt.%) are depicted in **Figure 2.6a** and **Figure 2.6b**, respectively. The thermal degradation of the polyurethane acrylate films occurs in the temperature range of 160-280 ºC for the first step, at 280-400 °C for the second step, and at 400-450 °C for the third step [46].
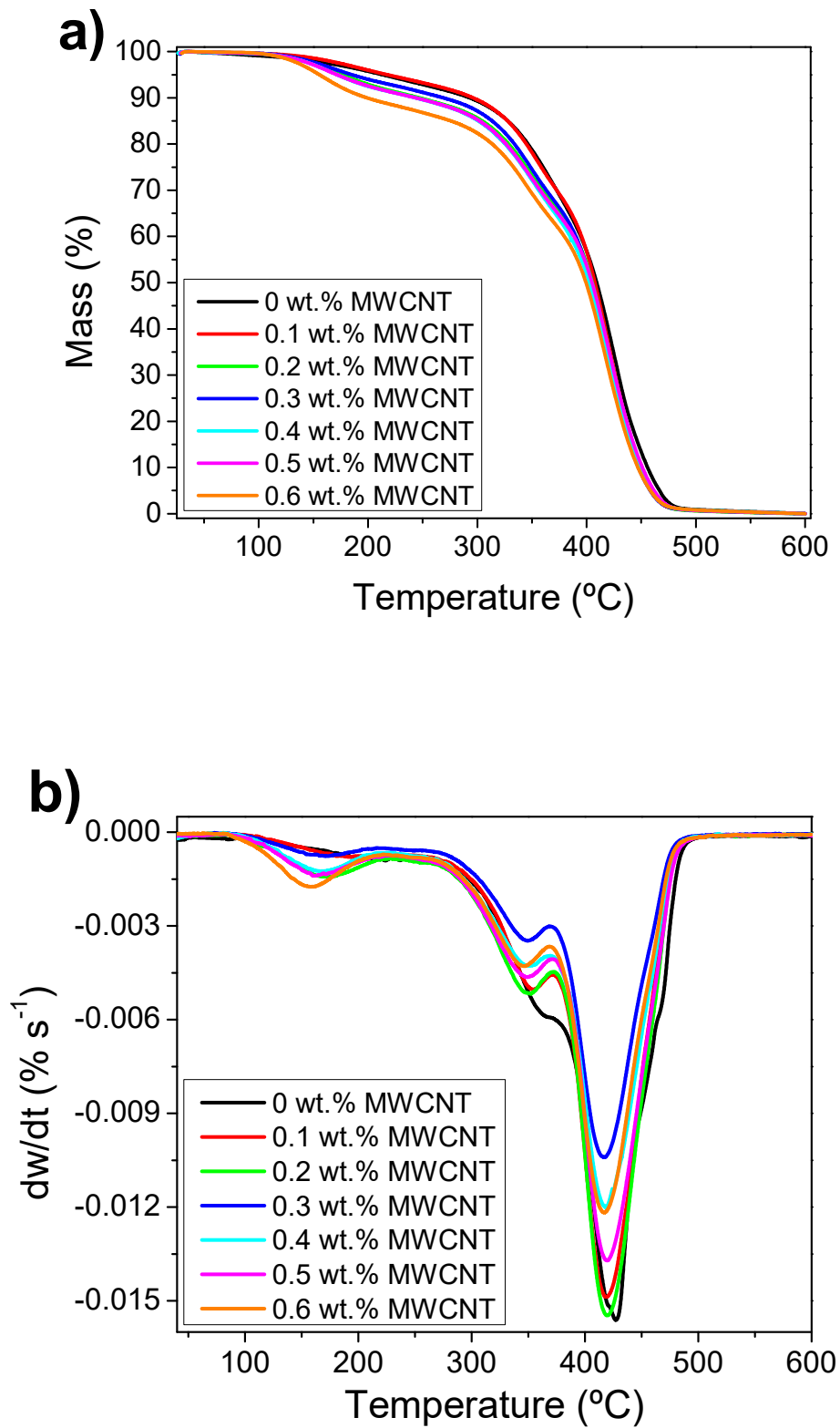
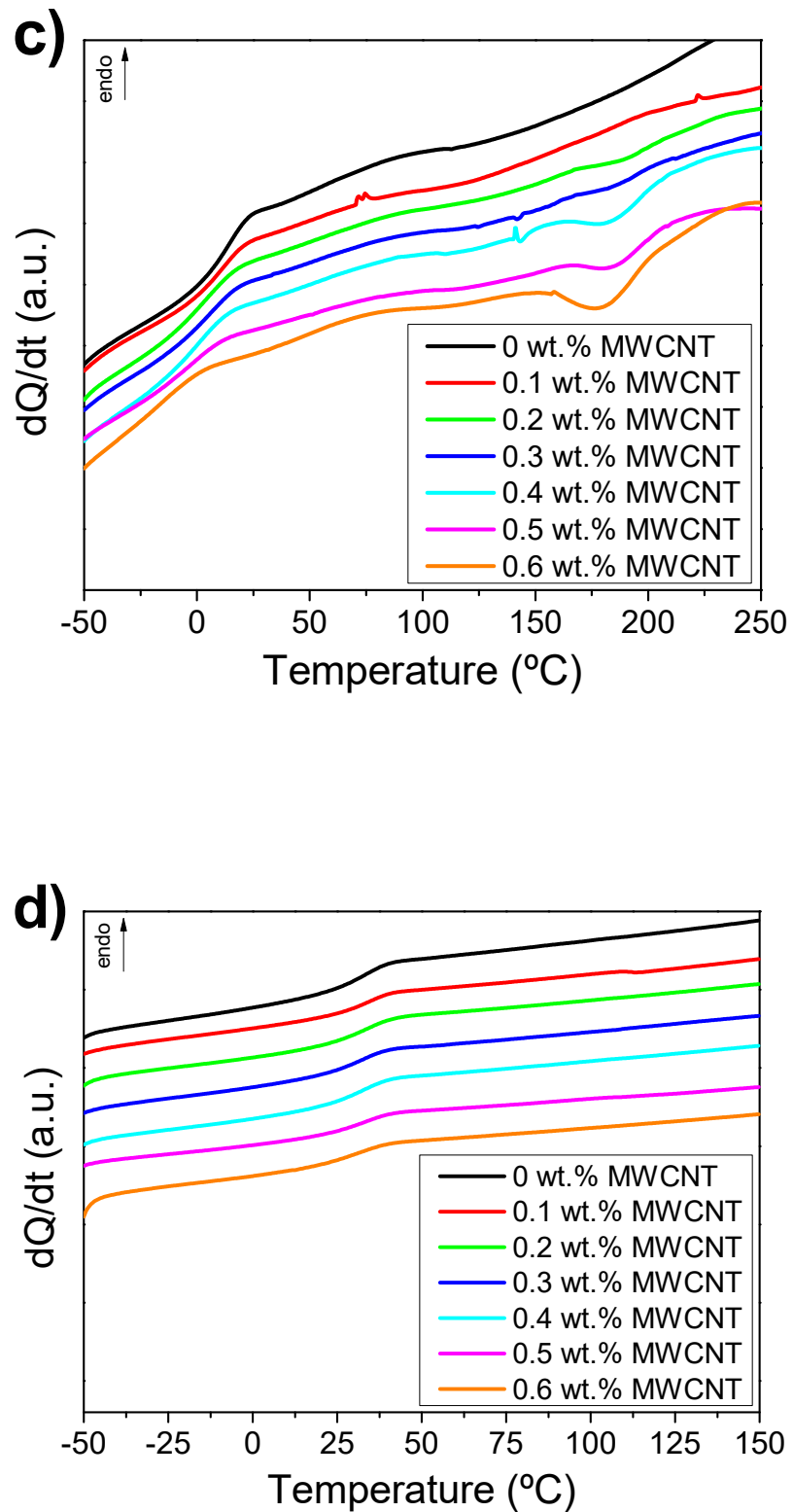**Figure 2.6 -** Thermal degradation (a), DTG (b), differential scanning calorimetry (DSC) thermograms in the first scan (c) and in the second scan (d) for PUA resin and MWCNT/PUA composites for 0.1 to 0.6 wt.% MWCNT content.

The first step was attributed to decomposition of urethane bonds; the second and third were considered consecutive and related to the decomposition of ester groups [47]. Similar degradation profiles were obtained for all the samples, the degradation beginnings earlier when the nanofiller content increases indicating a slightly lower thermal stability for samples with higher MWCNT content. MWCNT does not suffer degradation until 600 ºC, temperature at which the polymer matrix is completely degraded [47]. This decrease in thermal stability of the polymer matrix with the addition of MWCNT is related to the differences in the UV-curing process [46], that is, the higher MWCNT hinders the curing process. After 400 ºC the thermal degradation behaviour is similar for PUA and the composites.

The glass transition temperature (T_g) was measured by DSC (**Figure 2.6c**). The pristine SPOT-E^{TM} photoresin sample shows a T_g at around 20-25 ºC. The incorporation of MWCNT into the photoresin decreases the T_g. Moreover, with higher nanofiller content an exothermic peak appears indicating a thermal postcure of the samples [48]. In the second scan (**Figure 2.6d**) all samples present the same T_g which appears at around 37.5 ºC.

As previously indicated, the addition of nanofillers affects the photopolymerization process mainly due to the absorption of UV light by the MWCNT [35,36], hindering the light absorption by the photoinitiator and reducing the effectiveness of the curing process [49] (**Figure 2.2**). A postcuring process is observed for the samples with the higher amount of MWCNT (0.4, 0.5 and 0.6 wt.%) corroborating that UV irradiation does not lead to a full curing of the samples. In addition, the glass transition temperature decreases due to the nanofillers plasticizing effect: the presence of the fillers leads to a larger free volume within the polymer, which results in a lower T_g with increasing MWCNT content [50]. After the heating process, all the samples reach the same T_g (37.5 ºC) independently of the nanofiller content, indicating that the crosslinking degree is the same for all the samples (**Figure 2.5d**). Furthermore, as any exothermic peak is observed, the maximum crosslinking degree is obtained for all samples.

2.3.4. Mechanical and electrical properties

UV-curable acrylic coatings/films are limited in some application areas due to their poor resistance to high temperature, low strength and insulating properties. However, composites

with enhanced thermal and mechanical properties are prepared by adding nanofillers such as CNT, ZnO, SiO2, ZrO$_2$ and graphene into the polymer matrix [51].

Mechanical stress-strain measurements were performed for PUA photoresin film and the composites with 0.1 wt.% to 0.6 wt.% MWCNT content (**Figure 2.7**). The initial modulus was measured up to 1% of strain in 3 different samples.
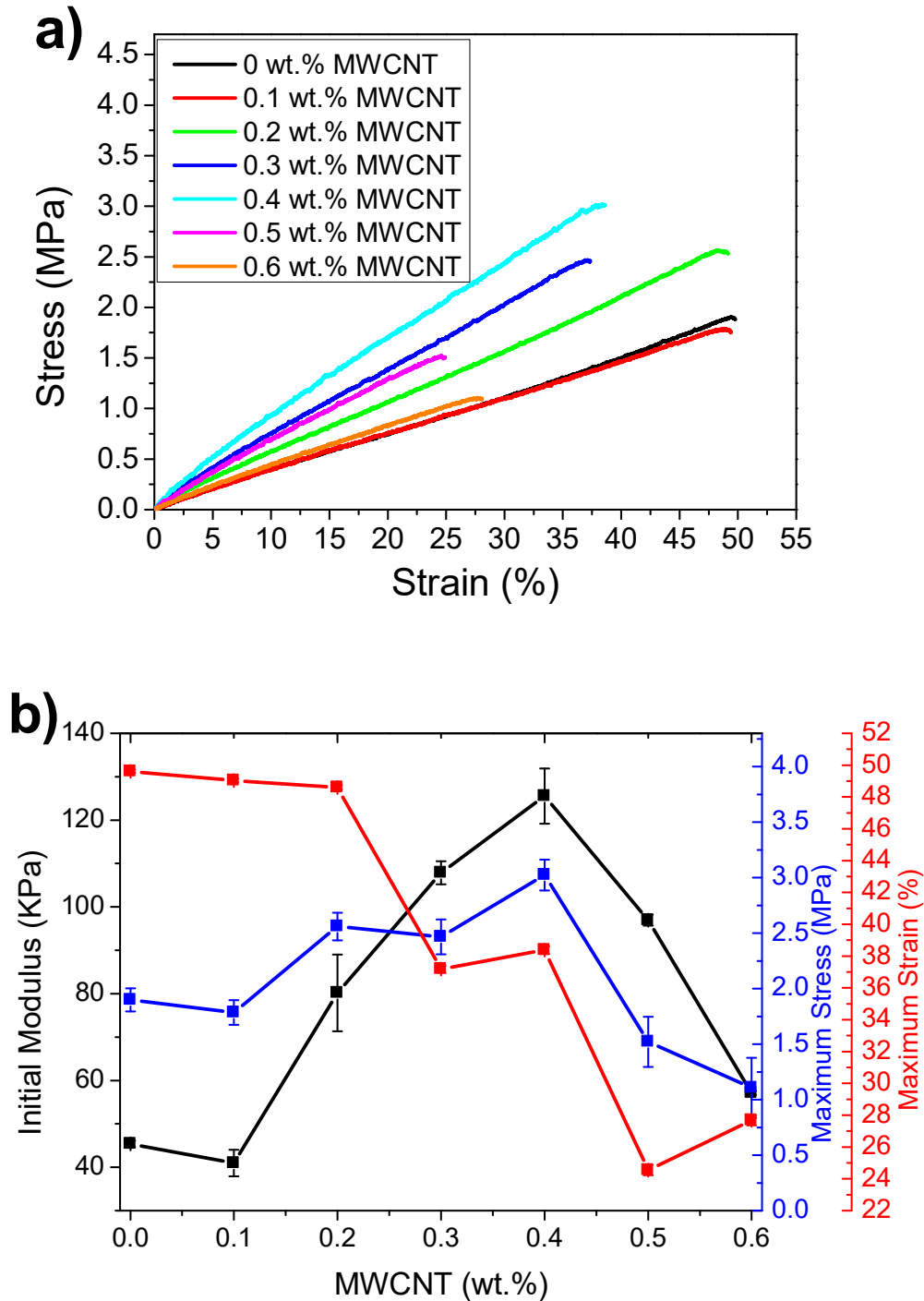
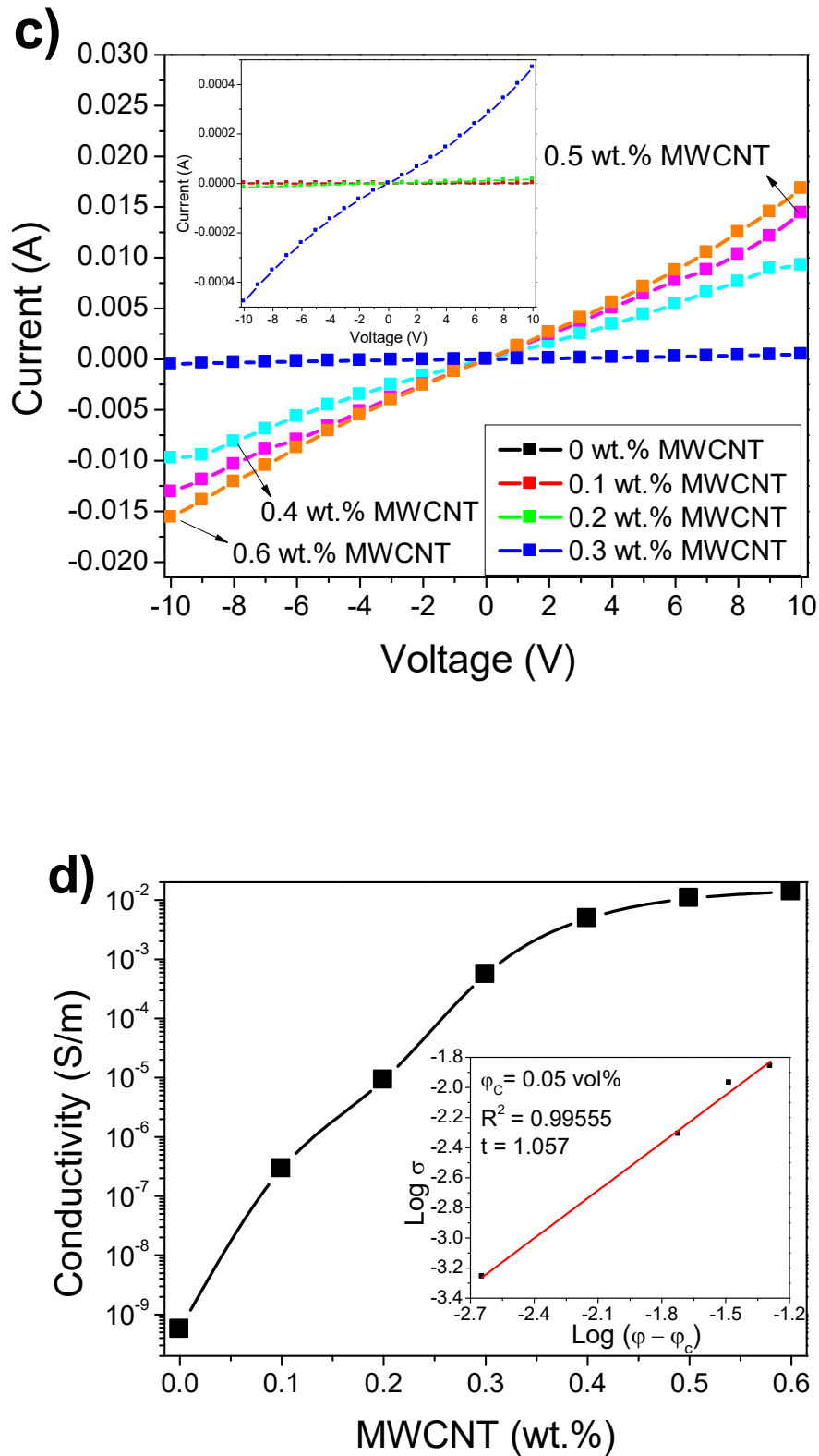**Figure 2.7** – Mechanical behavior at 1 mm·min^{-1} (a), initial modulus, maximum stress and maximum strain as a function of MWCNT content (b), current vs voltage (I–V) measurements (c) and electrical conductivity as a function of MWCNT content (d) of the PUA and composites up to 0.6 wt.% of MWCNT.

The maximum strain for the photoresin sample is around 50%, decreasing up to 25% for the composites with higher nanofiller content. On the other hand, the composites with multi-walled carbon nanotubes show an increase of the initial modulus when increasing the nanotube content. For the photoresin sample, the value of the initial modulus is around 45.4 ± 0.7 kPa and increases to 125.6 ± 6.4 kPa for composites with 0.4 wt.% filler content. Hence, it is demonstrated that the nanofiller acts as reinforcement, once the MWCNT show larger mechanical strength than the polymer matrix. It also demonstrated the good wettability of the fillers by the polymer matrix and the suitable mechanical properties of the materials for sensor applications [52–54].

For composites with 0.5 wt.% and 0.6 wt.% MWCNT content, a decrease of the initial modulus is observed. Taking into account the morphological results (**Figure 2.4**), agglomerations or MWCNT clusters are obtained with an increase on the nanofiller content, which act as defects with respect to the mechanical response. Therefore, the MWCNT dispersion has an important influence on the mechanical properties observing an increase of the initial modulus for composites with MWCNT dispersed (before 0.4 wt.% MWCNT content) and a decrease for composites with MWCNT clusters (after 0.5 wt.% MWCNT content) due to the surface area interaction between fillers and polymer matrix.

The electrical response of the materials as a function of nanofiller content is presented in **Figure 2.7**, which shows the intensity-current (I-V) characteristic curves (**Figure 2.7c**) and the electrical conductivity of the samples as a function of the nanofiller content (**Figure 2.7d**).

The electrical conductivity is 5.6 x 10^{-10} S/m for the PUA photoresin and increases with nanofiller content in the composites, as indicated by the increase on the slope of the I-V curves, which maintain its linear behaviour independently of the filler content. The electrical percolation threshold of the MWCNT/PUA composites is between 0.1 wt.% to 0.4 wt.% MWCNT content, with an electrical conductivity increment from 2.9 x 10^{-7} to 4.9 x 10^{-3} S/m, respectively. Similar results have been observed previously, for example, with functionalized carbon nanotubes [55]. The typical interpretation of this behaviour relies in the percolation theory [56], that allows to obtain the electrical percolation threshold Equation (2.5) [57]:

$$\sigma = \sigma_0(\varphi - \varphi_c)^t \qquad (2.5)$$

where σ_0 is the electrical conductivity, φ the volume fraction of the fillers, φ_c the percolation critical volume fraction and t is a critical exponent related to the dimensionality of the system. Thus, it can be determined form the slope of the log (σ) vs log $(\varphi$-$\varphi_c)$ representation.

According to the fitting of the log (σ) vs log $(\varphi$-$\varphi_c)$ (inset of **Figure 2.7d**), the percolation threshold of the MWCNT/PUA composites is near φ_c= 0.05 vol% (0.3 wt.%) and t is around 1.06, which represents a two-dimensional conductive system within the polymer matrix [57].

On the other hand, the largest electrical conductivity, ≈0.014 S/m is obtained for the composites with higher MWCNT content (0.6 wt.% MWCNT). The high electrical conductivity and low percolation threshold of MWCNT/PUA composites depends on the intrinsic properties of MWCNT, mainly their electrical conductivity and aspect ratio, and the composites preparation method, leading to proper filler dispersion, as it has been described in other similar systems [4]. The observed low percolation threshold with the consequent stabilization of the electrical conductivity over increasing filler content demonstrate the proper dispersion of the fillers [4] and that the prepared composites based on UV curing method show appropriate electrical and mechanical properties to be used on sensor applications.

2.3.5. Electromechanical properties

Taking into consideration that composites around electrical percolation threshold show the largest piezoresistive response [58,59], the electro-mechanical response of the MWCNT/PUA composites was evaluated around and above the percolation threshold (**Figure 2.8**) for deformations up to 5%. It is to notice that larger deformations show strong non-linear effects due to the strong decrease in the local concentration of the fillers, which destroys the conductive network [60,61].

a)

b)

c)

d)
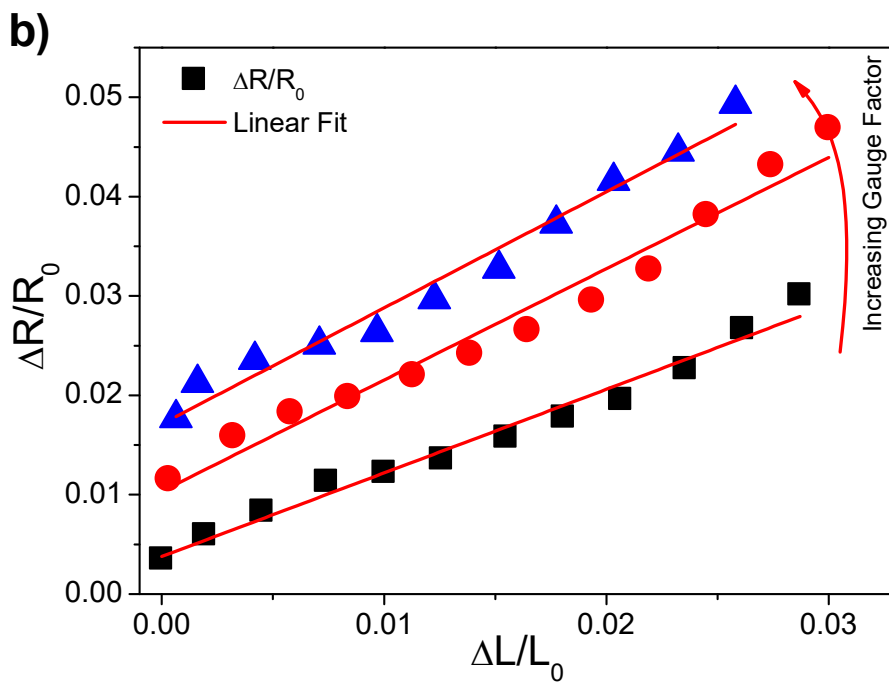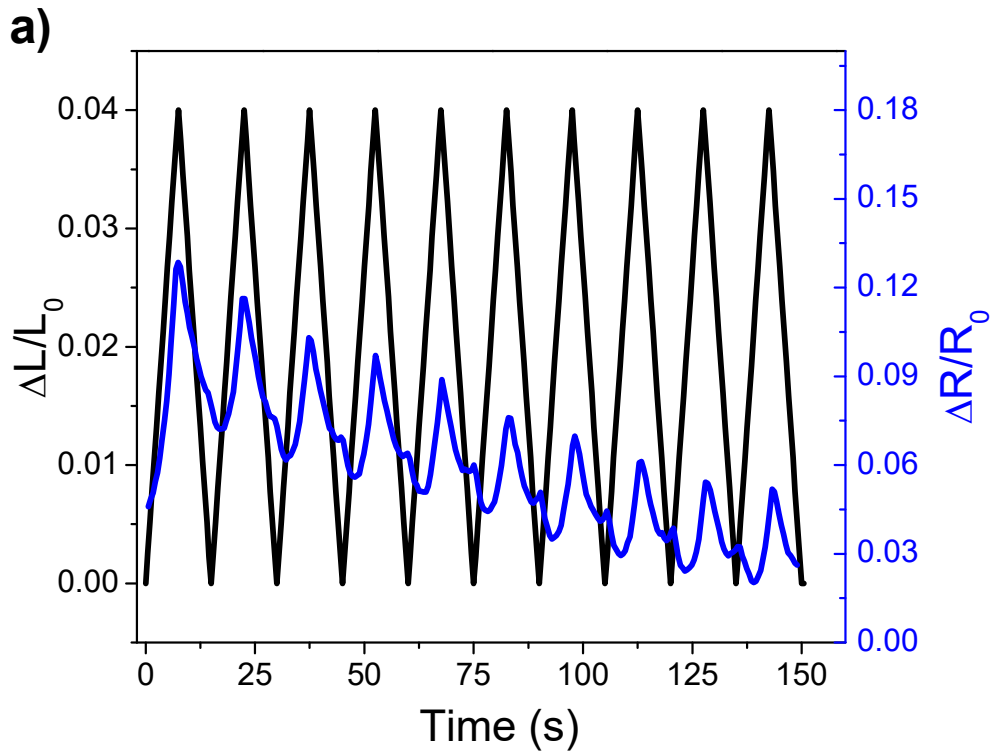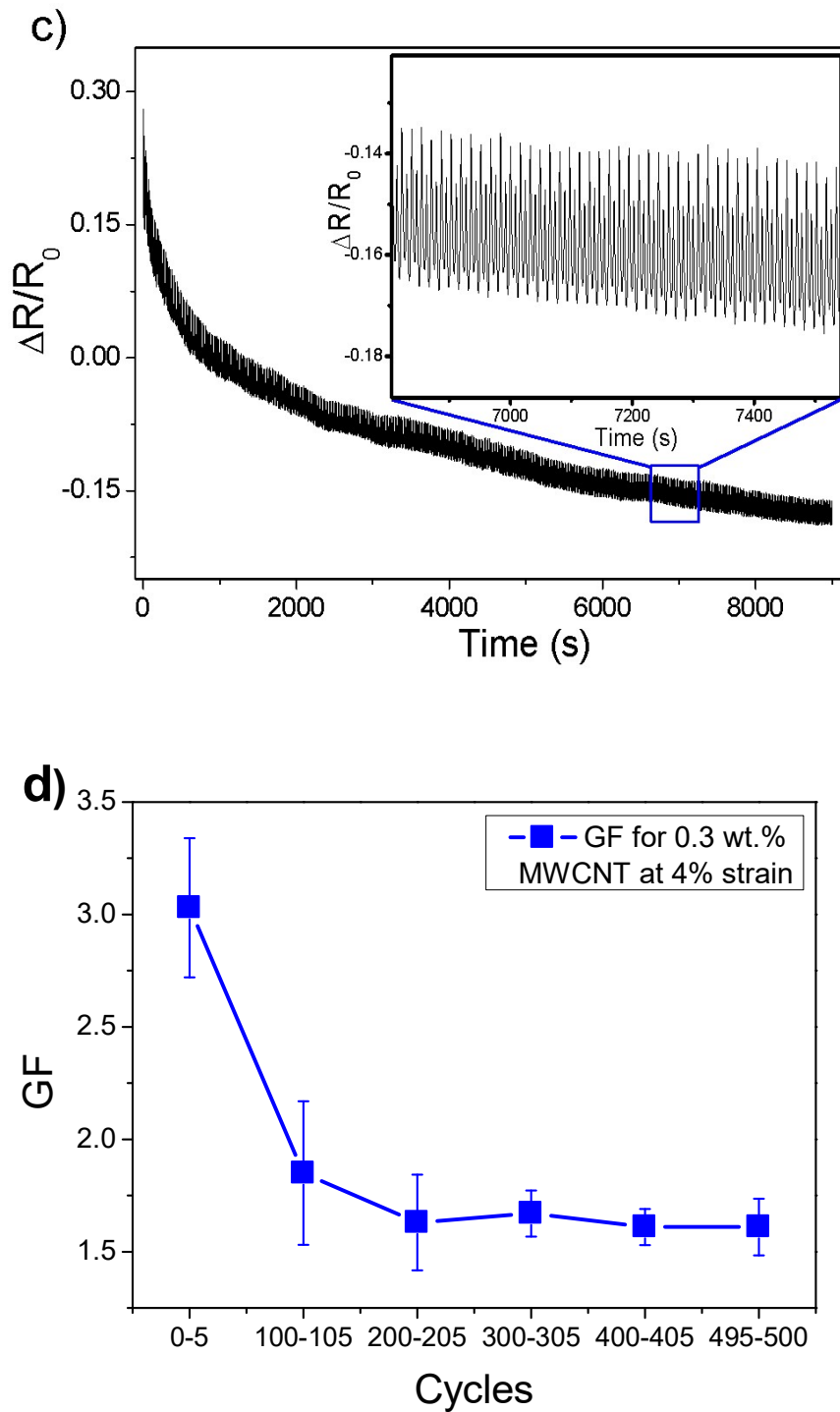
Figure 2.8 – Electro-mechanical properties of the MWCNT/PUA composites with 0.3 and 0.5 wt.% MWCNT content. A) Piezoresistive behavior of the 0.3 wt.% MWCNT/PUA composite at 4% strain, and B) exemplification of the GF calculation. C) Electromechanical test for 500 cycles for composite with 0.3 wt.% MWCNT in cycles of 4% deformation, and D) piezoresistive sensibility as a function of the number of cycles for 0.3 wt.% MWCNT sample at 0.4% of strain.

The electro-mechanical response under loading-unloading cycles (**Figure 2.2**) for composites with 0.3 and 0.5 wt.% MWCNT content are shown in **Figure 2.8**., showing that

the electrical resistance variation follows the mechanical strain applied to the composites and that increasing mechanical deformation leads to an increase of the electrical resistance of the samples. Similarly, a decrease of the strain leads to a decrease of the electrical resistance (see **Figure 2.8a** for 4% of deformation). A linear relationship between the electrical resistance and the mechanical deformation is observed for deformations up to 5%, which allows the calculation of the GF, as presented in **Figure 2.8b** [52–54].

The obtained GF are in the range between 0.8 and 2.6 for the composites with different MWCNT content and different applied strains, the composite with 0.5 wt.% MWCNT content showing a slightly higher piezoresistive response than the composite around percolation threshold. This behaviour has been found in more evident way in elastomeric matrices and has been also reported in related polyurethane matrices [52–54]. Further, the GF increases with increasing strain for the composites. As the Poisson coefficient is around 0.5 [62] for PUA and the geometric factor $(1 + 2\nu)$ is $GF_{geometric} \approx 2$ for both composites, the piezoresistive behaviour is mostly attributed to the geometric factor, and thus, sensibility is not larger for composites near percolation threshold.

Under repeated cycling (**Figure 2.8c**) it is observed that the minimum and maximum resistance decrease and tend to become constant after several stress-strain cycles. Thus, MWCNT/PUA composites need aging to stabilize their electro-mechanical response to be applied as quantitative force and/or deformation sensors. This behaviour is typical for polymer based piezoresistive composites, including polyurethane-based ones [53,54] and is related to irreversible reconfigurations of the conductive network (stress relaxation) that stabilizes after a given number of cycles.

Figure 2.8d shows the piezoresistive sensibility as a function of the number of cycles and it is observed that is larger for the first cycles (GF ≈ 3), decreasing and stabilizing is GF ≈ 1.7 for the remaining cycles, once the MWCNT irreversible reconfigurations are stabilized.

Thus, UV curable piezoresistive materials show suitable piezoresistive properties up to 5% deformation for applications in force and deformation sensing.

2.4. Conclusions

Stimuli responsive UV curable MWCNT/polyurethane acrylate resin (MWCNT/PUA) composites have been developed with appropriate electro-mechanical properties for sensor applications.

The MWCNT content affects the UV curing process, samples with larger MWCNT content, showing lower conversion and photopolymerization rate. This is corroborated with the DSC measurements that indicate a post-curing process of the samples with high temperatures. In addition, the thermal stability and the T_g of the composites decreases with increasing MWCNT content.

The electrical percolation threshold of the MWCNT/PUA composites is between 0.1 wt.% to 0.4 wt.% MWCNT content and the mechanical properties for this samples show appropriate values of initial modulus, maximum stress and maximum strain for sensor applications.

Composites with 0.3 wt.% and 0.5 wt.% MWCNT content show piezoresistive response characterized by GF values between 0.8 and 2.6, being larger for composite with higher nanofiller content (0.5 wt.%) than for composites around percolation threshold (0.3 wt.%). In addition, it is observed that the GF stabilizies after around 100 stress-strains cycles.

Overall, this work demonstrates the suitability of these materials for the development of piezoresistive sensors.

2.5. References

[1]   E.B. Murphy, F. Wudl, The world of smart healable materials, Prog. Polym. Sci. 35 (2010) 223–251. doi:10.1016/j.progpolymsci.2009.10.006.

[2]   N. Bari, G. Mani, S. Berkovich, Internet of things as a methodological concept, Proc. - 2013 4th Int. Conf. Comput. Geospatial Res. Appl. COM.Geo 2013. (2013) 48–55. doi:10.1109/COMGEO.2013.8.

[3]   J. Oliveira, V. Correia, H. Castro, P. Martins, S. Lanceros-Mendez, Polymer-based smart materials by printing technologies: Improving application and integration, Addit. Manuf. 21 (2018) 269–283. doi:10.1016/j.addma.2018.03.012.

[4]   B.F. Gonçalves, J. Oliveira, P. Costa, V. Correia, P. Martins, G. Botelho, S. Lanceros-Mendez, Development of water-based printable piezoresistive sensors for large strain applications, Compos. Part B Eng. 112 (2017) 344–352. doi:10.1016/j.compositesb.2016.12.047.

[5]   A.S. Zuruzi, T.M. Haffiz, D. Affidah, A. Amirul, A. Norfatriah, M.H. Nurmawati, Towards wearable pressure sensors using multiwall carbon nanotube/polydimethylsiloxane nanocomposite foams, Mater. Des. 132 (2017) 449–458. doi:10.1016/j.matdes.2017.06.059.

[6]   T. Yang, D. Xie, Z. Li, H. Zhu, Recent advances in wearable tactile sensors: Materials, sensing mechanisms, and device performance, Mater. Sci. Eng. R Reports. 115 (2017) 1–37. doi:10.1016/j.mser.2017.02.001.

[7]   A.S. Fiorillo, C.D. Critello, A.S. Pullano, Theory, Technology and Applications of Piezoresistive Sensors: a Review, Sensors Actuators A Phys. 281 (2018) 156–175. doi:10.1016/j.sna.2018.07.006.

[8]   J. Teixeira, L. Horta-Romarís, M.J. Abad, P. Costa, S. Lanceros-Méndez, Piezoresistive response of extruded polyaniline/(styrene-butadiene-styrene) polymer blends for force and deformation sensors, Mater. Des. 141 (2018) 1–8. doi:10.1016/j.matdes.2017.12.011.

[9]   D. Lee, H.P. Hong, M.J. Lee, C.W. Park, N.K. Min, A prototype high sensitivity load cell using single walled carbon nanotube strain gauges, Sensors Actuators, A Phys.

180 (2012) 120–126. doi:10.1016/j.sna.2012.04.015.

[10]   O. Kanoun, C. Müller, A. Benchirouf, A. Sanli, T. Dinh, A. Al-Hamry, L. Bu, C. Gerlach, A. Bouhamed, Flexible Carbon Nanotube Films for High Performance Strain Sensors, Sensors. 14 (2014) 10042–10071. doi:10.3390/s140610042.

[11]   P. Costa, S. Ribeiro, S. Lanceros-Mendez, Mechanical vs. electrical hysteresis of carbon nanotube/styrene-butadiene-styrene composites and their influence in the electromechanical response, Compos. Sci. Technol. 109 (2015) 1–5. doi:10.1016/j.compscitech.2015.01.006.

[12]   B.F. Gonçalves, P. Costa, J. Oliveira, S. Ribeiro, V. Correia, G. Botelho, S. Lanceros-Mendez, Green solvent approach for printable large deformation thermoplastic elastomer based piezoresistive sensors and their suitability for biomedical applications, J. Polym. Sci. Part B Polym. Phys. 54 (2016) 2092–2103. doi:10.1002/polb.24118.

[13]   W. Obitayo, T. Liu, A review: Carbon nanotube-based piezoresistive strain sensors, J. Sensors. 2012 (2012). doi:10.1155/2012/652438.

[14]   G. Harsányi, Polymer films in sensor applications : a review of present uses and future possibilities, Emerald Insight. 20 (2006) 98–105.

[15]   N. Roy, R. Sengupta, A.K. Bhowmick, Modifications of carbon for polymer composites and nanocomposites, Prog. Polym. Sci. 37 (2012) 781–819. doi:10.1016/j.progpolymsci.2012.02.002.

[16]   P. Costa, A. Ferreira, V. Sencadas, J.C. Viana, S. Lanceros-Méndez, Electro-mechanical properties of triblock copolymer styrene-butadiene- styrene/carbon nanotube composites for large deformation sensor applications, Sensors Actuators, A Phys. 201 (2013) 458–467. doi:10.1016/j.sna.2013.08.007.

[17]   W. Yi, Y. Wang, G. Wang, X. Tao, Investigation of carbon black/silicone elastomer/dimethylsilicone oil composites for flexible strain sensors, Polym. Test. 31 (2012) 677–684. doi:10.1016/j.polymertesting.2012.03.006.

[18]   G. Mittal, V. Dhand, K.Y. Rhee, S.J. Park, W.R. Lee, A review on carbon nanotubes and graphene as fillers in reinforced polymer nanocomposites, J. Ind. Eng. Chem. 21

(2015) 11–25. doi:10.1016/j.jiec.2014.03.022.

[19] A. Ferrreira, J.G. Rocha, A. Ansón-Casaos, M.T. Martínez, F. Vaz, S. Lanceros-Mendez, Electromechanical performance of poly(vinylidene fluoride)/carbon nanotube composites for strain sensor applications, Sensors Actuators, A Phys. 178 (2012) 10–16. doi:10.1016/j.sna.2012.01.041.

[20] G.T. Pham, Y. Bin Park, Z. Liang, C. Zhang, B. Wang, Processing and modeling of conductive thermoplastic/carbon nanotube films for strain sensing, Compos. Part B Eng. 39 (2008) 209–216. doi:10.1016/j.compositesb.2007.02.024.

[21] I. Kang, M.J. Schulz, J.H. Kim, V. Shanov, D. Shi, A carbon nanotube strain sensor for structural health monitoring, Smart Mater. Struct. 15 (2006) 737–748. doi:10.1088/0964-1726/15/3/009.

[22] A. Endruweit, M.S. Johnson, A.C. Long, Curing of Composite Components by Ultraviolet Radiation: A Review, Polym. Compos. 27 (2006) 119–128. doi:10.1002/pc.20166.

[23] D. Thuau, C. Ayela, P. Poulin, I. Dufour, Highly piezoresistive hybrid MEMS sensors, Sensors Actuators, A Phys. 209 (2014) 161–168. doi:10.1016/j.sna.2014.01.037.

[24] E.C. Sengezer, G.D. Seidel, R.J. Bodnar, Anisotropic piezoresistivity characteristics of aligned carbon nanotube-polymer nanocomposites, Smart Mater. Struct. 26 (2017). doi:10.1088/1361-665X/aa78c3.

[25] J. Lee, M.O. Faruk Emon, M. Vatani, J.W. Choi, Effect of degree of crosslinking and polymerization of 3D printable polymer/ionic liquid composites on performance of stretchable piezoresistive sensors, Smart Mater. Struct. 26 (2017). doi:10.1088/1361-665X/aa5c70.

[26] M. Liu, Y. Zhao, Y. Shao, Q. Zhang, C. Liu, 3D Printed Force Sensor with Inkjet Printed Piezoresistive Based Strain Gauge, Proc. IEEE Sensors. 2018-Octob (2018) 2018–2021. doi:10.1109/ICSENS.2018.8589771.

[27] O.F. Emon, J. Choi, A preliminary study on 3D printed smart insoles with stretchable piezoresistive sensors for plantar pressure monitoring, in: Proc. ASME 2017 Int.

Mech. Eng. Congr. Expo. IMECE2017, ASME Digital Collection, Tampa, Florida, USA, 2017: pp. 1–6. doi:10.1115/IMECE2017-71817.

[28] M.O.F. Emon, J.W. Choi, Flexible piezoresistive sensors embedded in 3D printed tires, Sensors (Switzerland). 17 (2017). doi:10.3390/s17030656.

[29] E. Davoodi, H. Fayazfar, F. Liravi, E. Jabari, E. Toyserkani, Drop-on-demand high-speed 3D printing of flexible milled carbon fiber/silicone composite sensors for wearable biomonitoring devices, Addit. Manuf. 32 (2020) 101016. doi:10.1016/j.addma.2019.101016.

[30] O. Llorente, M.J. Fernández-Berridi, A. González, L. Irusta, Study of the crosslinking process of waterborne UV curable polyurethane acrylates, Prog. Org. Coatings. 99 (2016) 437–442. doi:10.1016/j.porgcoat.2016.06.020.

[31] P. Costa, J. Silva, A. Ansón-Casaos, M.T. Martinez, M.J. Abad, J. Viana, S. Lanceros-Mendez, Effect of carbon nanotube type and functionalization on the electrical, thermal, mechanical and electromechanical properties of carbon nanotube/styrene-butadiene-styrene composites for large strain sensor applications, Compos. Part B Eng. 61 (2014) 136–146. doi:10.1016/j.compositesb.2014.01.048.

[32] C.L. Cao, C.G. Hu, Y.F. Xiong, X.Y. Han, Y. Xi, J. Miao, Temperature dependent piezoresistive effect of multi-walled carbon nanotube films, Diam. Relat. Mater. 16 (2007) 388–392. doi:10.1016/j.diamond.2006.07.008.

[33] M.H.G. Wichmann, S.T. Buschhorn, J. Gehrmann, K. Schulte, Piezoresistive response of epoxy composites with carbon nanoparticles under tensile load, Phys. Rev. B - Condens. Matter Mater. Phys. 80 (2009) 1–8. doi:10.1103/PhysRevB.80.245437.

[34] J.H. Sandoval, R.B. Wicker, Functionalizing stereolithography resins: Effects of dispersed multi-walled carbon nanotubes on physical properties, Rapid Prototyp. J. 12 (2006) 292–303. doi:10.1108/13552540610707059.

[35] Y. Xu, H. Xu, L. Wang, J. Yan, H. Li, Y. Song, L. Huang, G. Cai, The CNT modified white C3/N4 composite photocatalyst with enhanced visible-light response photoactivity, Dalt. Trans. 42 (2013) 7604–7613. doi:10.1039/c3dt32871f.

[36] H.A. Zeinabad, A. Zarrabian, A.A. Saboury, A.M.O. Alizadeh, M. Falahati, Interaction of single and multi wall carbon nanotubes with the biological systems: Tau protein and PC12 cells as targets, Sci. Rep. 6 (2016). doi:10.1038/srep26508.

[37] Z. Doğruyol, G. Temel, S.K. Doğruyol, Ö. Pekcan, N. Arsu, Investigation of PSt-MWCNT concentration on epoxyacrylate photopolymerization and conductivity of polymer films, Prog. Org. Coatings. 76 (2013) 944–949. doi:10.1016/j.porgcoat.2012.10.013.

[38] M. Alishiri, A. Shojaei, *In situ* preparation and characterization of biocompatible acrylate-terminated polyurethane containing chemically modified multiwalled carbon nanotube, Polym. Compos. 39 (2018) E297–E307. doi:10.1002/pc.24423.

[39] H. Lorenz, J. Fritzsche, A. Das, K.W. Stöckelhuber, R. Jurk, G. Heinrich, M. Klüppel, Advanced elastomer nano-composites based on CNT-hybrid filler systems, Compos. Sci. Technol. 69 (2009) 2135–2143. doi:10.1016/j.compscitech.2009.05.014.

[40] P. Cardoso, J. Silva, D. Klosterman, J.A. Covas, F.W.J. van Hattum, R. Simoes, S. Lanceros-Mendez, The role of disorder on the AC and DC electrical conductivity of vapour grown carbon nanofibre/epoxy composites, Compos. Sci. Technol. 72 (2012) 243–247. doi:10.1016/j.compscitech.2011.11.008.

[41] K. Tsuchiya, A. Sakai, T. Nagaoka, K. Uchida, T. Furukawa, H. Yajima, High electrical performance of carbon nanotubes/rubber composites with low percolation threshold prepared with a rotation-revolution mixing technique, Compos. Sci. Technol. 71 (2011) 1098–1104. doi:10.1016/j.compscitech.2011.03.015.

[42] SPOT-A Materials, Material Safety Data Sheet for SPOT-E, (2012). https://spotamaterials.com/wp/wp-content/uploads/2015/07/Spot-E_MSDS_tmp.pdf (accessed August 27, 2020).

[43] E. Pretsch, P. Bühlmann, C. Affolter, Structure Determination of Organic Compounds Tables of Spectral Data, Third Edit, Springer, Germany, 2000.

[44] T. Nardi, M. Sangermano, Y. Leterrier, P. Allia, P. Tiberto, J.A.E. Månson, UV-cured transparent magnetic polymer nanocomposites, Polymer (Guildf). 54 (2013) 4472–4479. doi:10.1016/j.polymer.2013.06.052.

[45] D. Kunwong, N. Sumanochitraporn, S. Kaewpirom, Curing behavior of a UV-curable coating based on urethane acrylate oligomer: The influence of reactive monomers, Songklanakarin J. Sci. Technol. 33 (2011) 201–207.

[46] Y. Jiang, S.Y. Zhang, X.L. Zhang, T. Zhang, Improving the performance of UV-curable coatings with carbon nanomaterials, Express Polym. Lett. 12 (2018) 628–639. doi:10.3144/expresspolymlett.2018.53.

[47] G. Trovati, E.A. Sanches, S.C. Neto, Y.P. Mascarenhas, G.O. Chierice, Characterization of Polyurethane Resins by FTIR, TGA, and XRD, J. Appl. Polym. Sci. 115 (2010) 263–268. doi:10.1002/app.31096.

[48] C. Mendes-Felipe, D. Patrocinio, J.M. Laza, L. Ruiz-Rubio, J.L. Vilas-Vilela, Evaluation of postcuring process on the thermal and mechanical properties of the Clear02™ resin used in stereolithography, Polym. Test. 72 (2018) 115–121. doi:10.1016/j.polymertesting.2018.10.018.

[49] M. Reda Berber, I. Hazzaa Hafez, Carbon Nanotubes. Current Progress of their Polymer Composites, First Edit, ExLi4EvA, 2016.

[50] B. Fernández-D'Arlas, A. Eceiza, Functionalization of multiwalled carbon nanotubes with urethane segments and their interaction with solvents and a polyurethane elastomer, J. Nanoparticle Res. 16 (2014) 1–10. doi:10.1007/s11051-013-2166-4.

[51] J. Xu, X. Cai, F. Shen, Preparation and property of UV-curable polyurethane acrylate film filled with cationic surfactant treated graphene, Appl. Surf. Sci. 379 (2016) 433–439. doi:10.1016/j.apsusc.2016.04.104.

[52] J.R. Dios, C. Garcia-Astrain, S. Gonçalves, P. Costa, S. Lanceros-Méndez, Piezoresistive performance of polymer-based materials as a function of the matrix and nanofiller content to walking detection application, Compos. Sci. Technol. 181 (2019) 107678. doi:10.1016/j.compscitech.2019.107678.

[53] K. Ke, V. Solouki Bonab, D. Yuan, I. Manas-Zloczower, Piezoresistive thermoplastic polyurethane nanocomposites with carbon nanostructures, Carbon N. Y. 139 (2018) 52–58. doi:10.1016/j.carbon.2018.06.037.

[54] Y. Zheng, Y. Li, K. Dai, M. Liu, K. Zhou, G. Zheng, C. Liu, C. Shen, Conductive

thermoplastic polyurethane composites with tunable piezoresistivity by modulating the filler dimensionality for flexible strain sensors, Compos. Part A Appl. Sci. Manuf. 101 (2017) 41–49. doi:10.1016/j.compositesa.2017.06.003.

[55]   A.M.F. Lima, V.G. de Castro, R.S. Borges, G.G. Silva, Electrical conductivity and thermal properties of functionalized carbon nanotubes/polyurethane composites, Polímeros. 22 (2012) 117–124. doi:10.1590/S0104-14282012005000017.

[56]   P. Costa, J. Silva, V. Sencadas, R. Simoes, J.C. Viana, S. Lanceros-Méndez, Mechanical, electrical and electro-mechanical properties of thermoplastic elastomer styrene-butadiene-styrene/multiwall carbon nanotubes composites, J. Mater. Sci. 48 (2013) 1172–1179. doi:10.1007/s10853-012-6855-7.

[57]   J.F. Gao, Z.M. Li, Q. jie Meng, Q. Yang, CNTs/ UHMWPE composites with a two-dimensional conductive network, Mater. Lett. 62 (2008) 3530–3532. doi:10.1016/j.matlet.2008.03.053.

[58]   J.C. Dawson, C.J. Adkins, Conduction mechanisms in carbon-loaded composites, J. Phys. Condens. Matter. 8 (1996) 8321–8338. doi:10.1088/0953-8984/8/43/024.

[59]   A. Ferreira, P. Cardoso, D. Klosterman, J.A. Covas, F.W.J. Van Hattum, F. Vaz, S. Lanceros-Mendez, Effect of filler dispersion on the electromechanical response of epoxy/vapor-grown carbon nanofiber composites, Smart Mater. Struct. 21 (2012). doi:10.1088/0964-1726/21/7/075008.

[60]   T.C. Theodosiou, D.A. Saravanos, Numerical investigation of mechanisms affecting the piezoresistive properties of CNT-doped polymers using multi-scale models, Compos. Sci. Technol. 70 (2010) 1312–1320. doi:10.1016/j.compscitech.2010.04.003.

[61]   J. Silva, S. Ribeiro, S. Lanceros-Mendez, R. Simões, The influence of matrix mediated hopping conductivity, filler concentration, aspect ratio and orientation on the electrical response of carbon nanotube/polymer nanocomposites, Compos. Sci. Technol. 71 (2011) 643–646. doi:10.1016/j.compscitech.2011.01.005.

[62]   K.H. Liao, Y. Qian, C.W. MacOsko, Ultralow percolation graphene/polyurethane acrylate nanocomposites, Polymer (Guildf). 53 (2012) 3756–3761. doi:10.1016/j.polymer.2012.06.020.

Chapter 3

Photocurable dielectric materials

The development of UV curable barium titanate/polyurethane acrylate (BaTiO$_3$/PUA) composites with varying ceramic sizes and contents is addressed in order to tailor the dielectric response of the material. Filler size and content effects on morphological, thermal, mechanical and electrical properties has been evaluated. High dielectric UV curable composites are obtained suitable for microelectronics applications.

3.1. Introduction

Technology is nowadays increasingly driven by the Industry 4.0 concept that includes and takes advantages of the Internet of things (IoT), cyber-physical systems and the Internet of services (IoS) [1,2]. As it is described in chapter 1 of this thesis, IoT represents the network that allows a dynamic connection between different everyday objects [3,4], this system allowing digitalization and computerization of daily tasks and, therefore, energy saving, increased security and improved quality of life, among others [5]. Further, in order to achieve full development and improved performance, IoT and Industry 4.0 still need the development of advanced –smart and multifunctional– materials and production methods [6–8].

In this context, flexible electronics composed by organic and inorganic nano-structured materials show the necessary requirements for IoT applications: mechanically flexible devices, possibility to be implemented in large areas, conformable in different sizes and shapes, low cost and flexible fabrication methods and lower environmental impact [9,10]. Thus, a large variety of materials have been investigated as appropriate materials for IoT related devices, including thermoelectric materials [11], wearable antennas for autonomous communication and sensing [12], or piezoelectric, magnetostrictive, and magnetoelectric materials for sensing and energy harvesting applications [7,8,13–15].

Directly related with the production of flexible electronics, printing techniques emerge as suitable approach as they allow the additive manufacturing deposition on large areas in rigid as well as flexible or irregular surfaces of (multi)functional materials [8,16]. In particular, among the different printing techniques, non-contact methods such as inkjet printing, laser-induced forward transfer or aerosol-jet printing can transfer inks to substrates without damage or contamination risks [17]. Therefore, they enable material deposition on irregular surfaces and are attractive for the production of printed electronics [18–20].

Printed electronics has been traditionally focusing on conductive materials [21–24]. Nevertheless, passive electronic components are essential for the fabrication of sensing and/or wireless systems and devices. In fact, the printing of those passive components will improve device integration, as passive electronic components, including capacitors or coils, are still the most voluminous parts of the current printed electronic circuits [25].

Electronic circuits require very specific functional characteristics, and this continues to be a challenge for printing techniques. In order to overcome this challenge, two different approaches can be distinguishing: process engineering where the currently existing materials are tailored in terms of shape, geometry and interconnectivity [25], or material engineering where new materials with tailored functional characteristic for each application (such as electrical conductivity or dielectric constant) are developed.

In particular, for dielectric materials, the main approach for tailoring dielectric constant is to include large dielectric constant ceramic particles into polymeric matrix [26]. Polymers offer advantages such as easy processability or good mechanical properties, while ceramic particles provide high dielectric features [27]. Further, composite with related properties such as piezoelectric, pyroelectric or ferroelectric properties can be also processed [8]. The most used ferroelectric ceramic for this purpose is barium titanate, $BaTiO_3$, crystallizing in perovskite structure, as it is a lead free ceramic with high dielectric constant (ε), depending on its purity, grain size, temperature or preparation method [28,29]. In the case of polymers, polymethylmethacrylate [30], polyetheretherketone (PEEK) [31], polystyrene [32], or polyvinylidene fluoride (PVDF) [33,34] have been used for the developing of those composites.

In the context of materials for printed electronics, photopolymerizable or UV curable polymers emerge as a good alternative to solvent or melting processing due to the advantages of photopolymerization process mentioned in chapter 1. Up to now, just a few studies on UV curable dielectric materials have been reported. Among them, polyethylene glycol diacrylate composites with $BaTiO_3$ particles with two different sizes and filler concentrations up to 50 wt.% has been developed [27], as well as composites based on UV-curable resin Loctite® with Ag and $BaTiO_3$ nanoparticle content up to 56.2 vol.% [35], leading to films with dielectric constants between 25 and 300, depending on the filler size and concentration. Also, low dielectric loss and high breakdown strength photocured high-κ composites containing perfluoroalkylsilane treated $BaTiO_3$ nanoparticles have been synthetized using commercial acrylic resin as polymer matrix [36].

Some of those UV curable dielectric materials were used in printed electronics to obtain completely functional transistors. Castro *et al.* [37] prepared all-inkjet-printed bottom-gate thin film transistors using a UV curable dielectric ink that actuates as insulating material for the gate dielectric. Prepared transistors show a stable channel length of about 10 μm, an

electron mobility of 0.012 cm^2 V^{-1} s^{-1} and an on/off ratio of 10^3. Another study was carried out by Kwon *et al.* [38] by not only printing functional transistors but also synthetizing a series of UV curable materials applicable for gate dielectric on organic field-effect transistors (OFETs). A facile, fluorinated, UV-assisted cross-linker series using a fluorophenyl azide (FPA), which reacts with the C−H groups of a conventional polymer was reported. The effect of the cross-linked structure, the patternability and the dielectric properties of the resulted films were investigated for low/high κ amorphous/crystalline gate dielectric materials. After the OFETs preparation using the obtained UV cured materials, their leakage current density (J), hysteresis, and charge trap density were evaluated.

Recently, UV curable dielectric materials are employed in the area of 3D printed dielectric elastomer actuators (DEA) [39]. 3D DEA devices are composed by an electrode of conductive elastomer ink, based on carbon black particles and poly(ethylene glycol ethylene sulfide) (PEG-PES) polymer, encapsulated in a self-healing dielectric matrix of a plasticized UV cured polyurethane acrylate. Obtained DEAs printed using direct ink writing (DIW) exhibit breakdown fields of 25 V μm^{-1} and actuation strains of up to 9%. 3D dielectric structures were also prepared by stereolithography (SLA) [40]. McGhee *et al.* have studied both the effect of the curing time on the microwave electromagnetic properties of the photoinitiated resin and in the fabrication of artificial dielectric isotropic and anisotropic lattice structures. Due to the high resolution of the SLA process, low permittivity high resolution lattices can be manufactured, allowing for varying permittivity between 1.23 and 2.80 through the control of the density of the structure.

It is to notice that, despite the interesting investigations carried out related to dielectric materials, relevant parameters such as mechanical ones or in depth theoretical modelling/interpretation of the observed behaviours have not been reported for these or related systems. In this work, UV curable BaTiO$_3$ based nanocomposites with tailored dielectric response have been developed. The influence of the barium titanate content and size were evaluated in terms of morphological, thermal, mechanical and dielectric properties of the composites. Further, the effect of the inclusion of the filler in the curing process of the polymer has been assessed as well as a theoretical evaluation providing insights on the relevant interactions determining the experimental dielectric results.
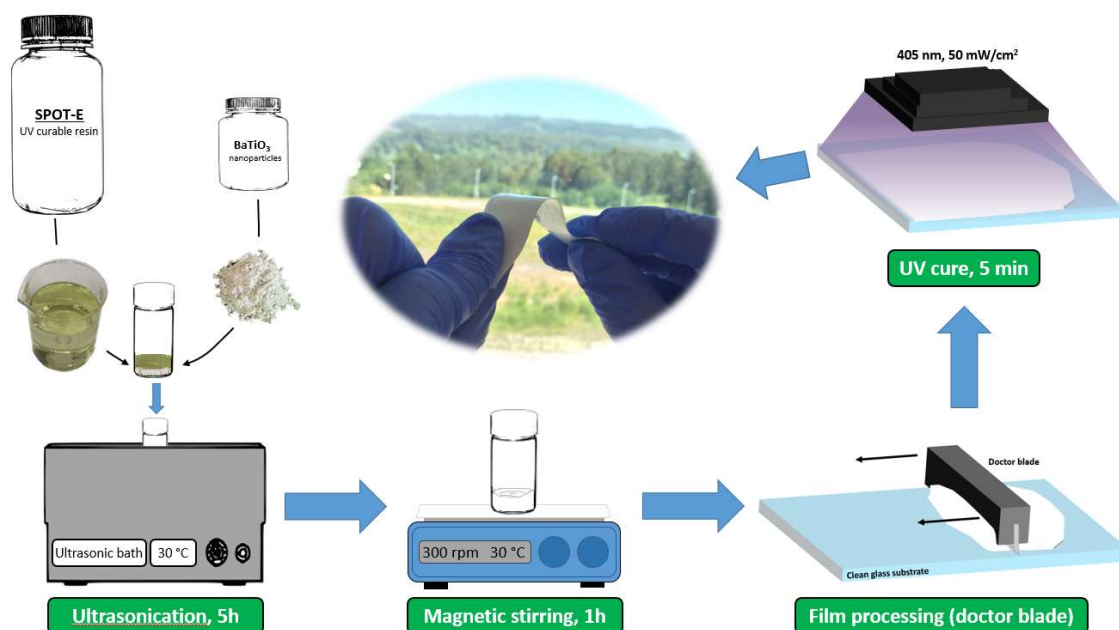
3.2. Experimental

3.2.1. Materials

Polyurethane acrylate (PUA) photoresin SPOT-E^{TM} (SPOT-A Materials®) was selected as the UV curable polymer matrix. Barium titanate (BaTiO$_3$) nanopowder, with three different grain sizes (50-70 nm, 100 nm and 200 nm), was used as filler for the preparation of the composite films. All powders showed a purity of 99.9% and a density of 5.85 g/cm^3, were provided by SkySpring Nanomaterials, Inc. 2-Propanol (99.9%, Octopus® fluids) was used as sample cleaner. All composites samples were processed using the BaTiO$_3$ and the photoresin as received.

3.2.2. Samples preparation

The samples were prepared mixing different amounts of the barium titanate particles of 100 nm size with the corresponding volume of the polyurethane acrylate (PUA) resin to obtain 0, 20, 40, 60, 65 wt.% BaTiO$_3$ content samples. Samples with 40 wt.% content and barium titanate powders of 50-70 nm and 200 nm sizes have been also prepared. To promote a good dispersion of the barium titanate particles, the samples were placed in an ultrasound bath (ATU® ATM series Model ATM3L) during 5 h at a temperature of 30ºC. Then, samples were magnetically stirred at room temperature for 1h. After a complete dispersion was obtained, flexible films were prepared using doctor blade technique on a clean glass substrate. The samples were cured at room temperature for 5 minutes with a UV-LEDs lamp (405 nm wavelength, 50 mW/cm^2 of irradiance). **Figure 3.1** shows the schematic process of the PUA and BaTiO$_3$/PUA composites preparation. Highly flexible composite films with a thickness around 250 μm were obtained, determined by a coater measurement gauge Fisher DualScope MPOR. Samples were stored at room temperature in the absence of illumination for further studies. The prepared samples are summarized in **Table 3.1**.

Table 3.1 – Nomenclature and composition of the prepared samples.

Sample	PUA resin (wt.%)	50-70nm BaTiO$_3$ (wt.%)	100nm BaTiO$_3$ (wt.%)	200nm BaTiO$_3$ (wt.%)
PUA0	100	-	-	-
PUA20_100	80	-	20	-
PUA40_50	60	40	-	-
PUA40_100	60	-	40	-
PUA40_200	60	-	-	40
PUA60_100	40	-	60	-
PUA65_100	35	-	65	-

Figure 3.1 – Schematic representation of the preparation procedure of neat PUA and the corresponding BaTiO$_3$/PUA composites films.

3.2.3. Sample characterization

The evaluation of the photopolymerization reaction was carried out by Fourier transform infrared spectroscopy (FTIR) in a Thermo Nicolet Nexus 670 at the same time as the sample was illuminated with a UV laser at 405 nm. To perform the measurements, one drop of the different samples was deposited onto a KBr pellet and the absorbance spectrum as a function of time (one spectra per second, between 0 and 20 minutes) was collected in the spectral range from 4000 to 400 cm^{-1} with a spectral resolution of 4 cm^{-1}. The photopolymerization

reaction was evaluated by monitoring the decrease in the absorbance of the double bond group centred at 1635 cm^{-1}. The conversion degree (α) of these double bonds was calculated considering the absorbance at 1635 cm^{-1} normalized with the carbonyl peak centred at 1730 cm^{-1}, according to equation **¡Error! No se encuentra el origen de la referencia.** [41]:

$$\alpha = \frac{(A_{C=C}/A_{C=O})_{t_0} - (A_{C=C}/A_{C=O})_t}{(A_{C=C}/A_{C=O})_{t_0}} \qquad (3.1)$$

where A represents the absorbance of the different functional groups (C=C or C=O) at initial time (t_0) or at different times of reaction (t).

The dispersion of the barium titanate fillers within the polymer matrix was evaluated by Scanning Electron Microscopy (SEM). The images on the cross-section of the cold fractured samples were obtained in a Hitachi S-4800 scanning electron microscope at accelerating voltage of 10 kV with magnifications of 400× and 5000×. Fourier transform infrared spectroscopy in the total attenuated reflection mode (FTIR-ATR) was also used to study the possible interactions between the polymer and the nanofillers. Measurements were performed with a Nexus FTIR Nicolet spectrophotometer in the spectral range of 4000 to 600 cm^{-1} with a spectral resolution of 4 cm^{-1} and 64 scans.

The thermal stability of the samples was evaluated by thermogravimetric analysis (TGA) in a Mettler Toledo TGA/SDTA851 instrument. The tests were performed from room temperature to 800 ºC, at heating rate of 10 ºC min^{-1} under nitrogen atmosphere. Two parameters were obtained from the thermograms: the degradation temperature (T_{deg}), measured as the extrapolated onset of the curve, and the temperature of maximum degradation rate (T_{max}), calculated as the first derivative peak temperature.

The effect of the inclusion of the fillers on the thermal transitions (glass transition temperature, T_g) of the polymer was evaluated by differential scanning calorimetry (DSC). Experiments were carried out using a DSC 822e from Mettler Toledo from -50 to 250 ºC at a rate of 20 ºC min^{-1} under nitrogen atmosphere in two successive scans. The glass transition temperature was calculated as the extrapolated onset of the baseline shift.

Mechanical properties were evaluated with a universal testing machine Shimadzu model AG-IS with a load cell of 1 kN. Measurements were performed at room temperature, in tensile mode, at a velocity of 3 mm min^{-1}, in samples with dimensions of 30 mm x 10 mm and an average thickness of 250 μm. The secant modulus (E) of the samples (calculated from

the slope of the linear region), the maximum stress (σ_b) and the strain at break (ε_b) were determined. The values reported represent the mean average value and the standard deviation over 5 specimens.

The dielectric properties were obtained after measuring the capacity, C, and the dielectric losses, tan δ, at room temperature. An automatic Quadtech 1929 Precision LCR meter was used in frequency scans between 100 Hz and 1 MHz at an applied voltage of 0.5 V. Measurements were performed in samples in the parallel plate condenser approximation and thus, two circular gold electrodes of 5 mm diameter were deposited onto both sides of the samples by magnetron sputtering Quorum Q150T SC502 sputter coater. The real part of the relative permittivity or dielectric constant (ε') was calculated by applying equation **¡Error! No se encuentra el origen de la referencia.** [42]:

$$\varepsilon' = \frac{C \cdot d}{\varepsilon_0 \cdot A} \qquad (3.2)$$

where C is the measured capacity, d is the thickness of the sample and A is the area of the gold deposited electrodes.

3.3. Results and discussion

3.3.1. Photopolymerization process

The photopolymerization reaction conversion (α) as a function of the exposure time for the pristine resin and the prepared samples is shown in **Figure 3.2a** (filler content dependence) and **Figure 3.2b** (filler size dependence). It is observed that increasing barium titanate content and size induce an important decrease on acrylic double bond conversion. Thus, the absorption of the UV light by the ceramic powder induces a decrease of the light absorption by the photoinitiator and consequently, a decrease on the photopolymerization and conversion rate [27,41,43].

It is important to notice that the maximum conversion is achieved in less than 1 minute for both PUA photoresin and composites, with a maximum conversion close to 100% for pristine resin and decreasing to 40% for the PUA65_100 composite, the one with the maximum $BaTiO_3$ content. This decrease of the acrylic double bond conversion [27] is related with the efficiency of the radical photoinitiator, which can be measured in terms of quantum yields of initiation and quantum yields of polymerization. The absorption of UV

light by barium titanate particles decrease the amount of light absorbed by the photoinitiator decreasing therefore the efficiency of the radical photoinitiator and, as a consequence, the obtained final conversion.
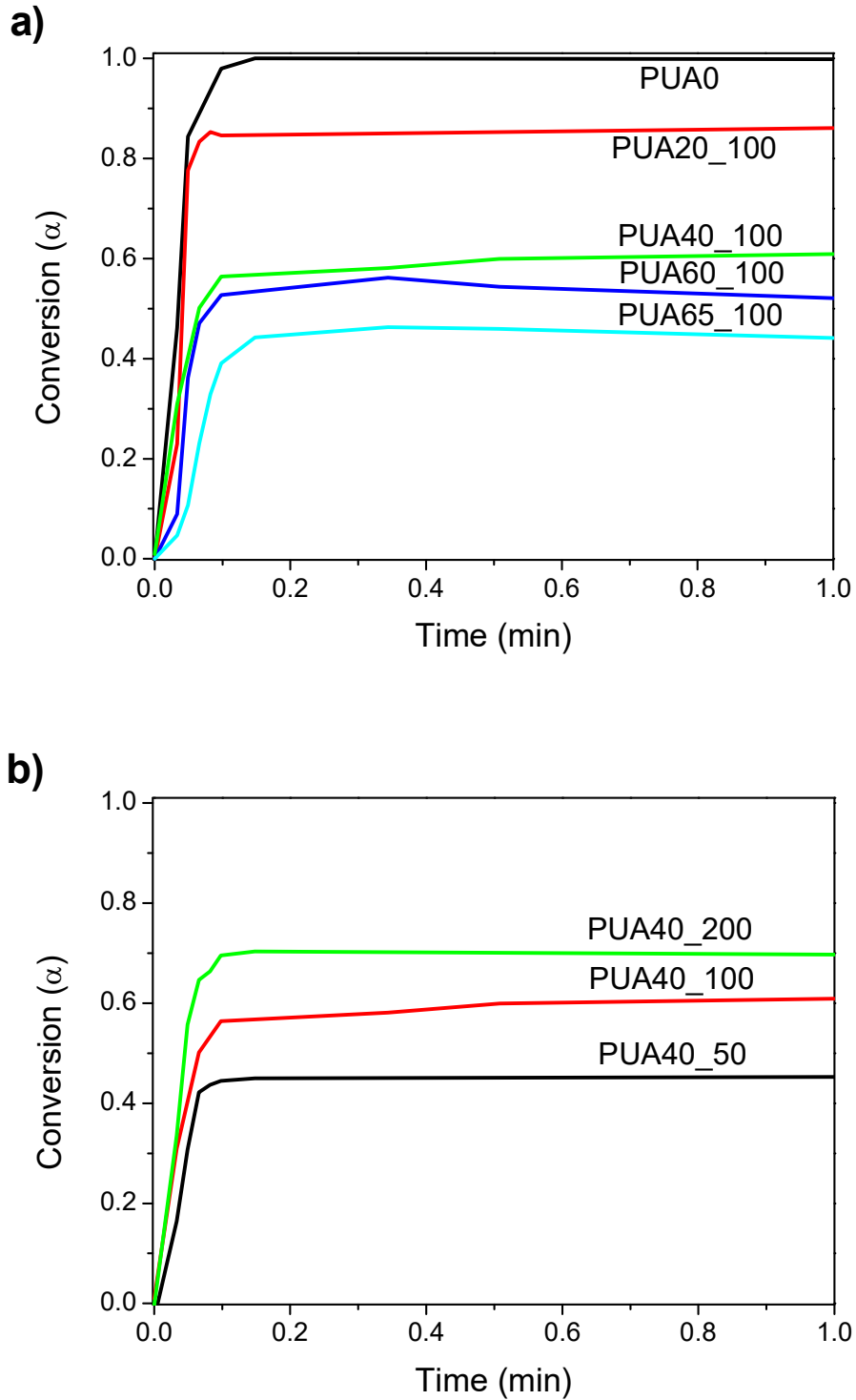
a)

b)

Figure 3.2 – Curing conversion of PUA and BaTiO$_3$/PUA composites for different nanoparticle content (a) and size (b).

3.3.2. Morphological and chemical characterization

The dispersion and distribution of the $BaTiO_3$ particles into the PUA photoresin has been studied using the SEM images of the cross-section of the samples with nanofiller contents between 0 to 65 wt.% and different filler sizes shown in **Figure 3.3**.
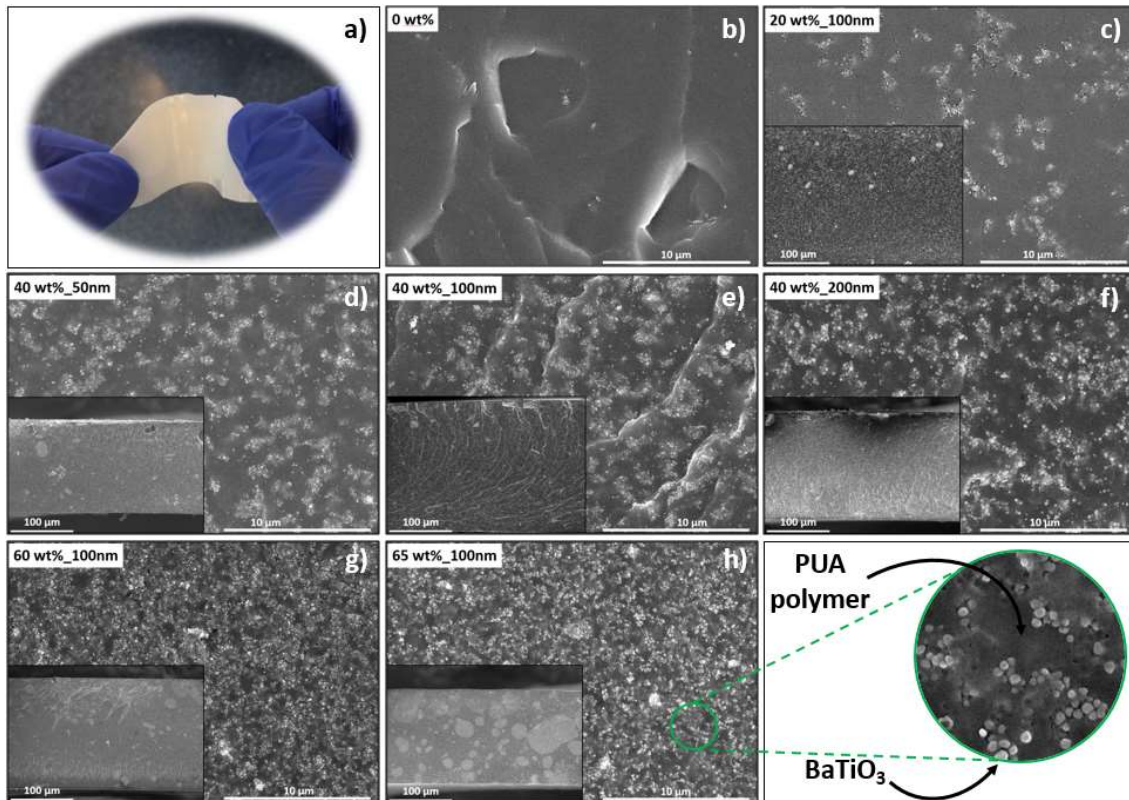

Figure 3.3 - Optical photograph showing the bendability and the macroscopic appearance of composite samples (a). Representative scanning electron microscopy (SEM) images at magnifications of 400x and 5000x of the cross-section of samples PUA0 (b), PUA20_100 (c), PUA40_50 (d), PUA40_100 (e), PUA40_200 (f), PUA60_100 (g), PUA65_100 (h).

In polymer nanocomposites, a suitable dispersion of the filler into the matrix is desirable as it affects electrical and mechanical properties [44,45]. SEM images (**Figure 3.3**) demonstrate the good dispersion of the $BaTiO_3$ particles within the PUA matrix up to 40 wt.% concentration: no large agglomerates or voids are observed and good wettability of the filler by the matrix is verified.

On the other hand, samples with higher concentration of barium titanate particles (60 wt.% or above) show larger agglomerates (insets of **Figure 3.3g and h)**. Despite those agglomerates, $BaTiO_3$ particles are well dispersed along the samples (bright dots). Similar results for photopolymerized $BaTiO_3$-acrylic composites have been reported [27]. With

respect to filler size, results are similar for average filler sizes of 100 nm and 200 nm (**Figure 3.3e and f**), whereas barium titanate nanoparticles of 50-70 nm size, show larger well dispersed agglomerates (**Figure 3.3d**).

Fourier transformed infrared spectroscopy (FTIR) allows to evaluate possible physico-chemical interactions between the polymer matrix and the filler as well as to study the conformational properties of the obtained composites. **Figure 3.4** shows the FTIR spectra of pristine photoresin and the prepared composites with different filler sizes and contents in the range of 4000 to 600 cm^{-1}. The polymer shows the characteristics peaks of the polyurethane acrylate, N-H stretching at 3330-3400 cm^{-1}, between 2855 and 2955 cm^{-1} the CH_2 and CH_3 stretch, C=O stretching at 1725 cm^{-1}, combined stretching of C-N and N-H bonds of the polyurethane group at 1550 cm^{-1}, C-N stretching at 1360 cm^{-1} and the C-O-C stretching at 1110 cm^{-1} [46].

The spectras are similar for the polymer matrix and the composites: no band displacement or the appearance of new peaks are observed upon the addition of barium titanate particles, indicating no intermolecular interactions between the PUA polymer and the $BaTiO_3$ nanoparticles, independently of the filler content or size.
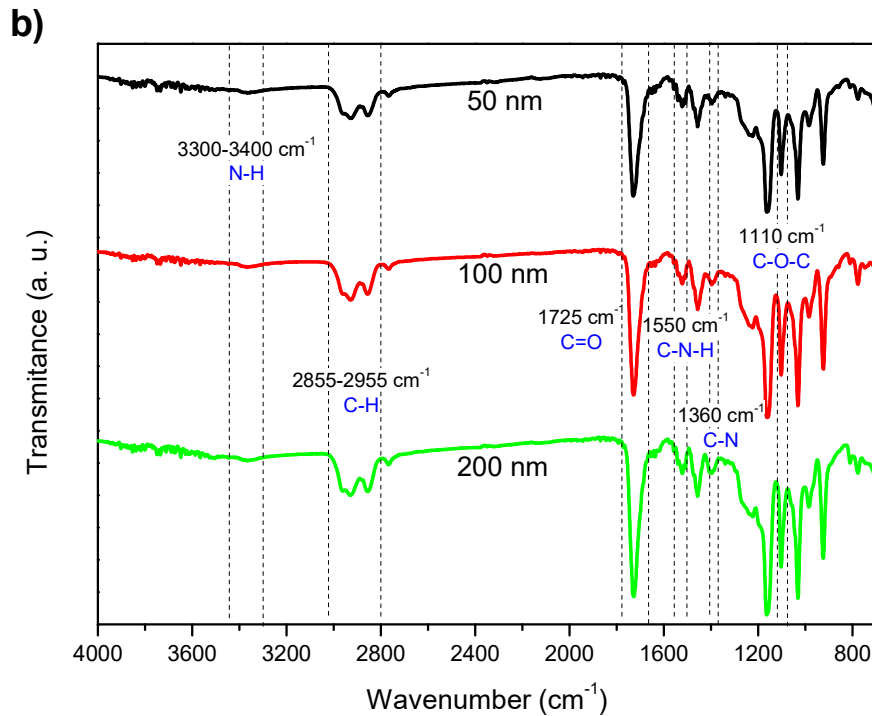
b)
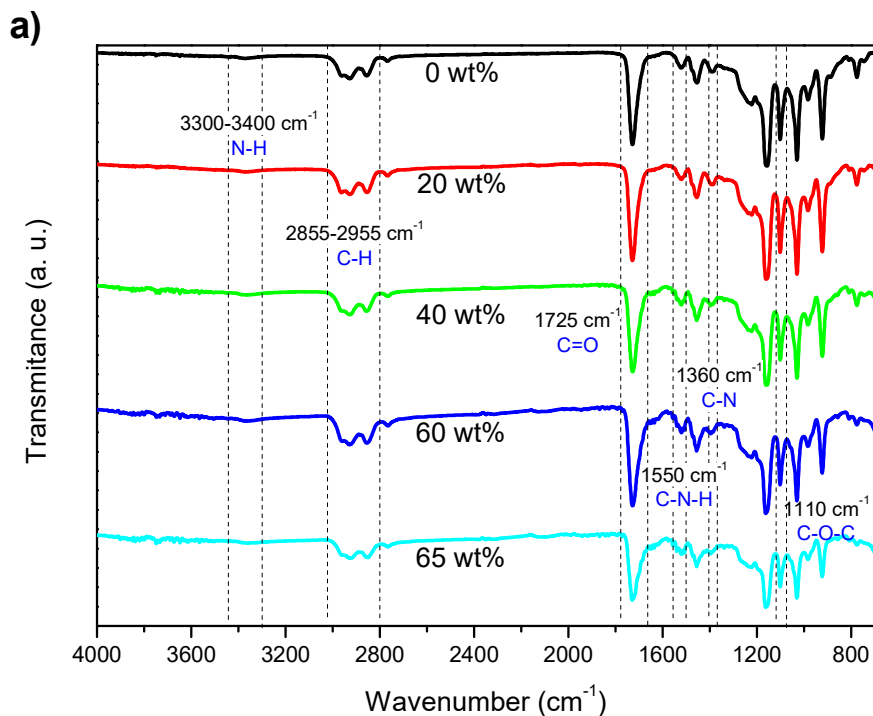
Figure 3.4 - Fourier Transformed Infrared (FTIR) spectra for PUA resin and corresponding composites with varying BaTiO$_3$ content (a) and size (b).

3.3.3. Thermal characterization

Thermogravimetric analyse (TGA) and Differential Scanning Calorimetry (DSC) were used to characterize the thermal properties of the composites in terms of the variations of the thermal degradation and glass transition temperatures, respectively, as a function of filler size and content.

Figure 3.5a shows the thermogravimetric (TG) and the differential thermal gravimetric (DTG) curves for PUA photoresin and the prepared composites for different BaTiO$_3$ content. TG and DTG for samples with different nanoparticle sizes are show in **Figure 3.5b**. The thermal degradation of neat polyurethane occurs in three steps: the first one in the temperature range of 160-280 ºC, the second one at 280-400 °C and the third step at 400-450 °C [46]. Residual monomers and physically absorbed solvent caused the first small decomposition step. The second step is assigned to the decomposition of the main polymer chains. Finally, the third degradation step is ascribed to the combustion of the carbonaceous residues [27,47].
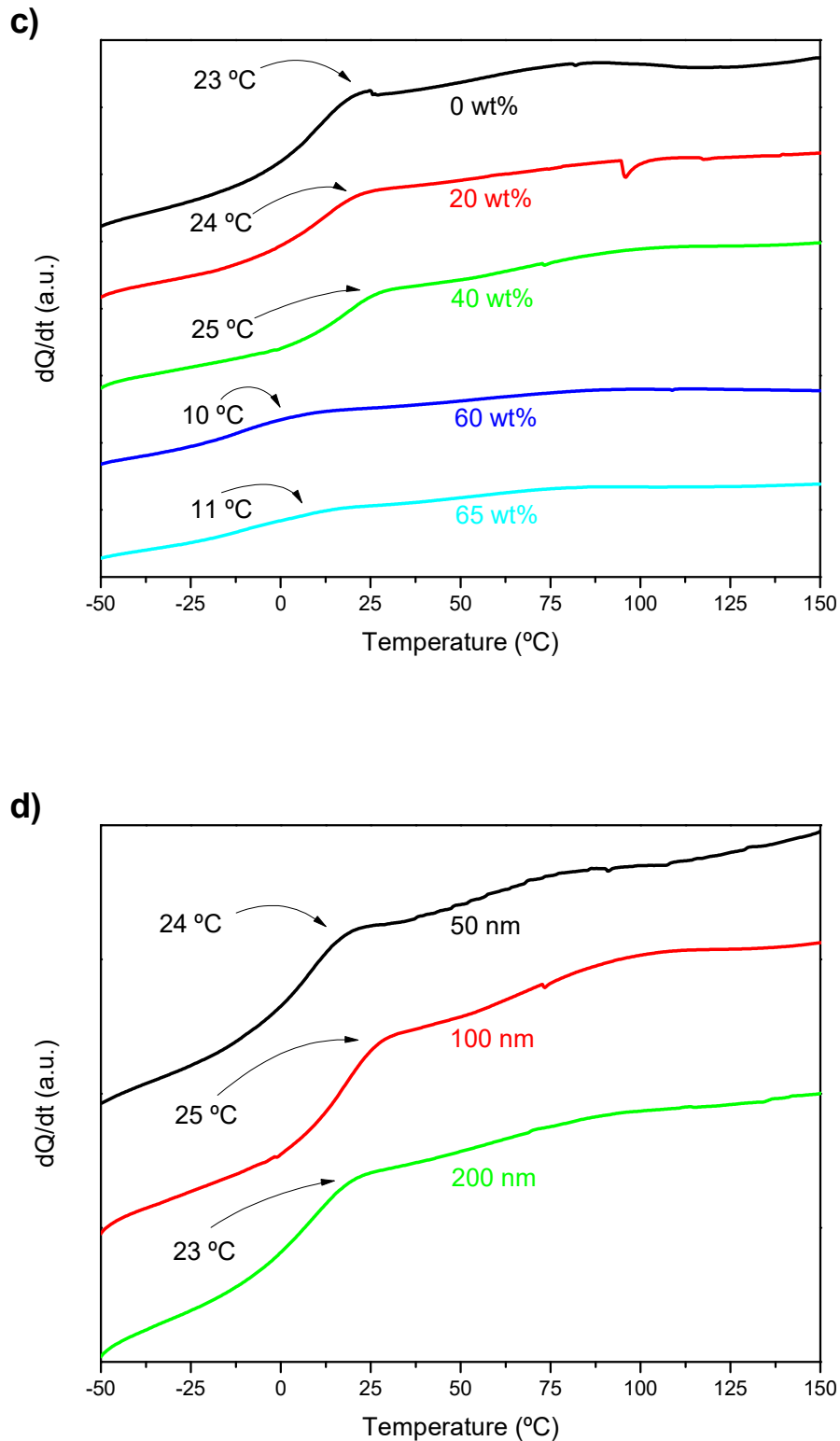
c)

d)
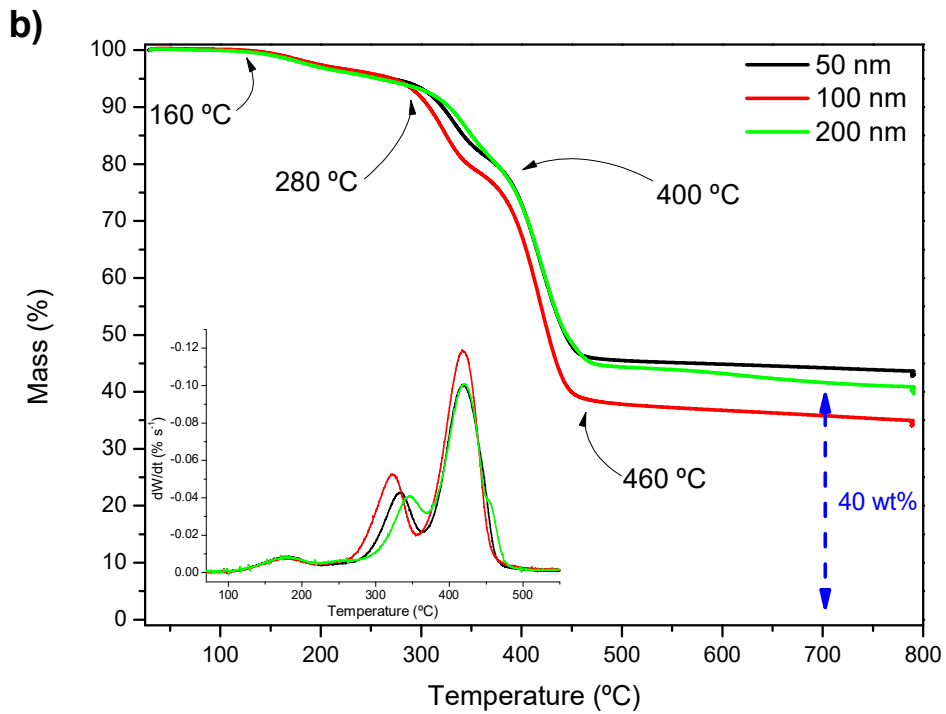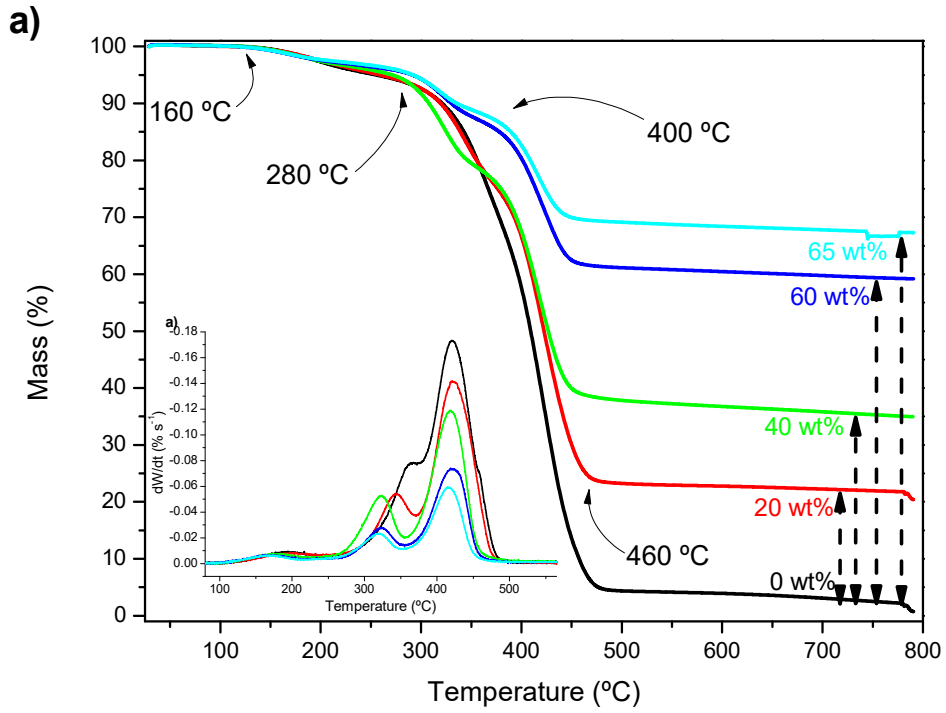
Figure 3.5 - Thermogravimetric (TG) and differential thermogravimetric (DTG) curves for neat PUA and the different BaTiO$_3$ composites with varying filler content (a) and size (b). Differential scanning calorimetry (DSC) thermograms in the first scan for neat PUA and the prepared composites with different BaTiO$_3$ content (c) and size (d).

Similar degradation profiles were obtained for composites independently of the filler content and size, being observed the same three differentiated degradation steps for all samples. On the other hand, the TG curves show that the degradation starts later when the filler content increases, denoting a slightly increase on the thermal stability of the PUA polymer. This behaviour is larger for samples with higher filler contents and is attributed to the thermal insulator behaviour as well as barrier effect of the barium titanate, which influences the thermo-oxidative process of the PUA polymer [27]. This idea is reinforced by the fact that $BaTiO_3$ does not suffer degradation in the studied temperature range and the residual solid is in good agreement with the amount of ceramic filler loaded in each sample. Finally, there is not relevant influence of the barium titanate nanoparticle size on the thermal stability.

DSC thermograms of neat PUA and the $BaTiO_3$/PUA composites (**Figure 3.5c and d**) show that all samples exhibit similar thermal behaviour characterized by a glass transition that in neat polymer is around room temperature (23 ºC). The incorporation of ceramic particles into the photoresin slightly decreased the T_g of the PUA, being this decrease larger for increasing barium titanate content, being 23 ºC for the PUA0 sample and 11 ºC for PUA65_100 sample.

As previously indicated, the presence of nanofillers into the curable material affects the photopolymerization process mainly due to the absorption of UV light by the ceramic material. This produces a decrease on the light absorption by the photoinitiator and therefore, the effectiveness of the curing process is affected. Thus, the acrylic double bond conversion is reduced when the barium titanate content increases, leading to a plasticizing effect. This effect induces a lower crosslink density and a larger free volume within the polymer which results in a lower T_g [27]. As in the thermal stability results, barium titanate nanoparticle size has not influence on the T_g of the composites.

3.3.4. Mechanical characterization

UV-curable acrylate materials are limited for some applications due to their low strength and poor resistance to high temperature. However, thermal and mechanical properties can be tuned by adding nanofillers such as graphene, carbon nanotubes o ceramic particles [48,49]. In this study, the effect of barium titanate nanofillers on the mechanical properties of the composites has been addressed (**Figure 3.6**). The secant modulus (E), maximum stress (σ_b) and strain at brake (ε_b) were obtained by evaluating the results of uniaxial tensile tests of the

samples. **Figure 3.6a** shows the representative stress-strain curves for PUA and the corresponding composites. **Figure 3.6b and c** show the evolution of the main mechanical parameters as a function of BaTiO$_3$ particles concentration and sizes, respectively. **Table 3.2** summarizes the corresponding values of the mechanical properties.

Table 3.2 – Main mechanical parameters obtained from the tensile test for the prepared nanocomposites. E: Initial modulus; σ_b: stress at yield; ε_b: elongation at yield; $E_{Halpin-Tsai}$: theoretical initial modulus predicted by the Halpin-Tsai model [50].

Sample	E (MPa)	σ_b (MPa)	ε_b (%)	$E_{Halpin-Tsai}$ (MPa)
PUA0	5.8 ± 0.1	2.1 ± 0.2	40.4 ± 3.5	5.8
PUA20_100	6.9 ± 0.3	2.6 ± 0.2	37.9 ± 1.9	7.0
PUA40_50	10.2 ± 0.4	2.6 ± 0.2	31.7 ± 3.0	-
PUA40_100	8.5 ± 0.6	3.3 ± 0.7	37.2 ± 4.2	8.9
PUA40_200	8.6 ± 0.5	3.7 ± 0.5	39.0 ± 4.1	-
PUA60_100	21.0 ± 0.2	4.3 ± 0.2	23.8 ± 1.5	12.7
PUA65_100	27.8 ± 1.1	5.4 ± 0.3	25.3 ± 1.5	14.4

Neat UV cured PUA polymer shows a mechanical behaviour [51] characterized by a secant modulus, E, of 5.8 ± 0.1 MPa and strain at brake, ε_b, of 40.4 ± 3.5. The addition of BaTiO$_3$ nanoparticles produces an increase of the initial modulus up to 27.8 ± 1.1 for the sample PUA65_100, together with a corresponding decrease of the maximum strain from 40.1 ± 3.5 to 25.3 ± 1.5. Thus, it is demonstrated that the inclusion of barium titanate [52] acts as mechanical reinforcement due to the high tensile modulus of the inorganic component compared to the organic one, as well as due to the good wettability between filler and matrix. It is observed that the larger agglomerates observed for samples PUA60_100 and PUA65_100 cause a decrease on the maximum elongation, as those act as breaking points on the polymer matrix due to stress accumulation [53]. It is worth noting that the secant modulus increases exponentially with ceramic particles content (**Figure 3.6b**), which is explained by the fact that the internal network created by the ceramic filler, that is responsible for the reinforcement effect, has been formed when the content of BaTiO$_3$ within the polymer matrix is larger than 50 wt.% [51].
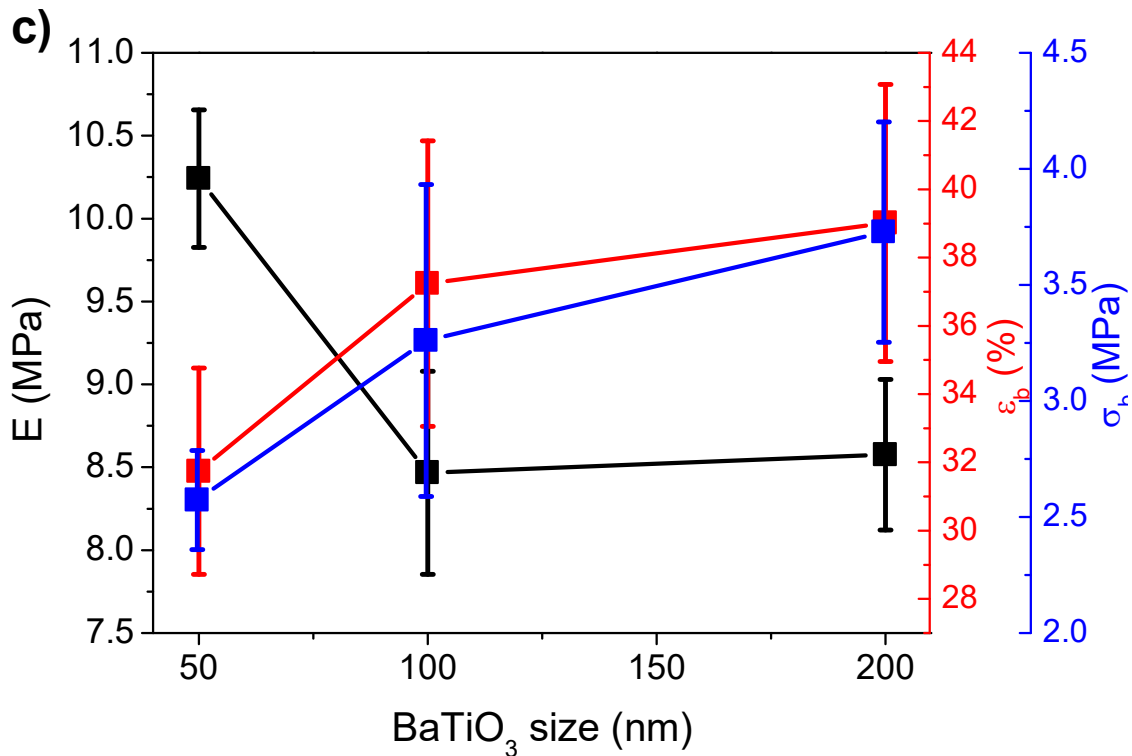
a)

b)

c)
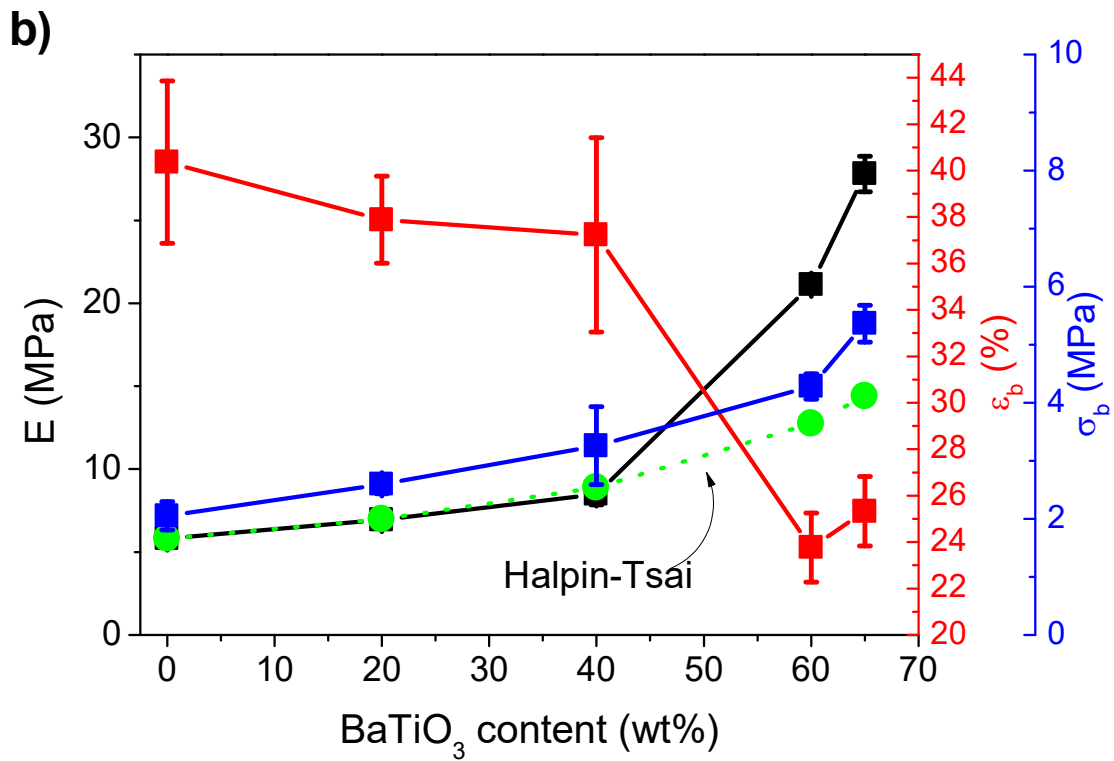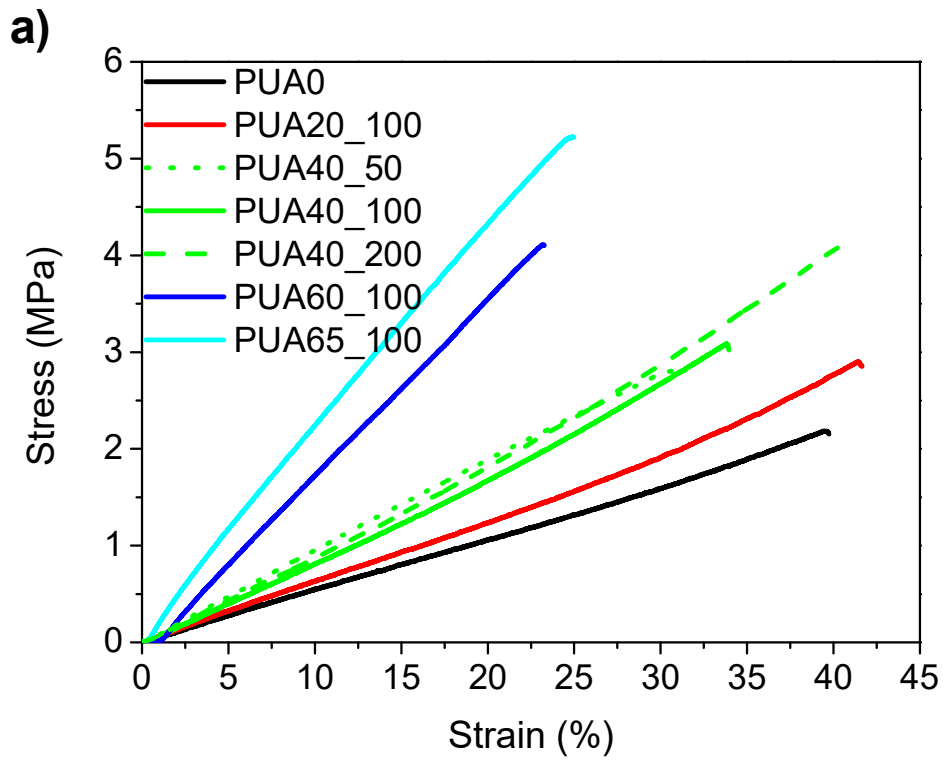
Figure 3.6 – Representative stress-strain curves for neat PUA and the corresponding composites (a), experimental data and fitting results of neat PUA and the prepared composites with different amounts of BaTiO$_3$ nanoparticles determined according to the modified Halpin-Tsai model (b) and experimental results for neat PUA and the prepared composites with different BaTiO$_3$ nanoparticles sizes.

Comparing samples with different nanoparticle sizes, the same tensile behaviour is observed for samples PUA40_50, PUA40_100 and PUA40_200, showing that the nanoparticles reinforce effect of the polymer matrix occurs for the three filler sizes. However, attending to the mechanical parameters (**Figure 3.6c**), a slight difference is observed for the three particle sizes. The tensile modulus decreases from 10.2 ± 0.4 MPa for the same sample with smallest particle size to 8.6 ± 0.5 MPa for the sample that contains 200 nm BaTiO$_3$ nanoparticles. In the case of σ_b and ε_b, a slight increase is observed between 2.6 ± 0.2 to 3.7 ± 0.5 and between 31.7 ± 3.0 to 39.0 ± 4.1, respectively, for the same samples. These results are explained in terms of the surface area interaction between the fillers and the polymer. Thus, small agglomerates in the samples with smallest particle size can actuate as breaking points and despite the inorganic matrix reinforce of the PUA polymer (higher E), the composite becomes more fragile, leading to an early break (lower σ_b and ε_b). Similar results were observed by Capsal *et al.* with polyamide 11/Barium titanate ferroelectric composites [53].

The experimentally obtained results for samples with 100 nm BaTiO$_3$ nanoparticles were compared with the theoretical predictions of the Halpin-Tsai model [50]:

$$\frac{E_c}{E_m} = \left(\frac{3}{8}\right)\left(\frac{1 + 2\rho\eta_L V_{BaTiO_3}}{1 - \eta_L V_{BaTiO_3}}\right) + \left(\frac{5}{8}\right)\left(\frac{1 + 2\eta_T V_{BaTiO_3}}{1 - \eta_T V_{BaTiO_3}}\right) \tag{3.3}$$

$$\eta_L = \frac{E_r - 1}{E_r + 2\rho} \; ; \; \eta_T = \frac{E_r - 1}{E_r + 2}$$

where E_c and E_m are the initial modulus of the composite and matrix [54] respectively, ρ is the BaTiO$_3$ nanoparticles aspect ratio (set at 1, spherical), V_{BaTiO_3} is its volume fraction within the nanocomposite and E_R is defined as the ratio between the Young´s modulus of the filler and the matrix. The density of ceramic filler is obtained from the technical datasheet of the suppliers, being 5.85 g/cm^3, and the density of PUA polymer is 1.55 g/cm^3.

Figure 3.6b shows that the experimental values can be markedly well described by the model for BaTiO$_3$ nanoparticles contents up to 40 wt.% and remain above the theoretical predictions for higher ceramic particles contents. Those results indicate that the Halpin-Tsai model properly describes the experimental results until the formation of large agglomerates (see **Figure 3.3g and h**) that affect the mechanical properties [50].

3.3.5. Dielectric properties

The dielectric constant or relative permittivity ($\varepsilon´$) and the dielectric losses (tan δ) as a function of the frequency are among the most relevant parameter on this types of composites [33]. In this sense, **Figure 3.7a** shows the frequency dependence of the room temperature dielectric constant for neat PUA and the different BaTiO$_3$/PUA composites, and **Figure 3.7b** and c show the relative permittivity measured and the corresponding losses at 1 kHz for the same samples, whereas **Figure 3.7d** shows that dielectric constant as a function of filler size.

a)

b)

c)

d)

e)

f)
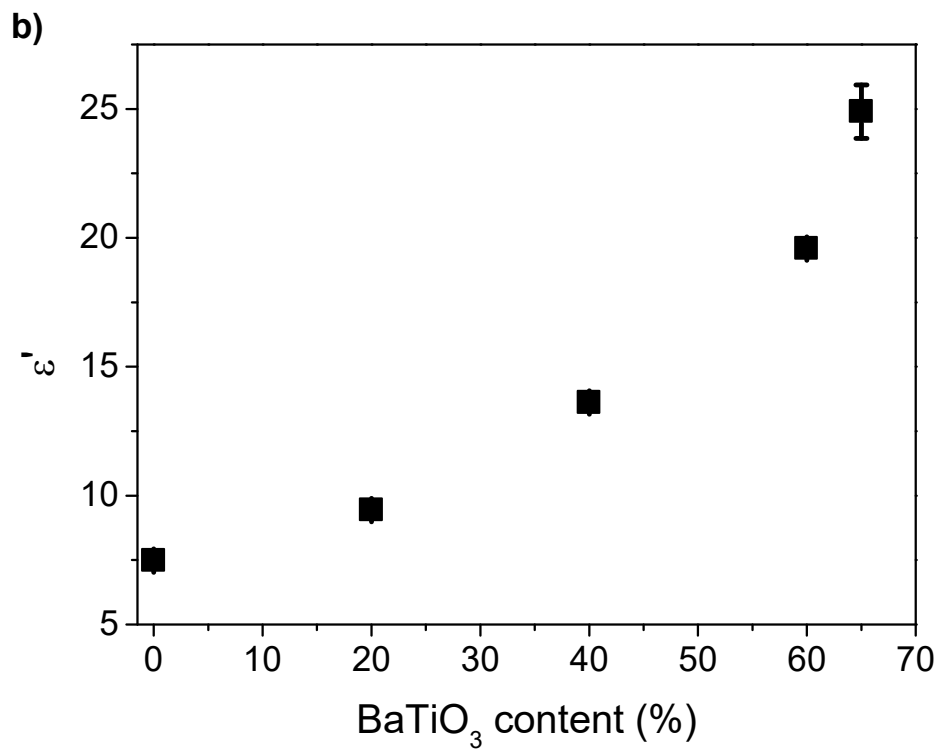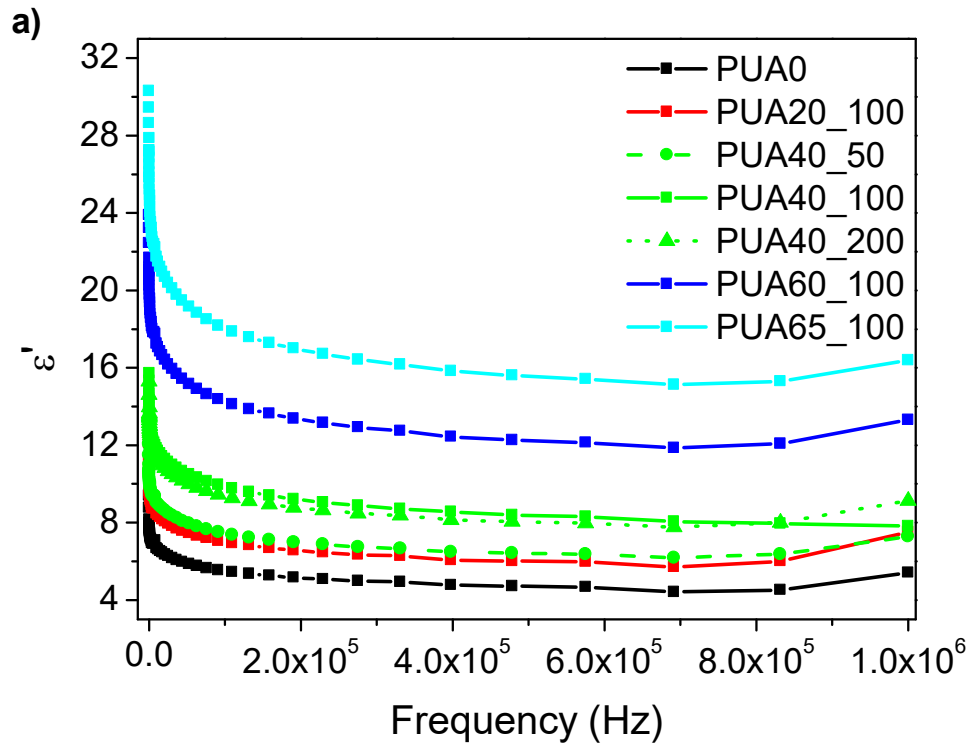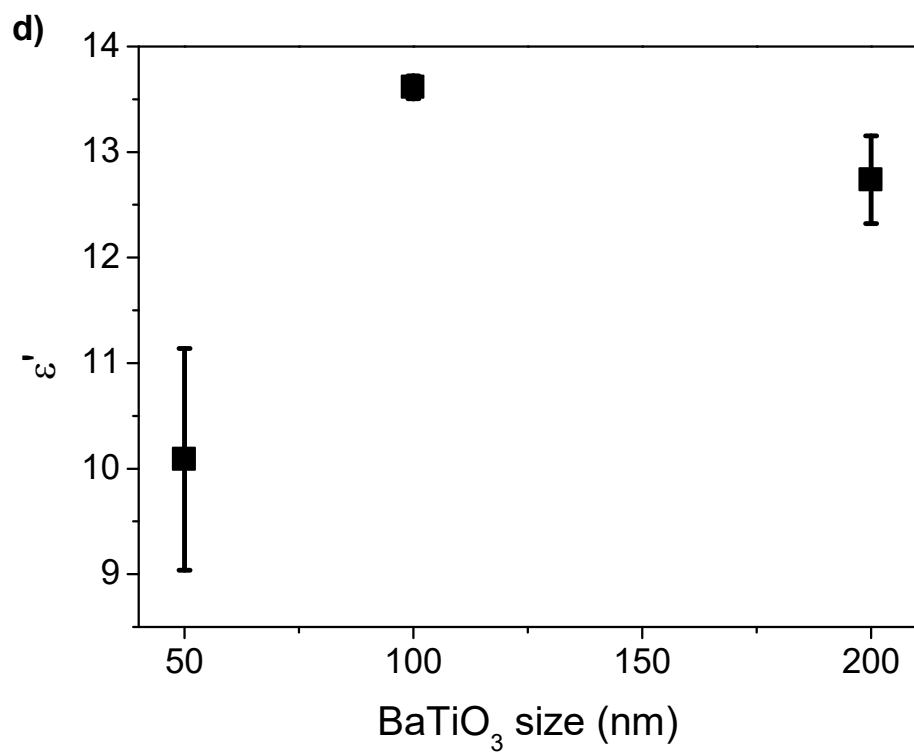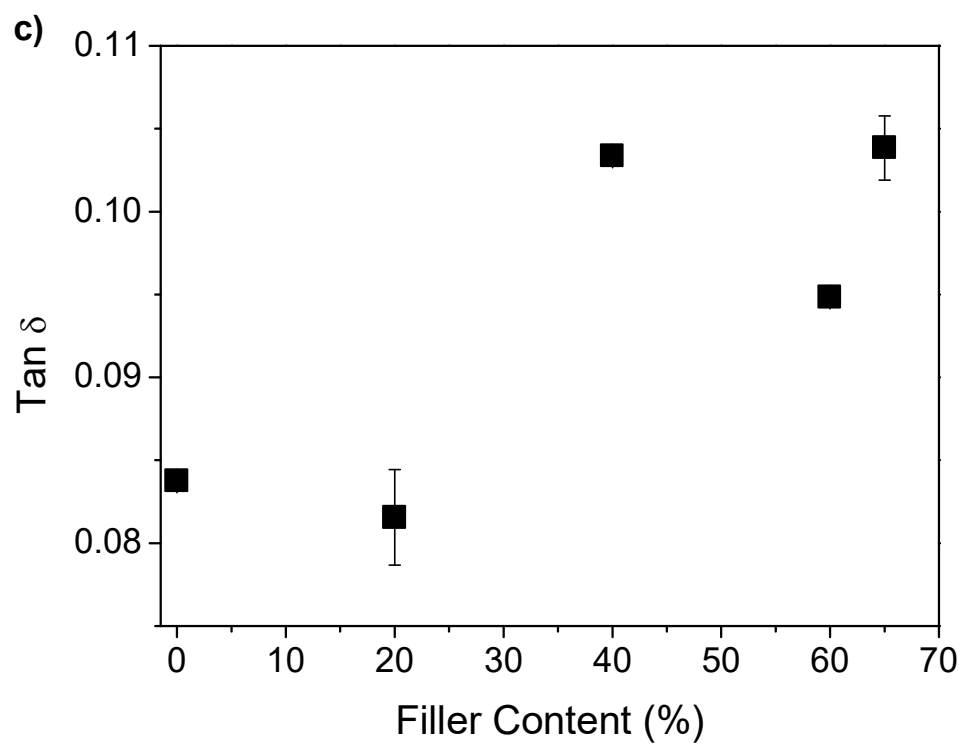
Figure 3.7 – (a) Relative permittivity as a function of frequency at room temperature for neat PUA and all prepared composites. Rel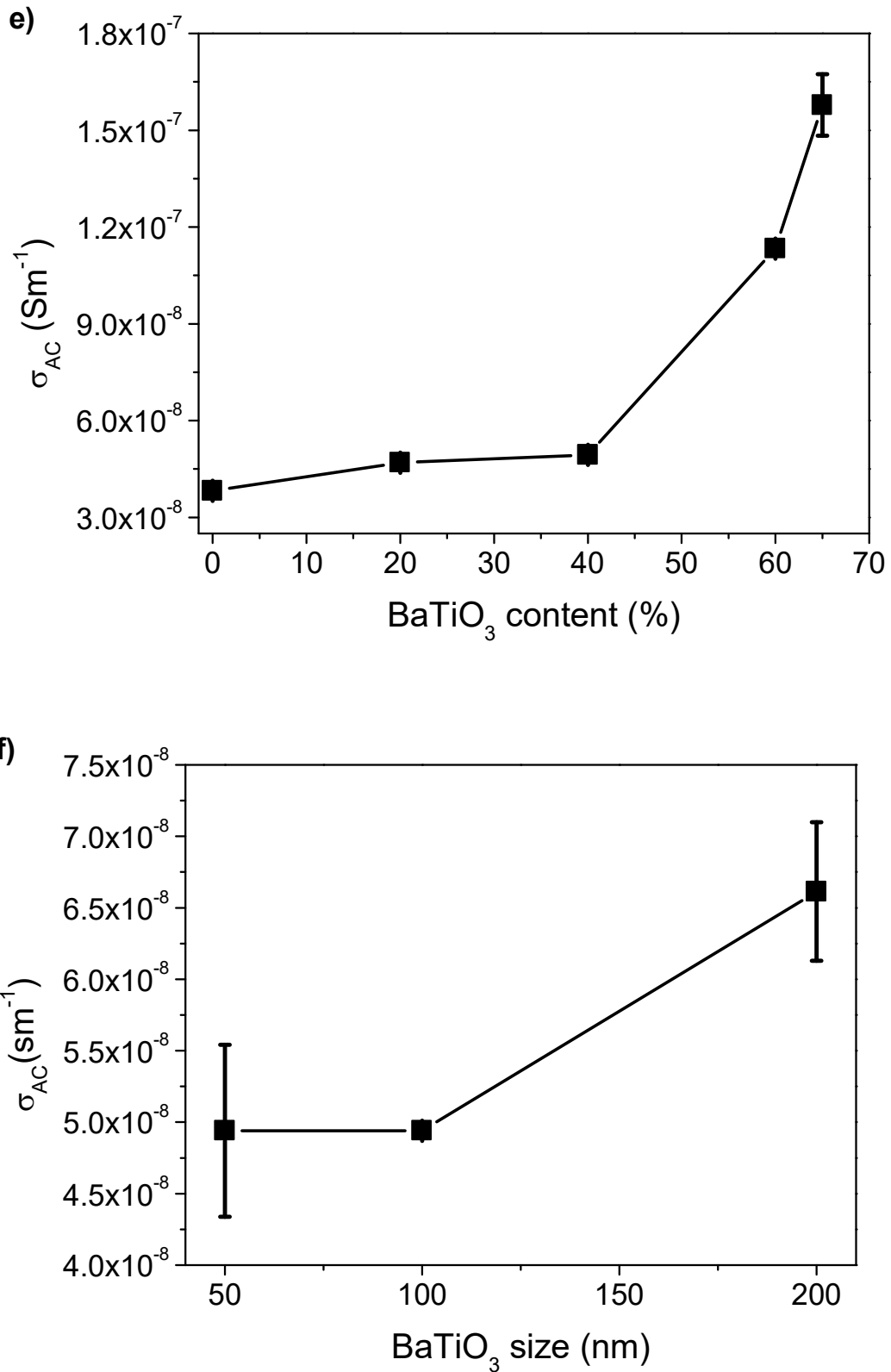ative permittivity (b) and the tan δ dielectric loss values (c) at 1KHz at room temperature as a function of $BaTiO_3$ content. Relative permittivity at 1 kHz at room

temperature as a function BaTiO₃ nanoparticles size (d). Electrical conductivity at room temperature and 1 kHz of the neat PUA and the prepared composites as a function of filler content for 100 nm nanoparticles (e) and filler size (f).

It is shown that ε' decreased with the frequency for all samples, independently of the filler size or content. This behaviour is attributed to the dipolar relaxation with increasing frequency as well as to interfacial polarization effects. The titanium ions of the BaTiO₃ structure occupy a position that is too large for that ion. Thus, when a field is applied, the positively charged ion (Ti^{4+}) can move in the direction of the negative pole easily over a small distance creating a very large polarization and thereby increasing the dielectric constant or relative permittivity of the material. When the field is removed, the ion is reoriented. At large frequencies, the titanium ion does not have enough time to reorient itself in the structure giving rise to the relaxation of the dipoles, which is accompanied with the corresponding variations in the dielectric losses [55,56].

Relative permittivity measured at 1 kHz increases as a function of filler content increase (**Figure 3.7c**) from 7.48 ± 0.08 for neat polymer up to 13.61 ± 0.11 for the PUA40_100 sample. The maximum relative permittivity value was achieved for the maximum concentration of BaTiO₃ nanoparticles in sample PUA65_100 that shows and ε' of 24.90 ± 1.04. Further, the relative permittivity measured at 1 kHz as a function of filler size shows that an increase on the filler size allows a slightly increase on the ε'. Thus, the PUA40_50 sample shows a dielectric constant of 10.09 ± 1.05 and PUA40_200 sample of 12.74 ± 0.41. **Figure 3.7d** shows that the dielectric constant reaches a nearly constant value, which is explained in terms of agglomeration of the smallest BaTiO₃ nanoparticles that induces a similar electrical behaviour than the 100 nm and 200 nm particles [27]. Similar values and behaviours were found in the literature for several polymer/ceramic particle composites [27,33,57–59], but with slightly differences based on the different polymer matrix and the interaction of the polymer and the ceramic particles. Thus, a study of this interaction was evaluated.

In addition, the dependence of the electrical conductivity (σ) (obtained at 1 kHz) with the BaTiO₃ nanoparticle concentration and size was obtained using the equation **¡Error! No se encuentra el origen de la referencia.** [50]:

$$\sigma = 2\pi f \varepsilon_0 \varepsilon''$$
(3.4)

where f is the frequency in Hz, ε_0 represents the vacuum permittivity (8.854×10^{-12} F·m^{-1}) and ε'' is the imaginary part of the permittivity represented as $\varepsilon'' = \varepsilon' \cdot \tan \delta$. The results obtained are represented in **Figure 3.7e and f**.

All prepared composites can be considered as insulating materials due to their low σ values (in order of 10^{-8} S·m^{-1}), in particular, the neat PUA matrix with a value of conductivity about 3.82×10^{-8} S·m^{-1}. Similar to dielectric properties, the a.c. conductivity increases with increasing ceramic content being 4.94×10^{-8} S·m^{-1} for PUA40_100 sample and reaching the highest value of conductivity (1.58×10^{-7} S·m^{-1}) for the sample with higher BaTiO$_3$ content. These slightly but pronounced increase on the conductivity upon BaTiO$_3$ addition is associated with the increase of interfacial charges and is related to Maxwell-Wargner-Sillars effects [55,56].

In the case of size dependence, a slight increase of the a.c. electrical conductivity is observed when the barium titanate nanoparticle size increases. Nevertheless, this increase is lower than 1 order of magnitude and the maximum conductivity obtained for PUA40_200 sample is 6.61×10^{-8} S·m^{-1}.

3.3.6. Theoretical evaluation of the dielectric properties

The theoretical models for the analysis of the dielectric constant allow to evaluate the nature of the interactions between the matrix and the fillers, responsible for the dielectric response of the composites. The BaTiO$_3$/PUA composites have been analyzed, considering the nanoparticles size (Φ=100 nm) and concentration (20 wt.%, 40 wt.%, 60 wt.% and 65wt.% corresponding to volume fractions of 0.06212, 0.15012, 0.28440 and 0.32979, respectively). The most appropriate models considering filler size and concentration will be presented and discussed.

The differences between models are related to differences in the considerations of the relevant interactions between the polymeric matrix and the fillers, as well as on the relevance of the effect of filler volume fraction. Although the different models consider different interactions, all of them predict the increase of the dielectric constant with increasing filler content. The most simple models include Maxwell-Garnett (equation (3.5)**¡Error! No se encuentra el origen de la referencia.**) and Furukawa (equation (3.7)), typically used to experimentally explain the dielectric behaviour of the composites [60,61], but being unable to predict the experimental results for higher fillers contents, as they do not consider filler

shape and size, which are needed to better understand the interactions and aggregation effects of the fillers [26,61], among other fenomena.

The models of Maxwell-Garnett [62,63] and Furukawa [64] consider the incorporation of spherical fillers into a polymeric matrix with no interactions among particles and between matrix and particles, also without considering filler size effects.

The Maxwell-Garnet model is represented by:

$$\varepsilon = \varepsilon_1 \left(1 + \frac{3v_2\gamma}{1 - v_2\gamma}\right) \tag{3.5}$$

where:

$$\gamma = \frac{\varepsilon_2 - \varepsilon_1}{\varepsilon_2 + 2\varepsilon_1} \tag{3.6}$$

and ε represents the dielectric constant, v is the volume fraction and the subscripts 1 and 2 represent the matrix and filler, respectively. Furukawa *et al.* [64] proposed an approximation in the Rayleigh model, considering that the dielectric constant of the fillers is usually much higher than the matrix ($\varepsilon_2 \gg \varepsilon_1$), so that the behaviour of the dielectric constant with filler content is represented by:

$$\varepsilon = \varepsilon_1 \frac{1 + 2v_2}{1 - v_2} \tag{3.7}$$

Later, models were developed considering also spherical dielectric inclusions into a polymeric matrix but considering also the materials polarization due to the applied electric field, the variation in local field and interactions between the fillers and the local and applied field [26]. When an electric field is applied to a composite material, the dielectric particles can be, in a good approximation, considered as electric dipoles changing the electric field in its surroundings. This effect can be neglected for low filler concentrations, however for higher concentrations the interaction between particles cannot be ignored [65]. Thus, Bruggeman established a symmetrical expression considering this phenomenon [62]:

$$v_1 \frac{\varepsilon_1 - \varepsilon}{\varepsilon_1 + (d - 1)\varepsilon} + v_2 \frac{\varepsilon_2 - \varepsilon}{\varepsilon_2 + (d - 1)\varepsilon} = 0 \tag{3.8}$$

where *d* is the dimensionality of the system. An improvement of the Maxwell-Garnett model considering also the interactions between fillers, lead to rewrite equation (3.5) as [63]:

$$\varepsilon = \varepsilon_1 \left[1 + \frac{3v_2\gamma}{1 - v_2\gamma - \frac{2}{3}v_2\gamma \ln\left(\frac{8+\gamma}{8-2\gamma}\right)} \right] \tag{3.9}$$

where γ is defined by equation (3.6).

Most precise and complex models also introduce the effects of the shape and relative orientation of the fillers, considering in most of the cases an ellipsoids shape for the fillers. This information appears in the equations as depolarization factor (n) or shape parameter (n'). Most precisely, the n factor is influenced by the principal axe's length of the fillers and the relative orientation to the applied filed [66]. An extension of the Sillars's work, led to van Beek to present the following equation, taking in consideration the factor n [67]:

$$\varepsilon = \varepsilon_1 \frac{\varepsilon_1 + [n(1-v_2) + v_2](\varepsilon_2 - \varepsilon_1)}{\varepsilon_1 + n(1-v_2)(\varepsilon_2 - \varepsilon_1)} \tag{3.10}$$

In particular, for composite samples with only one filler type, Tinga *et al.* [68] proposed the expression:

$$\frac{\varepsilon - \varepsilon_1}{\varepsilon_1} = v_2 \frac{\varepsilon_2 - \varepsilon_1}{\varepsilon_1 + n_2(\varepsilon_2 - \varepsilon_1) - n_1 v_2(\varepsilon_2 - \varepsilon_1)} \tag{3.11}$$

For models that introduce the n' factor, Yamada *et al.* [69] deduced an equation for an ellipsoidal particle dispersion:

$$\varepsilon = \varepsilon_1 \left[1 + \frac{n'v_2(\varepsilon_2 - \varepsilon_1)}{n'\varepsilon_1 + (\varepsilon_2 - \varepsilon_1)(1 - v_2)} \right] \tag{3.12}$$

Taking the same considerations, Wiener *et al.* [70] proposed the following equation:

$$\frac{\varepsilon - 1}{\varepsilon + n'} = \frac{v_2(\varepsilon_2 - \varepsilon_1)}{\varepsilon_2 + n'} + \frac{(1-v_2)(\varepsilon_1 - 1)}{\varepsilon_1 + n'} \tag{3.13}$$

The fittings or simulations of the experimental dielectric constant as a function of filler content was performed with the different models described by equations (3.5) to (3.13) making use of the Origin 9.4 software. **Figure 3.8** shows the corresponding fittings considering $\varepsilon_1 = 7.48$ (measured) for the polymer matrix and $\varepsilon_2 = 150$ [71] for the BaTiO$_3$ filler. The volume fraction change between 0 and 1 and the experimental data are also represented.

The prediction of the dielectric constant given by the Bruggeman model is represented for each value of *d*. In the case of d=1, the Bruggeman model has the worst prediction for the dielectric constant. The Maxwell-Garnett, Maxwell-Garnett 2 (taking into account the interactions between fillers and the applied field), Furukawa and Bruggeman (d=2) models

show the same behaviour for low filler concentrations ($v_2 < 0.2$) suggesting that, in this regime, the composite permittivity is almost independent from the filler permittivity. For higher volume fraction, the models start to show relevant differences one another. Increasing volume fraction leads to an increase of the dielectric constant of the composite until $v_2 = 1$, excepting for the Maxwell-Garnett model 2 which shows a vertical asymptote for $v_2 \approx 0.95$. Although Maxwell-Garnett 2 model takes into consideration interactions between fillers and the applied field, there is just a slight difference between the two author's models.
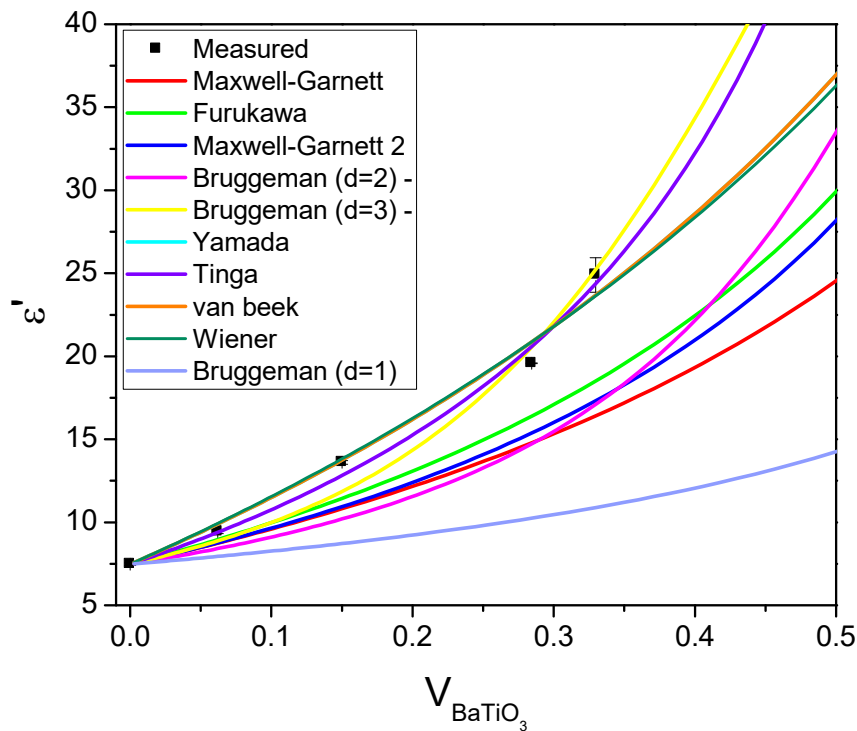
Figure 3.8 – Theoretical models and experimental results for a BaTiO$_3$/PUA composites of 100 nm diameter particles. The experimental results correspond to a frequency of 1kHz.

The Maxwell-Garnett, Maxwell-Garnett 2, Furukawa and Bruggeman (d=2) models predict the same behaviour for $v_2 = 0$ ($\varepsilon = \varepsilon_1$) and in the regime limit of $v_2 = 1$ the Maxwell-Garnett and Bruggeman (d=2) models predict a dielectric constant of $\varepsilon = \varepsilon_2$. In the case of the Furukawa model, ε goes to infinite. For these models, the Bruggeman's model (d=2) predict the higher dielectric constant for $v_2 > 0.4$.

The experimental-theoretical difference was calculated as relative percentage deviation $\langle \delta_r \rangle$, for Maxwell-Garnett, Furukawa, Maxwell-Garnett 2, Bruggeman (for d=1,2 and 3) models through equation (3.14):

$$\langle \delta_r \rangle = \frac{|\varepsilon_{exp} - \varepsilon_{mod}|}{\varepsilon_{exp}} \times 100 \ \% \tag{3.14}$$

where ε_{exp} is the experimental data measured and ε_{mod} the predicted dielectric constant for the corresponding model. The results are summarized in **Table 3.3**. All these models show deviations less than 12% for $\nu_2 = 0.06212$ (except Bruggeman (d=1)) but with increasing filler contents, the models that not considered the filler agglomeration effects (Maxwell-Garnett and Furukawa), are unable of predict the experimental data. This means that the interactions only become important for a certain volume fraction. Even though the models of Maxwell-Garnett 2 and Bruggeman (d=2) consider the interaction between nanoparticles and the field, they are unable to properly model the experimental data. Within these models, the Furukawa model is the one with better predictions. Only the Bruggeman (d=3) model can describe the data for all ν_2 with deviations less than 13%. This deviation values are related to the agglomerations affect that occurs for higher volume fraction leading to the break of homogeneity condition underlaying all models [26]. Further, the high surface area due to the filler size (Φ=100 nm), leading to an increase of the space charge distribution and Maxwell-Wagner-Sillars contributions to the dielectric behaviour [33], can also account for these deviations.

Table 3.3 – Relative percentage deviation for the theoretical models for each volume fraction.

Models\ Volume faction (ν_2)	Relative percentage deviation - $\langle \delta_r \rangle$ (%)			
	0.06212	0.15012	0.28440	0.32979
Maxwell-Garnett	7	21	24	34
Furukawa	5	16	16	26
Maxwell-Garnett 2	7	20	21	30
Bruggeman (d=1)	16	36	48	56
Bruggeman (d=2)	11	25	25	31
Bruggeman (d=3)	6	13	5	1

For the remaining models (van Beek, Tinga, Yamada and Wiener), the experimental data were fitted to determine the depolarization factor *n* or shape parameter *n'*, for the corresponding models, by computational iteration. These models predict in a more precise way the dielectric behaviour of the composite showing the important contributions of the filler's shape and orientation. The obtained results are summarized in **Table 3.4** showing the *n* and *n'* values and the respective R-square for the fitting procedure.

Table 3.4 – The parameters n and n' for the respective models obtained by computational iteration by fitting the experimental data.

	Models			
	Yamada	**Wiener**	**Tinga**	**van Beek**
n_1	--	--	0.357 ± 0.145	0.149 ± 0.009
n_2	--	--	0.211 ± 0.046	--
n'	6.724 ± 0.419	48.167 ± 3.634	--	--
R-Square	0.98397	0.98286	0.99071	0.98397

Although the Tinga model shows a vertical asymptote for $v_2 \approx 0.74$, when it was compared the R-Square values, all these models have a good fitting to the experimental data, with a more precise prediction for the Tinga model, followed by the Yamada, van Beek and Wiener models. The difference between the obtained factors is due to the physical principles considered by the models. The value *n'* can mean the ratio between ellipsoidal axis but also the size of agglomeration and homogeneity of the sample.

Thus, it can be concluded that the model that better predicts the behaviour of the BaTiO₃/PUA composites is the Tinga model and therefore, the relevant interactions, together with the filler and matrix dielectric constant and filler concentrations are the materials polarization due to the applied electric field, the variation in local field and interactions between the fillers and the local and applied field and the influence of the principal axe's length of the fillers and the relative orientation to the applied field. So, the equation (3.11), that is a special case of the Tinga model that describes a ellipsoidal inclusion of two phases, must be considered to properly tailor and understating composite dielectric response.

3.4. Conclusions

UV curable barium titanate/polyurethane acrylate (BaTiO₃/PUA) composites are presented with varying ceramic contents, allowing to obtain dielectric materials with tailored dielectric response for electronic applications, among others. PUA composites with BaTiO₃ filler contents up to 65 wt.% for filler sizes between 50 nm and 200 nm have been evaluated. A good dispersion stability up to 160 ºC and mechanical flexibility. Further, the dielectric constant can be as high as 25 for the samples with the highest filler content, independently

of the filler size, the dielectric response as a function of filler concentration being suitably described by the Tinga model for the dielectric behavior of composites.

3.5. References

[1]   Y. Lu, Industry 4.0: A survey on technologies, applications and open research issues, J. Ind. Inf. Integr. 6 (2017) 1–10. doi:10.1016/j.jii.2017.04.005.

[2]   V. Roblek, M. Meško, A. Krapež, A Complex View of Industry 4.0, SAGE Open. 6 (2016). doi:10.1177/2158244016653987.

[3]   I. Lee, K. Lee, The Internet of Things (IoT): Applications, investments, and challenges for enterprises, Bus. Horiz. 58 (2015) 431–440. doi:10.1016/j.bushor.2015.03.008.

[4]   P.P. Ray, A survey on Internet of Things architectures, J. King Saud Univ. - Comput. Inf. Sci. 30 (2018) 291–319. doi:10.1016/j.jksuci.2016.10.003.

[5]   A. Zanella, N. Bui, A. Castellani, L. Vangelista, M. Zorzi, Internet of things for smart cities, IEEE Internet Things J. 1 (2014) 22–32. doi:10.1109/JIOT.2014.2306328.

[6]   J. Gubbi, R. Buyya, S. Marusic, M. Palaniswami, Internet of Things (IoT): A vision, architectural elements, and future directions, Futur. Gener. Comput. Syst. 29 (2013) 1645–1660. doi:10.1016/j.future.2013.01.010.

[7]   C. Mendes-felipe, J. Oliveira, I. Etxebarria, J.L. Vilas-vilela, State-of-the-Art and Future Challenges of UV Curable Polymer-Based Smart Materials for Printing Technologies, 1800618 (2019) 1–16. doi:10.1002/admt.201800618.

[8]   J. Oliveira, V. Correia, H. Castro, P. Martins, S. Lanceros-Mendez, Polymer-based smart materials by printing technologies: Improving application and integration, Addit. Manuf. 21 (2018) 269–283. doi:10.1016/j.addma.2018.03.012.

[9]   J. Oliveira, R. Brito-Pereira, B.F. Gonçalves, I. Etxebarria, S. Lanceros-Mendez, Recent developments on printed photodetectors for large area and flexible applications, Org. Electron. Physics, Mater. Appl. 66 (2019) 216–226. doi:10.1016/j.orgel.2018.12.028.

[10]   Y. Zhan, Y. Mei, L. Zheng, Materials capability and device performance in flexible electronics for the Internet of Things, J. Mater. Chem. C. 2 (2014) 1220–1232. doi:10.1039/c3tc31765j.

[11]   M. Haras, T. Skotnicki, Thermoelectricity for IoT – A review, Nano Energy. 54 (2018) 461–476. doi:10.1016/j.nanoen.2018.10.013.

[12]   K.N. Paracha, S.K. Abdul Rahim, P.J. Soh, M. Khalily, Wearable Antennas: A Review of Materials, Structures, and Innovative Features for Autonomous Communication and Sensing, IEEE Access. 7 (2019) 56694–56712. doi:10.1109/ACCESS.2019.2909146.

[13]   F. Narita, M. Fox, A Review on Piezoelectric, Magnetostrictive, and Magnetoelectric Materials and Device Technologies for Energy Harvesting Applications, Adv. Eng. Mater. 20 (2018) 1–22. doi:10.1002/adem.201700743.

[14]   Y. Bai, H. Jantunen, J. Juuti, Energy harvesting research: The road from single source to multisource, Adv. Mater. 30 (2018) 1–41. doi:10.1002/adma.201707271.

[15]   M. Zhou, M.S.H. Al-Furjan, J. Zou, W. Liu, A review on heat and mechanical energy harvesting from human – Principles, prototypes and perspectives, Renew. Sustain. Energy Rev. 82 (2018) 3582–3609. doi:10.1016/j.rser.2017.10.102.

[16]   S. Khan, L. Lorenzelli, R.S. Dahiya, Technologies for printing sensors and electronics over large flexible substrates: A review, IEEE Sens. J. 15 (2015) 3164–3185. doi:10.1109/JSEN.2014.2375203.

[17]   K.K.B. Hon, L. Li, I.M. Hutchings, Direct writing technology-Advances and developments, CIRP Ann. - Manuf. Technol. 57 (2008) 601–620. doi:10.1016/j.cirp.2008.09.006.

[18]   M. Gao, L. Li, Y. Song, Inkjet printing wearable electronic devices, J. Mater. Chem. C. 5 (2017) 2971–2993. doi:10.1039/c7tc00038c.

[19]   A.H. Sirringhaus, T. Kawase, R.H. Friend, T. Shimoda, M. Inbasekaran, W. Wu, E.P. Woo, High-Resolution Inkjet Printing of All-Polymer Transistor Circuits, 290 (2016) 2123–2126.

[20]   Z.P. Yin, Y.A. Huang, N.B. Bu, X.M. Wang, Y.L. Xiong, Inkjet printing for flexible electronics: Materials, processes and equipments, Chinese Sci. Bull. 55 (2010) 3383–3407. doi:10.1007/s11434-010-3251-y.

[21]   A. Rida, L. Yang, R. Vyas, M.M. Tentzeris, Conductive inkjet-printed antennas on

flexible low-cost paper-based substrates for RFID and WSN applications, IEEE Antennas Propag. Mag. 51 (2009) 13–23. doi:10.1109/MAP.2009.5251188.

[22] K. Kordás, T. Mustonen, G. Tóth, H. Jantunen, M. Lajunen, C. Soldano, S. Talapatra, S. Kar, R. Vajtai, P.M. Ajayan, Inkjet printing of electrically conductive patterns of carbon nanotubes, Small. 2 (2006) 1021–1025. doi:10.1002/smll.200600061.

[23] A. Kamyshny, S. Magdassi, Conductive nanomaterials for printed electronics, Small. 10 (2014) 3515–3535. doi:10.1002/smll.201303000.

[24] F. Torrisi, T. Hasan, W. Wu, Z. Sun, A. Lombardo, T.S. Kulmala, G.W. Hsieh, S. Jung, F. Bonaccorso, P.J. Paul, D. Chu, A.C. Ferrari, Inkjet-printed graphene electronics, ACS Nano. 6 (2012) 2992–3006. doi:10.1021/nn2044609.

[25] V. Correia, K.Y. Mitra, H. Castro, J.G. Rocha, E. Sowade, R.R. Baumann, S. Lanceros-Mendez, Design and fabrication of multilayer inkjet-printed passive components for printed electronics circuit development, J. Manuf. Process. 31 (2018) 364–371. doi:10.1016/j.jmapro.2017.11.016.

[26] M.C. Araújo, C.M. Costa, S. Lanceros-Méndez, Evaluation of dielectric models for ceramic/polymer composites: Effect of filler size and concentration, J. Non. Cryst. Solids. 387 (2014) 6–15. doi:10.1016/j.jnoncrysol.2013.12.005.

[27] M. Lombardi, A. Guerriero, G. Kortaberria, I. Mondragon, M. Sangermano, L. Montanaro, Effect of the Ceramic Filler Features on the Properties of Photopolymerized BaTiO3-Acrylic Composites, Polym. Compos. 32 (2011) 1304–1312. doi:10.1002/pc.21154.

[28] H. Singh Nalwa, Handbook of Low and High Dielectric Constant. Materials and Their Applications, 1st Editio, Academic Press, London, England, 1999.

[29] P. Barber, S. Balasubramanian, Y. Anguchamy, S. Gong, A. Wibowo, H. Gao, H.J. Ploehn, H.C. Zur Loye, Polymer composite and nanocomposite dielectric materials for pulse power energy storage, 2009. doi:10.3390/ma2041697.

[30] H.C. Pant, M.K. Patra, A. Verma, S.R. Vadera, N. Kumar, Study of the dielectric properties of barium titanate-polymer composites, Acta Mater. 54 (2006) 3163–3169. doi:10.1016/j.actamat.2006.02.031.

[31] R.K. Goyal, V. V. Madav, P.R. Pakankar, S.P. Butee, Fabrication and properties of novel polyetheretherketone/ barium titanate composites with low dielectric loss, J. Electron. Mater. 40 (2011) 2240–2247. doi:10.1007/s11664-011-1743-5.

[32] Z. Yang, H. Peng, W. Wang, T. Liu, Crystallization behavior of poly(ε-caprolactone)/layered double hydroxide nanocomposites, J. Appl. Polym. Sci. 116 (2010) 2658–2667. doi:10.1002/app.

[33] S.F. Mendes, C.M. Costa, C. Caparros, V. Sencadas, S. Lanceros-Méndez, Effect of filler size and concentration on the structure and properties of poly(vinylidene fluoride)/BaTiO 3 nanocomposites, J. Mater. Sci. 47 (2012) 1378–1388. doi:10.1007/s10853-011-5916-7.

[34] H.I. Hsiang, K.Y. Lin, F.S. Yen, C.Y. Hwang, Effects of particle size of BaTiO3 powder on the dielectric properties of BaTiO3/polyvinylidene fluoride composites, J. Mater. Sci. 36 (2001) 3809–3815. doi:10.1023/A:1017946405447.

[35] S.W. Kim, H.R. Choi, C.S. Han, D. Bin Kim, J.W. Kim, Y.S. Cho, Dielectric and current-voltage characteristics of flexible Ag/BaTiO3 nanocomposite films processed at near room temperature, RSC Adv. 7 (2017) 56038–56043. doi:10.1039/c7ra11640c.

[36] Z.H. Jiang, W.D. Li, X. Yang, X. Chen, C. Wang, M.Y. Chen, G.J. Zhang, Low dielectric loss and high breakdown strength photosensitive high-k composites containing perfluoroalkylsilane treated BaTiO3 nanoparticles, Compos. Part B Eng. 192 (2020) 108013. doi:10.1016/j.compositesb.2020.108013.

[37] H.F. Castro, E. Sowade, J.G. Rocha, P. Alpuim, S. Lanceros-Méndez, R.R. Baumann, All-inkjet-printed bottom-gate thin-film transistors using UV curable dielectric for well-defined source-drain electrodes, J. Electron. Mater. 43 (2014) 2631–2636. doi:10.1007/s11664-014-3143-0.

[38] H.J. Kwon, X. Tang, S. Shin, J. Hong, W. Jeong, Y. Jo, T.K. An, J. Lee, S.H. Kim, Facile Photo-cross-linking System for Polymeric Gate Dielectric Materials toward Solution-Processed Organic Field-Effect Transistors: Role of a Cross-linker in Various Polymer Types, ACS Appl. Mater. Interfaces. 12 (2020) 30600–30615. doi:10.1021/acsami.0c04356.

[39] A. Chortos, E. Hajiesmaili, J. Morales, D.R. Clarke, J.A. Lewis, 3D Printing of Interdigitated Dielectric Elastomer Actuators, Adv. Funct. Mater. 30 (2020) 1–10. doi:10.1002/adfm.201907375.

[40] J.R. McGhee, T. Whittaker, J. Moriarty, J. Northedge, S. Zhang, D. Cadman, W. Whittow, J.Y. Vardaxoglou, Fabrication of Artificial Dielectrics via Stereolithography Based 3D-Printing, 14th Eur. Conf. Antennas Propagation, EuCAP 2020. (2020). doi:10.23919/EuCAP48036.2020.9135734.

[41] T. Nardi, M. Sangermano, Y. Leterrier, P. Allia, P. Tiberto, J.A.E. Månson, UV-cured transparent magnetic polymer nanocomposites, Polymer (Guildf). 54 (2013) 4472–4479. doi:10.1016/j.polymer.2013.06.052.

[42] E. Lizundia, A. Maceiras, J.L. Vilas, P. Martins, S. Lanceros-Mendez, Magnetic cellulose nanocrystal nanocomposites for the development of green functional materials, Carbohydr. Polym. 175 (2017) 425–432. doi:10.1016/j.carbpol.2017.08.024.

[43] M. Sangermano, G. Matucelli, E. Amerio, R. Bongiovanni, A. Priola, A. Di Gianni, B. Voit, G. Rizza, Preparation and characterization of nanostructured TiO2/epoxy polymeric films, Macromol. Mater. Eng. 291 (2006) 517–523. doi:10.1002/mame.200500420.

[44] P. Cardoso, J. Silva, D. Klosterman, J.A. Covas, F.W.J. van Hattum, R. Simoes, S. Lanceros-Mendez, The role of disorder on the AC and DC electrical conductivity of vapour grown carbon nanofibre/epoxy composites, Compos. Sci. Technol. 72 (2012) 243–247. doi:10.1016/j.compscitech.2011.11.008.

[45] J. Silva, S. Lanceros-Mendez, R. Simoes, Effect of cylindrical filler aggregation on the electrical conductivity of composites, Phys. Lett. Sect. A Gen. At. Solid State Phys. 378 (2014) 2985–2988. doi:10.1016/j.physleta.2014.08.011.

[46] E.S. Jang, S.B. Khan, J. Seo, Y.H. Nam, W.J. Choi, K. Akhtar, H. Han, Synthesis and characterization of novel UV-curable polyurethane-clay nanohybrid: Influence of organically modified layered silicates on the properties of polyurethane, Prog. Org. Coatings. 71 (2011) 36–42. doi:10.1016/j.porgcoat.2010.12.007.

[47] G. Trovati, E.A. Sanches, S.C. Neto, Y.P. Mascarenhas, G.O. Chierice,

Characterization of Polyurethane Resins by FTIR, TGA, and XRD, J. Appl. Polym. Sci. 115 (2010) 263–268. doi:10.1002/app.31096.

[48] R.W. Arcís, A. López-Macipe, M. Toledano, E. Osorio, R. Rodríguez-Clemente, J. Murtra, M.A. Fanovich, C.D. Pascual, Mechanical properties of visible light-cured resins reinforced with hydroxyapatite for dental restoration, Dent. Mater. 18 (2002) 49–57. doi:10.1016/S0109-5641(01)00019-7.

[49] A.A. Zandinejad, M. Atai, A. Pahlevan, The effect of ceramic and porous fillers on the mechanical properties of experimental dental composites, Dent. Mater. 22 (2006) 382–387. doi:10.1016/j.dental.2005.04.027.

[50] M. Rincón-Iglesias, E. Lizundia, S. Lanceros-Méndez, Water-Soluble Cellulose Derivatives as Suitable Matrices for Multifunctional Materials, Biomacromolecules. (2019). doi:10.1021/acs.biomac.9b00574.

[51] X. Cao, H. Dong, C.M. Li, New nanocomposite materials reinforced with flax cellulose nanocrystals in waterborne polyurethane, Biomacromolecules. 8 (2007) 899–904. doi:10.1021/bm0610368.

[52] P. Costa, J. Silva, V. Sencadas, R. Simoes, J.C. Viana, S. Lanceros-Méndez, Mechanical, electrical and electro-mechanical properties of thermoplastic elastomer styrene-butadiene-styrene/multiwall carbon nanotubes composites, J. Mater. Sci. 48 (2013) 1172–1179. doi:10.1007/s10853-012-6855-7.

[53] J.F. Capsal, C. Pousserot, E. Dantras, J. Dandurand, C. Lacabanne, Dynamic mechanical behaviour of polyamide 11/Barium titanate ferroelectric composites, Polymer (Guildf). 51 (2010) 5207–5211. doi:10.1016/j.polymer.2010.09.011.

[54] T. Trzepiecinski, M. Gromada, Characterization of mechanical properties of barium titanate ceramics with different grain sizes, Mater. Sci. Pol. 36 (2018) 151–156. doi:10.1515/msp-2018-0009.

[55] D.M. Correia, R. Sabater i Serra, J.A. Gómez Tejedor, V. de Zea Bermudez, A. Andrio Balado, J.M. Meseguer-Dueñas, J.L. Gomez Ribelles, S. Lanceros-Méndez, C.M. Costa, Ionic and conformational mobility in poly(vinylidene fluoride)/ionic liquid blends: Dielectric and electrical conductivity behavior, Polymer (Guildf). 143 (2018) 164–172. doi:10.1016/j.polymer.2018.04.019.

[56]   A.C. Lopes, C.M. Costa, R.S.I. Serra, I.C. Neves, J.L.G. Ribelles, S. Lanceros-Méndez, Dielectric relaxation, ac conductivity and electric modulus in poly(vinylidene fluoride)/NaY zeolite composites, Solid State Ionics. 235 (2013) 42–50. doi:10.1016/j.ssi.2013.01.013.

[57]   L. Gu, T. Li, Y. Xu, C. Sun, Z. Yang, D. Zhu, D. Chen, Effects of the particle size of BaTiO 3 fillers on fabrication and dielectric properties of BaTiO 3 /Polymer/Al films for capacitor energy-storage application, Materials (Basel). 12 (2019). doi:10.3390/ma12030439.

[58]   R.K. Goyal, S.S. Katkade, D.M. Mule, Dielectric, mechanical and thermal properties of polymer/BaTiO 3 composites for embedded capacitor, Compos. Part B Eng. 44 (2013) 128–132. doi:10.1016/j.compositesb.2012.06.019.

[59]   K. Suematsu, M. Arimura, N. Uchiyama, S. Saita, T. Makino, Synthesis of BaTiO3/polymer composite ink to improve the dielectric properties of thin films, Compos. Part B Eng. 104 (2016) 80–86. doi:10.1016/j.compositesb.2016.08.011.

[60]   Y. Bai, Z.Y. Cheng, V. Bharti, H.S. Xu, Q.M. Zhang, High-dielectric-constant ceramic-powder polymer composites, Appl. Phys. Lett. 76 (2000) 3804–3806. doi:10.1063/1.126787.

[61]   R.K. Goyal, A.B. Kulkarni, Electrical properties of novel three-phase polymer nanocomposites with a high dielectric constant, J. Phys. D. Appl. Phys. 45 (2012). doi:10.1088/0022-3727/45/46/465302.

[62]   D.J. Bergman, The dielectric constant of a composite material-A problem in classical physics, Phys. Rep. 43 (1978) 377–407. doi:10.1016/0370-1573(78)90009-1.

[63]   C.W. Nan, Comment on "Effective dielectric function of a random medium," Phys. Rev. B - Condens. Matter Mater. Phys. 63 (2001) 5–7. doi:10.1103/PhysRevB.63.176201.

[64]   T. Furukawa, K. Ishida, E. Fukada, Piezoelectric properties in the composite systems of polymers and PZT ceramics, J. Appl. Phys. 50 (1979) 4904–4912. doi:10.1063/1.325592.

[65]   N. Jayasundere, B. V. Smith, Dielectric constant for binary piezoelectric 0-3

composites, J. Appl. Phys. 73 (1993) 2462–2466. doi:10.1063/1.354057.

[66]   C. Kittel, Introduction to Solid State Physics, Eighth Edi, Phoenix, EEUU, 2005. doi:10.1021/ja01569a094.

[67]   G.F. Dionne, J.F. Fitzgerald, R.C. Aucoin, Dielectric constants of paraffin-wax-TiO2 mixtures, J. Appl. Phys. 47 (1976) 1708–1709. doi:10.1063/1.322753.

[68]   W.R. Tinga, W.A.G. Voss, D.F. Blossey, Generalized approach to multiphase dielectric mixture theory, J. Appl. Phys. 44 (1973) 3897–3902. doi:10.1063/1.1662868.

[69]   T. Yamada, T. Ueda, T. Kitayama, Piezoelectricity of a high-content lead zirconate titanate/polymer composite, J. Appl. Phys. 53 (1982) 4328–4332. doi:10.1063/1.331211.

[70]   Z. Ahmad, A. Prasad, K. Prasad, A comparative approach to predicting effective dielectric, piezoelectric and elastic properties of PZT/PVDF composites, Phys. B Condens. Matter. 404 (2009) 3637–3644. doi:10.1016/j.physb.2009.06.009.

[71]   S. Aldrich, Sigma Aldrich - Barium titanate (IV), materials datasheet 2019, (n.d.). https://www.sigmaaldrich.com/catalog/product/aldrich/467634?lang=es&region=ES (accessed November 20, 2019).

Chapter 4

Translucent dielectric photocurable materials

Polyurethane acrylate (PUA) composites with Indium Tin Oxide (ITO) are produced in order to tune morphology, optical, thermal, mechanical and dielectric properties. It is shown that ITO particles, compared to $BaTiO_3$ employed in chapter 3, allows the development of high dielectric constant materials with an optical transparency of 20% for the samples containing 10 wt% ITO content. The composite is used for developing capacitive sensors, showing the suitability of the UV curable materials for capacitive sensing applications.

4.1. Introduction

Modern society demands energy, infrastructures and solutions based on smart and multifunctional materials, in the scope of the Internet of Things (IoT) concept [1,2] explained in chapter 1 of this thesis. IoT is based on connectivity and needs responsive materials for the development of high-performance sensors and actuators [3].

New generations of those sensors and actuators are based on polymer composites [4] that can be fabricated by conventional techniques, such as solvent-casting or extrusion, but which are increasingly being produced by additive techniques, such as 3D printing, as they allow customized, low-cost, high-volume and large-area production as well as easy integration on devices [5,6].

In this scope, hyperbranched polymers (HBPs) such as polyurethane acrylate (PUA) are suitable materials for the preparation of polymer composites due to their physical and chemical properties, detailed in chapter 1 of this thesis and summarized in low viscosity, excellent photoreactivity, excellent mechanical properties, good adhesion, low melting viscosity, excellent abrasion resistance, high chemical stability and weatherability, environmental safety, biocompatibility, low swelling and high transparency. This makes PUA suitable for solvent-free printing technologies [7–10] and appropriate for a variety of applications such as coatings, adhesives, textiles and membranes [11] as well as for biomedical applications, ranging from microfluidics to tissue engineering [10].

In this scope, composites based on PUA have been used in antibacterial coatings and packaging. For antibacterial applications, polyurethane acrylate/zinc oxide (PUA/ZnO) films demonstrated excellent antibacterial activity, in particular for Escherichia coli. [11]. PUA composites with boron nitride (BN) were produced for sonar encapsulants, significantly improving both mechanical strength and long-term stability [12]. Furthermore, PUA films with surface-modified tetrapod zinc oxide whiskers (STZnO-W) were manufactured for packaging applications, the barrier and antibacterial properties of these films being enhanced with increasing STZnO-W content [13]. In addition, UV-curable polyurethane acrylate/surface-modified colloidal calcium carbonate (PUA/SCaCO$_3$) nanocomposites show excellent water resistance capacity [14].

With respect to the tailoring of electrical properties for electronic and coating applications, composites based on PUA and graphene have been developed with conductivity percolation

threshold below 0.5 wt.% [15], graphene derivatives, such as graphene oxide, have also allowed to improve thermal stability and mechanical properties of the polymer [16]. Multifunctionality has been explored also by producing PUA tricomposites with graphene oxide and titanium dioxide (TiO_2) as fillers, allowing electrical conductive and antibacterial coatings [17].

Thus, PUA polymer-based composites were rarely investigated for tuning optical and dielectric properties, which pay an essential role both in coating and electronic applications, including insulation and sensing as is commented in chapter 3. Huang H-C *et al.* investigated highly transparent UV-curable ZnO-acrylic nanocomposites. ZnO nanoparticles (4 nm diameter) were surface modified by employing 3-(trimethoxysilyl)propyl methacrylate (TPMA) to enable wettability of particles by the polymer matrix. The addition of ZnO nanoparticles also enhanced the dielectric constant of the nanocomposites values above 4 at frequencies ranging from 1 to 600 MHz in the samples containing 10 wt.% of ZnO nanoparticles. This samples also show a transparency near of 95 % in visible light wavelengths from 400 to 800 nm [18].

Further, Liao W *et al.* also employed ZnO particles to obtain high performance transparent UV-curable composites. In this case, poly(methylmethacrylate) grafted ZnO (ZnO-PMMA) particles were included in silicone-acrylate (SA) resin. ZnO-PMMA/SA composites presented higher UV-shielding efficiency and transmittance to visible light, improved thermal stability and lower dielectric loss. In particular, the addition of 0.05 wt.% of ZnO-PMMA can significantly improve the UV-shielding efficiency while maintaining high transmittance in visible light (88% at 650 nm). Moreover, the composite also shows high thermal stability and dielectric properties characterized by a dielectric constant between 3 and 2.7 at frequencies ranging from 10 to 10^6 Hz [19].

In this scope, tin-doped indium oxide, ITO, nanoparticles seem a suitable option due to their semiconductor properties and high transmittance in the visible region. In fact, it has been proven that PUA composites with ITO particles show high transparency in the visible light and can be applied as UV/IR shielding [20]. However, up to our knowledge, not investigations have been carried out using UV curable materials and ITO particles for tuning both optical and dielectric properties.

In this work, the influence of ITO content on the photopolymerization process, morphology, optical, chemical, thermal, mechanical and dielectric properties of PUA based composites have been evaluated. Further, the use of the developed material as capacitive sensor has been demonstrated.

4.2. Experimental

4.2.1. Materials

A commercial photoresin based on polyurethane acrylate (PUA) named SPOT-ETM from SPOT-A Materials ® was used as UV curable matrix. For the preparation of the nanocomposite thin films, indium tin oxide (ITO) nanoparticles from SkySpring Nanomaterials, Inc were selected. This blue powder has a purity of 99.99%, a size of 20-70 nm and a density of 7.12 g/cm^3. As a sample cleaner, 2-propanol from Alfa Aesar ® with a purity of 99.5% was used. All materials were used as received.

4.2.2. Samples preparation

Different quantities of ITO nanoparticles were mixed with the corresponding volume of the photopolymerizable resin to obtain 0, 1, 5, 10, 20 and 25 wt.% ITO content samples. To achieve a good dispersion of ITO nanoparticles into the resin, the different mixtures were placed in an ultrasound bath (ATU® ATM series Model ATM3L) during 3 h at a temperature of 30 ºC. Then, samples were magnetically stirred for 2 h at room temperature. After the complete dispersion, flexible/bendable films were formed using doctor blade technique on a clean glass substrate. Samples were then cured at room temperature for 90 seconds with a UV curing chamber UVACUBE 400 from Honle UV America, Inc., equipped with a mercury lamp that provides an irradiance of 1000 W/m^2 on the floor of the chamber. Flexible films were separated from the glass, washed with 2-propanol for 5 minutes, dried, and finally stored at room temperature without illumination for future characterization. The thickness of the samples was around 200 μm, determined with a Powerfix® electronic digital calliper. The schematic representation of the preparation process of PUA and ITO/PUA composite films is shown in **Figure 4.1**.
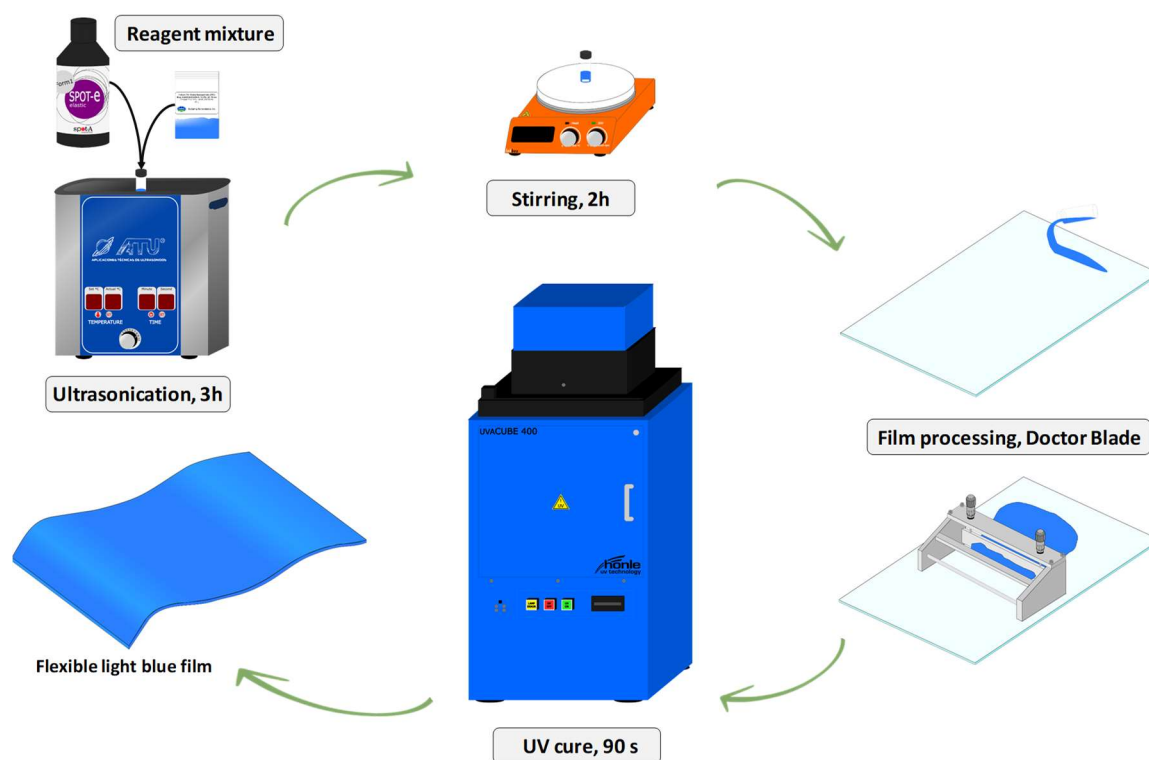
Figure 4.1 – Schematic representation of the preparation of the PUA and ITO/PUA composite films.

4.2.3. Samples characterization

The photopolymerization process of the ITO/PUA nanocomposites was characterized by photo-differential scanning calorimetry (photo-DSC) using a DSC 2920 Modulated DSC equipped with a differential photocalorimetry accessory from TA Instruments ®. Samples were illuminated in air at room temperature for 5 minutes and the heat flow was monitored over time, normalizing then the DSC curves by the weight of the liquid photoresin.

The conversion degree of the C=C double bonds (α) was calculated according to equation (4.1) [21]:

$$\alpha = \frac{\Delta H_t}{\Delta H_0^{theor}} \tag{4.1}$$

where ΔH_t is the reaction enthalpy at time t (obtained by integrating the area under the peak of the DSC curves), and ΔH_0^{theor} is the theoretical enthalpy for the total conversion. The final value of the enthalpy after the complete UV curing process of the pure resin was considered as the theoretical enthalpy [22].

The photopolymerization rate (R_p) was obtained using equation (4.2):

$$R_p = \frac{d\alpha}{dt} = \frac{dH/dt}{\Delta H_0^{theor}} \tag{4.2}$$

where the maximum photopolymerization rate (R_p^{max}) and the corresponding time spent to reach the R_p^{max} (t^{max}) were obtained.

Scanning Electron Microscopy (SEM) was used to study the ITO nanoparticles dispersion within the PUA films. Cross-section images of the cold fractured samples were obtained with a Hitachi S-4800 microscope at an accelerating voltage of 10 kV with a magnification of 5000×.

Possible interactions between the nanoparticles and the polymer were evaluated by Fourier transformed infrared spectroscopy in the total attenuated reflection mode (FTIR-ATR). A Nexus FTIR Nicolet spectrophotometer was used in the spectral range from 4000 to 400 cm^{-1} with a spectral resolution of 4 cm^{-1} and 64 scans.

Thermal behaviour of the samples was evaluated by thermogravimetric analysis (TGA) in a Mettler Toledo TGA/SDTA851 instrument. Measurements were performed from room temperature to 800 ºC at heating rate of 10 ºC/min under air atmosphere. For each sample, the degradation temperature (T_{deg}) and the temperature of the maximum degradation rate (T_{max}), calculated from the first derivative peak, were obtained. In addition, the glass transition temperature (T_g) of the ITO/PUA samples was evaluated by differential scanning calorimetry (DSC), determined in two successive scans under nitrogen atmosphere from -50 to 250 ºC at 20 ºC/min in the first case and from -50 to 150 ºC at 20 ºC/min in the second scan. Measurements were carried out using a DSC 822e from Mettler Toledo. The glass transition temperature was calculated as the extrapolated onset of the baseline shift.

Optical properties of the neat PUA and the ITO/PUA samples were evaluated by ultraviolet−visible (UV−vis) spectroscopy measurements. An Agilent Cary 60 UV/vis spectrophotometer was used in the range of 200−800 nm with a sampling interval of 1 nm and 25 accumulations.

Mechanical properties were studied using a TST350 set-up from Linkam Scientific Instruments in the tensile mode. Stain-stress tensile experiments were performed at room temperature at velocity of 3 μm/min in samples with dimensions of 30 mm x 10 mm and an

average thickness of 200 μm. Secant modulus (E), obtained by calculating the slope of the linear region, maximum stress (σ_b) and strain at break (ε_b) were determined for neat PUA and for the ITO/PUA samples, reporting the mean average values and the standard deviation over 3 specimens.

Dielectric response was characterized using a Quadtech 1920 LCR precision meter. A parallel plate condenser was prepared by depositing 5 mm diameter circular gold electrodes on both sides of each sample with a Quorum Q150T SC502 sputter coater. The capacity (C) and dielectric losses (tan δ) were measured at room temperature in a frequency range from 100 Hz to 1 MHz at an applied voltage of 0.5 V. The dielectric constant (ε') and tan δ were calculated applying equations (4.3) and (4.4), respectively:

$$\varepsilon' = \frac{C \cdot d}{\varepsilon_0 \cdot A} \tag{4.3}$$

$$\tan \delta = \frac{\varepsilon''}{\varepsilon'} \tag{4.4}$$

where C is the measured capacity, A is the area of the gold electrodes, d is the thickness of the sample and ε'' is the imaginary part of the dielectric constant.

The a.c. electrical conductivity (σ') was determined after equation (4.5):

$$\sigma' = \varepsilon_0 \cdot \omega \cdot \varepsilon' \cdot \tan \delta \tag{4.5}$$

where ε_0 is the dielectric permittivity of vacuum (8.85 x 10^{12} F/m) and $\omega = 2\pi\upsilon$ is the angular frequency.

4.3. Results and discussion

4.3.1. UV curing process

Figure 4.2a shows the UV curing degree of conversion (α) as a function of time, while in **Figure 4.2b** the photopolymerization rate (R_p) is represented. **Table 4.1** summarizes the characteristic values α, R_p^{max} and t_{max} obtained from **Figure 4.2**.
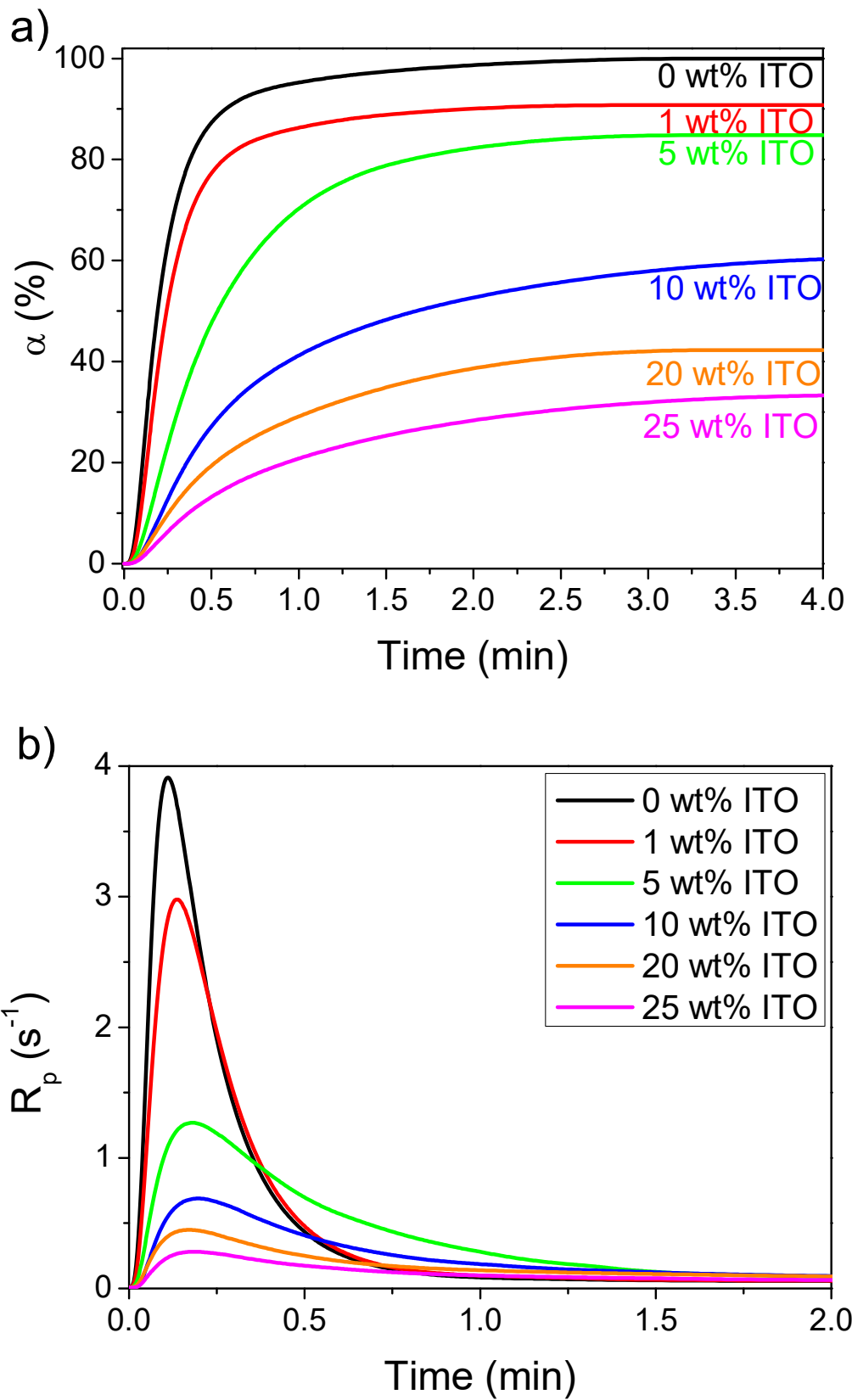
a)

b)

Figure 4.2 – Curing conversion (α) of neat PUA and the prepared composites (a), and the corresponding photopolymerization rate (R_p) (b).

Table 4.1 – UV curing parameters of PUA resin and the prepared composites.

Sample	α (%)	R_p^{max} (s⁻¹)	t^{max} (s)
0 wt.%	100	3.9	6.6 ± 0.3
1 wt.%	90	3.0	8.2 ± 0.4
5 wt.%	82	1.2	10.6 ± 0.3
10 wt.%	61	0.7	11.0 ± 0.5
20 wt.%	40	0.4	10.2 ± 0.7
25 wt.%	33	0.2	10.6 ± 0.6

Figure 4.2a show that an increase in ITO content produces a considerable decrease on the conversion degree, changing from 100 % for neat PUA to 82 % for the same samples with 5 wt.% ITO content and to 33 % for the 25 wt.% ITO loaded sample. Further, the photopolymerization rate strongly decreases due to the ITO incorporation, varying from 3.9 s⁻¹ to 1.2 s⁻¹ and to 0.2 s⁻¹ for the same samples. In addition, t_{max} increases rapidly for samples with less ITO content and remains stable for the samples with higher filler content (from 6.6 s for 0 wt.% sample to 10.6 s for 5 wt.% sample and the same value for 25 wt.% sample).

The C=C double bond conversion is influenced by the UV light absorption capacity of the liquid curable material. The final degree of polymerization, as well as R_p and the curing time, will be determined by the chemical structure and functionality of the oligomers and photoinitiator [23]. In addition, viscosity has an important role in the curing process as it increases rapidly during the liquid to solid phase change and, therefore, delays the polymerization. Also, it is affected by the addition of fillers [24]. These additives can absorb also the UV light and strongly competes with the light adsorption needed for the photoinitiator [22].

Thus, increasing ITO content lead to a reduction of the polymerization rate and the degree of conversion is reduced due to the absorption of UV radiation by the ITO nanoparticles [20] in the 350-500 nm range [25], the same region that the light absorption by the photoinitiator occurs. This absorption competes with the UV light absorption by the photoinitiator and therefore, less initiating radicals are produced, reducing the final conversion [20,26]. Furthermore, the addition of ITO increases the viscosity of the liquid material [21] and, thus,

when photopolymerization starts, the material becomes more rigid rapidly due to the further increase of the viscosity, leading the high decrease of R_p with ITO content increase, leasing to an increase in t_{max}.

4.3.2. Morphological, optical and chemical characteristics

The dispersion of the ITO nanoparticles within the PUA matrix has been evaluated by the SEM images of the cold fractured cross-section of the samples, presented in **Figure 4.3**.
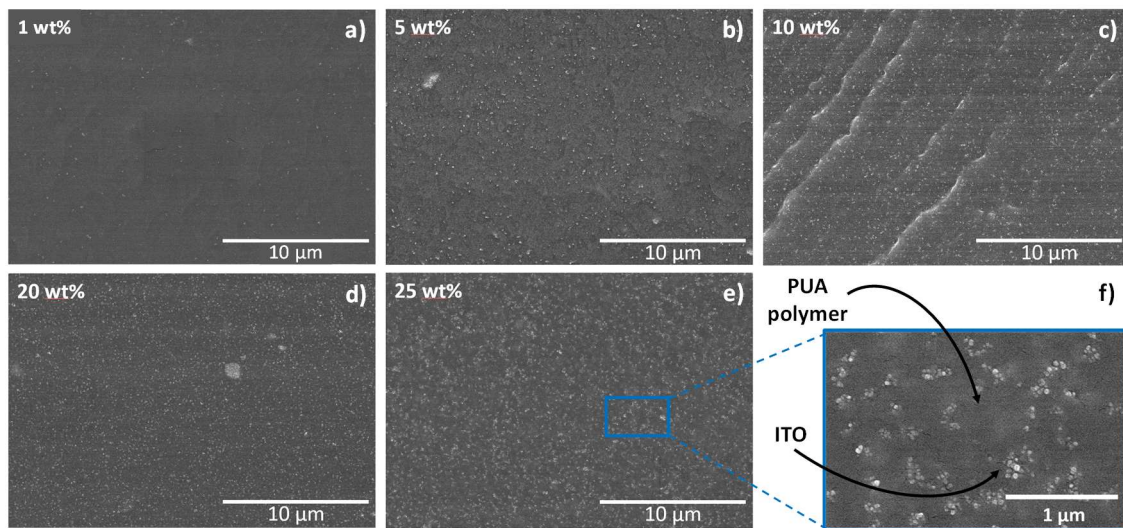

Figure 4.3 – SEM images of the ITO/PUA composites at magnifications of 5,000× (a to e) and 20,000× (f).

Particle dispersion within the polymer matrix has a significant influence on the electrical [27] and mechanical properties [28] of the composites. Thus, suitable filler dispersion is desirable. As reported in other ITO/polymer composites [20], ITO distribution can be identified as ITO nanoparticles appear as white dots in the SEM images. This dots concentration (**Figure 4.3**) increases as the filler content increases from 1 wt.% up to 25 wt.% and no large agglomerates or voids of ITO nanoparticles within the PUA matrix is observed, indicating good filler distribution and wettability of the filler by the polymer (**Figure 4.3f**). Only in the case of the sample with maximum filler concentration (**Figure 4.3e and f**) small nanoparticle agglomerates are appreciated.

It is to notice that mechanical and electrical properties can be affected by the existence of agglomerates [29], sometimes being better a suitable distribution of small agglomerates or cluster than well nanoparticles dispersion, in order to improve the electrical response [30].

In this context, the obtained filler dispersion even at 25 wt.% content is good enough to maintain suitable mechanical properties while strongly improving the dielectric response of the composites (see below).

The optical transmittance of the pristine photoresin and the prepared ITO/PUA composite films within the wavelength (λ) range from 200 to 800 nm is represented in **Figure 4.4a**. The optical transmittance value at 550 nm as a function of ITO nanoparticle concentration is represented in **Figure 4.4b**. Flexibility and transparency of the prepared films (10 wt.% ITO content sample) are shown in the inset image of **Figure 4.4b**.

The absorption mechanism of polymer composite films depends on the incident radiation wavelength and on the filler content [28]. According with the ASTM D1746-15 standar, Standard Test Method for Transparency of Plastic Sheeting [28], the ultraviolet-visible (UV/Vis) transmittance spectra of neat PUA and ITO/PUA composites has been evaluated in the 540 to 560 nm wavelength range. As it can be observed in **Figure 4.4a**, PUA polymer show a transparency about 85 %. Optical transparency decreases exponentially with increasing ITO content, being about 50 % for the 1 wt.% ITO content sample, 30 % for the 5 wt.% ITO content sample and 13 % for the 10 wt.% sample. The minimum transparency value is obtained for the samples with the highest ITO content: about 8 % for the 20 wt.% ITO content sample and 1 % for the 25 wt.% sample.

This decrease in optical transparency is due to increasing light scattering in the ITO/PUA nanocomposite films [31], associated to the difference of refractive index between the PUA (1.5-1.6) [32] and ITO nanoparticles (1.8-1.9) [33,34], as well as for the increase polyurethane acrylate-to-ITO nanoparticles interfacial region [28]. Moreover, optical transparency decreases due to the light absorption of ITO nanoparticles in the UV/Vis region, particularly in the 350-500 nm spectral region [25].

Attending to the trend of the optical transmittance as a function of ITO content shown in **Figure 4.4b**, the experimental results were fitted with the Beer-Lambert law. The fitting results gives an α absorption coefficient around 10 cm^{-1}, in good agreement with related polymer nanocomposite films [35]. The increase of ITO nanoparticle content promotes an exponential decrease on the transmittance signal, the obtained composite films keeping flexible and partially translucent for filler concentrations up to 10 wt.% (**Figure 4.4b inset**).
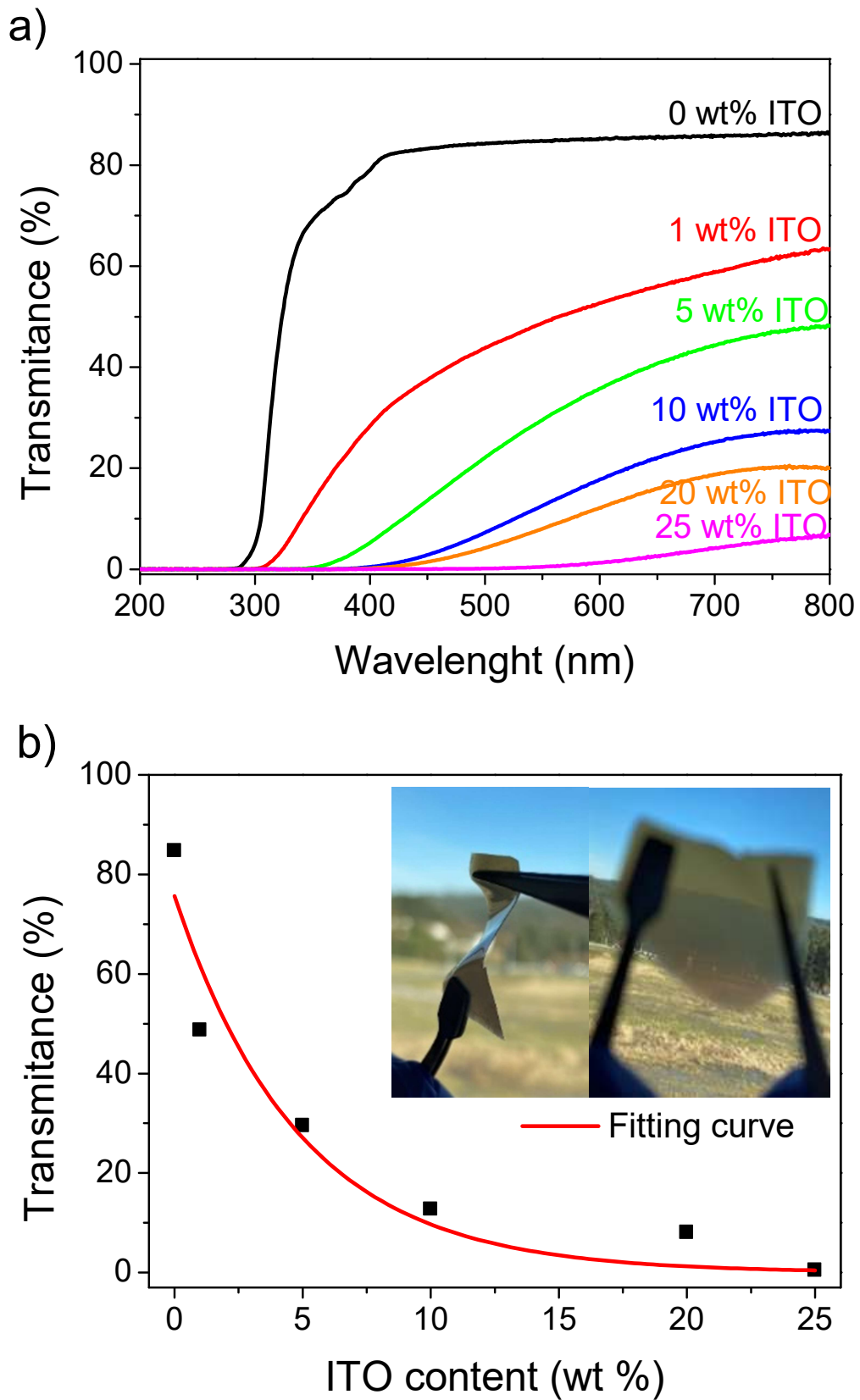
Figure 4.4 – UV/Vis transmittance for neat PUA and ITO/PUA composite films as a function of wavelength (a). Transmittance at $\lambda = 550$ nm as a function of ITO nanoparticle content (b). Flexible and translucent film with 10 wt.% ITO content (inset).

Fourier transformed infrared spectroscopy (FTIR) allows the evaluation of the possible physical-chemical interactions between the ITO nanoparticles and the PUA polymeric matrix. **Figure 4.5** shows the FTIR spectra of PUA photoresin and the prepared composites in the range of 4000 to 600 cm^{-1}. The resulting polymer films obtained after the UV curing process show the characteristic peaks for polyurethane acrylate polymer: N-H stretching band at 3300-3400 cm^{-1}, CH$_2$ and CH$_3$ stretching between 2855-2955 cm^{-1}, C=O stretching at 1725 cm^{-1}, combined stretching of N-H and the C-N band of the polyurethane group at 1550 cm^{-1}, C-N stretching band at 1360 cm^{-1} and the C-O-C stretching band at 1110 cm^{-1} [36].
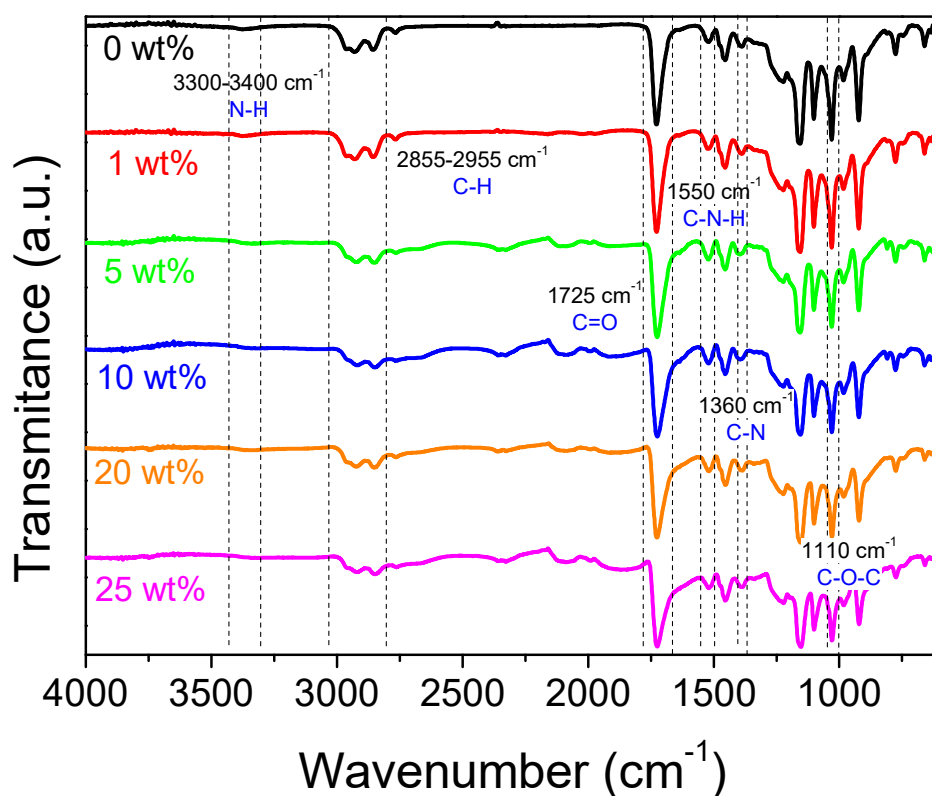

Figure 4.5 – Fourier Transformed Infrared (FTIR) spectra for neat PUA resin and for the ITO/PUA composites.

All obtained spectra are similar to the neat polymer –no new bands appear or band displacements are observed– indicating that no intermolecular interactions occur between the ITO nanoparticles and the polymer.

4.3.3. Thermal and mechanical properties

Thermogravimetric analysis (TGA) and Differential Scanning Calorimetry (DSC) have been employed to study the thermal properties of the composites. Variations on the thermal degradation and glass transition temperatures as a function of ITO nanoparticle content are studied. **Figures 4.6a and b** show the corresponding TGA and DTG curves, respectively, for pristine PUA and ITO/PUA composites with different nanoparticle content up to 25 wt.%, while **Figures 4.6c and d** represent the 1st and 2nd DSC scan thermograms, respectively, for the same samples.

Figures 4.6a and b show that the thermal degradation of pristine PUA films occurs in four steps. The first step, indicated in **Figure 4.6a**, occurs in the range 160 to 280 ºC and is attributed to the evaporation of residual monomers of the films. The second degradation step, observed in the 280-400 ºC range, is related with the decomposition of the main polyurethane chains of the polymer films. Finally, the third and the fourth steps are assigned to the combustion of carbonaceous residues [36–38].

Similar profiles with the same degradation steps are observed for all the composite samples independently of the ITO content. However, small differences are observed in **Figure 4.6b** related to the initial degradation temperature of the different processes. A slight decrease on the thermal stability of the composites with respect to the neat polymer is observed which increases with ITO filler content. This behaviour, observed for other UV curable composites [39], is related to the differences in the UV curing process. As previously indicated, the presence of ITO hinders the curing process and leads to lower degree of crosslinking. It is to notice that ITO nanoparticles do not suffer degradation in the studied temperature range, which is confirmed by the obtained residual mass after degradation in good agreement with the amount of ITO in each sample.

DSC thermograms presented in **Figures 4.6c and d** demonstrate a similar thermal behaviour for neat PUA and ITO/PUA composites, characterized by a glass transition around room temperature. As **Figure 4.6c** shows, the glass transition temperature (T_g) slightly increases when ITO nanoparticle content increases, being 25 ºC for the pristine photoresin and 27ºC for the 25 wt.% ITO content sample. Further, not exothermic peak is observed indicating that no post-curing process occurs. The added ITO nanoparticles lead to changes in the photopolymerization process and, as a consequence, the kinetics of the glass transition.
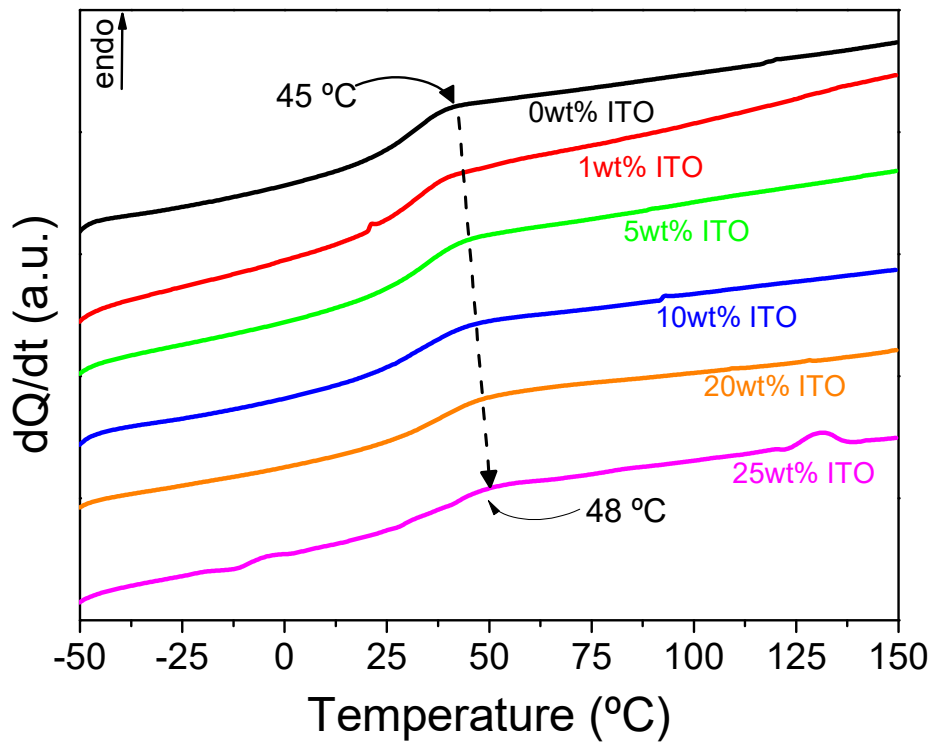
a)

b)
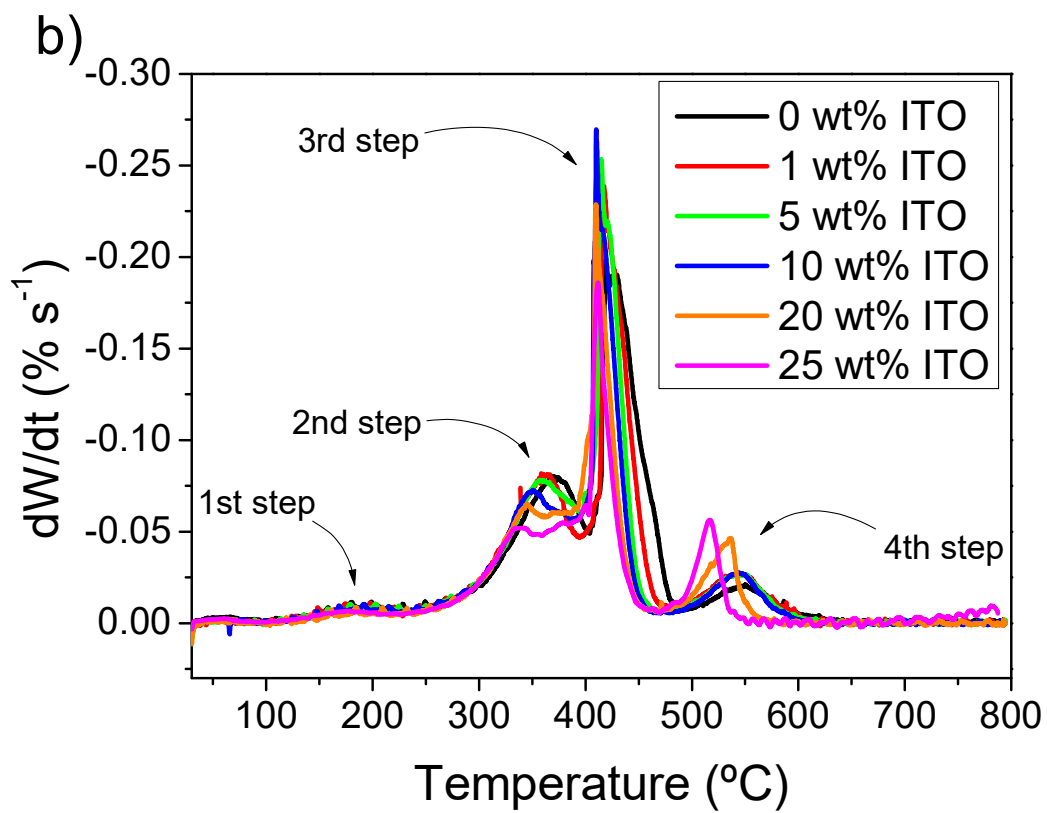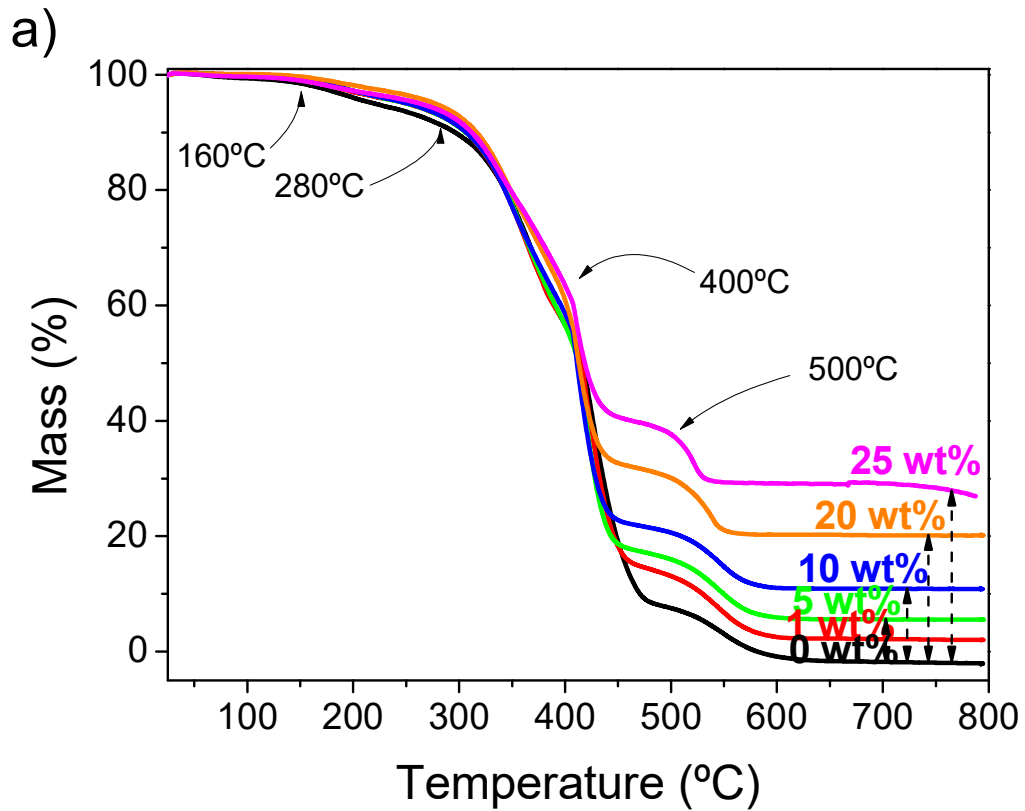
c)
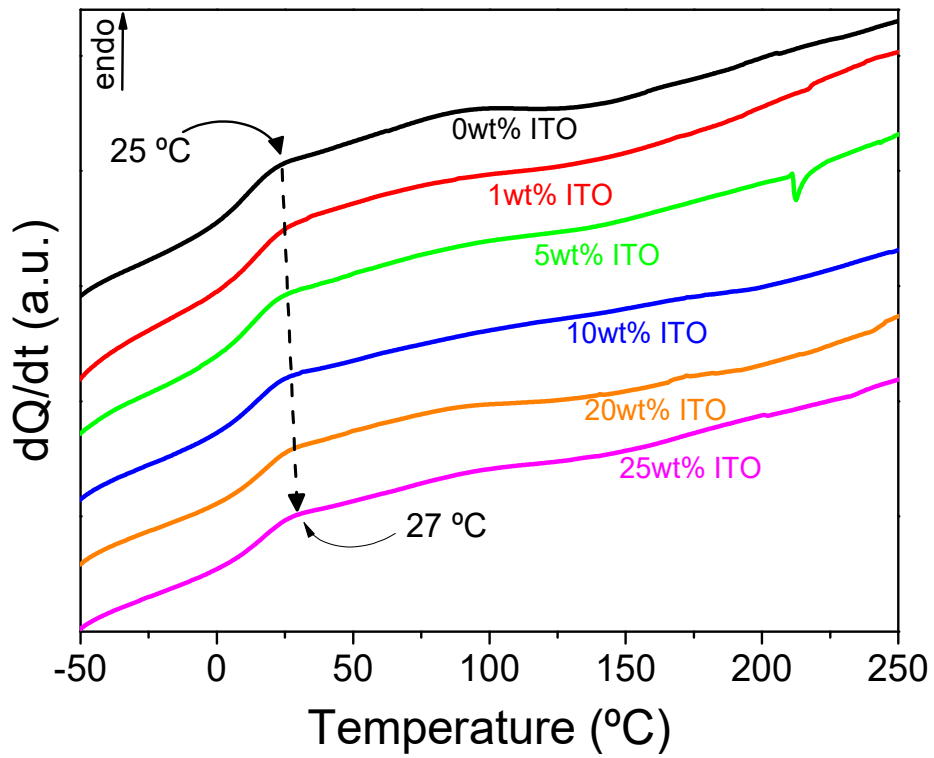
d)

Figure 4.6 – Thermogravimetric (a) and differential thermogravimetric results (b); and differential scanning calorimetry (DSC) thermogram in the first scan (c) and second scan (d) for pristine PUA films and composites with different ITO nanoparticle contents.

Attending to the FTIR evaluation (**Figure 4.4**), physical interactions between the PUA polymer and the dispersed nanoparticles occurs, restricting the segmental motion of polymer chains and, therefore, T_g slightly increases [36]. However, the observed differences in T_g are small and can be considered within the experimental error range.

After the heating process, an increase on the T_g of the UV curable polymer can be observed in **Figure 4.6d**, being 25 ºC for neat PUA in the 1st scan and 45 ºC in the 2nd scan. T_g of the samples with different ITO content increases in the same way. For the sample with 25wt.% ITO content, T_g increases from 27 ºC in the 1st scan to 48 ºC in the 2nd DSC scan. This increase, as observed in related UV curable polymeric composites [22], is because the samples, after heating process, undergo the same thermal treatment and, therefore, reach the same polymeric structural relaxations with a similar final T_g.

The effect of ITO nanoparticles on the mechanical properties of ITO/PUA composites has been examined (**Figure 4.7**). The average secant modulus (E), strain (ε_b) and stress (σ_b) at break presented in **Table 4.2** were calculated by evaluating the results of the multiple (triplicate for each sample) uniaxial stress-strain tests. **Figure 4.7a** depicts representative curves for neat PUA and the ITO/PUA composites, while **Figure 4.7b** shows the evolution of E and ε_b as a function of ITO content.

Polyurethane acrylate photoresin stress-strain curve is shown in **Figure 4.7a**. Its secant modulus yields a value of 5.82 ± 0.12 MPa. At higher strains, the stress increases nearly linearly with the strain up to the breaking of the film at ε_b of 40.4 ± 3.5 % and σ_b of 2.05 ± 0.24 MPa [40]. When ITO nanoparticles are added, the modulus decreases and just in the case of the samples with more than 10 wt.% ITO content an increase of E can be observed. Thus, an E value of 8.48 ± 0.36 MPa for the sample with 25 wt.% is obtained, as observed in **Figure 4.7b**. Hence, it is demonstrated that ITO nanoparticles firstly act as a defects on the polymer matrix and then, as also observed for fillers such as barium titanate nanoparticles or multiwalled carbon nanotubes [41,42], act as mechanical reinforcement due to the high modulus of the inorganic component compared to the organic one as well as due to the good ITO dispersion and homogeneous morphology [40]. In addition, it has to be mentioned that the secant modulus increases exponentially with ITO content (**Figure 4.7b**), as has been observed in related polyurethane acrylate reinforced with cellulose nanocrystals [40].
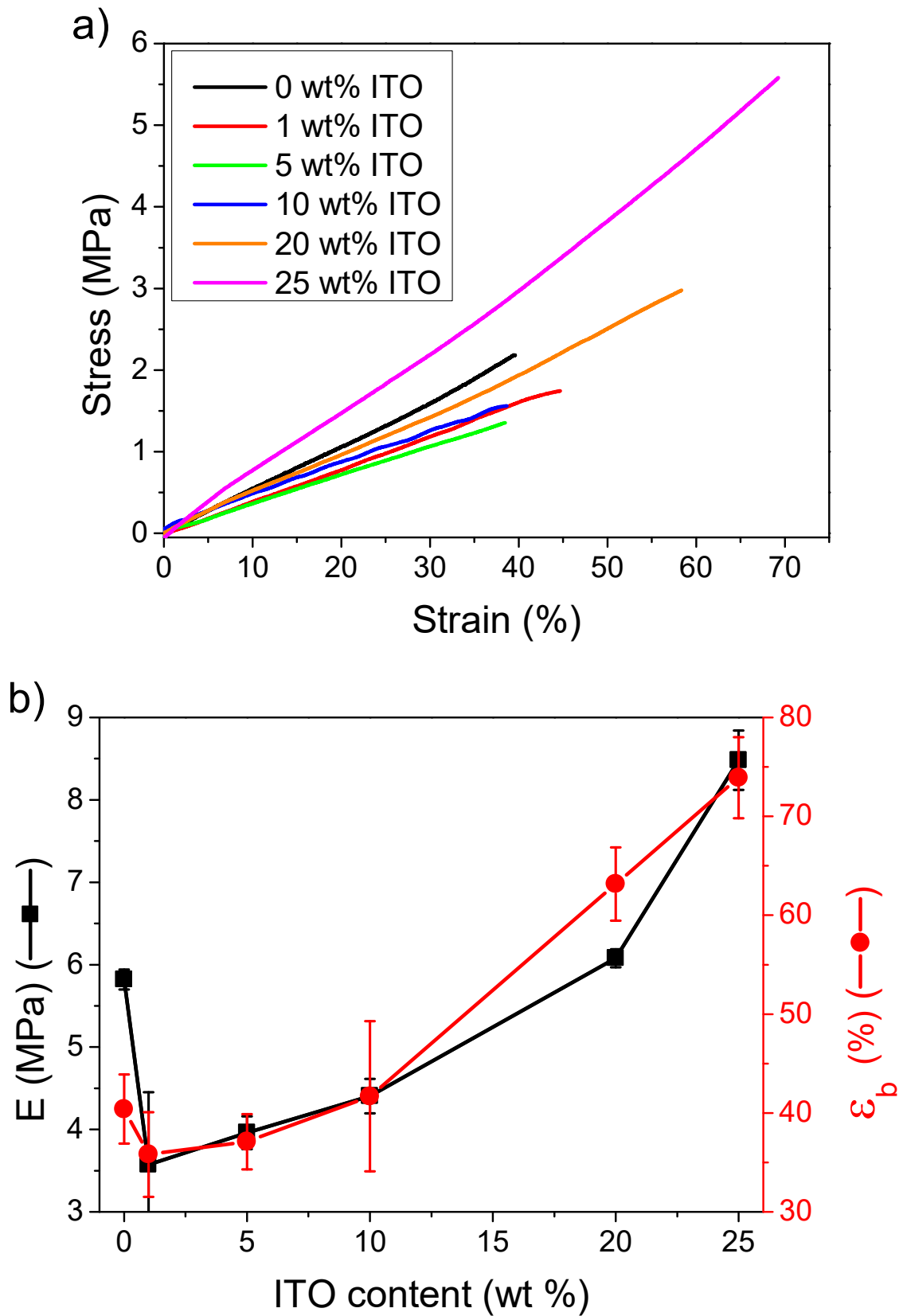
Figure 4.7. Representative stress–strain characteristic curves for pristine PUA and the ITO composites (a) and secant modulus and stress at break for the same samples (b).

Table 4.2 – Main mechanical parameters obtained from the uniaxial stress-strain tests for the prepared nanocomposites: E (initial modulus), σ_b (stress at break); ε_b (strain at break).

Sample	E (MPa)	ε_b (%)	σ_b (MPa)
0 wt.%	5.82 ± 0.12	40.4 ± 3.5	2.05 ± 0.24
1 wt.%	3.57 ± 0.88	35.8 ± 4.27	1.19 ± 0.22
5 wt.%	3.96 ± 0.20	37.1 ± 2.8	1.26 ± 0.06
10 wt.%	4.41 ± 0.21	41.7 ± 7.6	1.38 ± 0.18
20 wt.%	6.08 ± 0.11	63.2 ± 3.7	3.38 ± 0.52
25 wt.%	8.48 ± 0.36	73.9 ± 4.1	4.79 ± 0.68

Interestingly, the addition of ITO nanoparticles does not decrease the maximum elongation of the material as typically observed for other polymer composites [22], where the presence of fillers induces an early fracture as they act as breaking points on the polymer due to stress accumulation [29]. In this case, low amounts of nanoparticles result in increased elongation at break which increases further as nanoparticles amount increases being 40.4 ± 3.5 % for neat polymer and 73.9 ± 4.1 for 25 wt.% ITO content sample. Stress at break also follows the same trend and higher stress is needed to break sample when ITO nanoparticle content increases (from 2.05 ± 0.24 MPa for pristine photoresin to 4.79 ± 0.68 for the sample with highest ITO content).

Polyurethane acrylates are elastomers, usually amorphous, with flexibility and mobility provided by the relatively long and entangled polymeric chains [43]. These entanglements or crosslinks can be chemical or physical linkages that are distantly connected in the polymer network structure and provides elasticity, allowing the chains to stretch long distance [43]. When fillers are added, interactions between particles and between particles and matrix restrict the segmental motion of the polymer chains [40], as it has been observed in the DSC results (**Figure 4.6**) for the inclusion of ITO nanoparticles, resulting in a decrease of maximum elongation (**Table 4.2**). However, attending to the photopolymerization results (**Figure 4.2**), when ITO nanoparticles content increases the final conversion as well as the photocrosslinking degree decreases. Theoretically, a lower degree of crosslinking on the obtained material results in a high chain mobility and, as a consequence, high elongation [44]. In this case, the mentioned effects offset each other and the mechanical properties of the obtained composites are not strongly affected by the inclusion of ITO nanoparticles.

Interestingly, all film samples present bending ability (see **Figure 4.4b inset**) and they not become fragile with increasing filler content, making them suitable materials for flexible applications.

4.3.4. Electrical properties

The dielectric constant (ε'), dielectric losses (tan δ) and electrical conductivity (σ') of the samples are presented in **Figure 4.8**. **Figure 4.8a** shows the frequency dependence of the room temperature dielectric constant for the different ITO/PUA composites, while **Figure 4.8b** shows the dielectric constant of the samples at 1 kHz. Regardless of ITO content, **Figure 4.8a** shows that the dielectric constant is frequency dependent, decreasing with increasing frequency due to slow dipole relaxation [45]. This frequency dependence is not observed for tan δ (**Figure 4.8c**) where the value just slightly increases when frequency increases (except for 25 wt.% ITO content sample that presents a minimum).

In addition, regardless of the frequency, the dielectric constant increases with increasing ITO filler content (**Figure 4.8a**) due to increase of the interface polarization effects (Maxwell–Wagner–Sillars (MWS) effect) in which the ITO filler-polymer interfaces hinder carrier transport, increasing charge trapping at the interfaces and local ionic conductivity [46,47]. The high dielectric constant for the composite with 25 wt.% ITO content is due the fact that ITO nanoparticles form local microcapacitors as well as from contributions of localized charge dynamics [48].

In addition, **Figure 4.8c** for the composite with 25wt.% of ITO filler content shows a high tan δ value independently of the applied frequency, which is mainly related to the interfacial polarization and localized charge dynamics caused by the higher ITO content [45].

Figure 4.8d shows the electrical conductivity at room temperature of the ITO/PUA composites as a function of frequency. Regardless of the ITO amount, the electrical conductivity increases with increasing frequency due to charge carrier mobility at localized states. Also, for 25wt.% of ITO filler content, it is observed an overall increase of a.c. conductivity due the increase of charge carriers, most provably due to the larger surface area and defective interfaces.
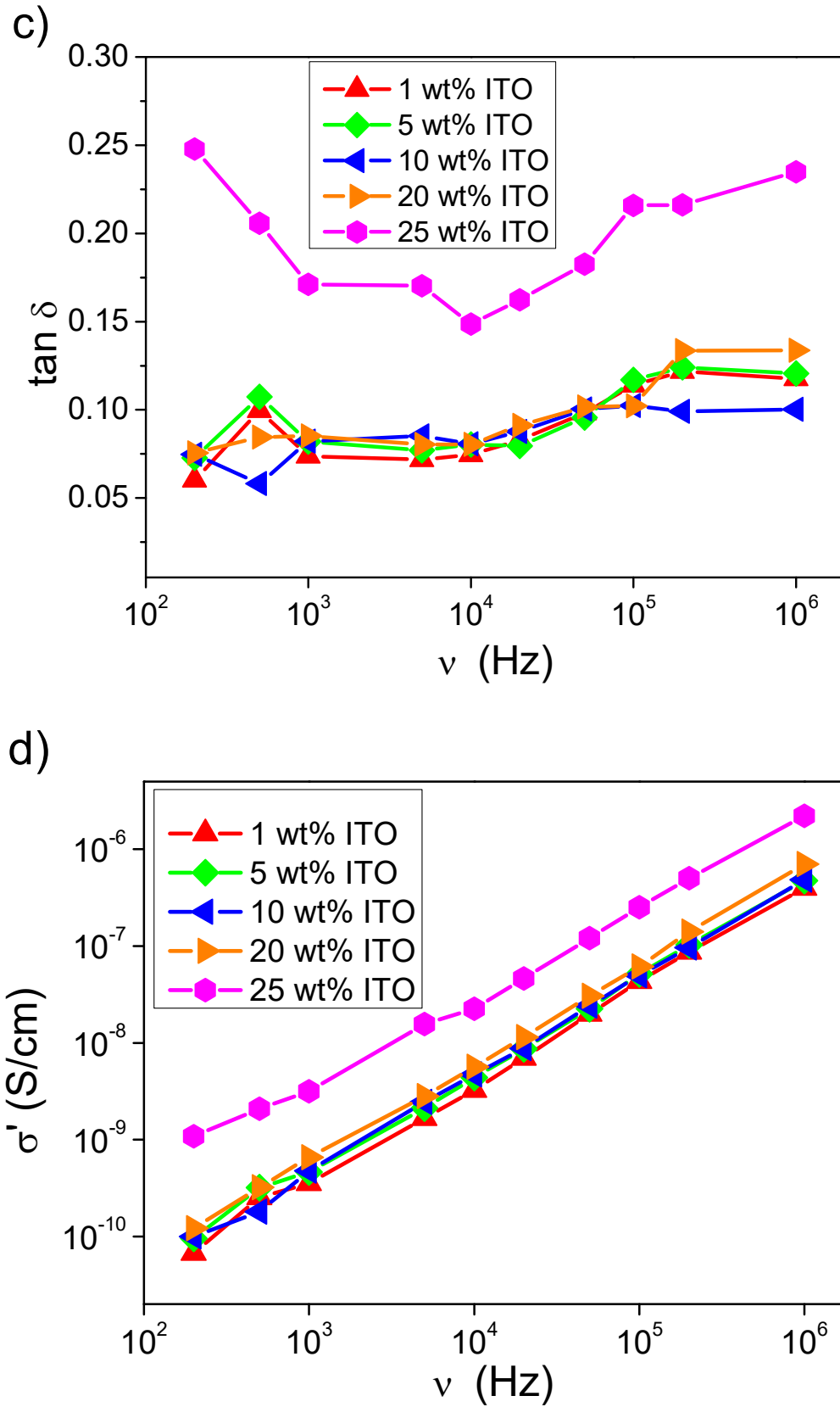
a)

b)
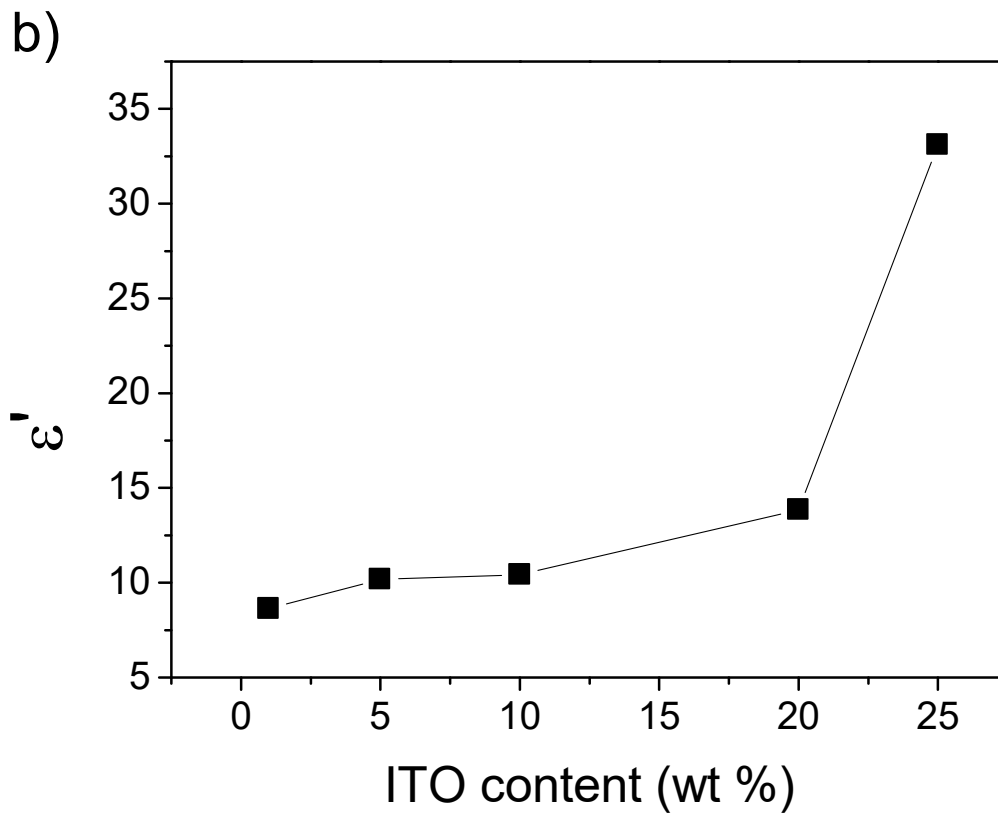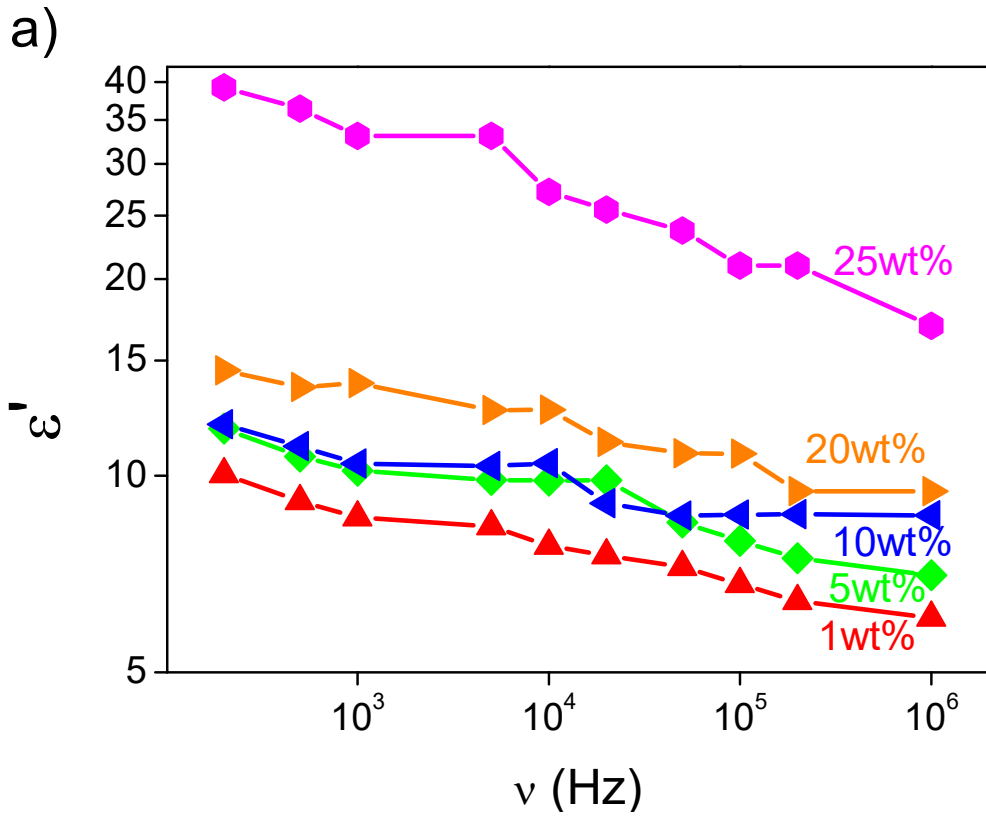
Figure 4.8 – Room temperature dielectric constant as a function of frequency (a) and ITO content at 1 kHz (b) for neat PUA and the prepared composites. Tan δ values (c) and electrical conductivity (d) as a function of frequency for the same samples.

4.3.5. Implementation of a capacitive sensor

Due to the high dielectric constant, optical transmittance and flexibility, the prepared samples can be used for capacitive sensing applications, as demonstrated in **Figure 4.9a** for the sample with 25 wt.% ITO content. The electrical system is composed by a microcontroller (Microchip ATmega328P working at a frequency of 16 MHz) connected to a computer via Universal Serial Bus (USB) and a red LED used as indicator for touch detection on the sensor.

The sample was connected to the circuit by two strips of aluminum foil glued to the electrodes by electric paint (Bare Conductive). The sample was properly isolated with adhesive tape to prevent the finger from touching the electrodes directly.

The electrical circuit (**Figure 4.9a**) of the system consisted in a high value resistor of 10 MΩ, and two pins connected to a microcontroller, one acting as source signal and another as a sensing pin. The sensor was composed by two electrodes. These two electrodes create a very small capacitance, which increases when a finger is placed nearby.
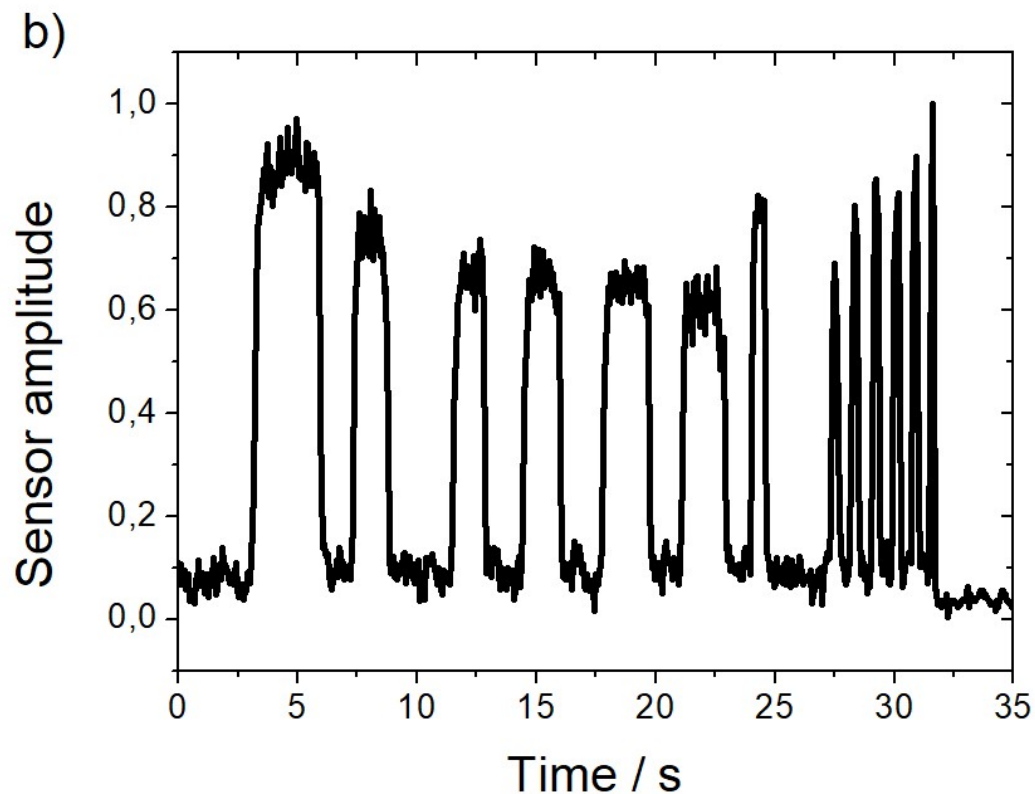
b)
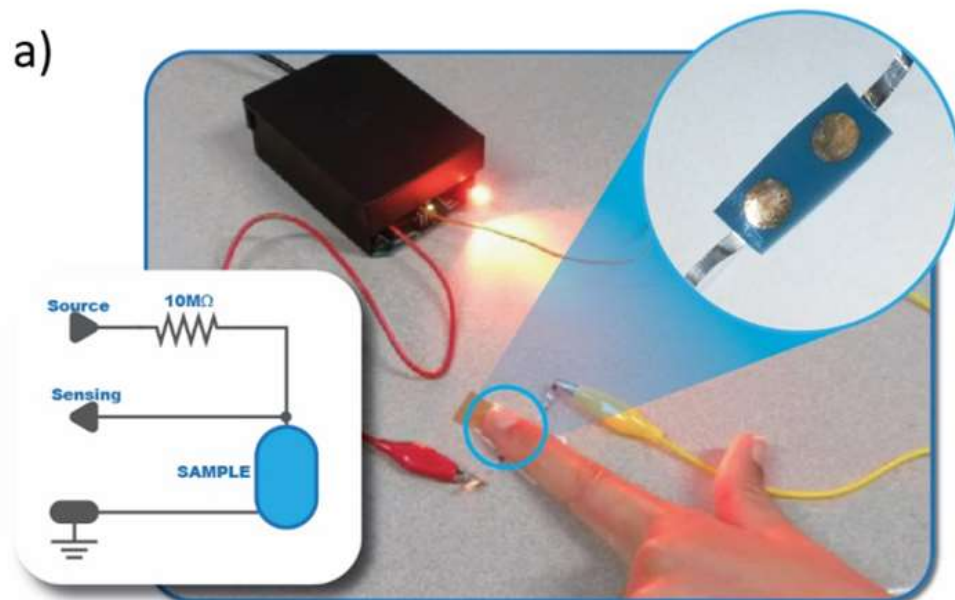
Figure 4.9 – Developed capacitive sensing prototype, with the circuit diagram and a magnified view of the sensor (a). Capacitance sensor response (unitless) measured by the microcontroller during a set of slow and fast finger touch events (b).

The algorithm used to determine the capacitive touch events in the sensor is presented in **Figure 4.10**. Initially, both source and sensing pins are connected to ground, and the capacitor created by the sensor remains with 0 V. Then, the sensing pin is configured as high impedance input, and the source pin puts out a voltage of 5 V. At that moment, the microcontroller starts a timer to measure the time that the sensing pin takes to change its logic level. If no finger is in the sensor, this time will be very short because of the low capacitance of the sensor, but if a finger is close to the sensor, the capacitance to ground increases, and the sensing pin will take more time to change its logic level, and the microcontroller interprets that as a touch event. The time calculated by the microcontroller is presented as a relative value of the capacitance of the sensor, therefore no units or conversion factor can be determined. The firmware of the microcontroller averages each 50 samples to reduce noise and executes a calibration by determining the minimum and maximum values measured since the start of the execution.
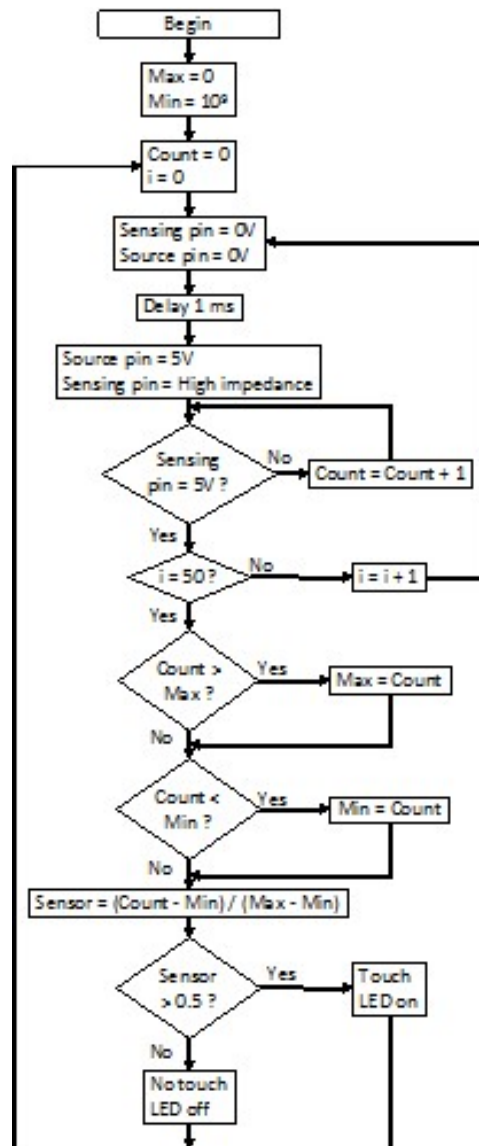
Figure 10 – Microprocessor algorithm for determining the sensor state.

The capacitance measured by the sensor, C_s (in F) is a sum of two elements: the base capacitance C_0 (in F), and the measured amplitude of the sensor A_s (unitless), and it can be calculated through the following equation (4.6):

$$C_s = C_0 + A_s \cdot C_0 \tag{4.6}$$

where k_s (in F) is the factor capacitance of the sensor per unit of amplitude. In the present work, for electronic simplicity, no system was implemented to determine C_0 or k_s, and therefore C_s is not calculated. However, the variations of A_s are already enough to determine finger touch and release events, as it is the case in most capacitive controllers. An example of the collected amplitude variations of the sensor, A_s, is shown in the plot of **Figure 4.9b**.

The microcontroller calculates the historic minimum and maximum values of the sensor, and, to calculate A_s it performs the following operations: first, subtracts the minimum to the read value, and second, converts the resulting value to a relative scale of 0 to 1, using the maximum as 1. Finally, if A_s is higher than 0.5, it considers a finger touch, else it considers that the finger is not in touch.

Its response is proportional to the force of the finger touch and the peaks show the application and recovery of the force.

Different capacitive sensors have been developed using composites reinforced with carbon fiber and graphene oxide [49] and composites based on Ag nanowires and polimide [50]. Nevertheless, considering environmental issues (UV curable, with no solvents or high temperature involved), simple integration by additive manufacturing processability, optical transparency and high dielectric response, the present approach shows an advanced material with large potential for coatings and sensors, being suitable for the new generation of interface electronic applications.

4.4. Conclusions

Polyurethane acrylate (PUA)/Indium Tin Oxide (ITO) composites were produced by UV photopolymerization with filler contents up to 25 wt.% in order to improve the dielectric response of the material. The polymerization time and conversion depends on the ITO amount. The ITO fillers are well dispersed for all filler concentrations and no large agglomerates are observed, leading to thermal properties independent of the ITO amount and an improvement of the mechanical properties. On the other hand, the optical transmittance decreases with increasing ITO amount –the optical transparency 20 % decrease of the optical transmittance in the visible range for samples containing 10 wt.% ITO content– whereas the dielectric constant increase with increasing ITO content up to $\varepsilon = 33$ for the composite with 25wt.% ITO. This sample was used for the development of a capacitive sensor, demonstrating high reproducibility and performance. It is concluded that it is possible to develop high dielectric constant UV curable polymer composites based on ITO/PUA, allowing an environmental friendlier solvent-free approach for printed electronics and functional coatings.

4.5. References

[1]   J. Gubbi, R. Buyya, S. Marusic, M. Palaniswami, Internet of Things (IoT): A vision, architectural elements, and future directions, Futur. Gener. Comput. Syst. 29 (2013) 1645–1660. doi:10.1016/j.future.2013.01.010.

[2]   I. Lee, K. Lee, The Internet of Things (IoT): Applications, investments, and challenges for enterprises, Bus. Horiz. 58 (2015) 431–440. doi:10.1016/j.bushor.2015.03.008.

[3]   C. Boller, Composites for Sensors and Actuators, in: Encycl. Mater. Sci. Technol., Elsevier, Oxford, England, 2001: pp. 1376–1382. doi:10.1016/b0-08-043152-6/00256-4.

[4]   J. Kim, Multifunctional Smart Biopolymer Composites as Actuators, Elsevier Inc., 2017. doi:10.1016/B978-0-12-809261-3.00011-5.

[5]   X. Wang, M. Jiang, Z. Zhou, J. Gou, D. Hui, 3D printing of polymer matrix composites: A review and prospective, Compos. Part B Eng. 110 (2017) 442–458. doi:10.1016/j.compositesb.2016.11.034.

[6]   C. Mendes-Felipe, J. Oliveira, I. Etxebarria, J.L. Vilas-Vilela, S. Lanceros-Mendez, State-of-the-Art and Future Challenges of UV Curable Polymer-Based Smart Materials for Printing Technologies, Adv. Mater. Technol. 4 (2019) 1–16. doi:10.1002/admt.201800618.

[7]   H. Xiang, X. Wang, G. Lin, L. Xi, Y. Yang, D. Lei, H. Dong, J. Su, Y. Cui, X. Liu, Preparation, characterization and application of UV-curable flexible hyperbranched polyurethane acrylate, Polymers (Basel). 9 (2017). doi:10.3390/polym9110552.

[8]   F. Wang, J.Q. Hu, W.P. Tu, Study on microstructure of UV-curable polyurethane acrylate films, Prog. Org. Coatings. 62 (2008) 245–250. doi:10.1016/j.porgcoat.2007.12.005.

[9]   H. Xu, F. Qiu, Y. Wang, W. Wu, D. Yang, Q. Guo, UV-curable waterborne polyurethane-acrylate: Preparation, characterization and properties, Prog. Org. Coatings. 73 (2012) 47–53. doi:10.1016/j.porgcoat.2011.08.019.

[10]   S.J. Choi, H.N. Kim, W.G. Bae, K.Y. Suh, Modulus- and surface energy-tunable ultraviolet-curable polyurethane acrylate: Properties and applications, J. Mater. Chem. 21 (2011) 14325–14335. doi:10.1039/c1jm12201k.

[11]   J.H. Li, R.Y. Hong, M.Y. Li, H.Z. Li, Y. Zheng, J. Ding, Effects of ZnO nanoparticles on the mechanical and antibacterial properties of polyurethane coatings, Prog. Org. Coatings. 64 (2009) 504–509. doi:10.1016/j.porgcoat.2008.08.013.

[12]   K. Kim, M. Kim, J. Kim, Fabrication of UV-curable polyurethane acrylate composites containing surface-modified boron nitride for underwater sonar encapsulant application, Ceram. Int. 40 (2014) 10933–10943. doi:10.1016/j.ceramint.2014.03.092.

[13]   D. Kim, M. Jang, J. Seo, K.H. Nam, H. Han, S.B. Khan, UV-cured poly(urethane acrylate) composite films containing surface-modified tetrapod ZnO whiskers, Compos. Sci. Technol. 75 (2013) 84–92. doi:10.1016/j.compscitech.2012.12.007.

[14]   K.H. Nam, K. Seo, J. Seo, S.B. Khan, H. Han, Ultraviolet-curable polyurethane acrylate nanocomposite coatings based on surface-modified calcium carbonate, Prog. Org. Coatings. 85 (2015) 22–30. doi:10.1016/j.porgcoat.2014.12.004.

[15]   K.H. Liao, Y. Qian, C.W. MacOsko, Ultralow percolation graphene/polyurethane acrylate nanocomposites, Polymer (Guildf). 53 (2012) 3756–3761. doi:10.1016/j.polymer.2012.06.020.

[16]   B. Yu, X. Wang, W. Xing, H. Yang, L. Song, Y. Hu, UV-Curable Functionalized Graphene Oxide/Polyurethane Acrylate Nanocomposite Coatings with Enhanced..., Ind. Eng. Chem. Res. 51 (2012) 14629–14636. doi:10.1021/ie3013852.

[17]   X. Li, S. Wang, J. Xie, J. Hu, H. Fu, Polyurethane acrylate-supported rGO/TiO 2 electrical conductive and antibacterial nanocomposites, Int. J. Polym. Mater. Polym. Biomater. 68 (2019) 319–327. doi:10.1080/00914037.2018.1452227.

[18]   H.C. Huang, T.E. Hsieh, Preparation and characterizations of highly transparent UV-curable ZnO-acrylic nanocomposites, Ceram. Int. 36 (2010) 1245–1251. doi:10.1016/j.ceramint.2010.01.010.

[19]   W. Liao, A. Gu, G. Liang, L. Yuan, New high performance transparent UV-curable

poly(methyl methacrylate) grafted ZnO/silicone-acrylate resin composites with simultaneously improved integrated performance, Colloids Surfaces A Physicochem. Eng. Asp. 396 (2012) 74–82. doi:10.1016/j.colsurfa.2011.12.044.

[20]   H. Zhou, H. Wang, X. Tian, K. Zheng, Z. Wu, X. Ding, X. Ye, Preparation of UV-curable transparent poly(urethane acrylate) nanocomposites with excellent UV/IR shielding properties, Compos. Sci. Technol. 94 (2014) 105–110. doi:10.1016/j.compscitech.2014.01.022.

[21]   O. Llorente, M.J. Fernández-Berridi, A. González, L. Irusta, Study of the crosslinking process of waterborne UV curable polyurethane acrylates, Prog. Org. Coatings. 99 (2016) 437–442. doi:10.1016/j.porgcoat.2016.06.020.

[22]   C. Mendes-Felipe, J. Oliveira, P. Costa, L. Ruiz-Rubio, A. Iregui, A. González, J.L. Vilas, S. Lanceros-Mendez, Stimuli responsive UV cured polyurethane acrylated/carbon nanotube composites for piezoresistive sensing, Eur. Polym. J. 120 (2019) 109226. doi:10.1016/j.eurpolymj.2019.109226.

[23]   A. Endruweit, M.S. Johnson, A.C. Long, Curing of Composite Components by Ultraviolet Radiation: A Review, Polym. Compos. 27 (2006) 119–128. doi:10.1002/pc.20166.

[24]   K. Zahouily, C. Decker, High-performance UV-cured composite and nanocomposite materials, JEC Compos. Mag. 44 (2007) 75–79.

[25]   J. Ba, A. Feldhoff, D.F. Rohlfing, M. Wark, M. Antonietti, M. Niederberger, Crystallization of indium tin oxide nanoparticles: From cooperative behavior to individuality, Small. 3 (2007) 310–317. doi:10.1002/smll.200600425.

[26]   Y. Yin, S. Zhou, G. Gu, L. Wu, Preparation and properties of UV-curable polymer/nanosized indium-doped tin oxide (ITO) nanocomposite coatings, J. Mater. Sci. 42 (2007) 5959–5963. doi:10.1007/s10853-006-1133-1.

[27]   J. Silva, S. Lanceros-Mendez, R. Simoes, Effect of cylindrical filler aggregation on the electrical conductivity of composites, Phys. Lett. Sect. A Gen. At. Solid State Phys. 378 (2014) 2985–2988. doi:10.1016/j.physleta.2014.08.011.

[28]   M. Rincón-Iglesias, E. Lizundia, C.M. Costa, S. Lanceros-Méndez, Tailoring

Electrical and Mechanical Properties of All-Natural Polymer Composites for Environmentally Friendlier Electronics, ACS Appl. Polym. Mater. 2 (2020) 1448–1457. doi:10.1021/acsapm.9b01098.

[29]   C. Mendes-Felipe, T. Rodrigues-Marinho, J.L. Vilas, S. Lanceros-Mendez, UV curable nanocomposites with tailored dielectric response, Polymer (Guildf). 196 (2020). doi:10.1016/j.polymer.2020.122498.

[30]   P. Cardoso, J. Silva, D. Klosterman, J.A. Covas, F.W.J. van Hattum, R. Simoes, S. Lanceros-Mendez, The role of disorder on the AC and DC electrical conductivity of vapour grown carbon nanofibre/epoxy composites, Compos. Sci. Technol. 72 (2012) 243–247. doi:10.1016/j.compscitech.2011.11.008.

[31]   D. Kim, K. Jeon, Y. Lee, J. Seo, K. Seo, H. Han, S. Khan, Preparation and characterization of UV-cured polyurethane acrylate/ZnO nanocomposite films based on surface modified ZnO, Prog. Org. Coatings. 74 (2012) 435–442. doi:10.1016/j.porgcoat.2012.01.007.

[32]   J.Y. Jang, J.Y. Do, Synthesis and evaluation of thermoplastic polyurethanes as thermo-optic waveguide materials, Polym. J. 46 (2014) 349–354. doi:10.1038/pj.2014.7.

[33]   D. Ebert, B. Bhushan, Transparent, superhydrophobic, and wear-resistant coatings on glass and polymer substrates using SiO2, ZnO, and ITO nanoparticles, Langmuir. 28 (2012) 11391–11399. doi:10.1021/la301479c.

[34]   N. Sakai, Y. Fujiwara, M. Arai, K. Yu, T. Tatsuma, Electrodeposition of gold nanoparticles on ITO: Control of morphology and plasmon resonance-based absorption and scattering, J. Electroanal. Chem. 628 (2009) 7–15. doi:10.1016/j.jelechem.2008.12.008.

[35]   K. Zeranska-Chudek, A. Lapinska, A. Wroblewska, J. Judek, A. Duzynska, M. Pawlowski, A.M. Witowski, M. Zdrojek, Study of the absorption coefficient of graphene-polymer composites, Sci. Rep. 8 (2018) 1–8. doi:10.1038/s41598-018-27317-0.

[36]   E.S. Jang, S.B. Khan, J. Seo, Y.H. Nam, W.J. Choi, K. Akhtar, H. Han, Synthesis and characterization of novel UV-curable polyurethane-clay nanohybrid: Influence of

organically modified layered silicates on the properties of polyurethane, Prog. Org. Coatings. 71 (2011) 36–42. doi:10.1016/j.porgcoat.2010.12.007.

[37] M. Lombardi, A. Guerriero, G. Kortaberria, I. Mondragon, M. Sangermano, L. Montanaro, Effect of the Ceramic Filler Features on the Properties of Photopolymerized BaTiO3-Acrylic Composites, Polym. Compos. 32 (2011) 1304–1312. doi:10.1002/pc.21154.

[38] G. Trovati, E.A. Sanches, S.C. Neto, Y.P. Mascarenhas, G.O. Chierice, Characterization of Polyurethane Resins by FTIR, TGA, and XRD, J. Appl. Polym. Sci. 115 (2010) 263–268. doi:10.1002/app.31096.

[39] Y. Jiang, S.Y. Zhang, X.L. Zhang, T. Zhang, Improving the performance of UV-curable coatings with carbon nanomaterials, Express Polym. Lett. 12 (2018) 628–639. doi:10.3144/expresspolymlett.2018.53.

[40] X. Cao, C. Xu, Y. Wang, Y. Liu, Y. Liu, Y. Chen, New nanocomposite materials reinforced with cellulose nanocrystals in nitrile rubber, Polym. Test. 32 (2013) 819–826. doi:10.1016/j.polymertesting.2013.04.005.

[41] J.F. Capsal, C. Pousserot, E. Dantras, J. Dandurand, C. Lacabanne, Dynamic mechanical behaviour of polyamide 11/Barium titanate ferroelectric composites, Polymer (Guildf). 51 (2010) 5207–5211. doi:10.1016/j.polymer.2010.09.011.

[42] P. Costa, J. Silva, V. Sencadas, R. Simoes, J.C. Viana, S. Lanceros-Méndez, Mechanical, electrical and electro-mechanical properties of thermoplastic elastomer styrene-butadiene-styrene/multiwall carbon nanotubes composites, J. Mater. Sci. 48 (2013) 1172–1179. doi:10.1007/s10853-012-6855-7.

[43] A. Shrivastava, Introduction to Plastics Engineering, Elsevier, Amsterdam, The Netherlands, 2018. doi:10.1016/c2014-0-03688-x.

[44] R. Benavente, C. Mijangos, J.M. Perena, M. Krumova, D. López, Effect of crosslinking on the mechanical and thermal properties of poly (vinyl alcohol), Polymer (Guildf). 41 (2000) 9265–9272.

[45] F. Kremer, A. Schönhals, Broadband dielectric spectroscopy, 2003. http://books.google.com/books?id=sdG4ywL3qMsC.

[46] Z. Qilong, Z. Zhao, X. Nuoxin, H. Yang, Dielectric Properties of P(VDF-TrFE-CTFE) Composites Filled with Surface-Coated TiO2, Polymers (Basel). (2020).

[47] S. Song, S. Xia, S. Jiang, X. Lv, S. Sun, Q. Li, A facile strategy to enhance the dielectric and mechanical properties of MWCNTs/PVDF composites with the aid of MMA-co-GMA copolymer, Materials (Basel). 11 (2018). doi:10.3390/ma11030347.

[48] C.W. Nan, Y. Shen, J. Ma, Physical properties of composites near percolation, Annu. Rev. Mater. Res. 40 (2010) 131–151. doi:10.1146/annurev-matsci-070909-104529.

[49] K.Y. Chan, H. Lin, K. Qiao, B. Jia, K.T. Lau, Multifunctional graphene oxide paper embodied structural dielectric capacitor based on carbon fibre reinforced composites, Compos. Sci. Technol. 163 (2018) 180–190. doi:10.1016/j.compscitech.2018.05.027.

[50] K.S. Kim, S.O. Kim, C.J. Han, D.U. Kim, J.S. Kim, Y.T. Yu, C.R. Lee, J.W. Kim, Revisiting the thickness reduction approach for near-foldable capacitive touch sensors based on a single layer of Ag nanowire-polymer composite structure, Compos. Sci. Technol. 165 (2018) 58–65. doi:10.1016/j.compscitech.2018.06.016.

Chapter 5

Photocurable magnetic materials

Photocurable magnetic materials based on polyurethane acrylated (PUA) polymer and different magnetic particles including magnetite (Fe_3O_4), cobalt ferrite oxide (CFO) and neodymium iron boron alloy (NdFeB) have been prepared. The influence of the filler type and content on the photopolymerization process, morphology, Young modulus, electric, dielectric and magnetic properties has been investigated. It is demonstrated the possibility of developing materials with tailored magnetic response by additive manufacturing technologies.

5.1. Introduction

As it is commented in the Chapter 1 of this thesis, over the last few years, we have witnessed the advent of the Internet of Things (IoT) and Industry 4.0 as essential economic and technological raising paradigms. This, in turn, has also highlighted the need of multifunctional materials designed *ad hoc* to fulfil the requirements that each application demands. Further, additive manufacturing (AM) offers important advantages over traditional fabrication methods, such as design freedom, ability to adapt the shape of the material to the application, waste reduction and rapid fabrication with minimum times for prototyping [1]. AM has been used in a successful way to fabricate electronic circuitry in the field of printed electronics (PE) [2,3], in biomedicine [4], or for the development of sensors [5]. In this context, polymer composites are ideal for the development of multifunctional materials compatible with additive manufacturing processing technologies. On the one hand, polymer composites take advantage of the synergistic combination of inorganic and organic constituents. On the other hand, the polymeric matrix offers advantages in terms of processability (flexibility, ductility, etc.), while the filler usually allows to enhance one or more physico-chemical properties (hardness, electrical conductivity, ductility or magnetism, among others) [6].

Several types of polymeric nanocomposites, each with specific properties, have been investigated in the last few decades. Examples include conductive composites containing carbon nanotubes [7], dielectrics ones using barium titanate [8], that also allow piezoelectric response [9]. In particular, magnetic nanocomposites are essential for a large variety of applications, such as PE [10], electromagnetic shielding [11], permanent magnets [12], information recording [13] or magnetoresponsive structures [14].

In order to fabricate magnetic composites, multiple techniques have been employed [15]. Generally, to produce printable magnetic inks, the filler providing the magnetic properties is dispersed within a proper solvent (depending on the polymer being used), and thereafter the polymer is added to produce the printable composite. These solvent-based inks can be based on nano- [16] or micro- particles [17]. Other procedures, such as the sol-gel method [18] have been also successfully employed. Commercial inks are available as well, many of which also include other additives, such as humectants, binders, surfactants, and bactericides [19]. Also, magnetic composites have been prepared for fused deposition modelling (FDM)

[20]. Thermoplastic polymers were mixed with magnetic fillers to fabricate thermoplastic-bonded magnetic composites in the form of pellets that are then extruded to obtain a magnetic filament to be used in a FDM 3D printer. Thus, thermoplastic-bonded magnetic composites with both tailored geometries and magnetic properties can be 3D printed [21].

Regarding printing methods, direct ink writing (DIW) [22], fused deposition modelling (FDM) [21], inkjet printing [23], or doctor blade [24] have been used for the development of magnetic composites depending on the characteristics of the ink. Typically, the printing process also involves the sintering or curing of the inks, which provide the composites their final properties. In this sense, solvent-based inks are often thermally cured, so that the solvent is evaporated from the formulation. However, the main drawback of these process is the fact that the solvent is typically toxic, with obvious environmental and safety concerns, while in the case of FDM, elevated temperatures are needed. Further, all them present limitations in terms of the maximum definition that can be obtained during the printing process [25]. Hence, more environmentally friendly curing methods, such as UV curing, are being developed in the recent years, searching for green chemistry and sustainable production methods [26].

UV curing or photopolymerization, defined in Chapter 1, offers advantages such as fast curing process, room curing temperatures, reduced emission of volatile organic compounds (VOCs) or space and energy efficiency [27] that makes it an appropriate process for the fabrication of composite materials [28] applicable for biomedical [29], sensors [30] or actuator [31] applications, among others. Thus, a wide variety of functional materials (piezoresistive [32], piezoelectric [33], conductive [34], dielectric [35] or magnetic [6]) can be obtained, as it has been demonstrated in the previous chapters of this thesis. Together with its advantages, UV curing processing has an important drawback that is the limitation of the amount of filler added to the polymer. Most fillers absorb UV light and compete with the polymerization reaction, leading to a limitation on the functional properties of the obtained material [32]. This effect has significant relevance in the case of UV curable magnetic composites which just allow the incorporation of a few vol.% particle content and a few microns of maximum thickness in order to preserve a satisfactory degree of photopolymerization [6].

Regarding the possible magnetic fillers to tune magnetic properties of polymer composites, one possibility that has been explored is the use of nanometric-sized ferrites, in particular when lower magnetic performance is required [36]. Ferrite nanoparticles can be considered soft magnets, since their coercive field is smaller than that observed for hard magnets. In fact, magnetic properties of iron oxides are largely dependent on their size, as it is related to the magnetic interaction among particles, which may cause them to behave as a single, larger particle. In fact, if the size of the particles is sufficiently small, they enter the superparamagnetic regime, in which they are easily aligned with an applied magnetic field but show no coercivity [37]. This allows better control through external magnetic fields and prevent aggregation of the particles due to magnetic interactions. Among ferrites, cobalt ferrite ($CoFe_2O_4$, CFO) is one of the most widely employed fillers for polymer composites, exhibiting high chemical stability [38], moderate saturation magnetization and relatively high coercivity. Other ferrites, in particular magnetite (Fe_3O_4), have also been integrated into polymeric matrices, showing that the formation of the nanocomposites does not affect the magnetic properties of the nanoparticles to a large extent [39]. Hard magnetic materials, on the contrary, show a much larger coercivity (larger than 5000 Oe) and energy product (BH_{max}), which are the two main figures of merit for a permanent magnet. Thus, they retain their magnetization through a much wider range of magnetic field conditions [40]. These characteristics are desirable for many applications, such as permanent magnets, hard disk drives, motors, sensors and consumer electronics [41]. In particular, NdFeB ($Nd_2Fe_{14}B$) has been extensively used since General Motors and Sumitomo Special Metals discovered their magnetic characteristics in 1982. NdFeB magnets replaced SmCo magnets previously used for the same applications. They are usually obtained in the form of micron-sized powders. Despite these advantages, the quantity of rare earths is trending downwards, and giving that the demand of these rare-earth-based magnets in the industry of the e-mobility is going to contribute significantly to this scarcity, research associated with rare-earth-free alternatives is boosting [42].

Different magnetic materials have been obtained and many of them are based on the same magnetic filler: iron(II,III) oxide (Fe_3O_4), also known as magnetite. This filler, in most cases in the form of nanoparticles, has been mixed with different polymers such as 3,4-Epoxycyclohexylmethyl-3,4-epoxycyclohexanecarboxylate epoxy resin [43], polyethylene glycol diacrylate (PEGDA) [44,45], hexanediol diacrylate (HDDA) [44,46] or

hyperbranched polyester acrylated (HBPA) [39] to obtain magnetic UV curable composite films. In addition, magnetite has been coated with silica to obtain better photopolymerizable properties as well as transparent films [6]. Also, other iron oxides have been used to obtain magnetic UV curable films such as maghemite (Fe_2O_3) mixed with an epoxy commercial photoresin [47]. Another magnetic filler that has been used for composite development is Neodymium Iron Boron (NdFeB) alloy used together with di- and polyfunctional methacrylates [1] or with commercially available 3D printable acrylic matrices such as Formlabs ® Clear [48] and Grey [12]. Among them, just polymer-bonded magnets with different shapes have been 3D printed by UV-Assisted Direct Write (UADW) method.

In this context, polyurethane acrylated (PUA) has to be highlighted as a good polymer matrix to obtain composites due to its physico-chemical properties and low viscosity that allows easy filler dispersion [49]. Furthermore, PUA shows good adhesion, high chemical stability and weather resilience, and excellent abrasion resistance [50,51]. This polymer is also of large interest due to its biocompatibility, high transparency and low swelling [52]. Thus, a combination of urethane-acrylate and butyl acrylate resins as the reactive diluent of Fe_3O_4 nanoparticles was employed to 3D print magnetoresponsive polymeric materials with tunable mechanical and magnetic properties by digital light processing [14].

In this work, advanced magnetic UV curable composites with varying magnetic properties have been prepared using magnetite (Fe_3O_4), cobalt ferrite ($CoFe_2O_4$) and neodymium iron boron alloy (NdFeB) particles, and commercially available polyurethane acrylated (PUA) photoresin. The influence of magnetic particles type and content on the photopolymerization process, morphology, chemical, thermal, mechanical, electrical, dielectric and magnetic properties of PUA based composites has been evaluated and discussed.

5.2. Experimental

5.2.1. Materials

Polyurethane acrylate (PUA) based SPOT-E^{TM} clear photoresin (SPOT-A Materials®) was selected as UV curable polymer/matrix. Three different magnetic particles were used for the preparation of magnetic film composites: magnetite (Fe_3O_4) ref. 2651WJ and cobalt ferrite oxide or $CoFe_2O_4$ (CFO) ref. 1510FY from Nanostructured & Amorphous Materials Inc., and neodymium iron boron alloy (NdFeB) model MGFP-15-7 from Magnequench. These

powders present a purity of 99%, 98% and 99%, and a density of $4.8 - 5.1$ g/cm^3, 5.3 g/cm^3 and 7.6 g/cm^3, respectively. In addition, they show a particle size of 30 nm, $35 - 55$ nm and 5 μm, respectively. In addition, 2-propanol from Alfa Aesar ® with a purity of 99.5% was selected as a sample cleaner. All samples were processed using the materials as received.

5.2.2. Sample preparation

Three sample batches were prepared by mixing different quantities of magnetic particles with the corresponding volume of the UV curable resin. In this way, samples from 0 to 10 wt.% Fe_3O_4 content, from 0 to 6 wt.% CFO content and from 0 to 50 wt.% NdFeB were prepared. The different concentration added for each type of particles were selected according to the maximum amount of filler allowed for the composite to cure with UV light and to obtain a mechanically consistent film. After mechanically mixing, samples of different compositions and magnetic particles were placed in an ultrasound bath (ATU® ATM series Model ATM3L) during 3 h at a temperature of 35 ºC in order to obtain a good powder disaggregation. Then, samples were stirred at room temperature for 2 hours until a good filler dispersion was obtained. Later, the highly opaque viscous liquids obtained were coated on a clean glass substrate using doctor blade technique. Samples were then cured for 90 seconds at room temperature using a UV curing chamber UVACUBE 400 from Honle UV America, Inc. that provides an irradiance of 1000 W/m^2. Flexible/bendable films were detached from the glass substrate and subsequently washed in 2-propanol bath for 5 minutes in order to remove the residual liquid photoresin. Finally, samples were dried in air and stored at room temperature without illumination for their future characterization. The obtained films presented a thickness between 50 and 100 μm, determined using a Powerfix® electronic digital calliper. **Figure 5.1** shows a scheme of the fabrication process for all composite samples.
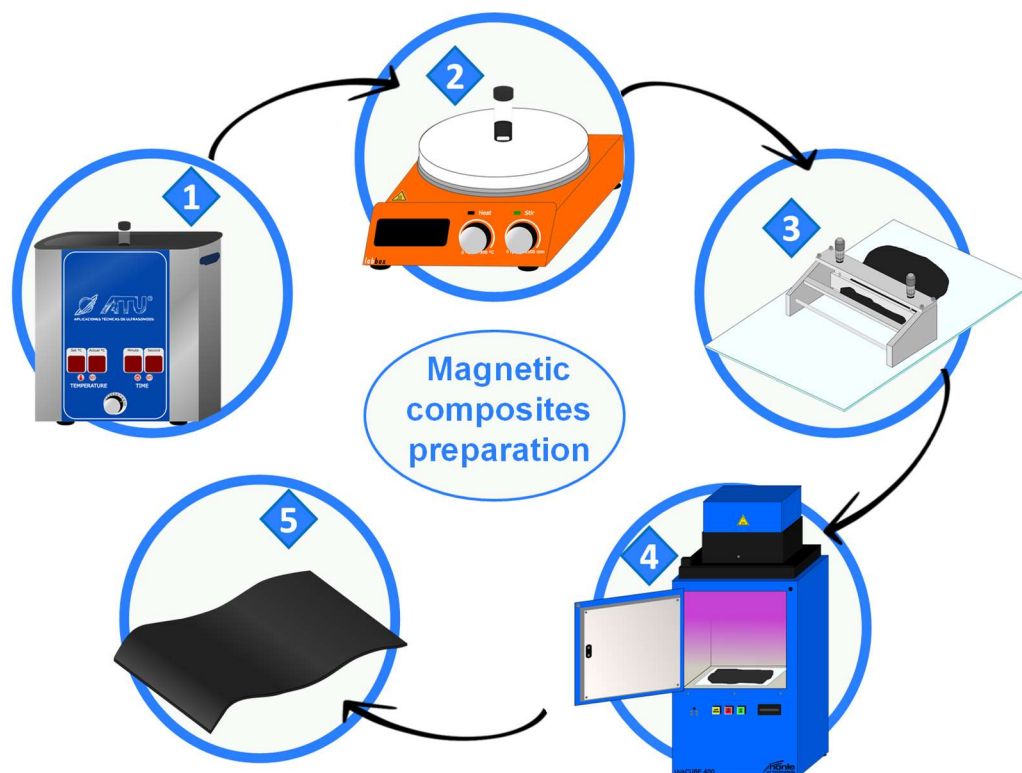
Figure 5.1 – Schematic representation of the preparation of neat PUA and magnetic particles/PUA composite films: 1 – ultrasonication, 2 – magnetic stirring, 3 – film processing by Doctor Blade technique, 4 – UV cure, 5 – obtained films.

5.2.3. Characterization techniques

The photopolymerization or UV curing process of the PUA and PUA magnetic liquids was evaluated by photo-differential scanning calorimetry (photo-DSC) using a DSC 2920 Modulated DSC equipped with a differential photocalorimetry accessory from TA Instruments®. One drop of opaque liquid samples was UV-light illuminated in air at room temperature during 5 minutes at the same time that the heat flow was monitored. Then, DSC curves were normalized by the weight of the samples taking into the account the amount of magnetic material added.

The conversion degree (α) of acrylate C=C double bonds of the PUA polymer was calculated according to equation 5.1 [53]:

$$\alpha = \frac{\Delta H_t}{\Delta H_{max}} \tag{5.1}$$

where ΔH_t is the reaction enthalpy at time t obtained integrating the area under the DSC curve, and ΔH_{max} is the final value of the enthalpy after the complete UV curing process of the commercial PUA photoresin [32,54].

The photopolymerization rate (R_p) was obtained using equation 5.2:

$$R_p = \frac{d\alpha}{dt} = \frac{dH/dt}{\Delta H_0^{theor}} \tag{5.2}$$

In addition, the maximum photopolymerization rate (R_p^{max}) and the needed time to reach the R_p^{max} (t^{max}) were obtained and evaluated.

After photopolymerization evaluation, the filler dispersion and distribution within the polymer was evaluated. Cross-section images of the cold fractured samples were obtained by Scanning Electron Microscopy (SEM) using a Hitachi S-4800 microscope at an accelerating voltage of 10 kV and different magnifications of 5000x and 1000x. In all cases, samples were coated with a 20 nm gold layer by sputtering with a Polaron SC502 apparatus.

Chemical characterization of the nanocomposite samples was studied by Fourier transformed infrared spectroscopy in the total attenuated reflection mode (FTIR-ATR). A Nexus FTIR Nicolet spectrophotometer was employed in the spectral range 4000 to 400 cm^{-1} with a spectral resolution of 4 cm^{-1} and 64 scans.

Thermal properties of the samples were evaluated in terms of the glass transition temperature (T_g) by differential scanning calorimetry (DSC) using an 822e calorimeter from Mettler Toledo. Two consecutive scans were measured under nitrogen atmosphere: the first one from -50 to 250 ºC at 20 ºC/min and the second one from -50 to 150ºC at 20ºC/min. The glass transition temperature was extracted as the extrapolated onset of the baseline shift.

Mechanical properties were studied employing a universal testing machine Shimadzu model AG-IS with a load cell of 1.0 kN. Films were tested in tensile mode, at room temperature and a deformation velocity of 1.0 mm/min using rectangular shape samples with dimensions of 30 mm x 10 mm. The secant modulus (E) of each assay was obtained by calculating the slope of the linear region. In addition, strain at break (ε_b) was determined for neat PUA and all magnetic composites. The mean average values and the standard deviation over 3 specimens are reported.

The direct current, d.c., electrical conductivity of the magnetic composites was studied measuring the intensity-current (I-V) curves with a Keithley 487 picoammeter/voltage source. The current-voltage response was obtained at room temperature with an applied voltage ranging between −10 V and +10 V. For that, two gold electrodes with diameter of 5 mm were deposited by magnetron sputtering Quorum Q150T S sputter coater on both sides of the samples.

The electrical conductivity (σ) is obtained as the inverse of the electrical resistivity (ρ) by applying equation 5.3:

$$\sigma = \frac{1}{\rho} = \frac{1}{R}\frac{d}{A}$$ (5.3)

where R is the electrical resistance of each magnetic composite sample, A is the area of the deposited electrodes and d represents the thickness of the films.

Magnetic properties of the composites were measured at room temperature by magnetic hysteresis loops using a MicroSense EZ7 vibrating sample magnetometer (VSM) from − 1.8 to 1.8 T.

5.3. Results and discussion

5.3.1. UV curing process

The influence of the presence of magnetic particles on the UV curing process of the commercial PUA photoresin was studied by photo-DSC. **Figures 5.2a, c and e** show the conversion degree (α) as a function of irradiation time whereas **Figures 5.2b, d and f** depict the photopolymerization rate (Rₚ) for Fe_3O_4/PUA, CFO/PUA and NdFeB/PUA samples, respectively. **Table 5.1** summarizes the UV curing characteristic values α, R_p^{max} and t^max for all samples against the nominal and experimental magnetic particle content. The experimental magnetic particle contents for all samples is obtained from magnetic measurements as it is explained in the "Magnetic properties" section. In the following, all samples will be identified with respect to the experimental content and not to the nominal one.
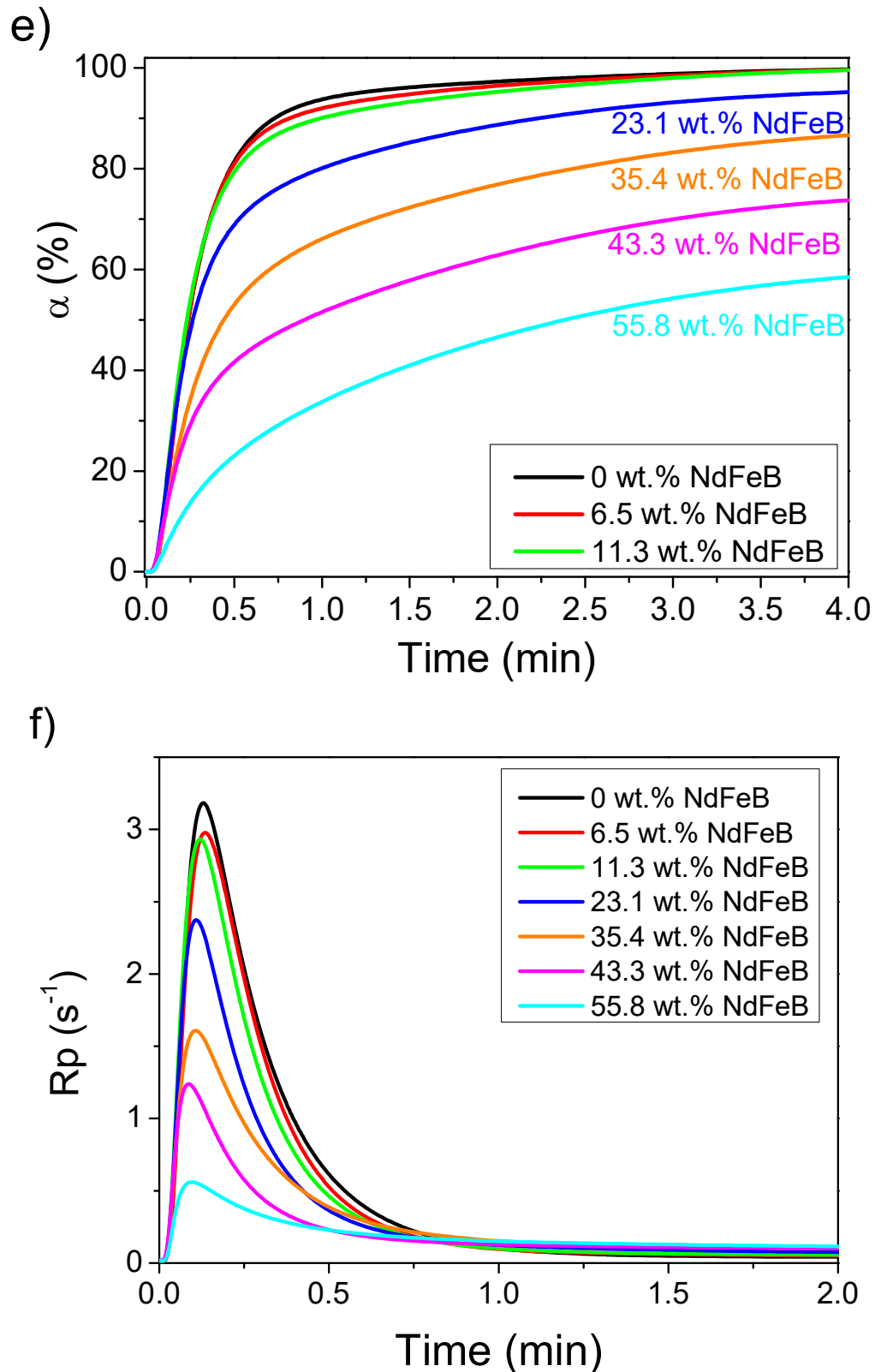
a)

b)

c)

d)
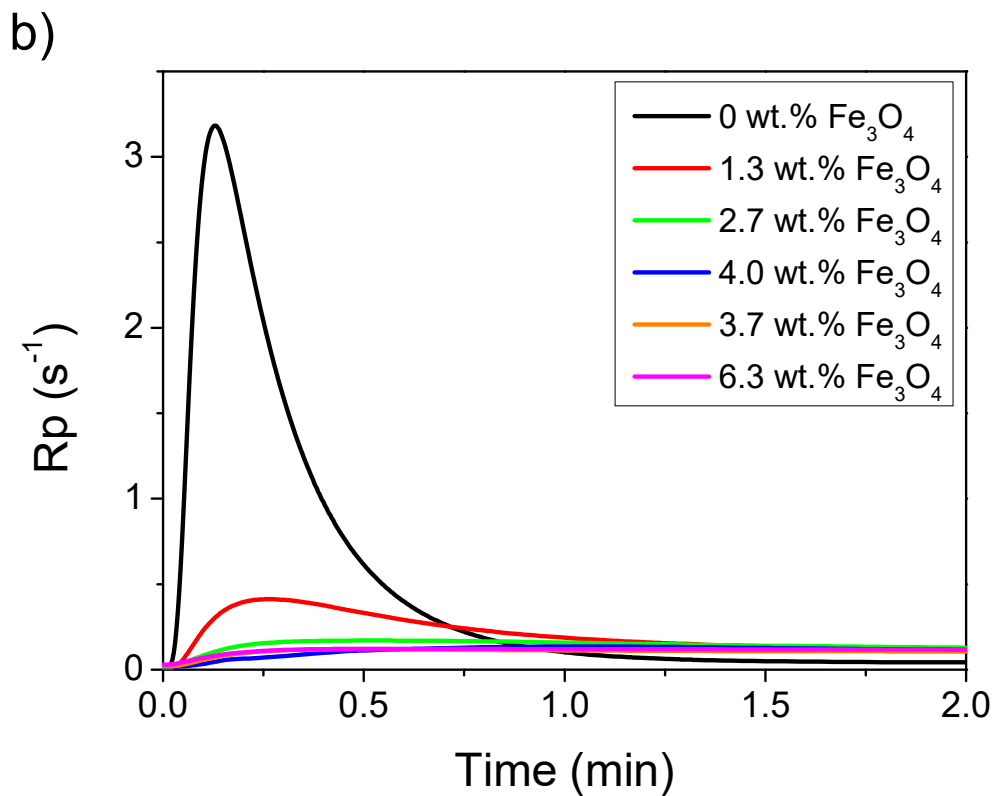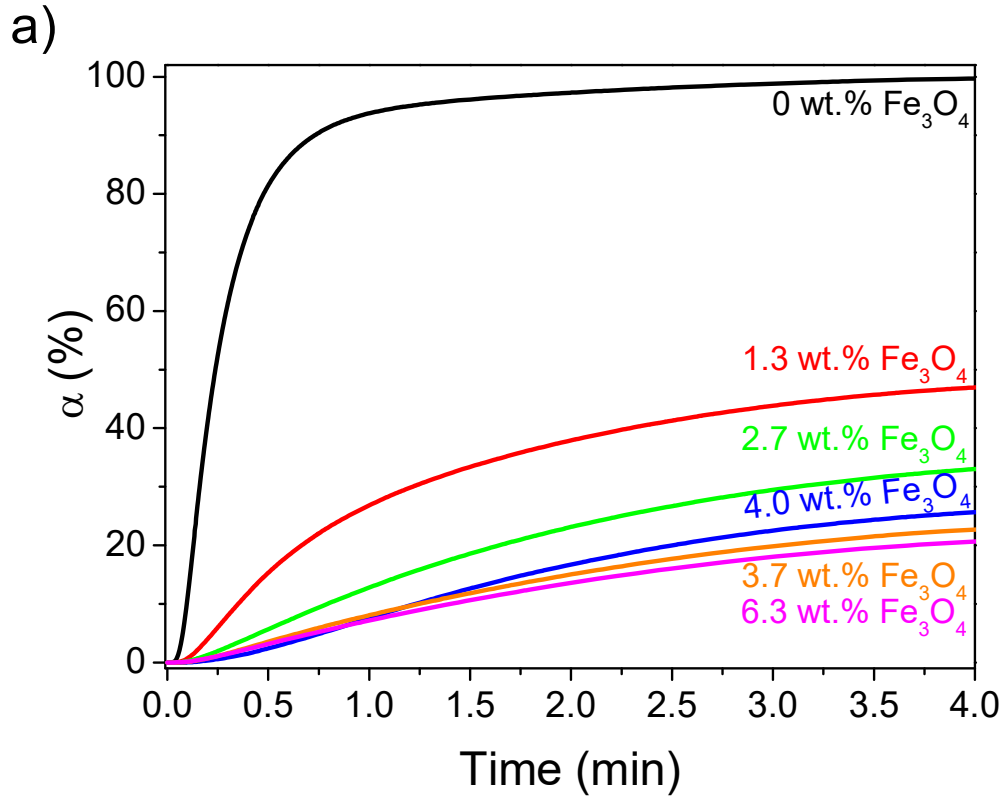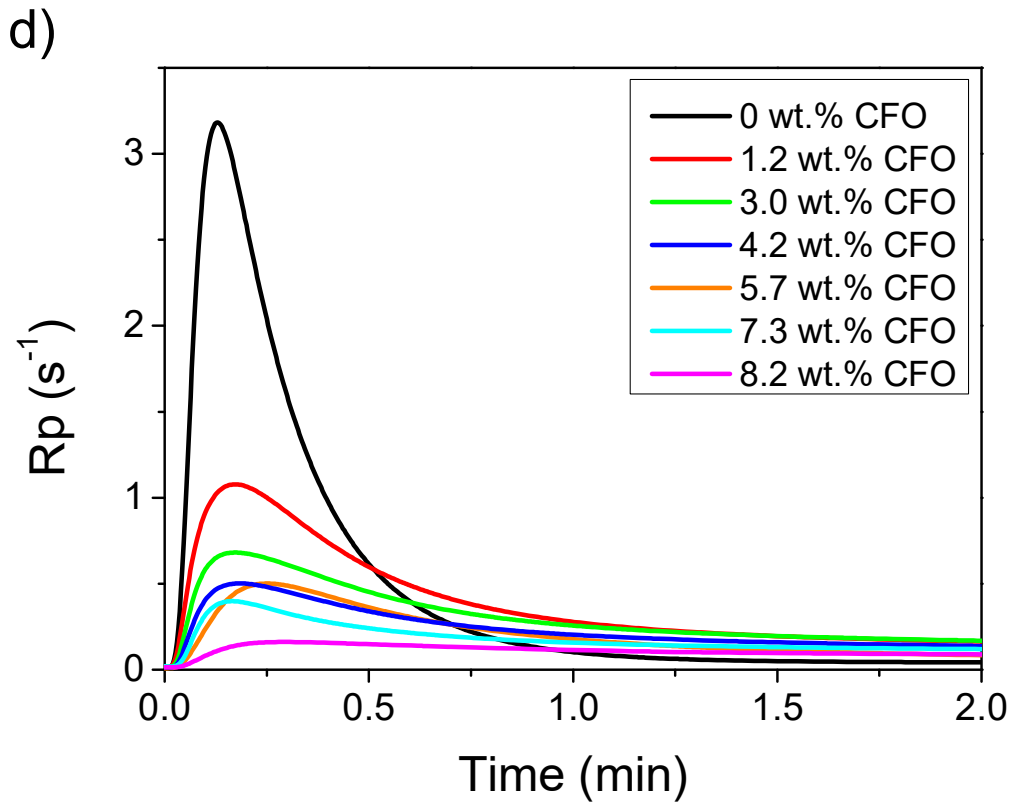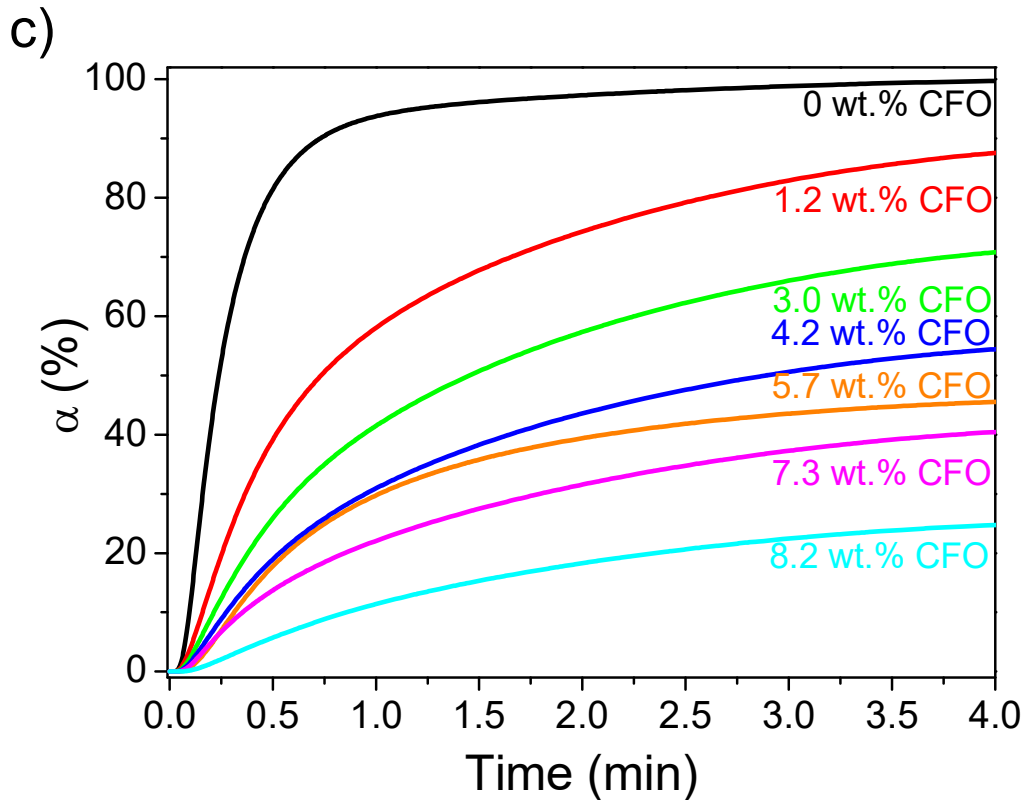
Figure 5.2 – Photopolymerization conversion (α) as a function of time for the Fe_3O_4/PUA (a), CFO/PUA (c) and NdFeB/PUA (e) samples, and the corresponding photopolymerization rate (R_p) for the same samples (b), (d) and (f), respectively.

Table 5.1 – Photopolymerization characteristic parameters (α, R_p^{max} and t[max]) of the pristine resin and the different magnetic composites.

Magnetic particle	Nominal content (wt.%)	Experimental content (wt.%)	α (%)	R_p^{max} (s⁻¹)	t[max] (s)
PUA	100	-	100	3.2	7.6
Fe₃O₄	2	1.3 ± 0.1	47	0.4	15.2
	4	2.7 ± 0.2	33	0.2	17.1
	6	4.0 ± 0.3	26	0.1	17.9
	8	3.7 ± 0.3	22	0.1	17.9
	10	6.3 ± 0.4	20	0.1	18.0
CFO	1	1.2 ± 0.1	88	1.1	9.8
	2	3.0 ± 0.2	71	0.7	10.1
	3	4.2 ± 0.3	55	0.5	10.1
	4	5.7 ± 0.4	45	0.5	13.7
	5	7.3 ± 0.5	41	0.4	10.6
	6	8.2 ± 0.5	26	0.2	13.5
NdFeB	6	6.5 ± 0.4	99	2.9	7.7
	10	11.3 ± 0.6	99	2.9	7.9
	20	23.1 ± 1.3	95	2.3	7.6
	30	35.4 ± 1.8	86	1.6	7.9
	40	43.3 ± 2.4	74	1.2	7.8
	50	55.8 ± 2.9	58	0.6	7.7

Figure 5.2 shows that an increase on magnetic particle content induces a larger decrease on the conversion degree (α), independently of the particle type. For the Fe₃O₄/PUA composites (**Figure 5.2a**) and in agreement with the literature [6,46], α decreases from 100% in the neat polymer sample to 47% in the 1.3 wt.% sample and 26% in the 4.0 wt.% sample. Fe₃O₄/PUA samples with the highest magnetite content show the lowest photopolymerization conversion being 22% for the 3.7 wt.% sample and 20% for the 6.3 wt.% sample. In the case of CFO/PUA composites (**Figure 5.2c**), similar behaviour is obtained but here with a lowest decrease of the total conversion when magnetic nanoparticles are added. The α values vary between 88% for the 1.2 wt.% sample and 26% for the 8.2 wt.% one. With respect to the

NdFeB/PUA samples (**Figure 5.2e**) and in contrast with the iron oxide-based particles, α is less influenced when NdFeB magnetic particles are added. Here, no clear decrease on the α value is observed until 23.1 wt.% content. For samples with higher NdFeB content, the polymerization conversion decreases, being 86% in the case of the 35.4 wt.% sample and the α value is around 58% after 4 minutes of curing for the 55.8 wt.% sample.

Related to the photopolymerization rate (R_p), the addition of magnetic particles results in a slower UV curing process. In this sense, R_p^{max} and t^{max} values for Fe$_3$O$_4$/PUA composite samples (**Figure 5.2b**) present a high decrease when a low amount of magnetic filler is added. R_p^{max} values of 0.4 s^{-1} just with a 1.3 wt.% filler content and up to 0.1 s^{-1} for the 6.3 wt.% sample are achieved, being obtained 15.2 s and 18.0 s for t^{max}, respectively. In the case of CFO/PUA samples (**Figure 5.2d**) t^{max} vary from 3.2 s^{-1} for the 0 wt.% sample to 1.1 s^{-1} for the 1.2 wt.% sample and to 0.5 s^{-1} for the 4.2 wt.% one. Here, t^{max} increases from 7.6 s for pure PUA sample to 9.8 s in 1.2 wt.% and finally 13.5 s for the sample with the highest CFO content. In the case of NdFeB/PUA samples (**Figure 5.2f**), the addition of magnetic particles slightly influences the curing process, which is reflected in the not significant change of t^{max} when NdFeB is added. The R_p^{max} value is reduced to 2.9 s^{-1} for samples with 6.5 wt.% filler content and continues decreasing linearly down to 0.6 s^{-1} when NdFeB content increases.

Comparing the iron oxide-based magnetic nanoparticles, Fe$_3$O$_4$/PUA 6.3 wt.% and CFO/PUA 5.7 wt.%, it is noticed that the modification of Fe$_3$O$_4$ by adding cobalt (CFO) induces a faster and more completed (high conversion degree) UV cure. Thus, a conversion of 20% and 45% for Fe$_3$O$_4$ and CFO samples, respectively, is achieved. In addition, photopolymerization rate is also increased as well as the maximum allowed filler content. On the other hand, when a metallic alloy such as NdFeB is used, higher photopolymerization conversion and polymerization rate is obtained, as well as higher filler content is allowed within the samples in comparison with both iron oxide-based magnetic particles. For the sample with 6.3 wt.% of NdFeB content, 99% conversion and a polymerization rate of 2.9 s^{-1} (similar to neat PUA) is obtained, both values improved with respect to iron oxide-based magnetic filler composites. Furthermore, higher NdFeB particle contents up to 55.8 wt.% are allowed in the composites with a decrease on α and R_p to similar values than samples that contain 1.3 wt.% of Fe$_3$O$_4$ or 4.2 wt.% of CFO nanoparticles.

The radical photopolymerization is a process that begins with the light absorption by a photoinitiator [26]. The efficiency of this absorption is directly related to the capacity of the photoinitiator to absorb light, here UV light. There are two main factors (quantum yields) that influence the process and that are also related to the absorbed photons: the number of starting polymer chains and the number of polymerized monomer units [6]. In the present case, and similar to other inorganic particles embedded in PUA polymer matrix [53,54], magnetic particles and, in particular, magnetic oxides, compete with UV light absorption of the photoinitiator due to their strong photon absorption on the UV spectra region [55–57]. Therefore, the light absorption by the magnetic particles implies a decrease of the photons absorbed by the radical photoinitiator, reducing the number of starting polymer chains contribution to the polymerization process [6]. This absorption is higher for Fe_3O_4 particles than for CFO ones, which explains the lower maximum particle content allowed for Fe_3O_4 composites with respect to CFO ones [55–57]. Magnetic particles composed by metal alloys such as NdFeB also absorb UV light and influence the photopolymerization process of PUA magnets [12], but to a lesser extent than iron oxide-based particles.

In addition, viscosity influences the UV curing process as it increases rapidly during the liquid to solid phase transformation and, therefore, delays the polymerization. When magnetic particle content increases, the sample viscosity increases and therefore, the photopolymerization rate decreases. Thus, when magnetic particle content increases, less amount of initiator contributed to the beginning of the photopolymerization reaction (or begins later) and the conversion degree as well as photopolymerization rate decrease.

5.3.2. Morphology and chemical properties

After characterization of the UV curing process, polymeric films were obtained and characterized. The polymer morphology variations due to magnetic particle inclusion as well as particle dispersion on the film were evaluated by scanning electron microscopy (SEM). **Figure 5.3** shows representative optical photograph of the composite films and SEM images of the cold fractured cross-section of the samples.
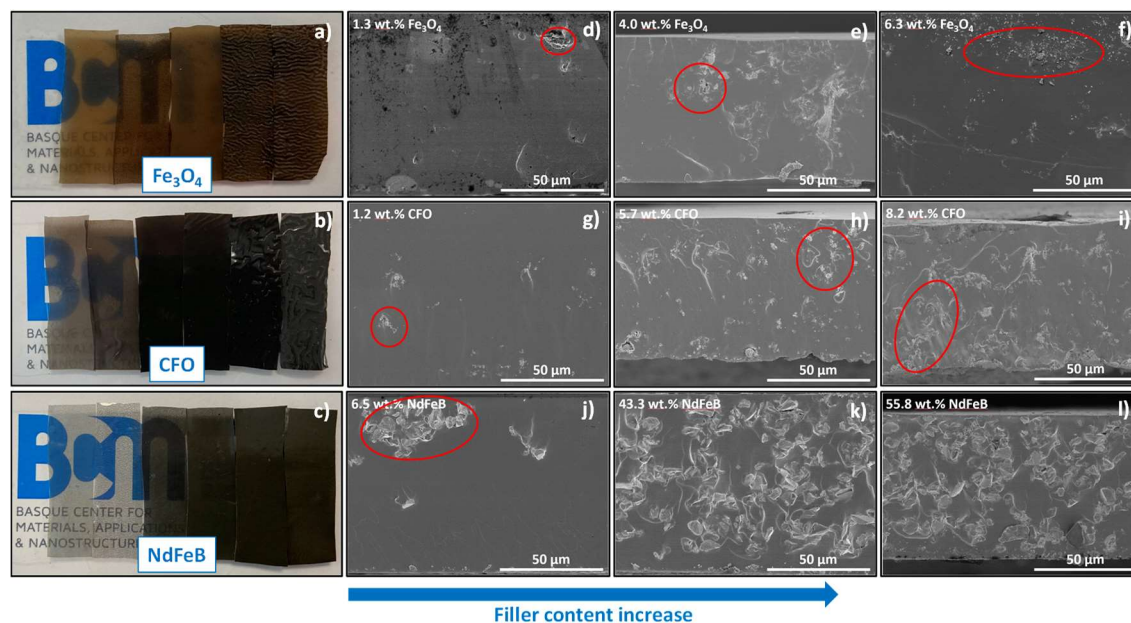
Figure 5.3 – Optical photographs of the Fe₃O₄/PUA (a), CFO/PUA (b) and NdFeB (c) samples. Representative SEM images of the Fe₃O₄/PUA samples at 1.3 wt.% (d), 4.0 wt.% (e) and 6.3 wt.% (f) filler content. SEM images of the CFO/PUA samples at 1.2 wt.% (d), 5.7 wt.% (e) and 8.2 wt.% (f) filler content. SEM images of the NdFeB/PUA samples at 6.5 wt.% (d), 43.3 wt.% (e) and 55.8 wt.% (f) filler content.

Morphology variations of the polymer has a significant influence on the mechanical and electrical properties [58,59] and those variations are dependent on filler type, size and distribution [32,54]. **Figure 5.3** shows optical images of the prepared magnetic films. With increasing filler content and independently on the filler type, optical transmittance of the films decreases drastically, maintaining a certain transparency up to 2.7 wt.%, 3.0 wt.% and 23.1 wt.% for Fe₃O₄, CFO and NdFeB, respectively. Also, brown colour is appreciated for Fe₃O₄/PUA composites, dark black for CFO/PUA composites and grey for NdFeB/PUA samples, which is related to the optical characteristics of the fillers.

Attending to the filler dispersion, **Figures 5.3d to f** show that Fe₃O₄ particles are not well dispersed within the PUA matrix, as demonstrated by the number of size (around 20 μm) of the small agglomerates, which are larger for larger filler content. Interestingly, Fe₃O₄ inclusion leads to no large variations in the PUA microstructure, not being observed any visible cracks, pores or patters, the samples being characterized by a smooth and flat microstructure. On the other hand, the presence of Fe₃O₄ induces a change in the PUA morphology, leading to a flake-like structure that is more marked for the samples with the highest particle amount.

In the case of the CFO/PUA samples, similar results than for the Fe_3O_4/PUA composites are obtained. For the sample with around 1 wt.% filler content (**Figure 5.3g**), small agglomerates are observed, while by increasing magnetic particle content up to around 6 wt.% (**Figure 5.3h**) agglomerates increase in size and quantity. In the case of samples with the highest filler content (8.2 wt.%, **Figure 5.3i**), large agglomerates are obtained (around 50 μm). In all cases and similar that for the Fe_3O_4 composites, a flake-like structure is induced in PUA by the presence of the CFO fillers, more notable for sample with higher filler content.

Regarding the NdFeB/PUA composites, **Figure 5.3j** shows that good dispersion of NdFeB particles is not achieved for low filler content (6.5 wt.%), mainly ascribed to the larger particle size. For samples with the highest magnetic particle content, despite NdFeB micro-particle agglomeration is obtained, good agglomerates dispersion can be achieved as shown in **Figures 5.3k and l** for samples with 43.3 wt.% and 55.8 wt.% filler content, respectively. In these samples, just like in iron oxide-based particles, a flake-like morphology appears and is more noticeable for samples with higher NdFeB content. In all cases, suitable wettability of the filler by the polymer is observed not voids around the fillers or filler agglomerates.

Possible physicochemical interactions between PUA polymer and the different magnetic particles were evaluated by Fourier transformed infrared spectroscopy (FTIR). **Figure 5.4** shows the FTIR spectra of PUA and the prepared composite samples in the range of 4000 to 400 cm^{-1}.

The pure photoresin film presents the characteristic peaks for polyurethane acrylate polymer and are summarized in the **Figure 5.4a**. Thus, in the highest infrared region, a N-H stretching band at 3300-3400 cm^{-1} is observed together with CH_2 and CH_3 stretching bands between 2855 and 2955 cm^{-1}. C=O stretching is identified at 1725 cm^{-1}, and a combined stretching of N-H and the C-N band of the polyurethane group at 1550 cm^{-1}. Finally, the C-N stretching band is observed at 1360 cm^{-1} and the C-O-C stretching band at 1110 $cm^{-1,}$ all representative of PUA [60].
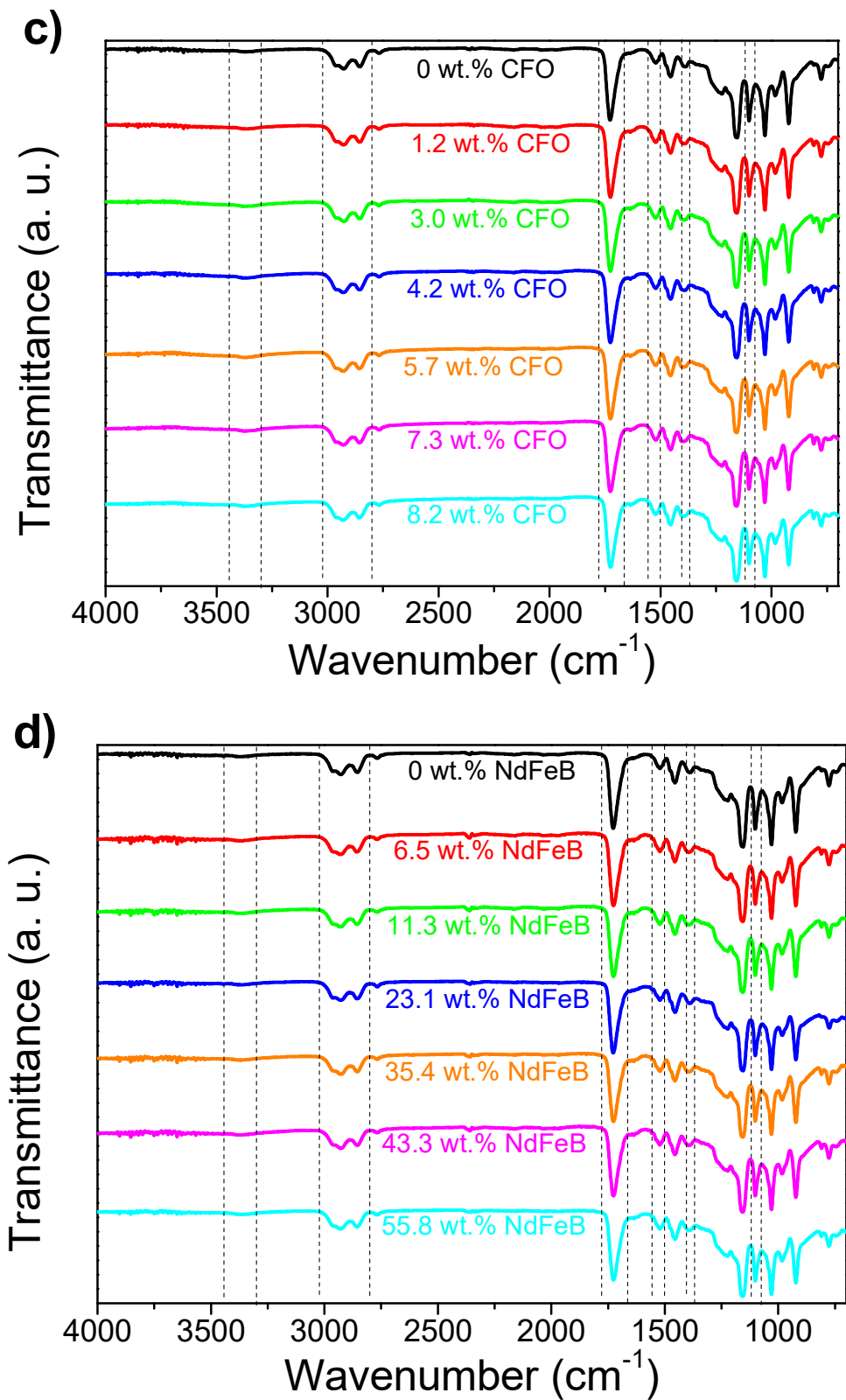
a)

b)
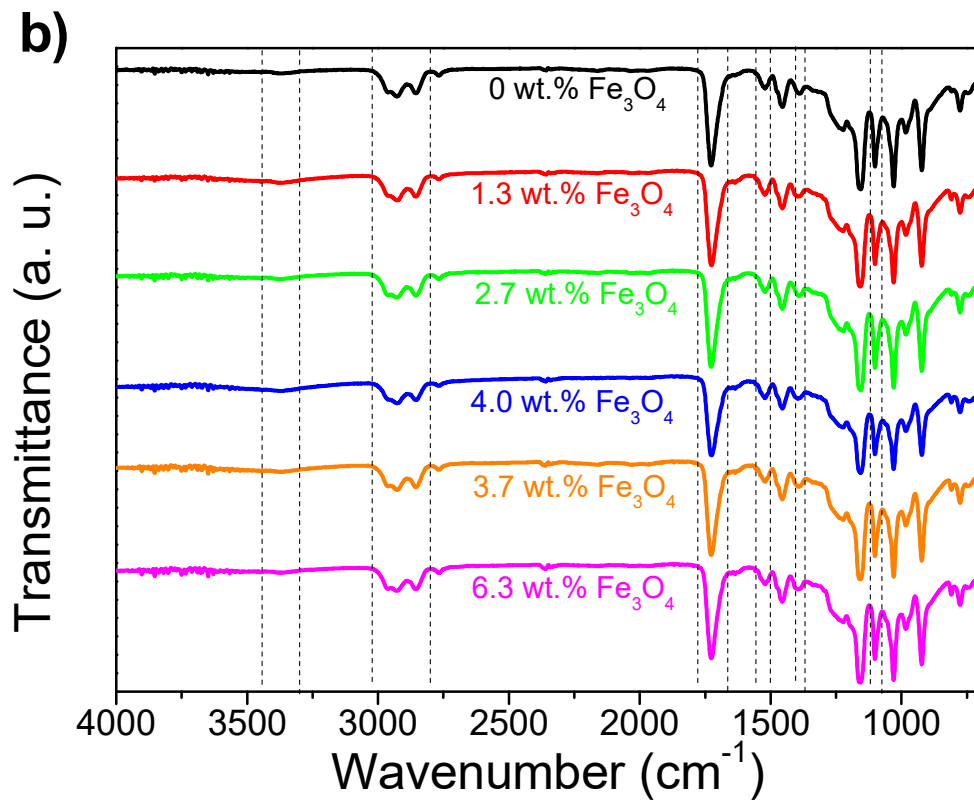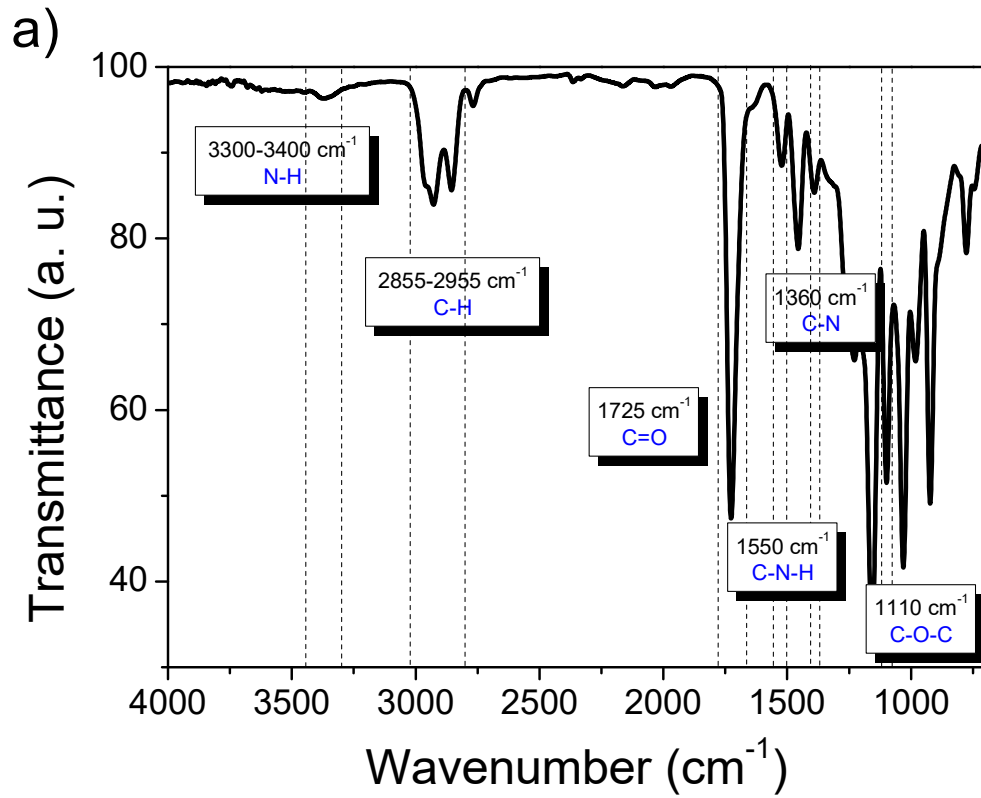
Figure 5.4 – FTIR spectra of neat PUA (a), Fe$_3$O$_4$/PUA (b), CFO/PUA (c) and NdFeB/PUA (d) samples containing different magnetic filler contents.

Fe_3O_4/PUA composites, as well as CFO/PUA and NdFeB/PUA sample films (**Figures 5.4b, c and d**), present the indicated bands characteristics for polyurethane acrylate polymer. It has to be mentioned that in all cases, the C=C stretching band tipically located at 1635 cm^{-1} [61] is present in a small amount, denoting a quasi-completely curing process both in PUA polymer and in all prepared composites. This band appears in a higher extent when the particle content increases, associated to the fact that less C=C conversion is obtained, as it is observed in UV curing results. In addition, no new bands appear in any case and no displacement of existing bands is observed indicating that no chemical interactions between the different magnetic particles and PUA polymer are present [53,54].

5.3.3. Thermal properties

The study of the thermal properties allows to address the influence of filler type and content on the glass transition temperature (T_g) [32] of the obtained polymeric films. **Figure 5.5** show the Differential Scanning Calorimetry (DSC) first scan thermogram obtained for neat PUA, Fe_3O_4/PUA, CFO/PUA and NdFeB/PUA prepared composites and the corresponding T_g values are summarized in **Table 5.2**.
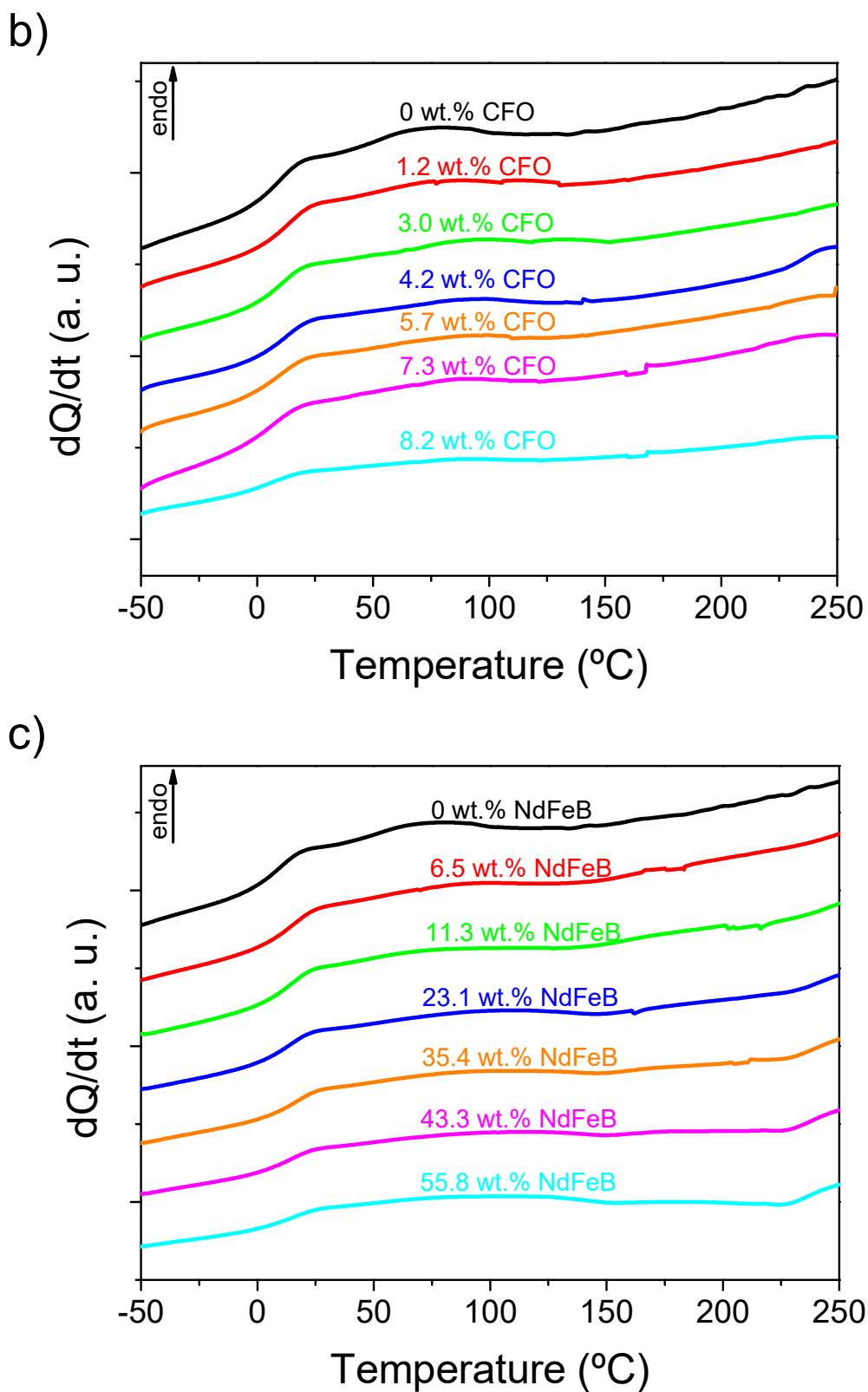
b)

c)
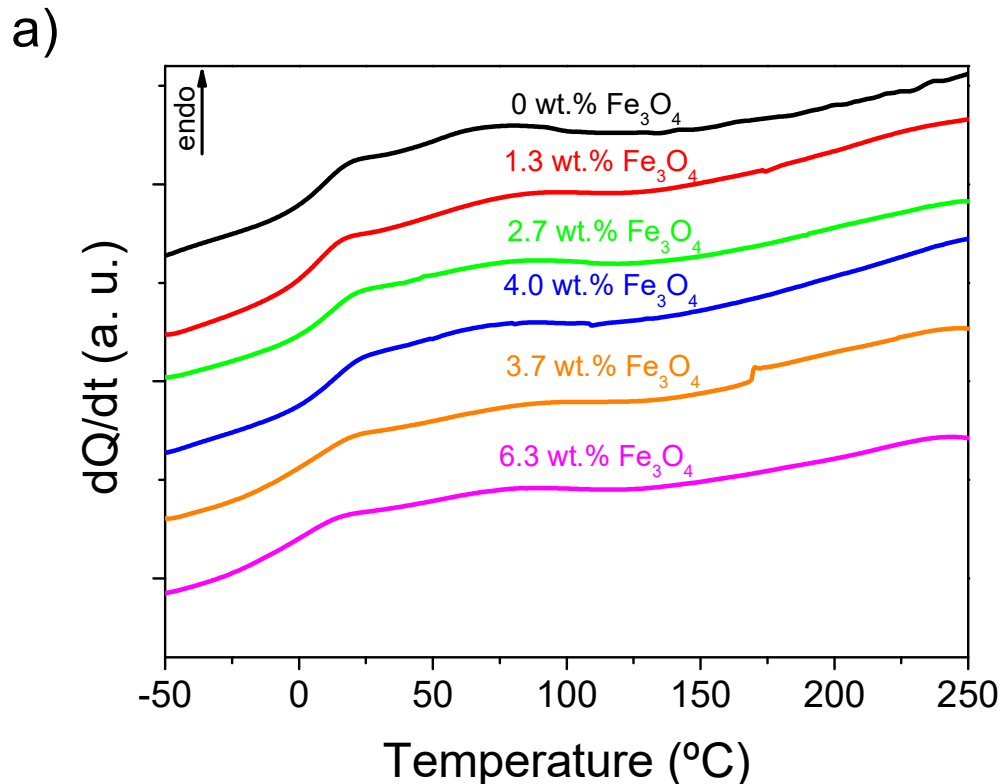
Figure 5.5 – DSC thermograms of neat Fe_3O_4/PUA (a), CFO/PUA (b) and NdFeB/PUA (c) samples for the first scan.

Table 5.2 – Glass transition temperature (T_g) for first scans, elastic modulus (E) and strain at break (ε_b) for PUA and the different magnetic composite films.

Magnetic particle	Experimental content (wt.%)	T_g (ºC)	E (MPa)	ε_b (%)
PUA	0	21	7.44 ± 0.68	36.5 ± 4.8
Fe_3O_4	1.3	18	7.17 ± 0.39	45.5 ± 13.6
	2.7	23	7.32 ± 1.47	50.1 ± 13.0
	4.0	23	7.25 ± 0.46	42.1 ± 2.5
	3.7	19	3.48 ± 0.23	29.5 ± 6.1
	6.3	19	1.54 ± 0.39	23.2 ± 2.6
CFO	1.2	22	8.02 ± 2.92	42.6 ± 7.9
	3.0	20	9.23 ± 0.93	39.0 ± 6.6
	4.2	23	8.64 ± 1.20	46.4 ± 4.9
	5.7	21	6.16 ± 0.53	39.3 ± 3.2
	7.3	19	3.54 ± 0.31	21.3 ± 2.9
	8.2	19	5.08 ± 0.16	33.0 ± 2.7
NdFeB	6.5	25	8.68 ± 0.70	40.6 ± 5.8
	11.3	24	9.64 ± 1.02	41.9 ± 0.8
	23.1	23	12.64 ± 2.14	53.3 ± 3.9
	35.4	26	16.45 ± 1.97	52.0 ± 5.6
	43.3	22	15.32 ± 1.51	45.2 ± 2.0
	55.8	25	17.08 ± 1.93	35.6 ± 2.3

It is verified that all samples present a similar thermal behaviour to PUA, characterized by the glass transition, T_g, which appears near room temperature at 21.4 ºC in the pure resin. **Figure 5.5a** shows that the addition of Fe_3O_4 nanoparticles has no effect on the mobility of PUA polymer chains, the T_g value remaining nearly constant, within experimental error, independently of filler content, as previously reported [46]. Just for the samples with the highest filler content (4.0 and 6.3 wt.%) there is a slight decrease of T_g that can be ascribed to both the reduction of double bond conversion and to the plasticizing effect [14]. A similar behaviour has been observed for the CFO/PUA samples (**Figure 5.5b**). The NdFeB/PUA samples (**Figure 5.5c**), on the other hand, shows analogous behaviour to the one observed in hard magnetic composites [62]. When the filler is added, T_g slightly increases for all

NdFeB/PUA samples compared to PUA, which is associated to the micrometric particle size and to the larger degree of agglomeration, causing the polymer chains to clump together and increase the T_g. On the other hand, this effect is independent on the filler content as observed in related NdFeB/polymer composites [62]. Therefore, not significant changes are observed in the evaluated thermal characteristics independently of the filler type or content.

5.3.4. Mechanical properties

PUA films obtained by photopolymerization are limited with respect to their mechanical properties and the addition of specific fillers has been used to improve them [32,54]. Here, the influence of the magnetic particles into the secant modulus (E) and maximum deformation strain (ε_b) of polyurethane acrylate polymer is evaluated. **Figure 5.6** shows the result of a uniaxial stress-strain tests and the evolution of E and ε_b as a function of the different studied magnetic particles. **Table 5.2** summarizes the obtained mechanical properties for the prepared composites.

Independently of the filler type and content, all samples show similar mechanical properties, characterized by a linear stress-strain region in which the material is stretched until it breaking. Neat PUA polymer films show a secant modulus around 7.44 ± 0.88 MPa and a breaking strain of $\varepsilon_b = 36.5 \pm 4.8$ %. As it is observed in **Figures 5.6a and c**, when Fe_3O_4 nanoparticles are added, E remains approximately constant at a value around 7.5 MPa up to a filler content of 4.0 wt.% and with increasing Fe_3O_4 nanoparticles content, the secant modulus of the material decreases down to 1.54 ± 0.39 MPa for the sample with the highest Fe_3O_4 content. The maximum strain remains constant at around 40 % up to 4.0 wt.% filler load and then strongly decreases, being 23.2 ± 2.6 % for the 6.3 wt.% sample.

The addition of Fe_3O_4 nanoparticles into polyurethane has a reinforcement effect due to high modulus of the inorganic component, approximately 175 GPa, and the good wettability of the filler by the polymer [63,64]. When the magnetic content increases, the ratio of inorganic/organic composition increases and, therefore, the content of the material with highest modulus too. Thus, by increasing the Fe_3O_4 amount, the mechanical properties should be enhanced. However, the dispersion of these particles into polyurethane polymer presents other issues that can cause a decrease on E and ε_b such as the agglomeration of the filler, leading to weaker adhesion between magnetic nanoparticles and the polymer matrix, or a decrease of intermolecular forces due to a disruption of hydrogen binding of
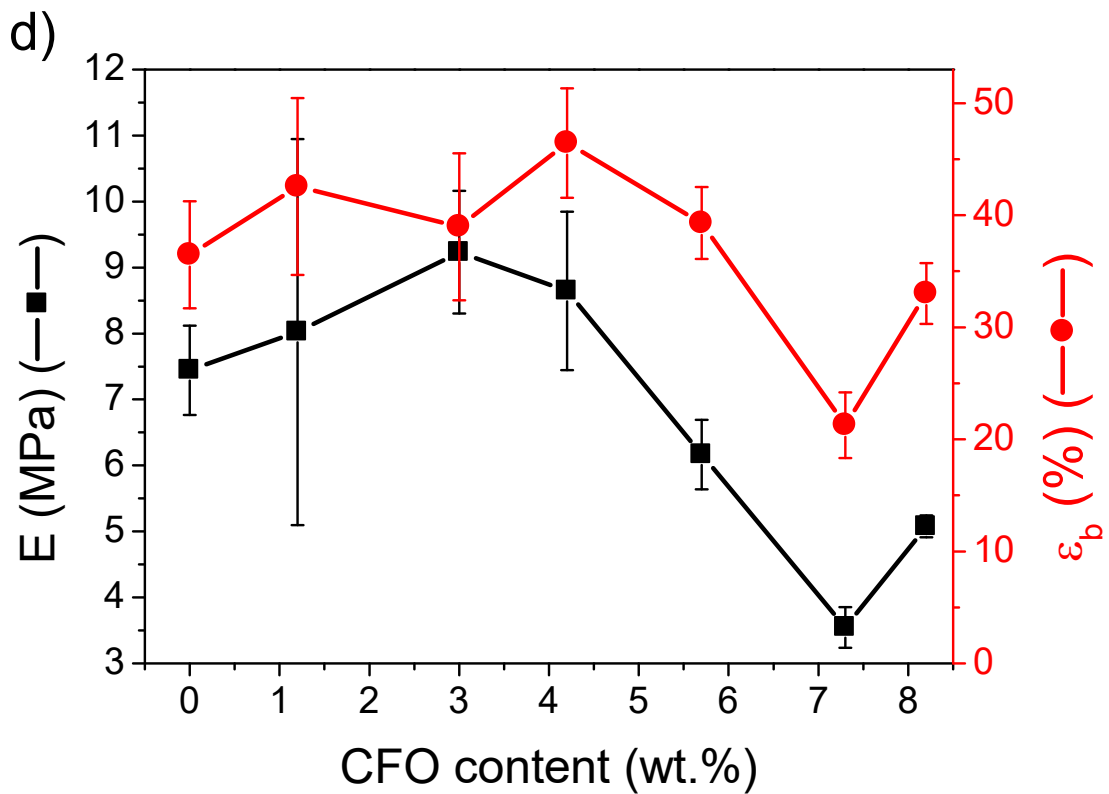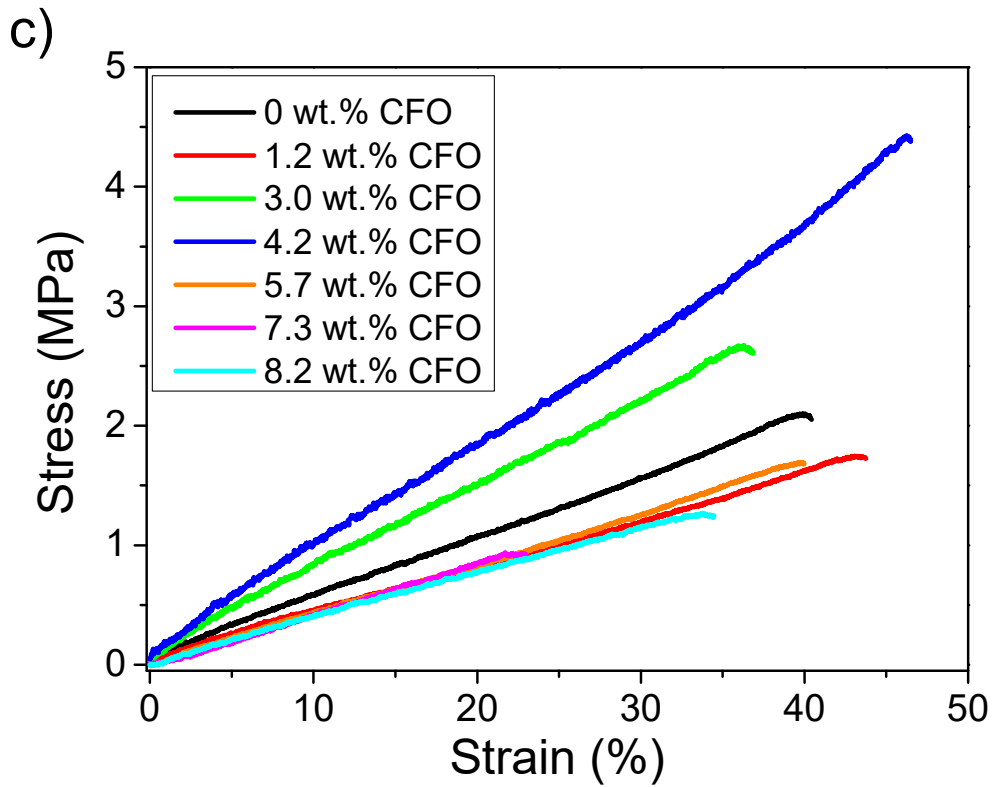
polyurethanes [65]. In particular, agglomeration has a significant role and can actuate at breaking points during the mechanical tests, which is detrimental for the mechanical properties of the material [66].

a)

b)

c)

d)

e)

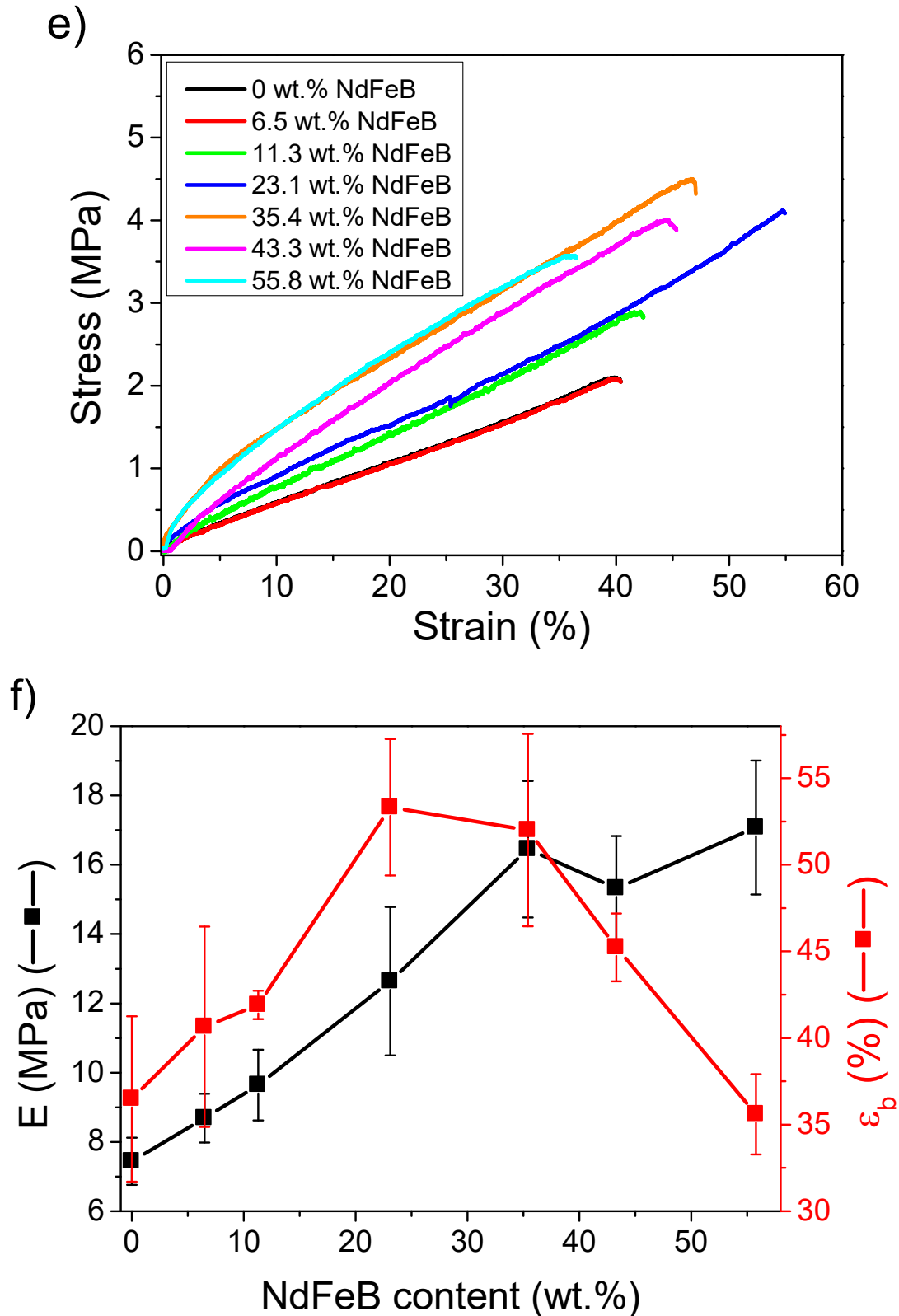

f)
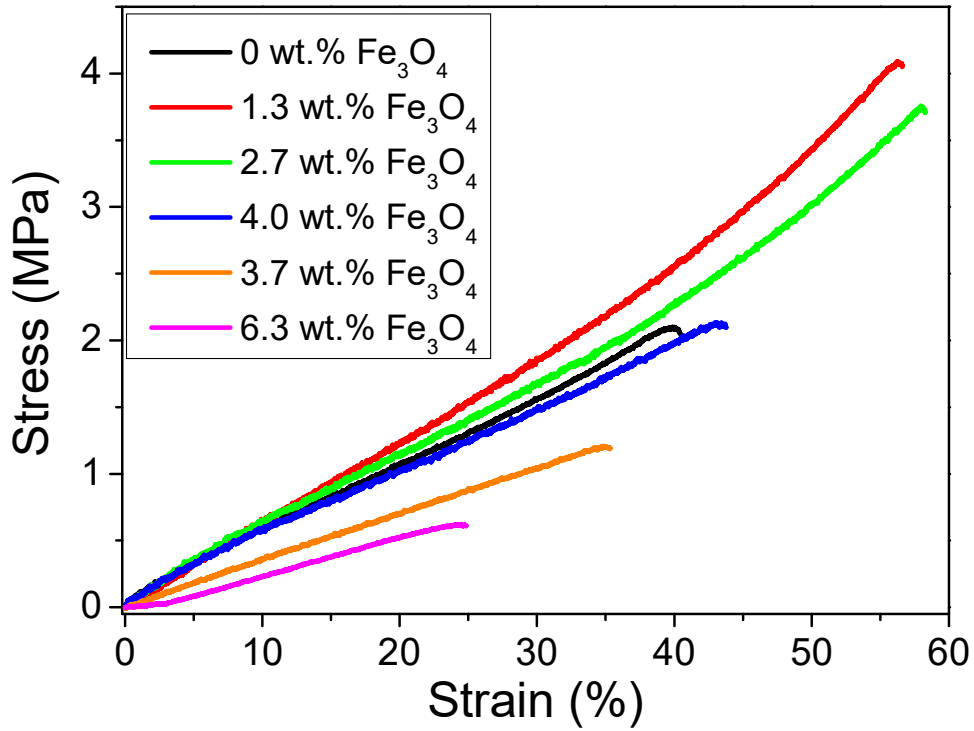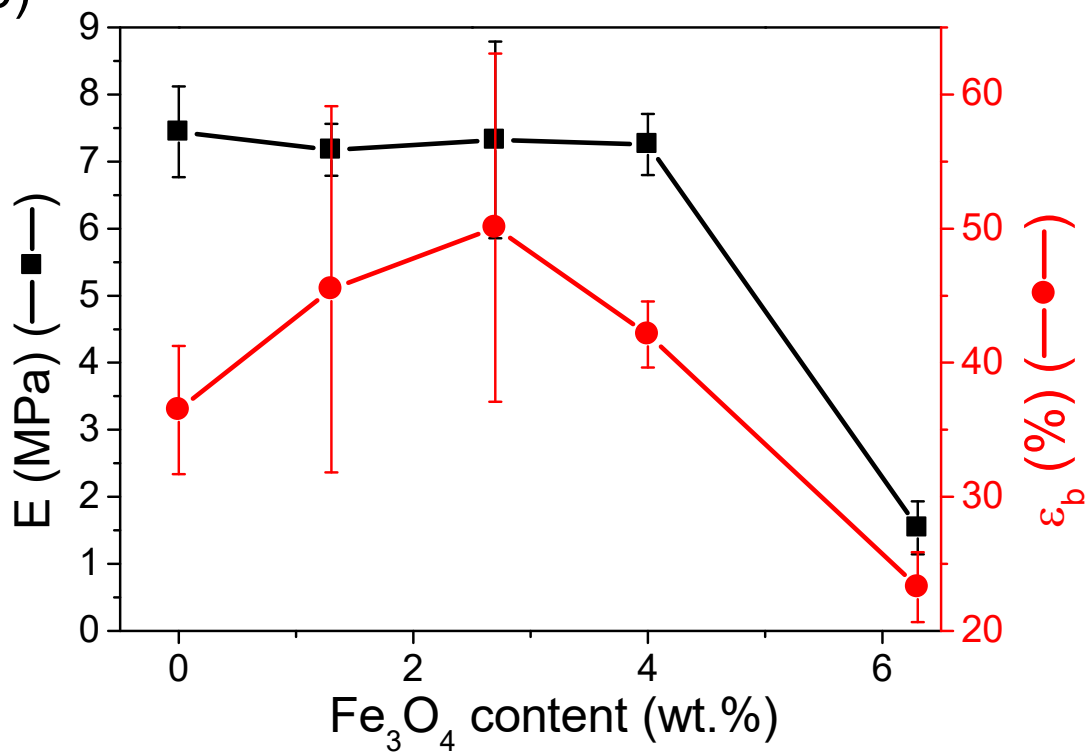
Figure 5.6 – Stress vs. strain mechanical characteristic curves for Fe_3O_4/PUA (a), CFO/PUA (c), NdFeB/PUA (e) and, secant modulus (E) and maximum deformation strain (ε_b) for same samples (b), (d) and (f), respectively.

Related to CFO/PUA nanoparticles (**Figures 5.6b and d**), when the filler amount increases, E increases up to 8.02 ± 2.92 MPa for 1.2 wt.% content sample and 9.23 ± 0.93 MPa for the 3.0 wt.% content sample. This effect is a consequence of the mechanical reinforcement of the inorganic nanoparticles into a polymer matrix [54], particularly in this case due to the high modulus of CFO nanoparticles (around 110 GPa) compared to the organic matrix [67]. When a higher amount of CFO is incorporated, E decreases to 3.54 ± 0.31 MPa and 5.08 ± 0.16 MPa for 7.3 wt.% and 8.2 wt.% content samples, respectively, which is related to small CFO nanoparticle aggregations that decrease the filler-matrix interactions and act as weak points in the material during the stress-strain test [66], as previously mentioned. Related to the maximum elongation, similar behaviour is observed, obtaining ε_b values that increase from 42.6 ± 7.9 % in 1.2 wt.% CFO sample to 46.4 ± 4.9 % in the 4.2 wt.% CFO one. When the highest amount of magnetic particles is added, the maximum strain value decreases up to 33.0 ± 2.7 %. Therefore, the addition of CFO nanoparticles, when compared to Fe_3O_4, induces a higher increase on the E values and similar maximum elongation.

In the case of NdFeB/PUA samples (**Figures 5.6c and f**), similarly to what occurs in the other studied composites, the magnetic fillers act as a reinforcement due to its high E value (round 150 GPa) compared with the PUA polymer [68]. Here, E increases for all NdFeB filler contents under evaluation and its value turns from 8.68 ± 0.70 MPa for the 6.3 wt.% sample to 9.64 ± 1.02 MPa for the 11.3 wt.%, to 12.64 ± 2.14 MPa for the 23.1 wt.% sample and finally 17.08 ± 1.93 for the sample with highest NdFeB content, similarly as other authors have reported [69].

On the other hand, ε_b first increases when the filler is added, being 40.6 ± 5.8 % for the 6.3 wt.% sample and 52.0 ± 5.6 % for the 35.4 wt.% sample. Then, for samples with the highest NdFeB content, a decrease is observed (45.2 ± 2.0 % for the 43.4 wt.% sample or 35.6 ± 2.3 % for the 55.8 wt.% sample). This effect is caused by the formation of agglomerates at high concentrations that can act as defects providing stress concentration around them and originating most of the cracks, voids and breaking points. Further, the presence of high content of magnetic particles hinders the chain elongation in the direction of the applied load, decreasing the elongation at breaks [70]. Comparing this magnetic filler to the iron oxide-based ones, higher modulus have been reached related to the high E value of the inorganic particles, their micron size and the higher amount of these on the composites

compared to Fe_3O_4 and CFO. Attending to the maximum elongation, similar results as in the best of the all studied cases are obtained using NdFeB alloy particles.

### 5.3.5. Electrical properties

Magnetic particle type [71], content [72] or their annealing treatments [73], as well as the organic component type and content [74] can have an important effect on the electrical properties of the magnetic composites. In this regard, the effect of magnetic particle type and content on the d.c. conductivity were evaluated by measuring the I-V curves of each sample, as represented in **Figure 5.8a, c and e**. The electrical conductivity of the magnetic composites as a function of the filler content is represent in **Figure 5.8b, d and f**.

All samples show a linear relationship between current and voltage, independently of the magnetic filler used or its content on the prepared films. However, at higher voltages (V > 8), a non-linear behaviour can be appreciated for the samples with higher filler contents, associated to interfacial contributions to the electrical conductivity [75].

Attending to the linear part of the I-V curves, the d.c. electrical conductivity of the samples increases with increasing filler content. Pristine PUA film presents a conductivity of about 2.3×10^{-11} S/m, when Fe_3O_4 particles are added, the electrical conductivity of the composite increases to 8.4×10^{-11} S/m for the 1.3 wt.% sample, 5.9×10^{-10} S/m for the 4.0 wt.% sample and finally 1.1×10^{-9} S/m for the sample with the highest content (a total increase on the electrical conductivity of two orders of magnitude). It has to be mentioned that the sample with the highest conductivity is also the one with the worst filler dispersion and, as it has been highlighted [72], iron oxide-based magnetic particles should have no influence on the electrical conductivity of magnetic nanocomposites. Thus, the increase on electrical conductivity of Fe_3O_4/PUA composites is associated to charges in the particle-polymer interfaces as well as to ionic conductivity contributions of the polymer matrix, which different degree of curing, depending on the filler content [54].

In the case of CFO/PUA samples, the addition of 3.0 wt.% magnetic particles induces an increase on the conductivity up to 1.3×10^{-10} S/m for the sample with highest filler content, due to the same effects discussed for the Fe_3O_4 samples [66].
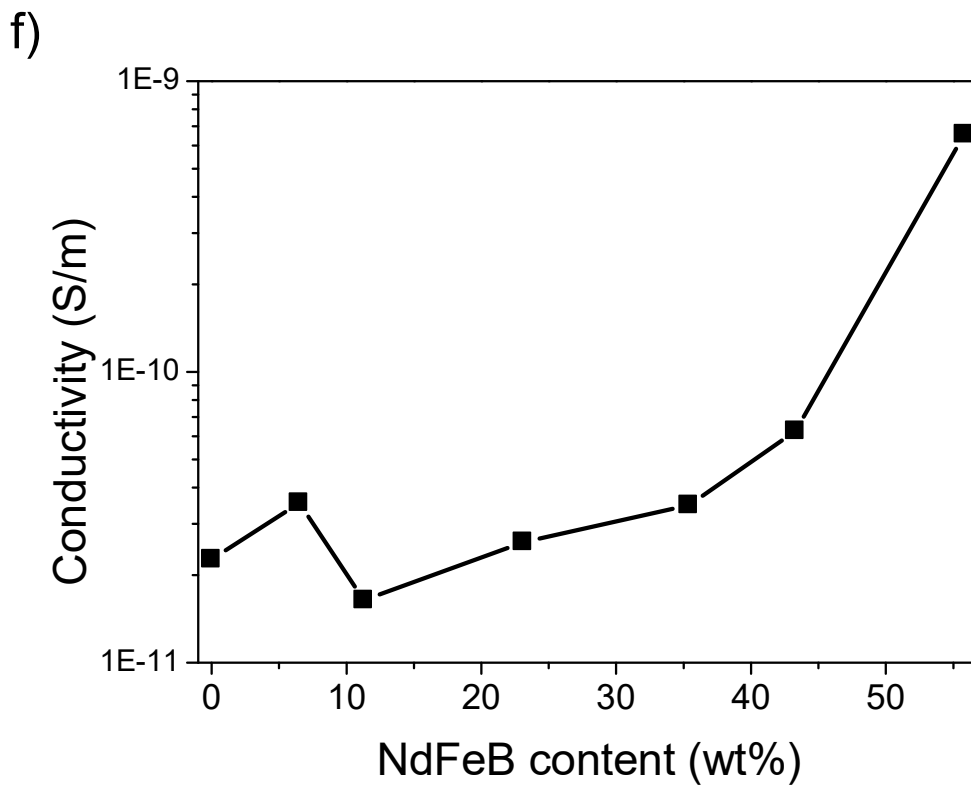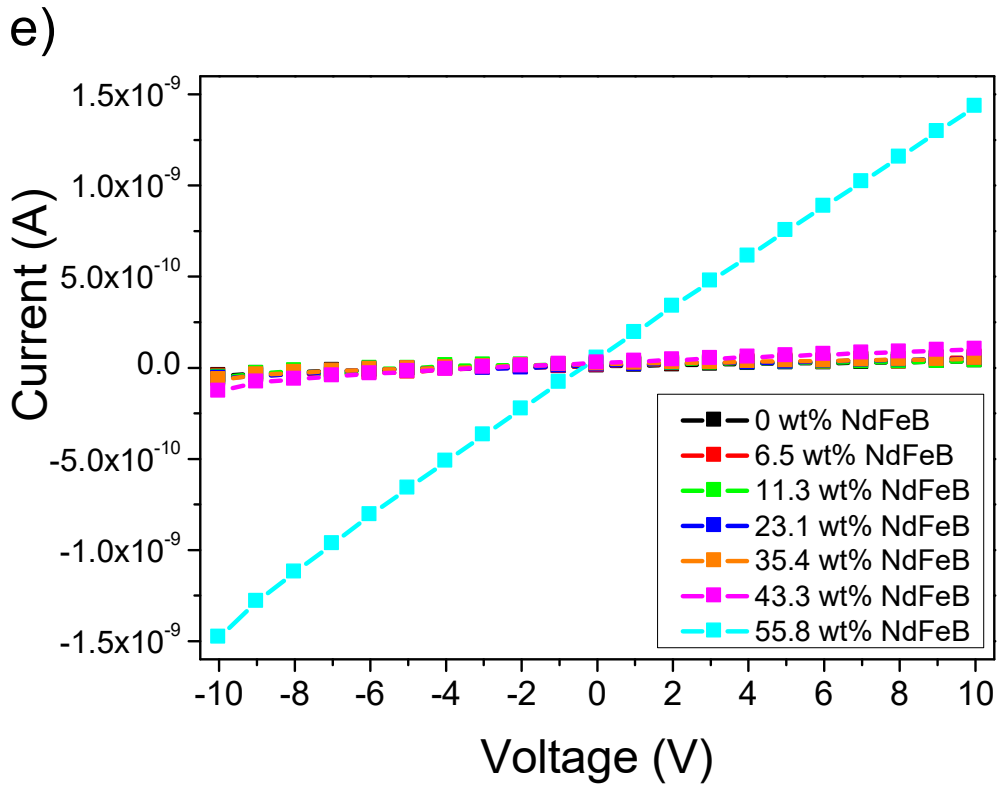
a)

b)

c)

d)

e)

f)
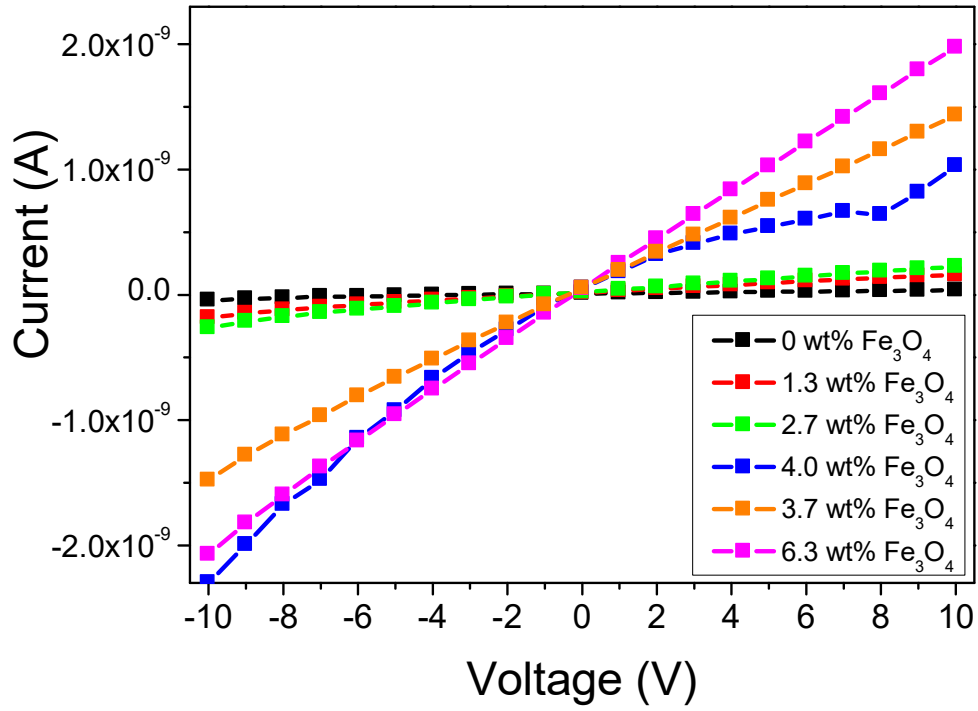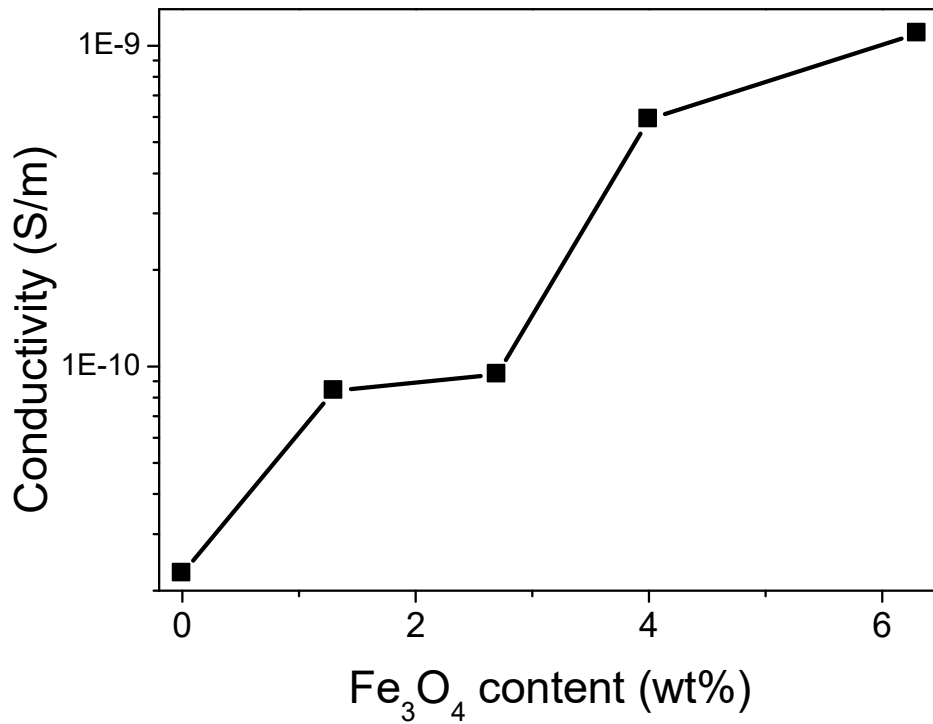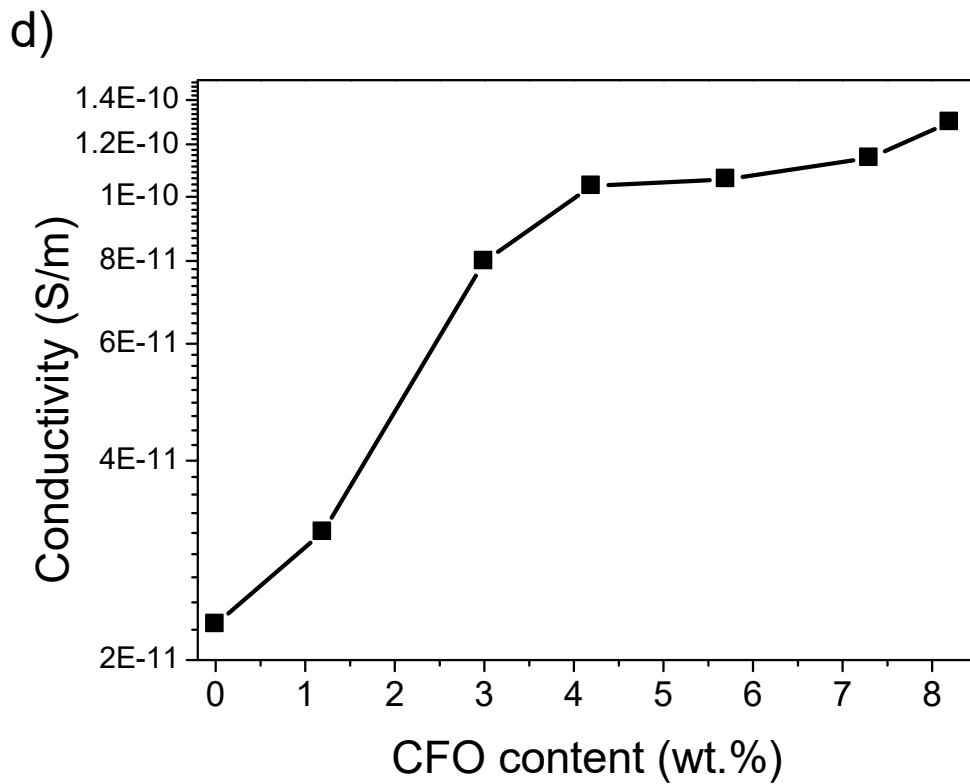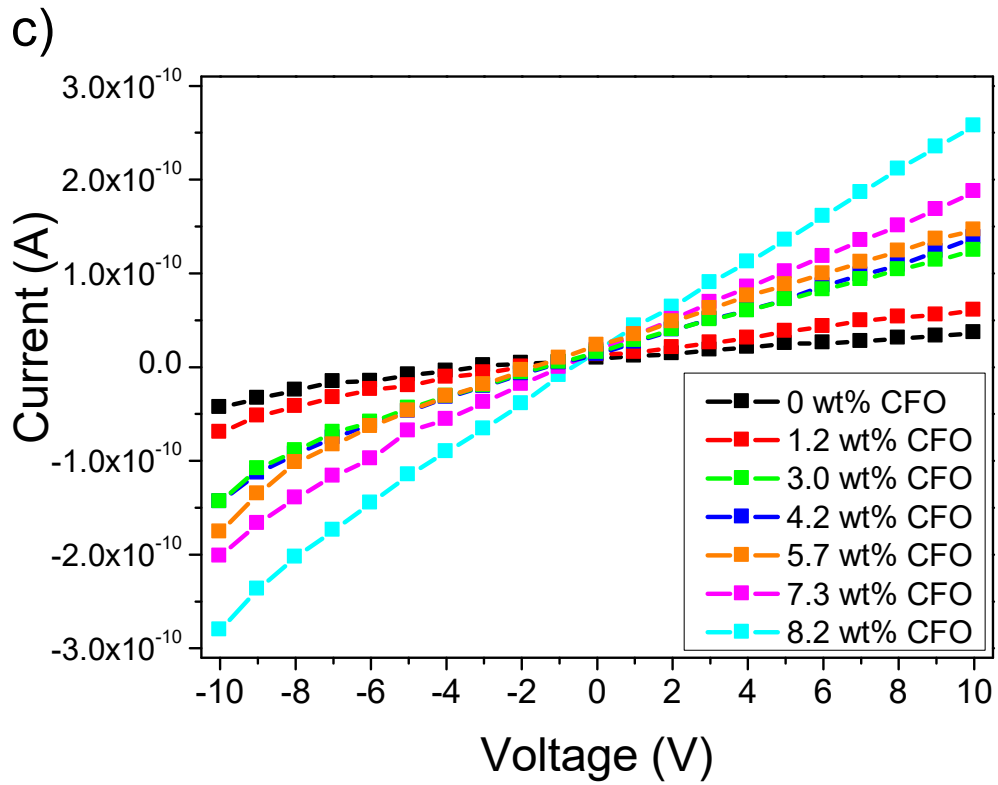
Figure 5.7 – I-V curves for Fe_3O_4/PUA (a), CFO/PUA (c) and NdFeB/PUA (e) samples and electrical conductivity (b), (d) and (f) for the same samples, respectively.

Related to NdFeB/PUA composites, the same electrical behaviour is obtained, with a maximum d.c. electrical conductivity of 6.6 x 10^{-10} S/m for the sample with the highest magnetic filler content of 55.8 wt.%. In this case, the slight increase in the electrical conductivity is directly associated to the increased filler content due to the intrinsic conductivity of the NdFeB particles [76]. On the other hand, no larger effects are observed due to the reasonable particle dispersion and for being below the percolation threshold, the PUA "encapsulating" the NdFeB micro-particles leading to an insulator behaviour [71].

5.3.6. Magnetic properties

The magnetic properties of the films were evaluated by measuring the hysteresis loops of each of the samples using a Vibrating Sample Magnetometer (VSM), at room temperature from -1.8 to 1.8 T. **Figures 5.7a, c and e** show the hysteresis loops at room temperature for different particle concentrations for the composite films with Fe_3O_4, CFO and NdFeB, respectively. Correspondingly, **Figures 5.7b, d and f** depict the change of relevant magnetic parameters namely, saturation magnetization (M_S) and remanence (M_R) as a function of the filler content.

As expected, the three samples show different magnetic behaviors. The first curve corresponds to the magnetite which is considered as a soft magnetic material, i.e. with high saturation magnetization (59.1 emu/g) and no coercivity. This is ascribed to the grain size (30 nm) since at that regime the system is in a superparamagnetic state, well below the estimated critical size: around 76 nm for cubic nanoparticles and 128 nm for spherical ones [77]. With respect to cobalt ferrite, the inclusion of Co in this kind of systems increases the magnetocrystalline anisotropy of the material, allowing developing coercivity of 2000 Oe for grain sizes of 35-55 nm, the threshold between single and multi-domain particles. Although M_S is slightly lower than for magnetite (42.4 emu/g) its remanence is above half the saturation magnetization, this value corresponding to a magnetic exchange-coupled system [78]. Following the description of the magnetic fillers, the metallic high-energy NdFeB hard magnetic material presents H_c = 7000 Oe, a saturation magnetization of 114 emu/g and a remanence higher than 0.75 emu/g, typically evidenced in these high-energy permanent magnets.

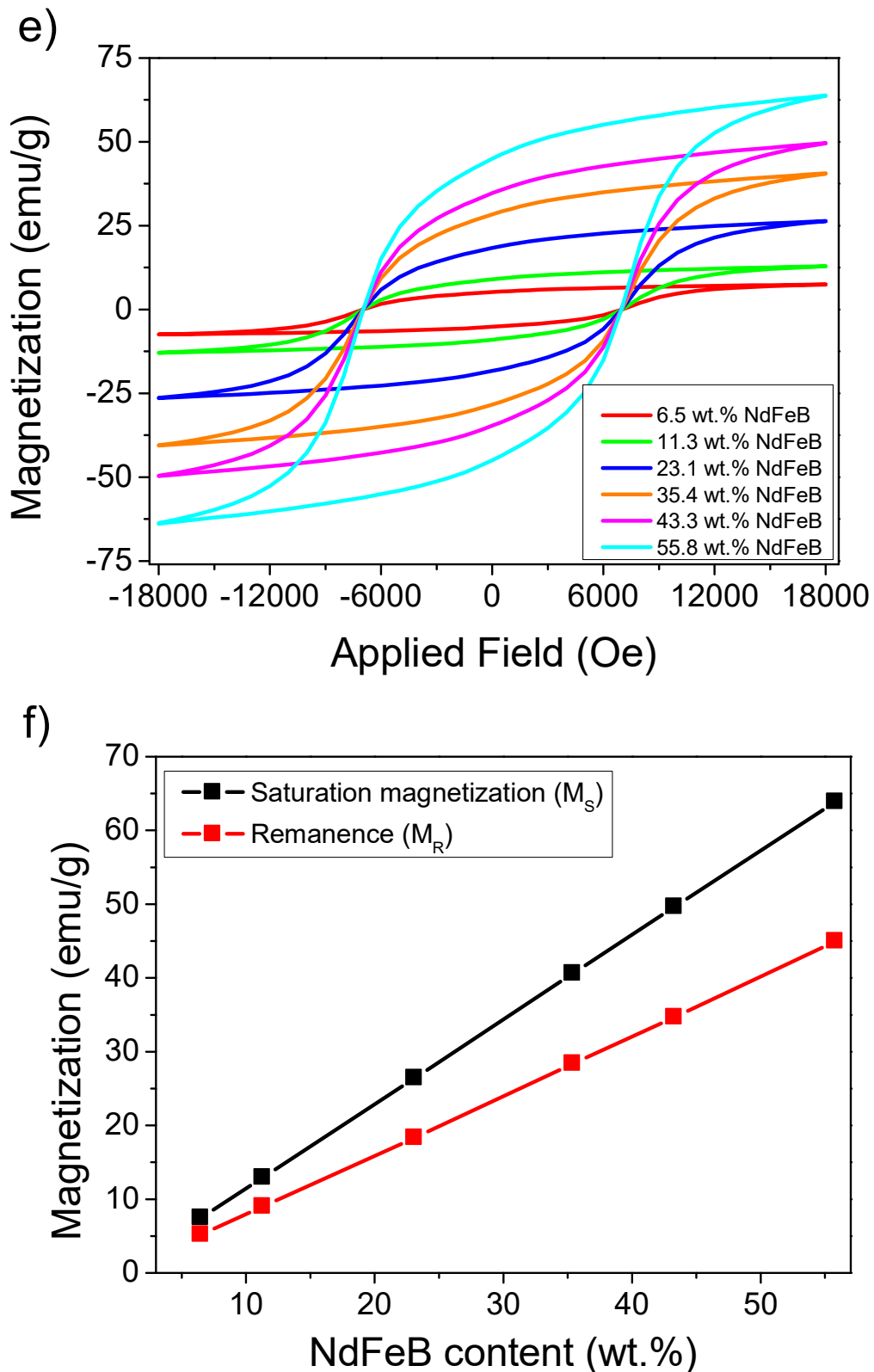a)

b)

c)

d)

e)

f)
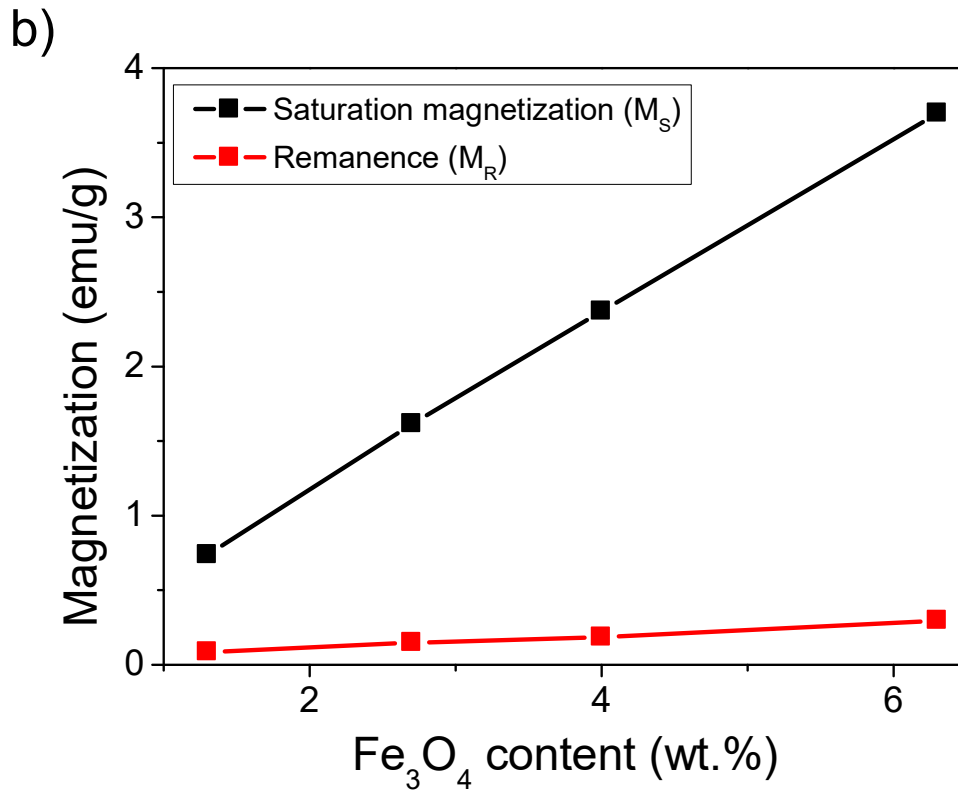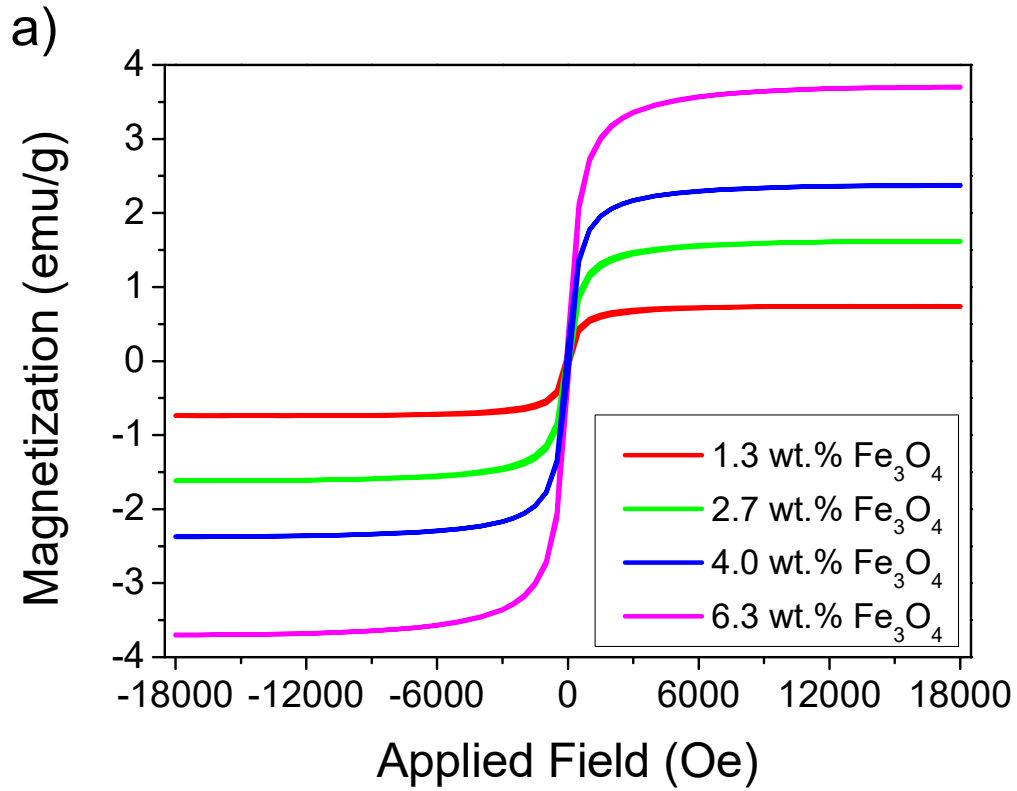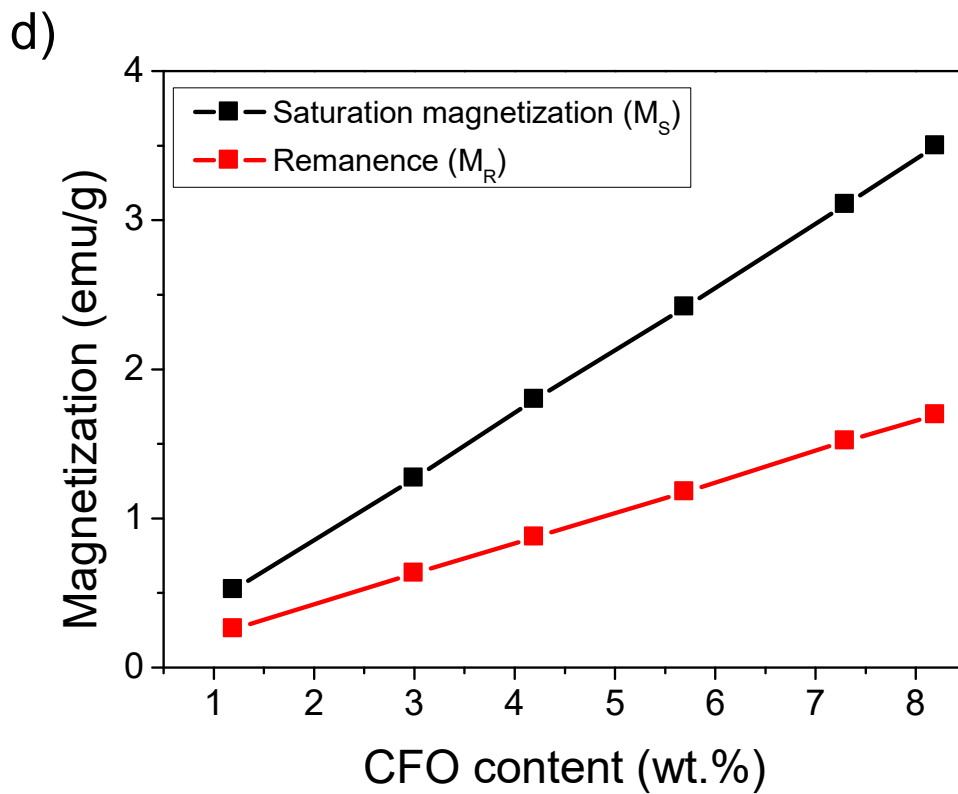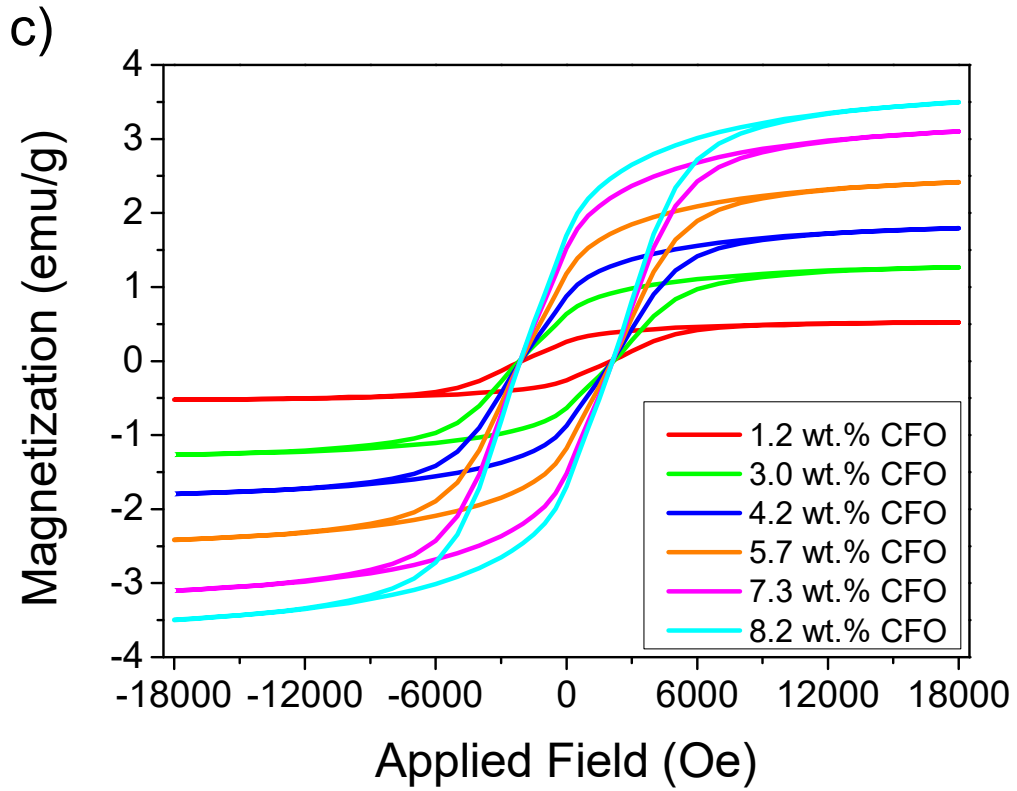
Figure 5.8 – Room-temperature hysteresis loops for Fe₃O₄/PUA (a), CFO/PUA (c) and NdFeB/PUA (e) and, magnetization saturation (M$_S$) and remanence (M$_R$) for same samples (b), (d) and (f), respectively.

Regarding the coercive field (H_c) of the magnetic composites, i.e. the magnetic field where the magnetization reversal takes place, another important parameter in magnetic materials, the coercive field remains constant for all the tested filler concentrations. Coercivity values are approximately 2.6 Oe, 2000 Oe and 7000 Oe for the composites with Fe_3O_4, CFO and NdFeB, respectively. The latter provides an insight of the magnetic hardness of these materials and, as expected, the largest is the rare earth-based magnet and the lower the soft ferrites.

The increased remanent magnetization is directly related to the magnetic filler content in the three composites. However, the normalized remanence (M_R/M_S) remains constant and, more importantly, is the same as the one for the bare magnetic materials. Thus, it can be suggested that the coercivity and the M_R/M_S ratio of the fillers remain unchanged, keeping the particles diluted into the polymeric matrix, with no spin canting effects or interaction between the particles and the polymer [79,80] or any reaction that could occur during the processing of the composite with the photocurable resin.

Regarding the evolution of the magnetic properties with filler concentration of the composites, a proportional trend is observed for all samples. First, the real composition of the magnetic filler into the composite was determined by comparing the saturation magnetization of the composites with the value obtained from the pristine magnetic material. These values of real compositions, which are summarized in the **Table 5.3** (experimental content), are quite close to the nominal ones. Mainly, two possible reasons are associated to the observed difference between the nominal and the real particle content; the solvent (monomer) evaporation and the filler saturation. Manufacturing of samples implies the mixing of additives by sonication at 35 ºC for 3h and then stirring for 2h, long enough to induce an evaporation of the monomeric compound. In addition, after polymerization of films and the subsequent washing process with 2-propanol, higher content samples released a liquid coming from the uncured regions of the samples and losing an undetermined content of particles associated with the filler saturation corresponding to the polymer with no acceptance of additional inorganic content.

The composites prepared with Fe_3O_4 exhibit very low remanence and the change is almost negligible when the nanoparticle content is increased, ranging from 0.09 emu/g for the 2 wt.% sample to 0.30 emu/g for the 10 wt.% one (**Figure 5.7b**). In the case of CFO, the remanence changes from 0.26 emu/g at 1 wt.% filler content to 1.69 emu/g at 6 wt.%, as

shown in **Figure 5.7d**. However, when the filler is NdFeB the values are much larger and the relative change is also higher (also due to the fact that the amount of filler added is much larger) and ranges from 5.18 emu/g for the 6 wt.% sample to 44.95 emu/g for the 50 wt.% sample (**Figure 5.7e**).

Table 5.3 – Saturation magnetization (M_S), remanence (M_R), coercive field (H_C) and normalized remanence (M_R/M_S)

Magnetic particle	Nominal content (wt.%)	Experimental content (wt.%)	M_S (emu/g)	M_R (emu/g)	H_C (T)	M_R/M_S
Fe$_3$O$_4$	100	100	59.1	6.26	0	0.11
	2	1.3	0.74	0.09	0	0.12
	4	2.7	1.62	0.15	0	0.10
	6	4.0	2.37	0.18	0	0.08
	8	3.7	2.16	0.16	0	0.08
	10	6.3	3.70	0.27	0	0.08
CFO	100	100	42.4	20.63	0.2	0.49
	1	1.2	0.52	0.26	0.2	0.5
	2	3.0	1.27	0.63	0.2	0.49
	3	4.2	1.80	0.87	0.2	0.49
	4	5.7	2.42	1.18	0.2	0.49
	5	7.3	3.10	1.52	0.2	0.49
	6	8.2	3.50	1.69	0.2	0.48
NdFeB	100	100	114	86.50	0.7	0.76
	6	6.5	7.46	5.18	0.7	0.7
	10	11.3	12.92	8.99	0.7	0.7
	20	23.1	26.40	18.32	0.7	0.7
	30	35.4	40.61	28.36	0.7	0.7
	40	43.3	49.64	34.67	0.7	0.7
	50	55.8	63.86	44.95	0.7	0.7

Comparing samples with experimental filler content about 6 wt.% for the three different fillers, it is observed a high stability of the magnetic particles after processing since they

keep proportionally constant in time. For example, remanence values of 0.27, 1.18 and 5.18 emu/g for Fe_3O_4, CFO and NdFeB, respectively, preserve the same M_R/M_S ratios: 0.08, 0.49 and 0.7. However, it is found a progressive dependence in other parameters such as T_g and R_p^{max}, being these 18.6, 20.7, 25.4 ºC and 0.1, 0.5, 2.9 s^{-1} for Fe_3O_4, CFO and NdFeB, respectively.

Taking into account that the SEM images show inhomogeneous dispersed nanoparticles within the matrix, possibly the region where the magnetic properties were measured in the nominal 6 wt.% sample has a larger concentration of magnetic material, or conversely, the sample containing Fe_3O_4 had lower particles concentration in the measured region.

As a final note, it is worth mentioning that the CFO and Fe_3O_4 nanoparticles show lower saturation magnetizations than the materials in bulk. In particular, bulk cobalt ferrite has a reported value of 80 emu/g [81] and for bulk magnetite is around 92 emu/g [77], while the particles had 42 emu/g and 59 emu/g, respectively. This trend for the saturation magnetization to decrease from bulk with decreasing size of the nanoparticles is well known, and experimental evidence suggests that the chemical environment that interact with the iron, as well as morphology considerations influence the magnetization to a great extent [82].

Thus, it is demonstrated that UV curable magnetic materials can be produced with a wide range of magnetic properties, for additive manufacturing of magnetic responsive components.

5.4. Conclusions

Photocurable magnetic materials based on polyurethane acrylated (PUA) polymer and different particles including magnetite (Fe_3O_4), cobalt ferrite oxide (CFO) and neodymium iron boron alloy (NdFeB) have been prepared by UV curing with filler variations between 1.3 and 6.3 wt.%, 1.2 and 8.2 wt.%, and 6.5 and 55.8 wt.% for Fe_3O_4, CFO and NdFeB, respectively. The polymerization conversion and photopolymerization rate strongly decrease with the inclusion of the magnetite based materials, allowing a total conversion of 20 % for higher filler content. The modification of the filler by adding cobalt (CFO) allows an increase on maximum particle content in the composite, showing a total conversion of 26 % for the 8.2 wt.% content sample. The influence on UV curing process is reduced by adding NdFeB

fillers, allowing composites with up to 55.8 wt.% filler content and a polymerization conversion of 58 %.

A suitable filler dispersion is obtained for the different magnetic particles with small agglomerated well dispersed along the polymer, which gains a flake-like morphology due to filler addition.

Magnetic composite films presented thermal properties (T_g) independent of the filler type and content, whereas the Young modulus decreases strongly for iron oxide-based composites. On the other hand, the Young modulus for NdFeB/PUA samples increase in all filler content range. The d.c. electrical conductivity is nearly independent on filler type and content, with a maximum of 1.0×10^{-9} S/m for the Fe_3O_4/PUA sample with 6.3 wt.% filler content.

Finally, magnetic properties demonstrate that particles did not suffer any degradation or oxidation process when included into the PUA matrix. Variable saturation magnetization, coercivity and remanence can be obtained by changing particle type and content. Thus, Fe_3O_4/PUA materials show a saturation magnetization up to 3.70 emu/g, remanence of 0.27 emu/g and no coercivity; while samples that contents magnetite with cobalt inclusion (CFO/PUA composites) show saturation magnetization up to 6.50 emu/g, remanence of 1.69 emu/g and coercivity of 2000 Oe. NdFeB/PUA composites showed a hard magnetic material behaviour with saturation magnetization up to 63.86 emu/g, remanence of 44.95 emu/ g and coercivity of 7000 Oe.

It is concluded that it is possible to develop magnetic materials processable by additive manufacturing with tailored magnetic response for specific application requirements.

5.5. References

[1]   C. Huber, G. Mitteramskogler, M. Goertler, I. Teliban, M. Groenefeld, D. Suess, Additive manufactured polymer-bonded isotropic ndfeb magnets by stereolithography and their comparison to fused filament fabricated and selective laser sintered magnets, Materials (Basel). 13 (2020) 1–8. doi:10.3390/MA13081916.

[2]   R. Polícia, A.C. Lima, N. Pereira, E. Calle, M. Vázquez, S. Lanceros-Mendez, P. Martins, Transparent Magnetoelectric Materials for Advanced Invisible Electronic Applications, Adv. Electron. Mater. 5 (2019) 1–5. doi:10.1002/aelm.201900280.

[3]   Y.S. Rim, S.H. Bae, H. Chen, N. De Marco, Y. Yang, Recent Progress in Materials and Devices toward Printable and Flexible Sensors, Adv. Mater. 28 (2016) 4415–4440. doi:10.1002/adma.201505118.

[4]   P. Ahangar, M.E. Cooke, M.H. Weber, D.H. Rosenzweig, Current biomedical applications of 3D printing and additive manufacturing, Appl. Sci. 9 (2019). doi:10.3390/app9081713.

[5]   B.F. Gonçalves, J. Oliveira, P. Costa, V. Correia, P. Martins, G. Botelho, S. Lanceros-Mendez, Development of water-based printable piezoresistive sensors for large strain applications, Compos. Part B Eng. 112 (2017) 344–352. doi:10.1016/j.compositesb.2016.12.047.

[6]   T. Nardi, M. Sangermano, Y. Leterrier, P. Allia, P. Tiberto, J.A.E. Månson, UV-cured transparent magnetic polymer nanocomposites, Polymer (Guildf). 54 (2013) 4472–4479. doi:10.1016/j.polymer.2013.06.052.

[7]   J. Nunes-Pereira, P. Sharma, L.C. Fernandes, J. Oliveira, J.A. Moreira, R.K. Sharma, S. Lanceros-Mendez, Poly(vinylidene fluoride) composites with carbon nanotubes decorated with metal nanoparticles, Compos. Part B Eng. 142 (2018) 1–8. doi:10.1016/j.compositesb.2017.12.047.

[8]   B. Jiang, J. Iocozzia, L. Zhao, H. Zhang, Y.W. Harn, Y. Chen, Z. Lin, Barium titanate at the nanoscale: Controlled synthesis and dielectric and ferroelectric properties, Chem. Soc. Rev. 48 (2019) 1194–1228. doi:10.1039/c8cs00583d.

[9]   P. Martins, A. Lasheras, J. Gutierrez, J.M. Barandiaran, I. Orue, S. Lanceros-Mendez,

Optimizing piezoelectric and magnetoelectric responses on CoFe 2O4/P(VDF-TrFE) nanocomposites, J. Phys. D. Appl. Phys. 44 (2011) 0–7. doi:10.1088/0022-3727/44/49/495303.

[10]   Y. Kim, H. Yuk, R. Zhao, S.A. Chester, X. Zhao, Printing ferromagnetic domains for untethered fast-transforming soft materials, Nature. 558 (2018) 274–279. doi:10.1038/s41586-018-0185-0.

[11]   M.S. Cao, J. Yang, W.L. Song, D.Q. Zhang, B. Wen, H.B. Jin, Z.L. Hou, J. Yuan, Ferroferric oxide/multiwalled carbon nanotube vs polyaniline/ferroferric oxide/multiwalled carbon nanotube multiheterostructures for highly effective microwave absorption, ACS Appl. Mater. Interfaces. 4 (2012) 6949–6956. doi:10.1021/am3021069.

[12]   A. Shen, C.P. Bailey, A.W.K. Ma, S. Dardona, UV-assisted direct write of polymer-bonded magnets, J. Magn. Magn. Mater. 462 (2018) 220–225. doi:10.1016/j.jmmm.2018.03.073.

[13]   M. Wang, H. Singh, T.A. Hatton, G.C. Rutledge, Field-responsive superparamagnetic composite nanofibers by electrospinning, Polymer (Guildf). 45 (2004) 5505–5514. doi:10.1016/j.polymer.2004.06.013.

[14]   S. Lantean, G. Barrera, C.F. Pirri, P. Tiberto, M. Sangermano, I. Roppolo, G. Rizza, 3D Printing of Magnetoresponsive Polymeric Materials with Tunable Mechanical and Magnetic Properties by Digital Light Processing, Adv. Mater. Technol. 4 (2019) 1–10. doi:10.1002/admt.201900505.

[15]   D. Abliz, Y. Duan, L. Steuernagel, L. Xie, D. Li, G. Ziegmann, Curing methods for advanced polymer composites -A review, Polym. Polym. Compos. 21 (2013) 341–348. doi:10.1177/096739111302100602.

[16]   G. Siqueira, D. Kokkinis, R. Libanori, M.K. Hausmann, A.S. Gladman, A. Neels, P. Tingaut, T. Zimmermann, J.A. Lewis, A.R. Studart, Cellulose Nanocrystal Inks for 3D Printing of Textured Cellular Architectures, Adv. Funct. Mater. 27 (2017). doi:10.1002/adfm.201604619.

[17]   A.J. Bandodkar, C.S. López, A. Mohanan, V. Mohan, L. Yin, R. Kumar, J. Wang, All-printed magnetically self-healing electrochemical devices, Appl. Sci. Eng.

(2016).

[18]   R. Brisse, R. Faddoul, T. Bourgeteau, D. Tondelier, J. Leroy, S. Campidelli, T. Berthelot, B. Geffroy, B. Jousselme, Inkjet printing NiO-based p-Type dye-sensitized solar cells, ACS Appl. Mater. Interfaces. 9 (2017) 2369–2377. doi:10.1021/acsami.6b12912.

[19]   K. Rajan, I. Roppolo, A. Chiappone, S. Bocchini, D. Perrone, A. Chiolerio, Silver nanoparticle ink technology: State of the art, Nanotechnol. Sci. Appl. 9 (2016). doi:10.2147/NSA.S68080.

[20]   L.M. Bollig, P.J. Hilpisch, G.S. Mowry, B.B. Nelson-Cheeseman, 3D printed magnetic polymer composite transformers, J. Magn. Magn. Mater. 442 (2017) 97–101. doi:10.1016/j.jmmm.2017.06.070.

[21]   G. Chatzipirpiridis, S. Gervasoni, C. Fischer, O. Ergeneman, E. Pellicer, B.J. Nelson, S. Pané, 3D Printing of Thermoplastic-Bonded Soft- and Hard-Magnetic Composites: Magnetically Tuneable Architectures and Functional Devices, Adv. Intell. Syst. 1 (2019) 1900069. doi:10.1002/aisy.201900069.

[22]   Q. Shi, H. Chen, K. Pang, Y. Yao, G. Su, F. Liang, N. Zhou, Permalloy/Polydimethylsiloxane Nanocomposite Inks for Multimaterial Direct Ink Writing of Gigahertz Electromagnetic Structures, J. Mater. Chem. C. (2020). doi:10.1039/d0tc03244a.

[23]   H. Song, J. Spencer, A. Jander, J. Nielsen, J. Stasiak, V. Kasperchik, P. Dhagat, Inkjet printing of magnetic materials with aligned anisotropy, J. Appl. Phys. 115 (2014) 17E308. doi:10.1063/1.4863168.

[24]   P. Martins, Y. V. Kolen'Ko, J. Rivas, S. Lanceros-Mendez, Tailored Magnetic and Magnetoelectric Responses of Polymer-Based Composites, ACS Appl. Mater. Interfaces. 7 (2015) 15017–15022. doi:10.1021/acsami.5b04102.

[25]   A. Alafaghani, A. Qattawi, M.A. Ablat, Design Consideration for Additive Manufacturing: Fused Deposition Modelling, Open J. Appl. Sci. 07 (2017) 291–318. doi:10.4236/ojapps.2017.76024.

[26]   C. Mendes-Felipe, J. Oliveira, I. Etxebarria, J.L. Vilas-Vilela, S. Lanceros-Mendez,

State-of-the-Art and Future Challenges of UV Curable Polymer-Based Smart Materials for Printing Technologies, Adv. Mater. Technol. 4 (2019) 1–16. doi:10.1002/admt.201800618.

[27] V. Shukla, M. Bajpai, D.K. Singh, M. Singh, R. Shukla, Review of basic chemistry of UV-curing technology, Pigment Resin Technol. 33 (2004) 272–279. doi:10.1108/03699420410560461.

[28] A. Endruweit, M.S. Johnson, A.C. Long, Curing of Composite Components by Ultraviolet Radiation: A Review, Polym. Compos. 27 (2006) 119–128. doi:10.1002/pc.20166.

[29] C. Felipe-Mendes, L. Ruiz-Rubio, J.L. Vilas-Vilela, Biomaterials obtained by photopolymerization: from UV to two photon, Emergent Mater. 3 (2020) 453–468. doi:10.1007/s42247-020-00114-0.

[30] Y. Xu, X. Wu, X. Guo, B. Kong, M. Zhang, X. Qian, S. Mi, W. Sun, The Boom in 3D-Printed Sensor Technology, China, 2017. doi:10.3390/s17051166.

[31] D. McCoul, S. Rosset, S. Schlatter, H. Shea, Inkjet 3D printing of UV and thermal cure silicone elastomers for dielectric elastomer actuators, Smart Mater. Struct. 26 (2017). doi:10.1088/1361-665X/aa9695.

[32] C. Mendes-Felipe, J. Oliveira, P. Costa, L. Ruiz-Rubio, A. Iregui, A. González, J.L. Vilas, S. Lanceros-Mendez, Stimuli responsive UV cured polyurethane acrylated/carbon nanotube composites for piezoresistive sensing, Eur. Polym. J. 120 (2019) 109226. doi:10.1016/j.eurpolymj.2019.109226.

[33] G. Malucelli, A. Fioravanti, L. Francioso, C. De Pascali, M.A. Signore, M.C. Carotta, A. Bonanno, D. Duraccio, Preparation and characterization of UV-cured composite films containing ZnO nanostructures: Effect of filler geometric features on piezoelectric response, Prog. Org. Coatings. 109 (2017) 45–54. doi:10.1016/j.porgcoat.2017.04.020.

[34] D.Y. Choi, Y.S. Oh, D. Han, S. Yoo, H.J. Sung, S.S. Kim, Highly Conductive, Bendable, Embedded Ag Nanoparticle Wire Arrays Via Convective Self-Assembly: Hybridization into Ag Nanowire Transparent Conductors, Adv. Funct. Mater. 25 (2015) 3888–3898. doi:10.1002/adfm.201500677.

[35] E.M. Hamad, S.E.R. Bilatto, N.Y. Adly, D.S. Correa, B. Wolfrum, M.J. Schöning, A. Offenhäusser, A. Yakushenko, Inkjet printing of UV-curable adhesive and dielectric inks for microfluidic devices, Lab Chip. 16 (2016) 70–74. doi:10.1039/c5lc01195g.

[36] M.N. Guzik, K.M. Golasiński, F.J. Pedrosa, P. Jenuš, A. Bollero, B.C. Hauback, S. Deledda, Influence of ultra-short cryomilling on the microstructural and magnetic properties of cobalt ferrite, J. Alloys Compd. 721 (2017) 440–448. doi:10.1016/j.jallcom.2017.05.290.

[37] U. Schwertmann, R.M. Cornell, Iron Oxides: Form Nature to Applications, Weinheim, Germany, 2016.

[38] I.C. Nlebedim, J.E. Snyder, A.J. Moses, D.C. Jiles, Dependence of the magnetic and magnetoelastic properties of cobalt ferrite on processing parameters, J. Magn. Magn. Mater. 322 (2010) 3938–3942. doi:10.1016/j.jmmm.2010.08.026.

[39] P. Allia, G. Barrera, P. Tiberto, T. Nardi, Y. Leterrier, M. Sangermano, Fe3O4 nanoparticles and nanocomposites with potential application in biomedicine and in communication technologies: Nanoparticle aggregation, interaction, and effective magnetic anisotropy, J. Appl. Phys. 116 (2014). doi:10.1063/1.4895837.

[40] J.M.D. Coey, Hard magnetic materials: A perspective, IEEE Trans. Magn. 47 (2011) 4671–4681. doi:10.1109/TMAG.2011.2166975.

[41] B.G. Compton, J.W. Kemp, T. V. Novikov, R.C. Pack, C.I. Nlebedim, C.E. Duty, O. Rios, M.P. Paranthaman, Direct-Write 3D-Printing of NdFeB Bonded Magnets Brett, Mater. Manuf. Process. 33 (2018) 1–17. doi:10.1017/CBO9781107415324.004.

[42] K.M. Goodenough, F. Wall, D. Merriman, The Rare Earth Elements: Demand, Global Resources, and Challenges for Resourcing Future Generations, Nat. Resour. Res. 27 (2018) 201–216. doi:10.1007/s11053-017-9336-5.

[43] M. Sangermano, P. Allia, P. Tiberto, G. Barrera, F. Bondioli, N. Florini, M. Messori, Photo-cured epoxy networks functionalized with Fe3O4 generated by non-hydrolytic sol-gel process, Macromol. Chem. Phys. 214 (2013) 508–516. doi:10.1002/macp.201200494.

[44] A. Chiolerio, P. Allia, P. Tiberto, L. Suber, G. Marchegiani, M. Sangermano,

Magnetic properties of acrylic UV-cured films containing magnetite nanoparticles, Mater. Res. Soc. Symp. Proc. 1312 (2011) 293–299. doi:10.1557/opl.2011.481.

[45]   P. Allia, P. Tiberto, M. Coisson, A. Chiolerio, F. Celegato, F. Vinai, M. Sangermano, L. Suber, G. Marchegiani, Evidence for magnetic interactions among magnetite nanoparticles dispersed in photoreticulated PEGDA-600 matrix, J. Nanoparticle Res. 13 (2011) 5615–5626. doi:10.1007/s11051-011-0249-7.

[46]   M. Sangermano, L. Vescovo, N. Pepino, A. Chiolerio, P. Allia, P. Tiberto, M. Coisson, L. Suber, G. Marchegiani, Photoinitiator-free UV-cured acrylic coatings containing magnetite nanoparticles, Macromol. Chem. Phys. 211 (2010) 2530–2535. doi:10.1002/macp.201000444.

[47]   M. Sangermano, A. Priola, G. Kortaberria, A. Jimeno, I. Garcia, I. Mondragon, G. Rizza, Photopolymerization of epoxy coatings containing iron-oxide nanoparticles, Macromol. Mater. Eng. 292 (2007) 956–961. doi:10.1002/mame.200700093.

[48]   A. Shen, X. Peng, C.P. Bailey, S. Dardona, A.W.K. Ma, 3D printing of polymer-bonded magnets from highly concentrated, plate-like particle suspensions, Mater. Des. 183 (2019) 108133. doi:10.1016/j.matdes.2019.108133.

[49]   H. Xiang, X. Wang, G. Lin, L. Xi, Y. Yang, D. Lei, H. Dong, J. Su, Y. Cui, X. Liu, Preparation, characterization and application of UV-curable flexible hyperbranched polyurethane acrylate, Polymers (Basel). 9 (2017). doi:10.3390/polym9110552.

[50]   F. Wang, J.Q. Hu, W.P. Tu, Study on microstructure of UV-curable polyurethane acrylate films, Prog. Org. Coatings. 62 (2008) 245–250. doi:10.1016/j.porgcoat.2007.12.005.

[51]   H. Xu, F. Qiu, Y. Wang, W. Wu, D. Yang, Q. Guo, UV-curable waterborne polyurethane-acrylate: Preparation, characterization and properties, Prog. Org. Coatings. 73 (2012) 47–53. doi:10.1016/j.porgcoat.2011.08.019.

[52]   S.J. Choi, H.N. Kim, W.G. Bae, K.Y. Suh, Modulus- and surface energy-tunable ultraviolet-curable polyurethane acrylate: Properties and applications, J. Mater. Chem. 21 (2011) 14325–14335. doi:10.1039/c1jm12201k.

[53]   C. Mendes-Felipe, J.C. Barbosa, S. Gonçalves, N. Pereira, C.M. Costa, J.L. Vilas-

Vilela, S. Lanceros-Mendez, High dielectric constant UV curable polyurethane acrylate/indium tin oxide composites for capacitive sensing, Compos. Sci. Technol. 199 (2020). doi:10.1016/j.compscitech.2020.108363.

[54] C. Mendes-Felipe, T. Rodrigues-Marinho, J.L. Vilas, S. Lanceros-Mendez, UV curable nanocomposites with tailored dielectric response, Polymer (Guildf). 196 (2020). doi:10.1016/j.polymer.2020.122498.

[55] Y.P. Yew, K. Shameli, M. Miyake, N. Kuwano, N.B. Bt Ahmad Khairudin, S.E. Bt Mohamad, K.X. Lee, Green Synthesis of Magnetite (Fe3O4) Nanoparticles Using Seaweed (Kappaphycus alvarezii) Extract, Nanoscale Res. Lett. 11 (2016). doi:10.1186/s11671-016-1498-2.

[56] R. Matsuno, K. Yamamoto, H. Otsuka, A. Takahara, Polystyrene- and poly(3-vinylpyridine)-grafted magnetite nanoparticles prepared through surface-initiated nitroxide-mediated radical polymerization, Macromolecules. 37 (2004) 2203–2209. doi:10.1021/ma035523g.

[57] M.W. Mushtaq, M. Imran, S. Bashir, F. Kanwal, L. Mitu, Synthesis , structural and biological studies of cobalt ferrite nanoparticles, Bulg. Chem. Commun. 48 (2015) 565–570.

[58] F. Dong, S. Maganty, S.J. Meschter, J. Cho, Effects of curing conditions on structural evolution and mechanical properties of UV-curable polyurethane acrylate coatings, Prog. Org. Coatings. 114 (2018) 58–67. doi:10.1016/j.porgcoat.2017.09.018.

[59] R. Kunanuruksapong, A. Sirivat, Electrical properties and electromechanical responses of acrylic elastomers and styrene copolymers: Effect of temperature, Appl. Phys. A Mater. Sci. Process. 92 (2008) 313–320. doi:10.1007/s00339-008-4513-3.

[60] E.S. Jang, S.B. Khan, J. Seo, Y.H. Nam, W.J. Choi, K. Akhtar, H. Han, Synthesis and characterization of novel UV-curable polyurethane-clay nanohybrid: Influence of organically modified layered silicates on the properties of polyurethane, Prog. Org. Coatings. 71 (2011) 36–42. doi:10.1016/j.porgcoat.2010.12.007.

[61] G. Mashouf, M. Ebrahimi, S. Bastani, UV curable urethane acrylate coatings formulation: Experimental design approach, Pigment Resin Technol. 43 (2014) 61–68. doi:10.1108/PRT-10-2012-0072.

[62]   H. Pan, M. Xu, X. Liu, Preparation of poly (arylene ether nitrile)/NzdFeB composite film with excellent thermal properties and tensile strength, IOP Conf. Ser. Mater. Sci. Eng. 274 (2017). doi:10.1088/1757-899X/274/1/012089.

[63]   D. Chicot, J. Mendoza, A. Zaoui, G. Louis, V. Lepingle, F. Roudet, J. Lesage, Mechanical properties of magnetite (Fe3O4), hematite (α-Fe2O3) and goethite (α-FeO·OH) by instrumented indentation and molecular dynamics analysis, Mater. Chem. Phys. 129 (2011) 862–870. doi:10.1016/j.matchemphys.2011.05.056.

[64]   A. Mohammadi, M. Barikani, M. Barmar, Synthesis and investigation of thermal and mechanical properties of in situ prepared biocompatible Fe3O4/polyurethane elastomer nanocomposites, Polym. Bull. 72 (2014) 219–234. doi:10.1007/s00289-014-1268-1.

[65]   A. Mohammadi, M. Barikani, M. Barmar, Effect of surface modification of Fe3O4 nanoparticles on thermal and mechanical properties of magnetic polyurethane elastomer nanocomposites, J. Mater. Sci. 48 (2013) 7493–7502. doi:10.1007/s10853-013-7563-7.

[66]   M. Rincón-Iglesias, E. Lizundia, S. Lanceros-Méndez, Water-Soluble Cellulose Derivatives as Suitable Matrices for Multifunctional Materials, Biomacromolecules. 20 (2019) 2786–2795. doi:10.1021/acs.biomac.9b00574.

[67]   K. V. Chandekar, K.M. Kant, Size-strain analysis and elastic properties of CoFe2O4 nanoplatelets by hydrothermal method, J. Mol. Struct. 1154 (2018) 418–427. doi:10.1016/j.molstruc.2017.09.104.

[68]   P. Vedrine, P. Tixador, Y. Brunet, J.C. Bobo, A. Fevrier, A. Leriche, Mechanical characteristics of NdFeB magnets at low temperature, Cryogenics (Guildf). 31 (1991) 51–53. doi:10.1016/0011-2275(91)90190-8.

[69]   A. Grujić, N. Talijan, D. Stojanović, J. Stajić-Trošić, Z. Burzić, L. Balanović, R. Aleksić, Magnetic and Dynamic Mechanical Properties of Nd-Fe-B Composite Materials with Polymer Matrix, J. Min. Metall. Sect. B Metall. 46 (2010) 25–32. doi:10.2298/JMMB1001025G.

[70]   L. Pigliaru, M. Rinaldi, L. Ciccacci, A. Norman, T. Rohr, T. Ghidini, F. Nanni, 3D printing of high performance polymer-bonded PEEK-NdFeB magnetic composite

materials, Funct. Compos. Mater. 1 (2020) 1–17. doi:10.1186/s42252-020-00006-w.

[71] T.J. Fiske, H.S. Gokturk, D.M. Kalyon, Percolation in magnetic composites, J. Mater. Sci. 32 (1997) 5551–5560. doi:10.1023/A:1018620407013.

[72] Y. Xiaotun, X. Lingge, N.S. Choon, C.S.O. Hardy, Magnetic and electrical properties of polypyrrole-coated γ-Fe2O3 nanocomposite particles, Nanotechnology. 14 (2003) 624–629.

[73] H. Shokrollahi, K. Janghorban, Different annealing treatments for improvement of magnetic and electrical properties of soft magnetic composites, J. Magn. Magn. Mater. 317 (2007) 61–67. doi:10.1016/j.jmmm.2007.04.011.

[74] M.M. Dias, H.J. Mozetic, J.S. Barboza, R.M. Martins, L. Pelegrini, L. Schaeffer, Influence of resin type and content on electrical and magnetic properties of soft magnetic composites (SMCs), Powder Technol. 237 (2013) 213–220. doi:10.1016/j.powtec.2013.01.006.

[75] A. Correia, J.L. Costa-Krämer, Y.W. Zhao, N. García, Non-linear contribution to intensity-voltage characteristics of gold nanowires, Nanostructured Mater. 12 (1999) 1015–1020. doi:10.1016/S0965-9773(99)00290-1.

[76] P. Jantarattana, C. Sirisathitkul, A. Hunyek, S. Maensiri, Electric and magnetic properties of recycled NdFeB-natural rubber composites, Adv. Compos. Lett. 20 (2011) 48–51. doi:10.1177/096369351102000203.

[77] Q. Li, C.W. Kartikowati, S. Horie, T. Ogi, T. Iwaki, K. Okuyama, Correlation between particle size/domain structure and magnetic properties of highly crystalline Fe3O4 nanoparticles, Sci. Rep. 7 (2017) 1–4. doi:10.1038/s41598-017-09897-5.

[78] A. López-Ortega, E. Lottini, C.D.J. Fernández, C. Sangregorio, Exploring the Magnetic Properties of Cobalt-Ferrite Nanoparticles for the Development of a Rare-Earth-Free Permanent Magnet, Chem. Mater. 27 (2015) 4048–4056. doi:10.1021/acs.chemmater.5b01034.

[79] S.P. Gubin, Y.A. Koksharov, G.B. Khomutov, G.Y. Yurkov, Magnetic nanoparticles: Preparation, structure and properties, Usp. Khim. 74 (2005) 539–574. doi:10.1070/rc2005v074n06abeh000897.

[80]   A. V. Bychkova, M.A. Rosenfeld, V.B. Leonova, O.N. Sorokina, A.L. Kovarski, Magnetic nanoparticles, Biosci. Methodol. Phys. Chem. An Eng. Mol. Approach. (2013) 315–333. doi:10.3390/magnetochemistry6010006.

[81]   T. George, A.T. Sunny, T. Varghese, Magnetic properties of cobalt ferrite nanoparticles synthesized by sol-gel method, IOP Conf. Ser. Mater. Sci. Eng. 73 (2015) 2–5. doi:10.1088/1757-899X/73/1/012050.

[82]   D.L. Huber, Synthesis, properties, and applications of iron nanoparticles, Small. 1 (2005) 482–501. doi:10.1002/smll.200500006.

Chapter 6

Photocurable thermally activated humidity sensors

Photocurable thermochromic and humidity responsive materials based on polyurethane acrylated (PUA) and bis(1-butyl-3-methylimidazolium) tetrachloronickelate ([Bmim]$_2$[NiCl$_4$]) ionic liquid (IL) have been developed. The influence of IL content on the photopolymerization process, morphology, Young modulus and electrical conductivity of the materials was evaluated. All composites exhibit humidity dependent thermochromism from colourless to blue independently of the IL content. Thus, suitable materials for humidity sensors have been developed.

6.1. Introduction

Additive manufacturing (AM), considered one of the main cornerstones related to Industry 4.0 and advanced technologies, has strongly developed in recent years at academic and industrial levels as a powerful research and fabrication tool based on its versatility, tunability and environmental friendly approaches [1]. AM is defined by the International Organization for Standardization (ISO)/American Society for Testing and Materials (ASTM) 52900:2015 as "the process of joining materials to make parts from 3D model data, usually layer upon layer". It includes seven categories: material extrusion, powder bed fusion, material jetting, binder jetting, sheet lamination, directed energy deposition and vat photopolymerization [2]. Among them, vat photopolymerization (VP) stands out due to its high resolution and accuracy, good surface finish and high fabrication speed.

VP is mainly composed by UV or visible light curable processes in which the light activates the photopolymerization process [3,4]. The use of UV curable materials is increasing rapidly because the advantages indicated at the first chapter of this thesis [5]. However, a small range of materials can be used, with limited functionality, and supporting materials are often required during fabrication [6]. In addition, the IoT has become one of the key element to truly implement the requirements of the Industry 4.0 [7–9]. In this context, sensors together with 2D and 3D printing technologies [10] are becoming increasingly demanded and significant over the past years [11]. In this respect, different photocurable materials for sensor applications have been obtained, in some cases using AM techniques, including biosensor [12], piezoresistive [13], tactile [14], acoustic and ultrasonic [15], optical [16], temperature [17] and gas detection [18] sensors.

Most of the indicated sensors are based on multifunctional materials that are generally obtained from nanocomposites. This makes nanocomposites an essential tool in the development of sensing materials and applications, mainly based in the synergetic effect of both nanomaterial and matrix [19], the former providing functionality and the second structure and processability. Thus, several studies have been carried out in the synthesis of polymer based nanocomposites [20–22], including UV curable one [23]. Nevertheless, performance, cost, environmental and safety concerns, as well as the processing of materials at industrial scale continues to be a problem for nanocomposites [24]. In this sense, hybrid materials based on ionic liquids (ILs) dispersed within a polymer matrix allow the

development of new materials with improved properties than conventional nanocomposites based on inorganic or organic nanoparticles. This increases the interest in developing those novel materials for different application areas, particularly for sensing [25].

ILs are molten salts composed entirely of organic cations and organic or inorganic anions [26]. Due to their tuneable intrinsic properties such as high ionic conductivity, mechanical, electrical, electromechanical and thermal stability, as well as, negligible vapour pressure, ILs have been attracting a great interest for an increasing number of applications. They have also been implemented as green solvents for polymeric, organic and inorganic materials presenting an alternative to volatile organic solvents and electrolytes [27].

These materials can also show the ability of responding in a controlled manner to external stimuli, namely pH or temperature, among others, by alteration of their intrinsic properties thus adapting to environmental conditions [28]. The tunability of ILs is possible due to the large variety of possible options of cations and anions, promoting their implementations as smart responsive and sensing materials, including electrochromic, pH sensitive and thermochromic materials, among others [27,28].

Different polymers were used as a matrix to develop ILs based hybrid polymer composites, such as poly(vinylidene fluoride) (PVDF) and its copolymers, poly(methyl methacrylate) (PMMA), poly(N-isopropylacrylamide) (PNIPAM), poly(urethane) (PU), polyethylene (PE) and poly(lactic acid) (PLA), among others [25]. Different and very diverse applications have been demonstrated for these nanocomposites, from sensors and actuators or batteries and fuel cells to air and water remediation or biomedical applications [25]. Furthermore, ILs/polymer hybrid materials were obtained based on UV curable materials such as PNIPAM with phosphonium-based ILs for ionogels fabrication [29] or methacrylic oligomer with imide salt type IL to be used as electrolytes for lithium-based batteries [30]. Further, UV cured IL/polymer hybrid materials were prepared by 3D printing, using photosensitive commercial photoresist (IP-L 780 or SU-8) combined with dicyanamide salt and printed by two-photon nanolithography to obtain good optical transparent and down to 200 nm resolution 3D structures [31]; or phosphonium polymerized ionic liquids structures for emerging electro-active membrane technologies printed by microstereolithography [32].

UV-curable polymers are particularly suited for smart coating applications, namely as coatings for corrosion protection, inks and adhesives [33]. However, besides the lartge

potential of these materials, few studies report on the development of smart coatings curing by UV light, being polyurethane (PU) coatings the most commonly employed. In this sense, PU coatings produced by UV curing presents many advantages, being related with their low environmental impact, energy and time saving processing and an efficient polymerization. Smart coatings based on pH-responsive polyurethane (pH-PU) and fluorated octavinyl polyhedral oligomeric silsesquioxane (F-OV-POSS) developed by UV curing revealed a self-cleaning ability and durability, based on their superhydrophobicity. These interesting results demonstrate their strong potential to be used in the still to develop area of smart and multifunctional coatings [33].

With the capability of reversibly changing colour as a function of temperature either by heating or cooling, thermochromic materials, in particular IL/polymer based materials have been gained special attention in the field of sensors, such as level sensors [34,35]. This thermochromic behaviour is present in halide complexes, many transition-metal complexes such as nickel or copper due to the interaction of the transition metal with an adequate donor solvent by the energy alteration of the d-d transitions and consequent configuration changes [36,37]. Systems based on thermochromic materials find applications in areas such as energy [38,39], flexible electronics [40,41] or sensors [35,42], among others [43–45]. In this sense, thermochromic materials and, particularly, ILs based ones, are the focus of increasing attention [25,35]. Besides the high interest in thermochromic materials, few studies reported on the IL/polymer based thermochromism. Printable level sensors based on the IL bis(1-butyl-3-methylimidazolium) tetrachloronickelate ([Bmim]$_2$[NiCl$_4$]) and the polymer PVDF able to change colour from transparent to a dark blue, have been reported [35].

The potentiality of the ILs as humidity sensors have also been explored in ILs/PVDF composites [46], photopolymerizable polymers with carbon nanotubes [47] or polyelectrolytes based on 2-(dimethylamino)ethyl methacrylate quaternized with n-butyl bromide [48] or based on trimethylolpropane triacrylate (TMPTA) and different ammonium salts[49] have been developed.

Besides the great advantages of the ILs for the development of multifunctional materials and the advantages of UV curable polymers for additive manufacturing and protective and functional coatings [50], up to our knowledge no studies concerning the development of thermochromic IL-based UV curable hybrid materials able to change the colour with the temperature and to detect relative humidity variations (humidity sensor) have been reported.

Thus, this study reports on the development of an UV curable ILs/polymer thermochromic and humidity responsive material based on polyurethane acrylate (PUA) and bis(1-butyl-3-methylimidazolium) tetrachloronickelate ($[Bmim]_2[NiCl_4]$) able to be implemented as multifunctional materials or coatings with thermochromic and for humidity sensing capability.

6.2. Experimental

6.2.1. Materials

SPOT-E^{TM} from SPOT-A Materials ® commercial photoresin was used as the UV curable matrix. This clear-yellowish material is based on polyurethane acrylate (PUA) polymer. The IL, 1-buthyl-3-methylimidazolium tetracholonickelate ($[Bmim]_2NiCl_4$), with a purity of 99% was synthetized as previously reported [51,52]. 2-propanol of 99.5 % purity from Alfa Aesar ® was used as a sample cleaner.

6.2.2. Samples preparation

Different contents of IL were mixed with the corresponding volume of the photoresin to obtain 0, 5, 10, 20 and 40 wt.% $[Bmim]_2NiCl_4$ content samples. To ensure a good mixture of the resin and the IL, the samples were dispersed under ultrasonication (ATU ® ATM series Model ATM3L) for 1 h at a temperature of 30 ºC and then magnetically stirred for 2 h at 45 ºC. After the completely homogeneous photoresin-IL mixture, flexible/bendable films were obtained by doctor blade technique spreading the mixture on a clean glass substrate. All samples were then cured at room temperature for 90 seconds with a UV curing chamber (UVACUBE 400, Honle UV America, Inc.) equipped with a mercury lamp ($1000 \ W/m^2$ of irradiance). Then, films were separated from the glass substrates, washed in a 2-propanol bath during 5 minutes, dried, and finally, stored in the dark at room temperature for the subsequent characterization. IL/PUA hybrid materials with a thickness around 150 μm, determined by an electronic digital caliper of Powerfix ®, were obtained. **Figure 6.1** shows a scheme of the preparation process for PUA and IL/PUA films.
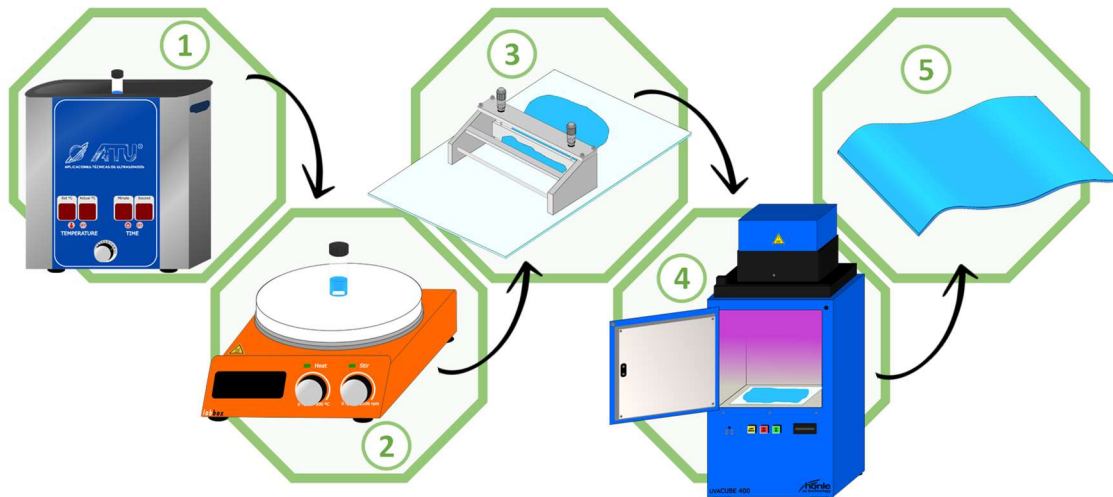
Figure 6.1 – Schematic representation of the procedure used for the development of the PUA and IL/PUA composite films (5, 10, 20 and 40 wt.%): 1 – ultrasonication, 2 – magnetic stirring at 45 ºC, 3 – film processing by Doctor Blade, 4 – UV cure, 5 – flexible films.

6.2.3. Samples characterization

The effect of the introduction of the IL within the polymer matrix in the UV curing process was evaluated by photo-differential scanning calorimetry (photo-DSC) using a DSC 2920 Modulated DSC equipment coupled to a differential photocalorimetry accessory from TA Instruments ®. All samples were irradiated with UV light in air at room temperature for 5 minutes while the heat flow was measured. The results were normalized by the weight of samples.

The C=C double bonds conversion (α) was calculated according to the Equation (6.1) [53]:

$$\alpha = \frac{\Delta H_t}{\Delta H_0^{theor}} \tag{6.1}$$

where ΔH_t is the enthalpy at time t (calculated by integrating the area under the peak of the measured DSC curves), and ΔH_0^{theor} is the theoretical enthalpy for the fully conversion. Due to fact that a commercial photoresin was used, the enthalpy value of the pure resin after the complete UV cure was considered as the theoretical enthalpy for totally conversion [13,54].

The photopolymerization rate (R_p) was obtained applying Equation (6.2):

$$R_p = \frac{d\alpha}{dt} = \frac{dH/dt}{\Delta H_0^{theor}} \tag{6.2}$$

Thus, the maximum photopolymerization rate (R_p^{max}) and the corresponding time to reach R_p^{max}, named t^{max}, were obtained.

Scanning Electron Microscopy (SEM) was employed to study the morphology variations of the samples as a function of IL content. Samples were cold fractured under liquid nitrogen bath and cross-section images were obtained by a Hitachi S-4800 microscope at an accelerating voltage of 10 kV with magnification of 500×.

Possible interactions between the IL and the polyurethane acrylate polymer were studied by Fourier transformed infrared spectroscopy in the total attenuated reflection mode (FTIR-ATR) using a Nexus FTIR Nicolet spectrophotometer. The FTIR-ATR analysis was performed in the range of 4000 to 400 cm^{-1} with a spectral resolution of 4 cm^{-1} and 64 scans.

Thermal behaviour of the samples was evaluated by differential scanning calorimetry (DSC) measured in two successive scans under nitrogen atmosphere from -50 to 250 ºC at 20 ºC/min in the first scan and from -50 to 150ºC at 20ºC/min in the second scan using a DSC 822e from Mettler Toledo. The glass transition temperature was calculated as the extrapolated onset of the baseline shift. In addition, the water absorption capability of the samples was also evaluated.

Contact angle measurements were employed to characterize the hydrophobic/hydrophilic behaviour of the prepared films as a function of the amount of IL in the samples. The Ossila Contact Angle Goniometer was used to measure the contact angle of each sample over time (3 experiments per sample). Drops of Mili-Q water were deposited on each sample (10 µL/drop) and the evolution of the contact angle over time was measured.

The mechanical properties of both pristine and hybrid samples were evaluated by tensile tests. Mechanical tests in the tensile mode were carried out at room temperature in a universal testing machine (Shimadzu model AG-IS) using a load cell of 50 N. Rectangular shaped (30 x 10 mm) samples were analyzed at a test velocity of 10 mm/min. Secant modulus (E), obtained by calculating the slope of the linear region, and strain at break (ε_b) were determined for pure PUA and IL/PUA films.

The electrical properties of the films were evaluated by current-voltage (I-V) measurements using a Keithley 6430 picoammeter/voltage source. Previous to the measurements, the samples were prepared in the form of a parallel plate condenser by depositing, by magnetron

sputtering (Polaron Coater SC502), circular gold electrodes of 5 mm diameter. The volumetric electrical conductivity was obtained at room temperature by the slope of the characteristic I-V curves and the electrical conductivity (σ) was calculated considering the geometrical factors of the samples according to Equation (6.3) [13]:

$$\sigma = \frac{L}{R \cdot A} \qquad (6.3)$$

where R is the electrical resistance, L the sample thickness and A is the area of the electrodes.

The thermochromic response was investigated by ultraviolet−visible (UV-Vis) spectroscopy as a function of temperature. UV−Vis spectra were collected with an Agilent Cary 60 UV/vis spectrophotometer with an external temperature controller. The spectra were obtained in the range of 300-800 nm, with a resolution of 1 nm, in the temperature range from 30 to 70 °C (temperature range in which sample colour changes) every 5 °C after 2 min stabilization period before each measurement. Further, the effect of temperature and relative humidity (RH) variation on the colour of the films was measured within a climate chamber Challenge 250E from ACS Company by recording photographs while RH and temperature were varied as indicated in **Table 6.1**. This analysis was carried out for the IL/PUA sample (2.5 x 2.5 cm square) with 20 wt.% IL content. In order to obtain the blue (dehydrated) initial state, the sample was kept at 70 °C for 5 minutes, while for the colourless (hydrated) state, the sample was kept under ambient conditions during 24 hours.

Table 6.1 – Experimental details for thermochromic and relative humidity (RH) variation assays.

Experiment	Initial state	Constant parameter and value	Variable parameter and interval	Studied intervals	Time of interval
1	Blue (dehydrated)	Temperature at 25 ºC	Relative humidity 15 – 85 %	10 %	
2	Blue (dehydrated)	Temperature at 45 ºC	Relative humidity 15 – 85 %	10 %	20 minutes at constant value and 15 minutes increasing to the next step
3	Blue (dehydrated)	Temperature at 15 ºC	Relative humidity 20 – 85 %	10 %	
4	Colourless (hydrated)	Relative humidity at 60 %	Temperature 25 – 75 ºC	10 ºC	
5	Colourless (hydrated)	Relative humidity at 40 %	Temperature 25 – 75 ºC	10 ºC	

6.3. Results and discussion

6.3.1. UV curing process

UV curing process for the different samples is depicted in **Figure 6.2**. The photopolymerization conversion (α) as a function of time is shown in **Figure 6.2a** and the photopolymerization rate (R_p) in **Figure 6.2b**. **Table 6.2** summarizes the main values that characterize the UV curing process, α, R_p^{max} and t^{max}, of the different samples, as a function of IL content.

Figure 6.2a shows that a decrease on the conversion degree occurs with increasing IL content. Neat photoresin shows a 100% conversion after approximately 4 minutes that becomes 95% for the sample with 10 wt.% IL content. Similar trend is further observed for the samples with 20 wt.% and 40 wt.% IL content, the total conversion decreasing to around 88% for the 40 wt.% IL content sample after 4 minutes. In addition, photopolymerization rate is also slightly affected by the incorporation of [Bmim]$_2$[NiCl$_4$], changing from 3.4 s^{-1} for neat PUA to 2.9 s^{-1} for 40 wt.% IL/PUA sample. In relation to the t^{max}, a slight decrease is observed with increasing IL content, varying between 8.0 s for the 0 wt.% IL/PUA sample to 6.2 s for the sample that contains the highest amount of IL.

The UV light absorption by the photoinitiator has significant influence in the C=C double bond conversion and, therefore, in the UV curing process [55]. The functionality and chemical structure of the employed oligomer has influence in the reactivity of the photocurable ink and as consequence in the final degree of conversion [3]. Further, the viscosity of the liquid curable ink/resin also plays an important role on the photopolymerization and is affected by the addition of additives [54]. Further, the fillers could absorb UV light, competing with the photoinitiator and, as a consequence, influencing the photopolymerization reaction and the characteristic photopolymerization parameters [13].
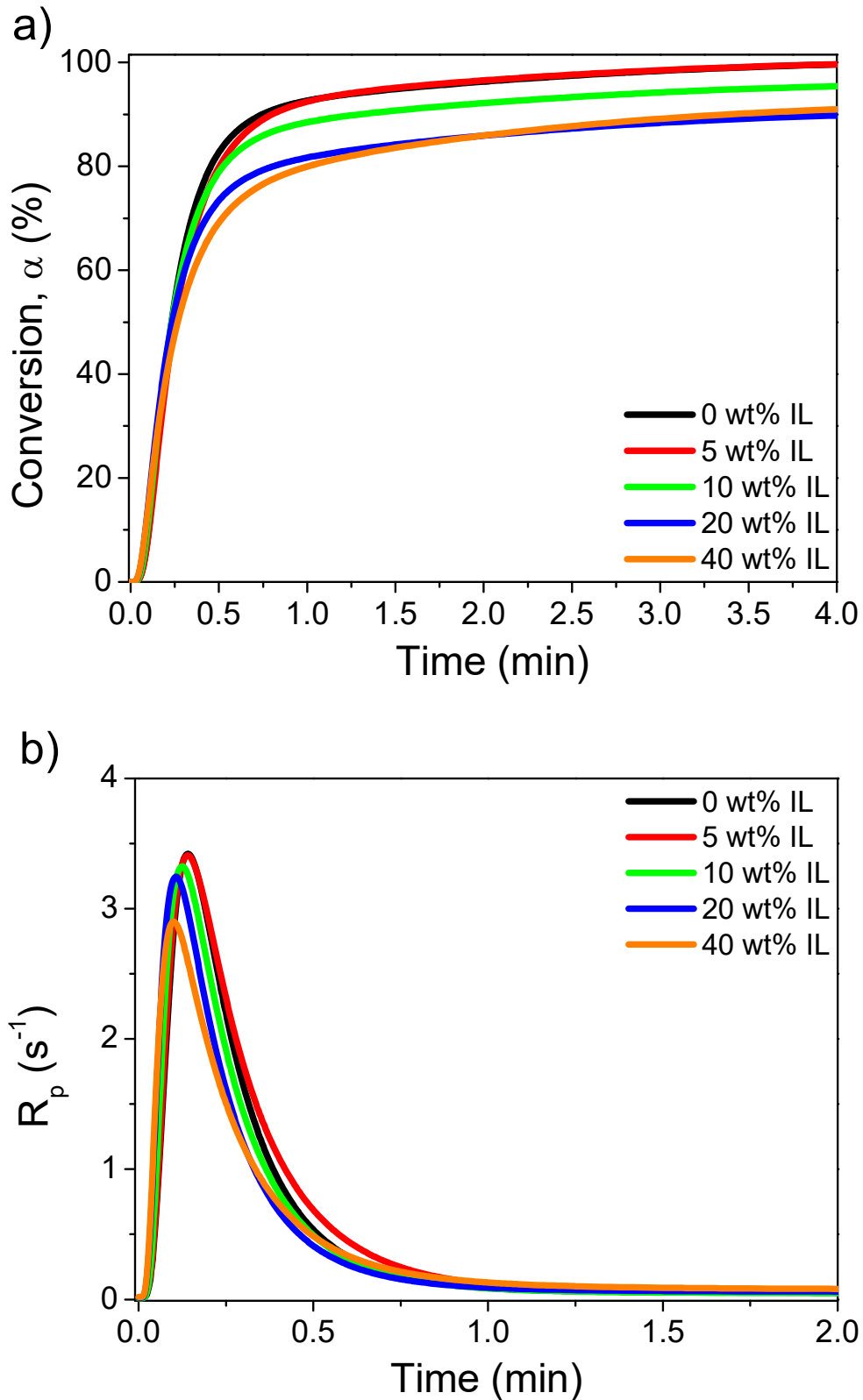
a)

b)

Figure 6.2 – Curing conversion (α) as a function of time of the pristine photoresin and the IL/PUA samples (a), and the corresponding photopolymerization rate (R_p)(b).

Table 6.2 – UV curing process parameters of the pristine resin and the IL/PUA samples for the different IL contents.

Sample	α (%)	R_p^{max} (s^{-1})	t^{max} (s)
0 wt.%	100	3.4	8.0 ± 0.1
5 wt.%	99	3.4	8.0 ± 0.2
10 wt.%	95	3.3	7.4 ± 0.1
20 wt.%	89	3.2	7.0 ± 0.3
40 wt.%	88	2.9	6.2 ± 0.4

In the present case, UV absorption by [Bmim]$_2$[NiCl$_4$] competes with the light absorption by the photoinitiator [51] and, therefore, lower amount of initiating radicals is produced. As a consequence, the final conversion and the rate at which the polymerization occurs are reduced when IL is added to PUA resin. Furthermore, increasing viscosity influences the photopolymerization by decreasing the rate and increasing the time to obtain the maximum curing degree [53]. Hence, two factors have to be taken into account: a) when the photopolymerization is taking place, the viscosity increases and b) the presence of IL also increases the viscosity of the photocurable material [29]. Thus, different viscosities could be obtained for two materials with the same degree of cure but different amount of IL content, being observed a decrease in the R_p and t^{max} with increasing [Bmim]$_2$[NiCl$_4$] content.

6.3.2. Morphological and contact angle characterization

Figure 6.3 shows the cross-sectional SEM images of neat PUA and IL/PUA samples in order to evaluate morphology variations due to the [Bmim]$_2$[NiCl$_4$] inclusion within the polymer matrix.
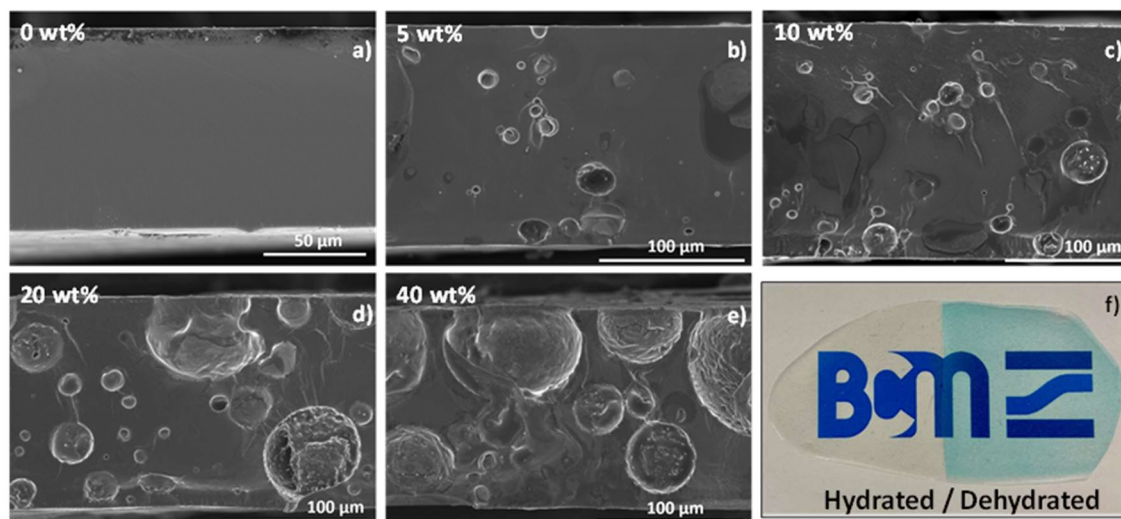
Figure 6.3 – SEM images of the PUA (a) and IL/PUA hybrid samples comprising different IL contents (b-e) at magnification of 300×. Thermochromism resulting from the dehydration process of IL/PUA with 10 wt.% IL content (f).

The filler induced morphological variations have significant influence over mechanical and electrical properties of the prepared samples [13,54], which depends on IL type and content [29]. **Figure 6.3** shows that the presence of [Bmim]$_2$[NiCl$_4$] modifies the PUA polymer morphology: whereas pristine PUA (**Figure 6.3a**) shows a smooth and flat structure, without any visible crack, pores or patters, the incorporation of the IL leads to spherical or porous like structures within the sample. This trend increases with increasing IL content within the PUA matrix and the pore distribution is homogeneous throughout the films. When IL content increases, the spherical (bubble type) structures appear in a greater extent and the pores seem to be larger [56].

The obtained SEM results are in agreement with elated studies with [Bmim]$_2$[NiCl$_4$] within different polymer matrix [35,46]. Further, as the IL [Bmim]$_2$[NiCl$_4$] is known by its thermochromic properties upon a hydration and dehydration process, an important property for the development of multifunctional materials for smart coatings and/or sensor applications, the thermochromism upon a hydration process was evaluated. **Figure 6.3f** shows the thermochromism occurring as a result of a hydration/dehydration process for the sample with 10 wt.% IL content, as demonstrated by a colour change from colourless/whitish to light blue, respectively. This effect will be quantitatively analysed in this work.

The surface wettability of the PUA and PUA/[Bmim]$_2$[NiCl$_4$] was evaluated by contact angle measurements (**Figure 6.4**). Attending to the contact angle values, the hydrophobic/hydrophilic behaviour of each sample can be evaluated.
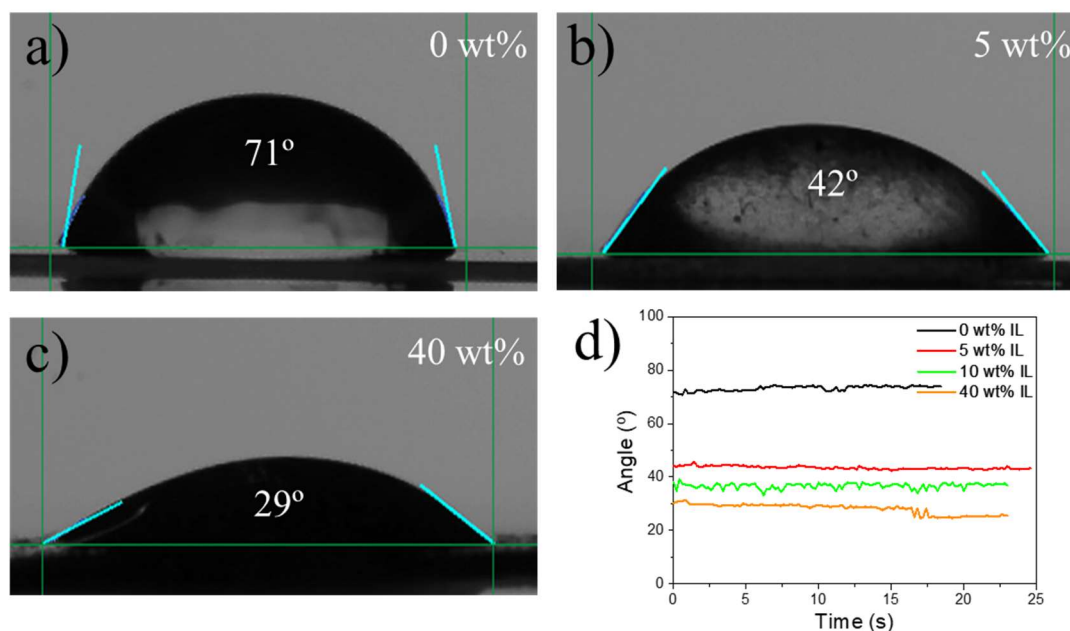

Figure 6.4 – Representative images of the water surface contact angle for neat PUA film (a) and IL/PUA samples containing 5 wt.% (b), 10 wt.% (c), 20 wt.% (d) and 40 wt.% (e). Evolution of the contact angle values as a function of time for the mentioned samples (f).

Figure 6.4 shows that the contact angle for neat PUA films present a value of 71º and that when the IL is added to the polymer matrix, the contact angle value decreases to 42º for the 5 wt.% IL/PUA sample and to a minimum value of 29º for the sample with the highest IL content (40 wt.%). The improvement of the surface wettability of the samples with increasing [Bmim]$_2$[NiCl$_4$] content shows that the inclusion of the IL into the polymer matrix improves the water absorption capability, increasing the absorbed water per unit mass in the IL/PUA samples [57]. These results are also in agreement with the increased porosity of the samples with increasing IL content presented in **Figure 6.3**, as higher porosity allows a larger contact between film and water drop and increased water absorption [56].

6.3.3. Thermal and chemical characterization

The thermal properties of pristine and IL/PUA samples were evaluated by the DSC thermograms shown in **Figure 6.5**. Only a single endothermic peak is observed for the neat

PUA in the first and second scans, corresponding to the glass transition temperature (T_g). The glass transition temperatures for the different samples are indicated in **Table 6.3**.
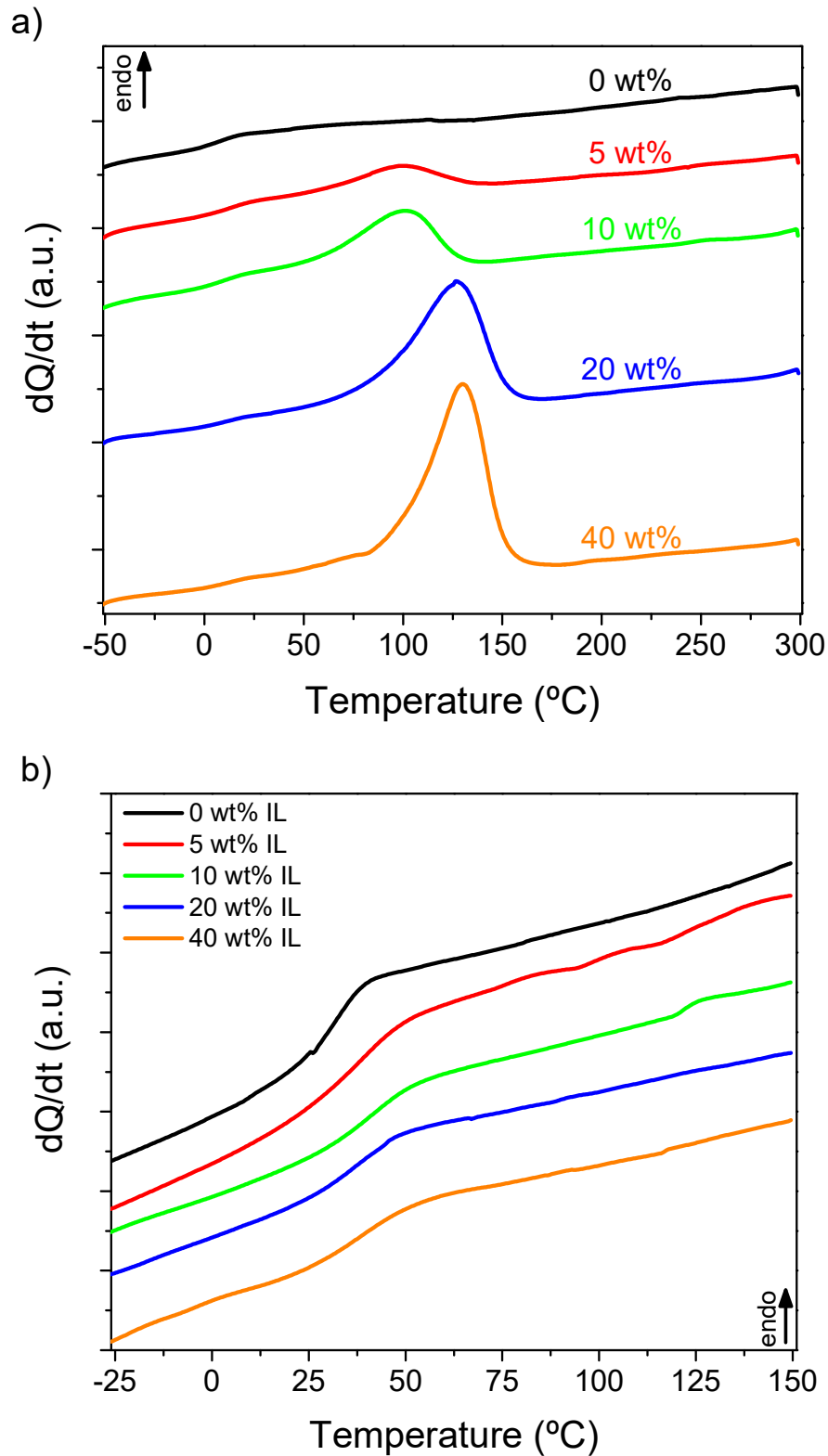

Figure 6.5 – DSC thermograms of neat PUA and IL/PUA samples for the first (a) and second (b) scans.

Table 6.3 – Glass transition temperature for first (T_{g1}) and second (T_{g2}) scans, strain at break (ε_b) and elastic modulus (E) for PUA and IL/PUA films.

Sample	T_{g1} (ºC)	T_{g2} (ºC)	ε_b (%)	E (MPa)
0 wt.%	20.2	41.2	45.8 ± 3.2	4.04 ± 0.35
5 wt.%	24.1	52.8	54.3 ± 4.4	4.87 ± 0.37
10 wt.%	23.5	53.3	29.1 ± 2.1	4.20 ± 0.13
20 wt.%	23.7	50.9	27.0 ± 2.5	4.27 ± 0.31
40 wt.%	23.6	56.7	32.9 ± 5.3	3.45 ± 0.02

For neat PUA the glass transition is located around room temperature ($T_g = 20$ ºC). With the incorporation of the IL [Bmim]$_2$[NiCl$_4$] an endothermic peak is observed between 60 and 150 ºC that increases with increasing IL content. This endothermic peak is attributed to water desorption and can appears at different temperature ranges depending on the H_2O molecular interactions [58], being indicative in the present case of a reversible water desorption on Ni (II) compounds in which H_2O molecules are coordinated to the metal [35,59]. The increase of the endothermic peak with increasing IL content is in agreement with contact angle results, where a higher wettability is observed for samples with higher IL content.

Figure 6.5a also shows that T_{g1} for neat PUA and IL/PUA samples (**Table 6.3**) slightly increases from 20 to ~24 ºC when [Bmim]$_2$[NiCl$_4$] is added. Thus, no significant differences are observed among the different samples.

After the heating process up to 300 ºC and the subsequent cooling to -50 ºC the peak corresponding to the water absorption does not appear (**Figure 6.5b**), indicating that the hydration process does not occur. Related to PUA, T_g increases compared with the first scan from 20 ºC (T_{g1}) to 41 ºC (T_{g2}), increasing further for the samples with IL content up to 40 wt.%, being 53 ºC for the sample containing 5 wt.% IL and 56 ºC for the sample with 40 wt.% IL. This increase of the T_{g1} of PUA with the IL incorporation indicates that the IL actually interacts with the polymer, reducing its mobility [60]. Thus, after the heating process and water evaporation (second scan), the increase of T_g indicative of the polymer mobility reduction that can be ascribed to a IL and PUA interactions when dehydration has occurred [60].

The possible physico-chemical interactions between the IL and the polymer matrix as well as the conformational variations of the IL/PUA samples after the hydration and dehydration processes were evaluated by FTIR-ATR. **Figure 6.6** shows both the room temperature, 25 ºC, (hydrated) and 80 ºC (dehydrated) FTIR spectra.

Figure 6.6a allows to identify the main characteristic absorption bands of neat PUA. The absorption band at 1550 cm^{-1} is attributed to the combined stretching vibrations of C-N and N-H bonds of the urethane group. C-N and C-O-C absorption bands appear at 1400 cm^{-1} and 1110 cm^{-1}, respectively. The PUA C=O stretching vibrations are observed at 1725 cm^{-1} and the CH$_2$ and CH$_3$ vibrations are observed between 2855 cm^{-1} and 2955 cm^{-1} [54]. No chemical changes occur in the FTIR-ATR spectra of PUA upon the IL incorporation within the polymer matrix. Additionally, it is also to notice that the characteristic IL imidazolium CH$_2$, CH$_3$ and C-N absorption bands of the cation [Bmim]$^+$ are overlapping with the polymer absorption bands [35,46]. Apart from that, no band displacement or new absorption bands are observed upon the addition of IL, showing that no notable intermolecular interactions occur between the IL and the PUA polymer [54].

Comparing samples before (hydrated) and after (dehydrated) the heating process, it is to notice the presence of two absorption bands at 1650 and 3330 cm^{-1} in the hydrated samples, which correspond to the stretching and bending modes of water molecules [35]. These results indicate that the change in colour from light blue to colourless (**Figure 6.3f**) can be attributed to the presence or not of water molecules within the coordination structure of the [Bmim]$_2$[NiCl$_4$] IL of the IL/PUA samples, as it will be analysed in detail latter.
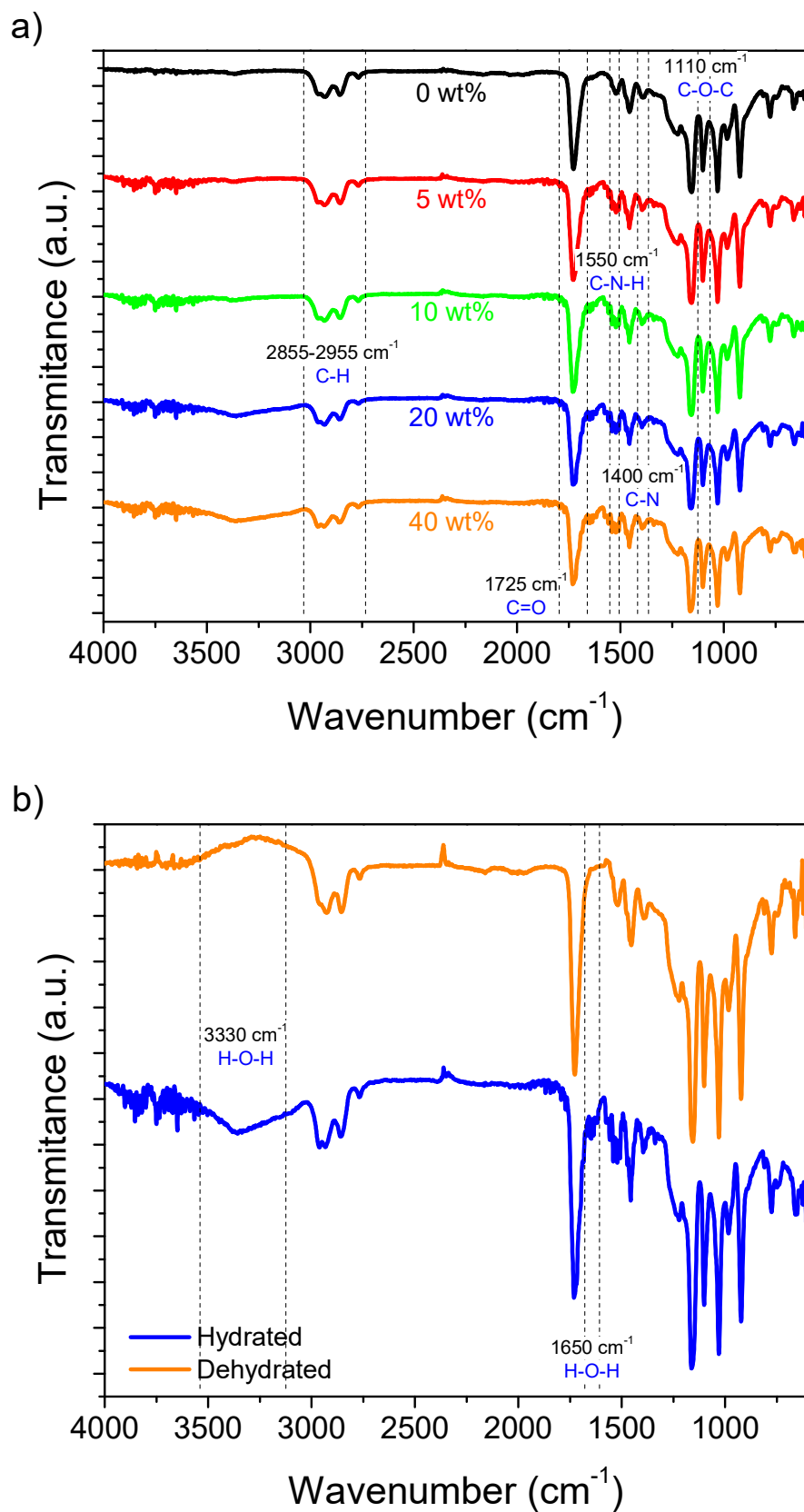
Figure 6.6 – FTIR spectra of neat PUA and IL/PUA samples containing different IL contents (a) and FTIR spectra at room temperature (hydrated) and at 80 °C (dehydrated) of 20 wt.% IL/PUA sample (b).

6.3.4. Mechanical and electrical properties

The mechanical characterization of neat PUA and IL/PUA films as a function of [Bmim]$_2$[NiCl$_4$] content from 5 up to 40 wt.% was performed by stress vs. strain measurements in tensile mode (**Figure 6.7a**) and the corresponding elastic modulus (**Figure 6.7b**) and strain at breaks (**Table 6.3**) were evaluated.
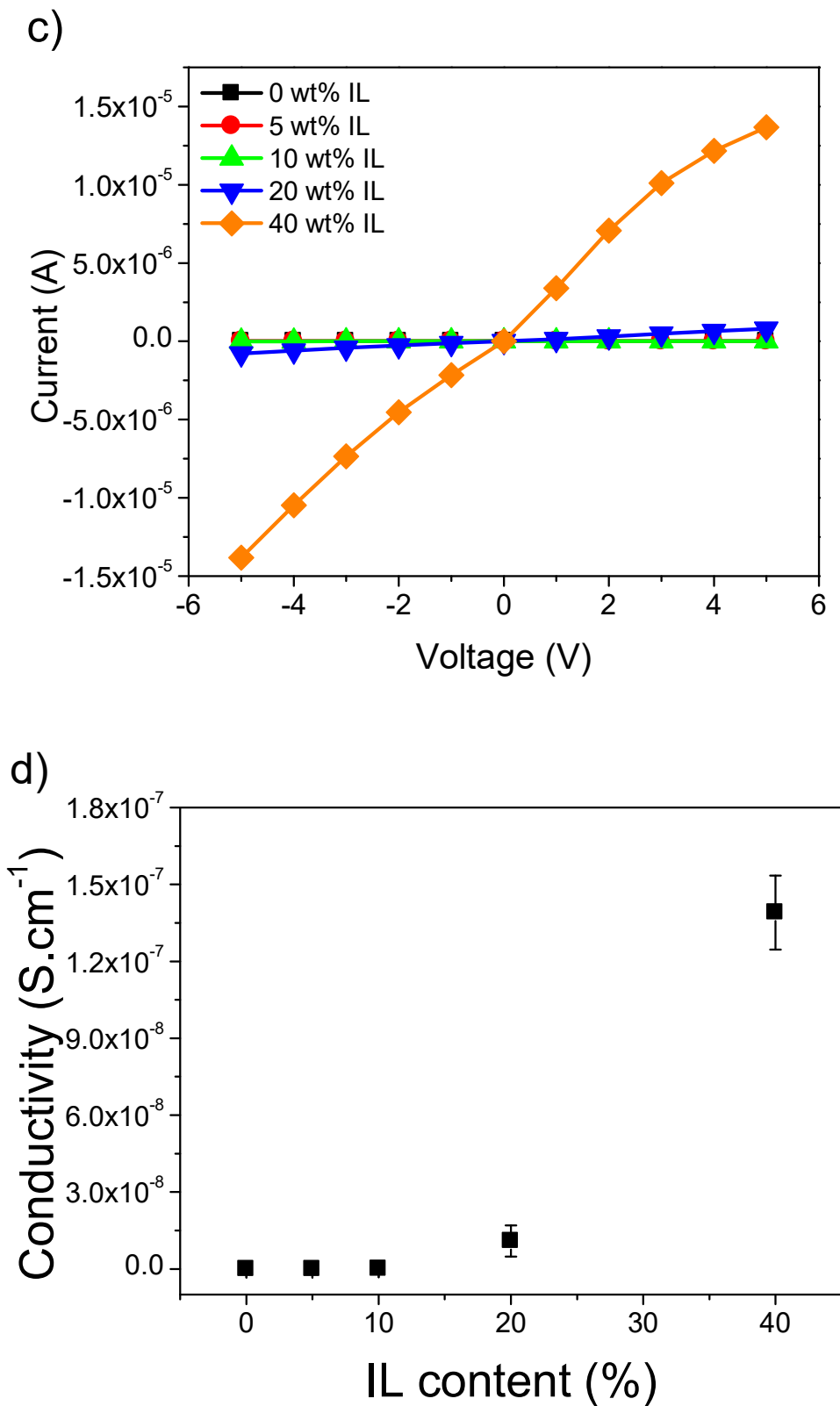
c)

d)
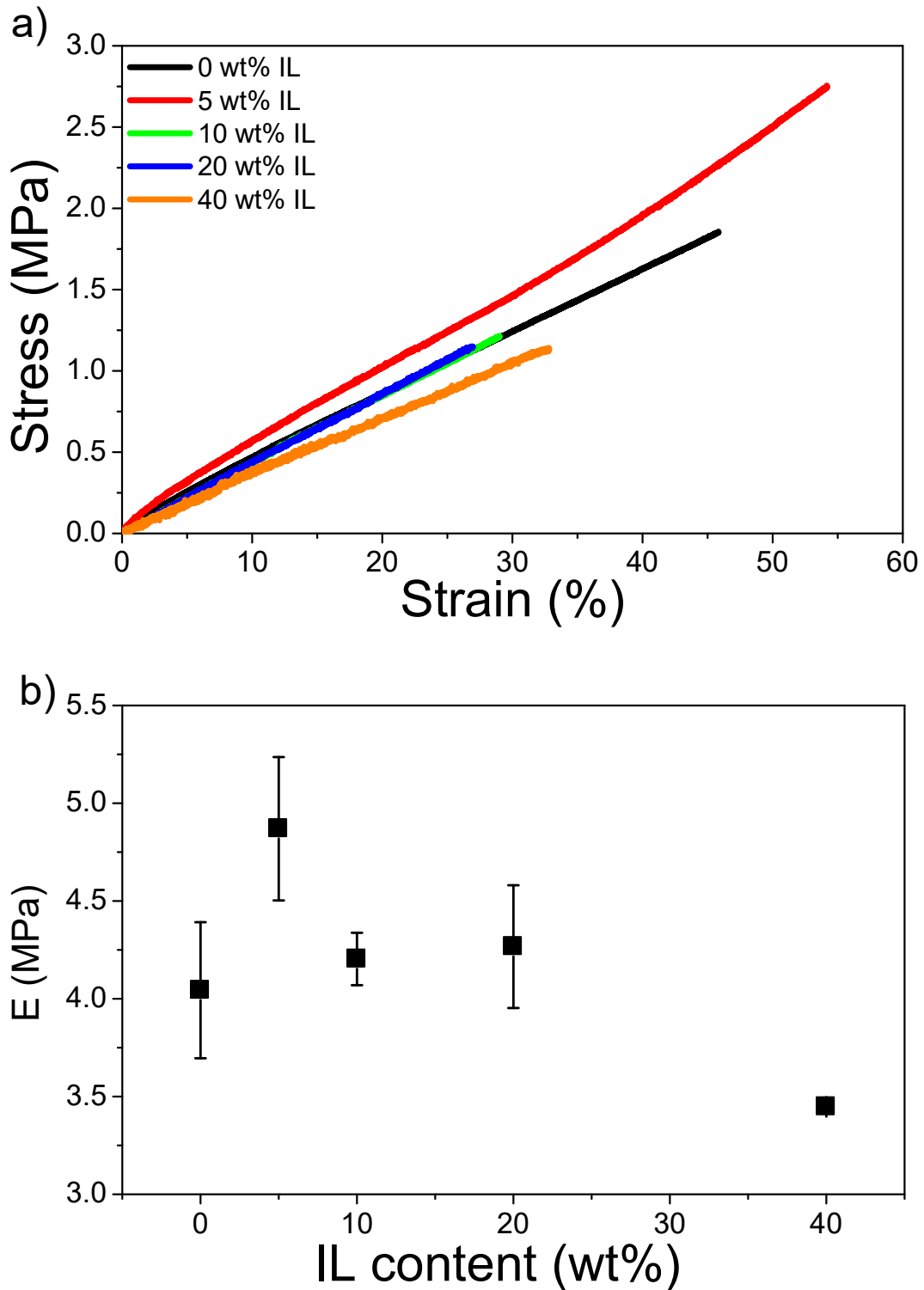
Figure 6.7 – Stress vs. strain mechanical characteristic curves (a) and Young modulus (b) for neat PUA and for IL/PUA samples containing different $[Bmim]_2[NiCl_4]$ contents. I-V curves (c) and electrical conductivity (d) for the same samples.

According to **Figure 6.7a**, all samples exhibit a linear elastic response up to a breaking point. The maximum strain for the PUA film is ~ 45 % decreasing down to ~ 27 % for the IL/PUA film with a $[Bmim]_2[NiCl_4]$ content of 20 wt.%. With respect to the Young's modulus (**Figure 6.7b**) it is 4.04 ± 0.35 MPa for the PUA photoresin film and slightly increase to 4.87 ± 0.37 MPa for the composite with 5 wt.% of $[Bmim]_2[NiCl_4]$. However, for concentrations higher than 5 wt.%, a reduction in the Young modulus is observed, being 4.20 ± 0.13 MPa and 4.27 ± 0.31 MPa for the samples containing 10 and 20 wt.% of $[Bmim]_2[NiCl_4]$, respectively. The IL/PUA film with 40 wt.% of $[Bmim]_2[NiCl_4]$ shows a Young modulus of 3.45 ± 0.02 MPa. The decrease in the Young modulus is mainly attributed to the plasticizing effect of the $[Bmim]_2[NiCl_4]$ as well as to the observed morphology variations increasing $[Bmim]_2[NiCl_4]$ content, appreciated in the SEM images [61].

Attending to the elongation level of the material, the addition of IL increases the maximum elongation of the materials for the lower IL contents being 45.8 ± 3.2 % for neat PUA and 54.3 ± 4.4 % for the 5 wt.% sample. When higher amounts of IL are added, the maximum elongation decreases down to 27.0 ± 2.5 % for the 20 wt.% sample. As shown before, the addition of IL induces variations on the morphology of the obtained polymer hybrids resulting in increasingly porous structures and, as consequence, the materials show lower levels of stretchability [62]. Interestingly, all films present bending ability and they not become fragile with increasing IL content, making them suitable materials for flexible applications.

The electrical properties of the PUA and IL/PUA films as a function of $[Bmim]_2[NiCl_4]$ content are shown in **Figure 6.7c and d**. **Figure 6.7c** shows the characteristic I-V curves and the corresponding volume electrical conductivity of the films is presented in **Figure 6.7d**.

All samples exhibit a typical I-V linear behavior independent of the IL content, with the slope increasing with the increasing $[Bmim]_2[NiCl_4]$ content (**Figure 6.7c**). The electrical conductivity of the samples, evaluated using Equation (6.3), shows a strong increase with increasing IL content (**Figure 6.7d**), the electrical conductivity of the PUA film being around 2.92×10^{-12} S·m^{-1} and the highest electrical conductivity being obtained for the sample with 40 wt.% $[Bmim]_2[NiCl_4]$ IL content: 5.51×10^{-6} S·m^{-1}. This increase results from the ionic properties of the ILs and to ion-dipole interactions, that occurs between the IL and the PUA being the electrical conductivity governed by the increase in the number and mobility of the

ions, ionic charge and viscosity of the [Bmim]$_2$[NiCl$_4$] [63]. By increasing the [Bmim]$_2$[NiCl$_4$] concentration in the polymeric matrix, the ion transport and dissociation of IL is promoted, increasing the number of ionic carriers. Further, it has been also reported that the IL-polymer interaction may decrease as the IL content increases, promoting a faster dissociation of the ionic transport from the polymer chain motion [35].

6.3.5. Temperature-activated humidity-sensitive materials

6.3.5.1.   UV-Vis characterization

The thermochromic effect of the PUA/[Bmim]$_2$[NiCl$_4$] films was evaluated by UV-Vis spectroscopy at different temperatures as shown in **Figure 6.8**. **Figure 6.8a** shows the UV−Vis spectra for PUA/[Bmim]$_2$[NiCl$_4$] composite with 20 wt.% of [Bmim]$_2$[NiCl$_4$] content in the temperature range from 30 to 70 ºC. **Figure 6.8b** shows the UV-Vis curves for the different composites with different IL contents at 70 ºC.
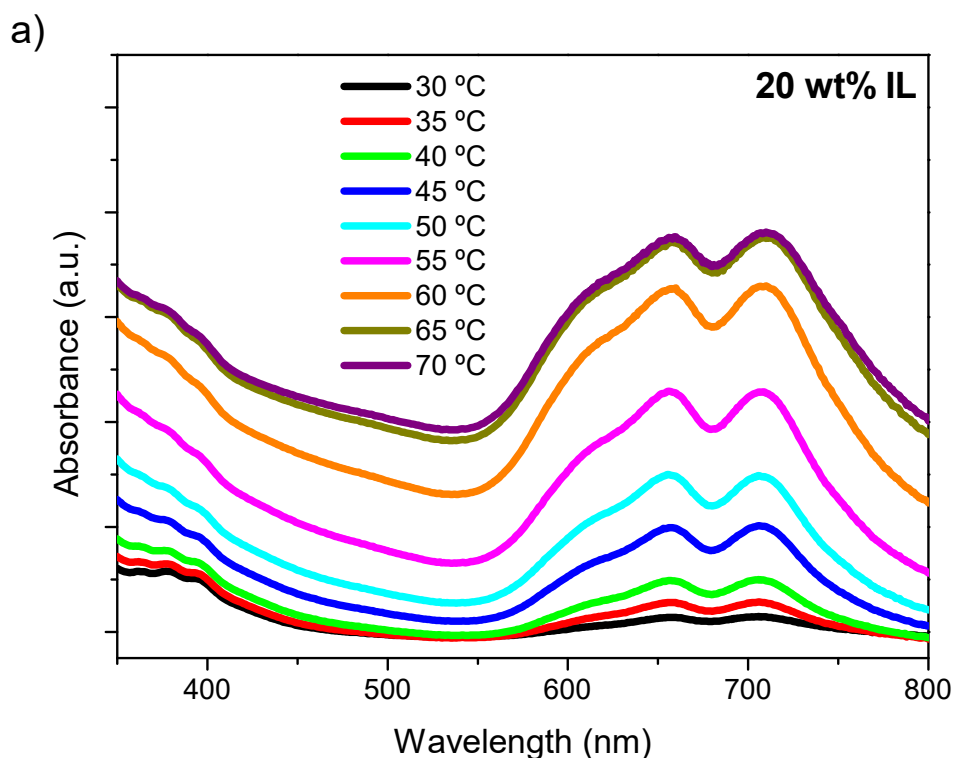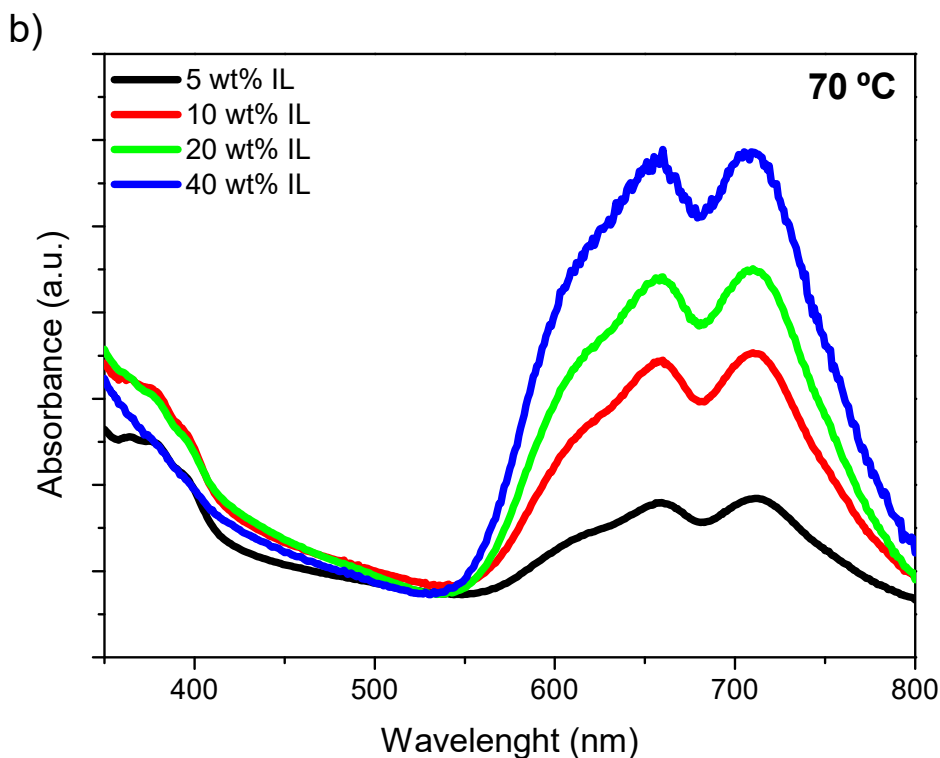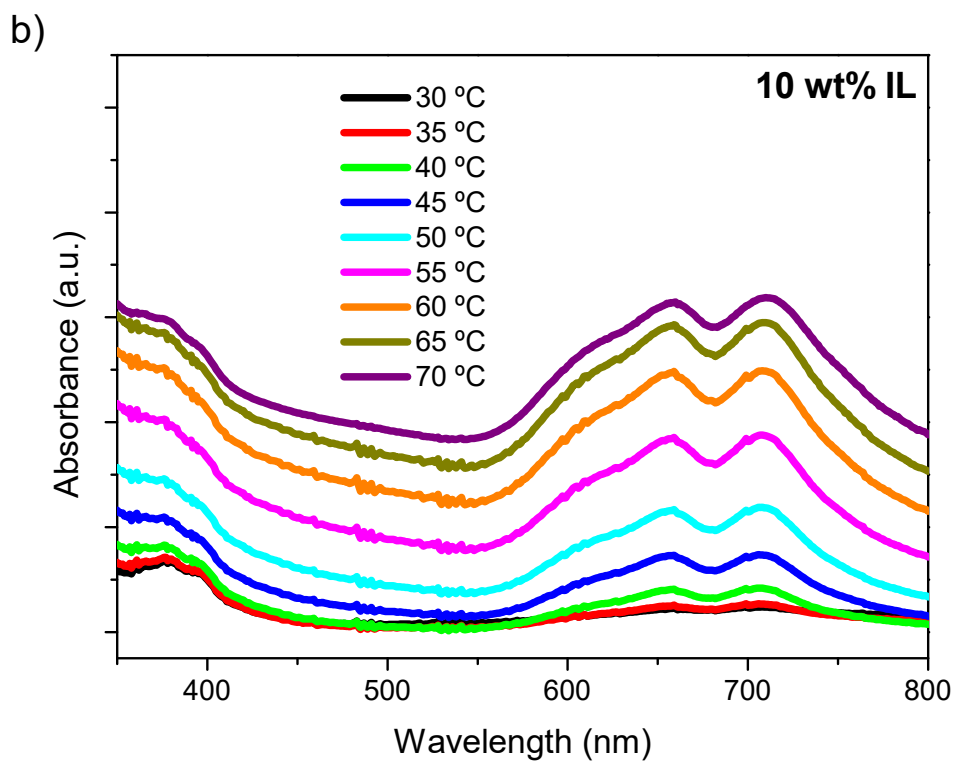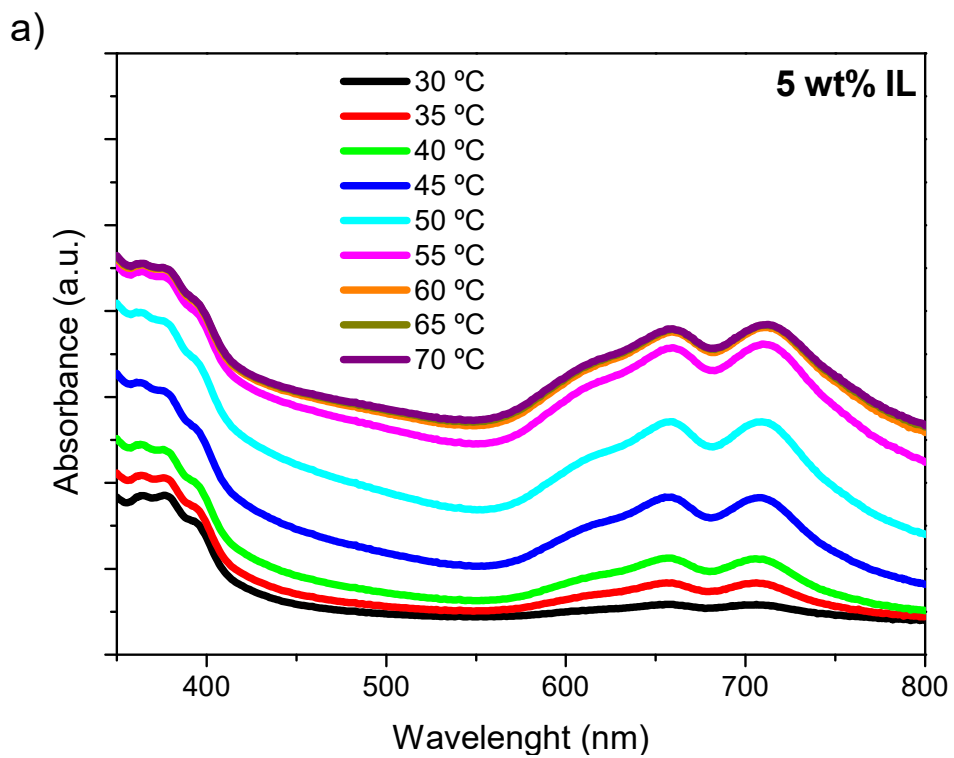
Figure 6.8 – UV-Vis spectra for the IL/PUA samples containing 20 wt.% of [Bmim]$_2$[NiCl$_4$] content in the temperature range from 30 to 70 °C (a) and UV-Vis curves for the different samples at 70 °C (b).

Upon the processing, and independently of the IL content, the films are colourless, changing their colour to blue upon the heating up to 70 °C, being the colour change a reversible and temperature-dependent process.

As shown in **Figure 6.8a**, the increase in temperature from 30 to 70 °C induces the appearance and subsequent increase of two absorption bands at 660 and 710 nm. Comparing these two peaks among them, similar intensity and shape is obtained regardless of the temperature. Furthermore, this process is observed for all IL/PUA samples, independently of the [Bmim]$_2$[NiCl$_4$] content, as it can be observed in the **Figure 6.9**, reaching maximum absorption at temperatures between 60 and 70 °C in all cases. In addition, an increase of the IL content from 5 to 40 wt.% induces an increase in the absorption bands, as presented in **Figure 6.8b**.
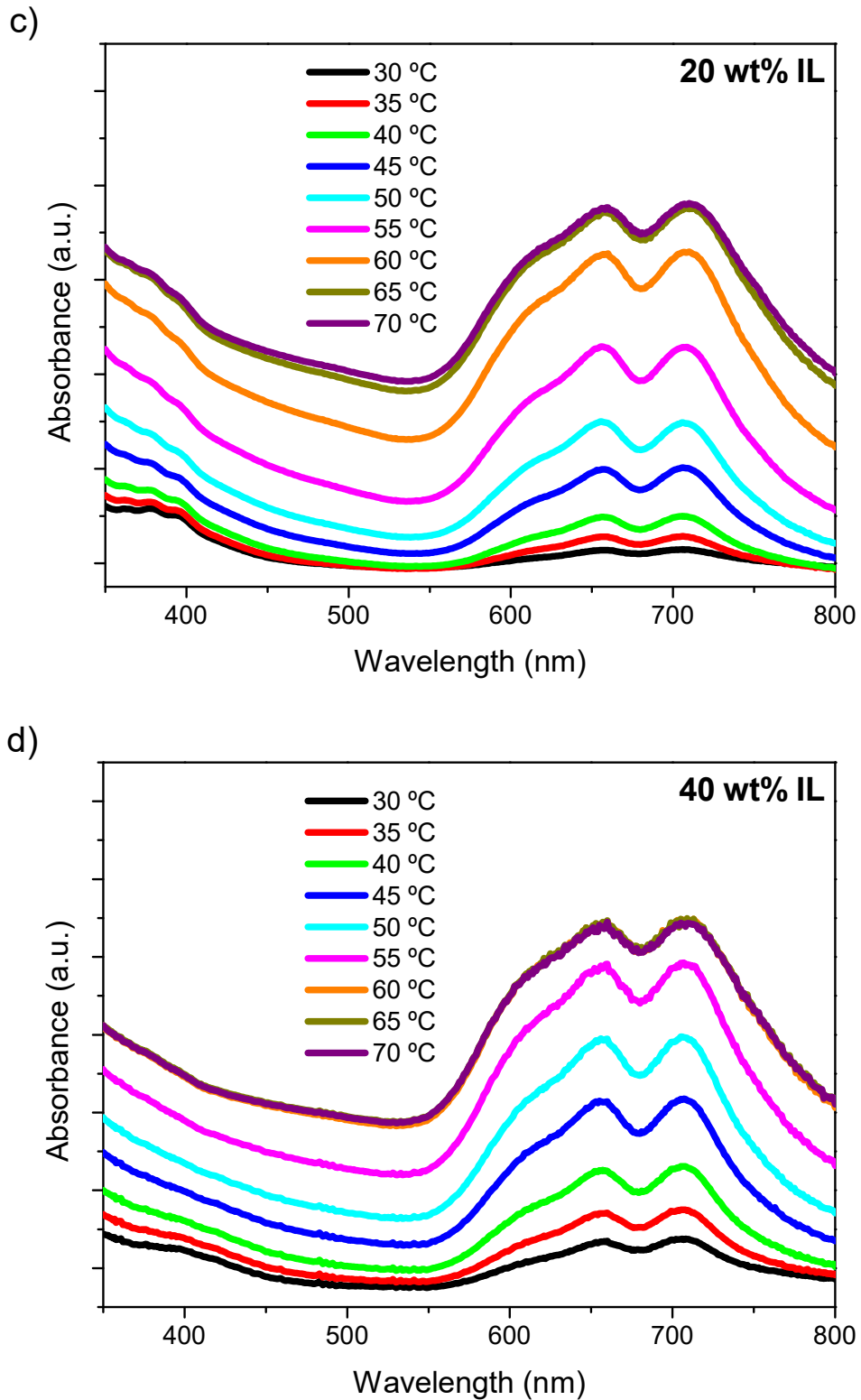
a)

b)

Figure 6.9 – UV-Vis spectra for IL/PUA samples in the temperature range from 30 to 70 °C for sample with [Bmim]$_2$[NiCl$_4$] content of 5 wt.% (a), 10 wt.% (b), 20 wt.% (c) and 40 wt.% (d).

The appearance of the two absorption bands with increasing temperature indicates colour change of the films from colourless to blue. As indicated, the absorption peaks appear at

wavelengths between 600 and 750 nm, ascribed to the blue region of the UV-Vis spectrum. In addition, these peaks reach a maximum absorption value that corresponds to the most intense blue colour obtained in the films and this colour is dependent on the IL content of the composite, increasing the peak intensity, and in this sense the colour intensity, with the IL content. The observed peaks of similar intensities are attributed to the $[NiCl_4]^{2-}$ complex in its tetrahedral conformation [64], being thus responsible for the colour variation. Therefore, the colour change of the films is explained by the modification of the coordination reaction [35].

6.3.5.2.   Temperature-humidity-colour change characterization

As the composites are thermally and humidity responsive, they show a strong potential for smart and multifunctional coatings and/or sensing materials. **Figure 6.10** shows the evolution of the colour with increasing relative humidity (RH) at constant temperature, and with increasing temperature at constant humidity.
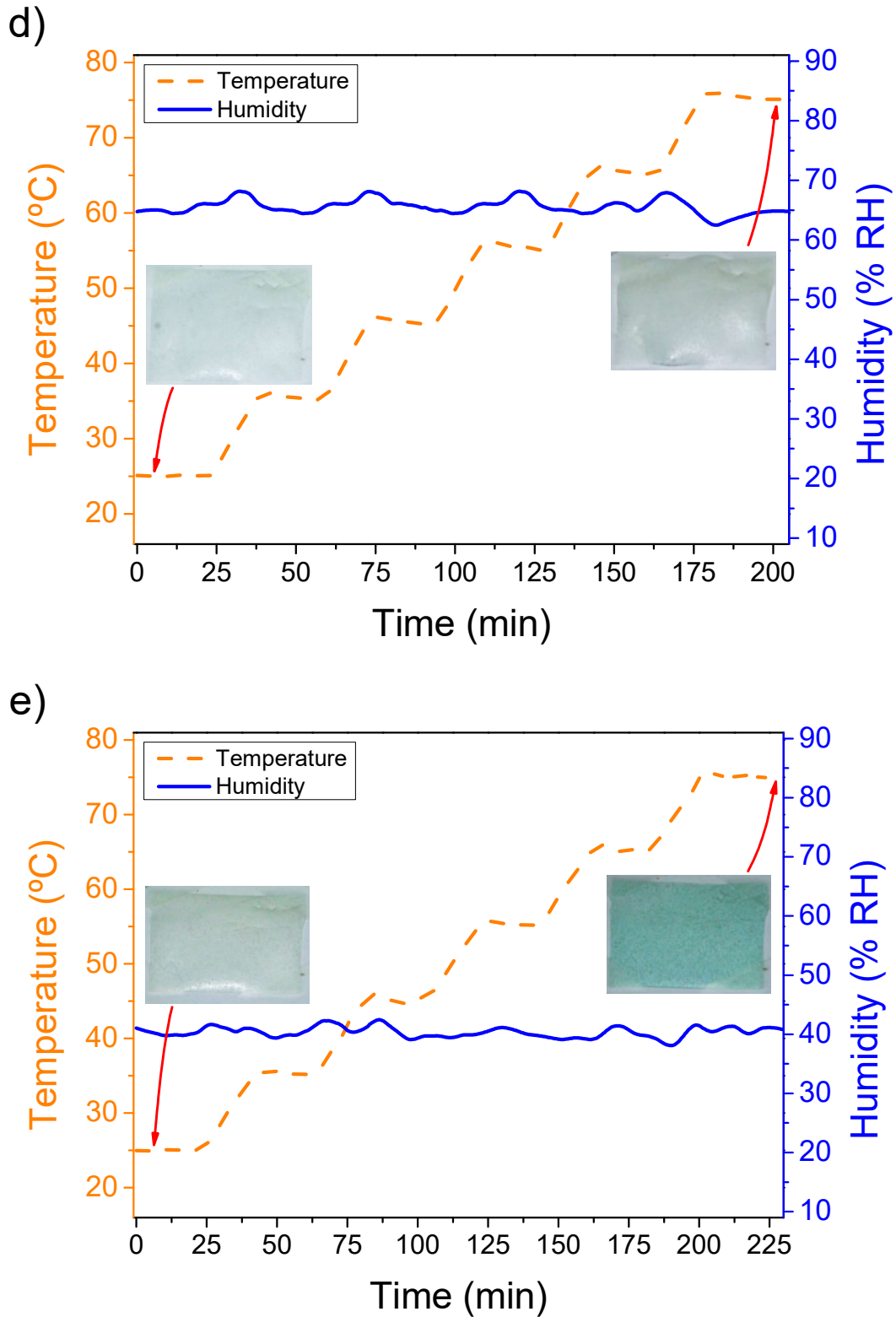
b)

c)

d)

e)
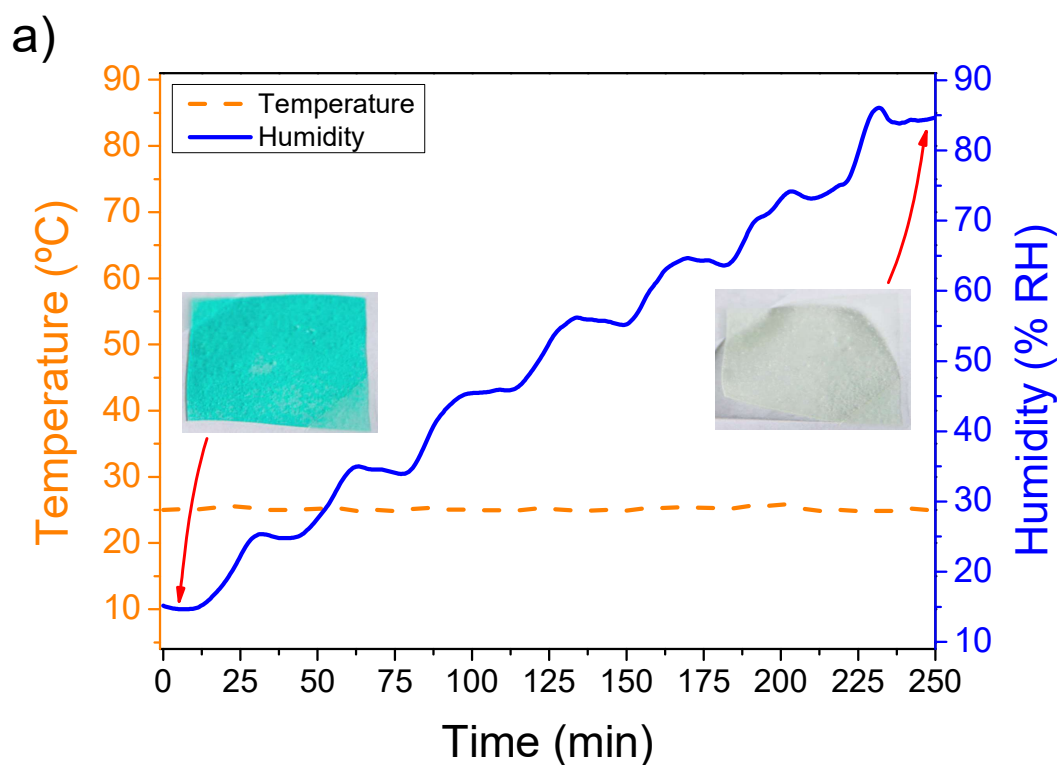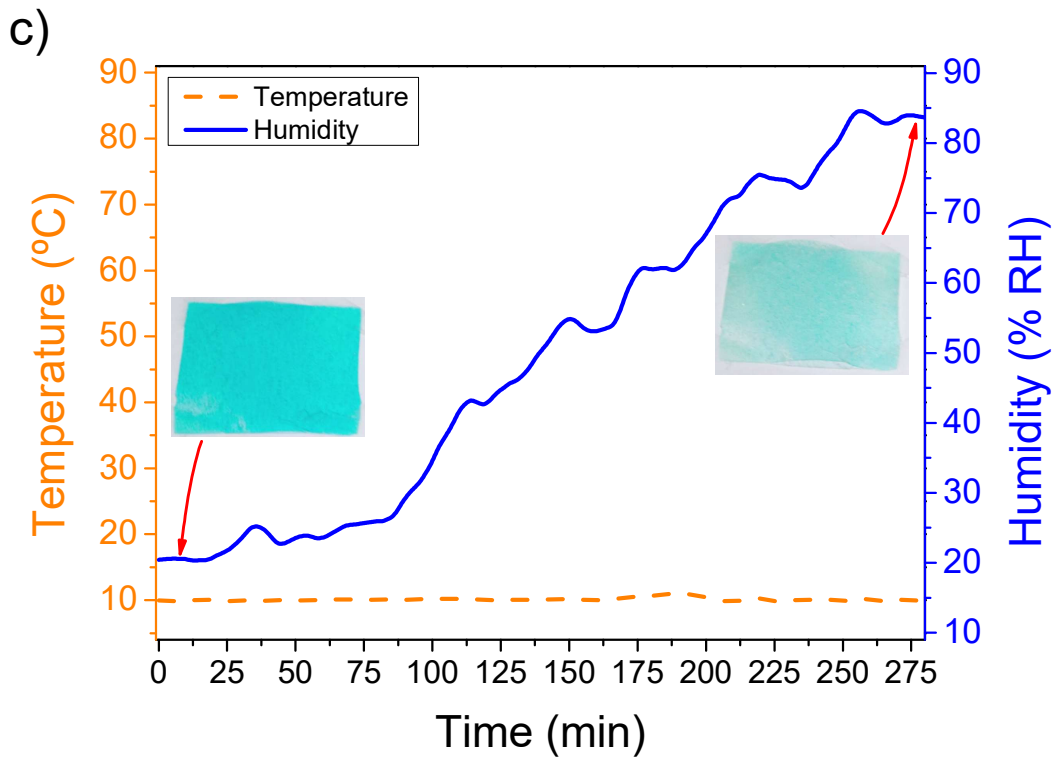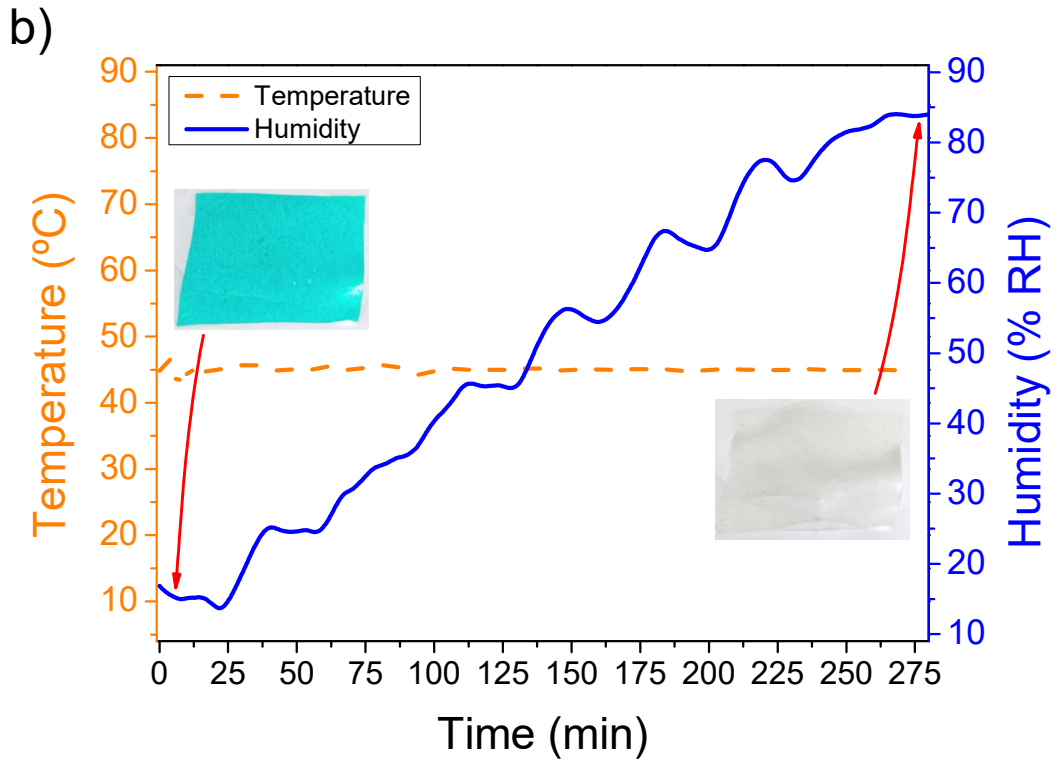
Figure 6.10 – Colour variation of the films (initial and final state) with increasing relative humidity at constant temperature of 25 ºC (a), 45 ºC (b) and 10 ºC (c), and with increasing temperature at constant relative humidity of 60 % (d) and 40 % (e).

Attending to **Figure 6.10a**, as the relative humidity increases, keeping the temperature constant, the film remains completely blue until 55 % of RH. At this moment, the film starts to change its colour to a lighter blue. When a RH of 75 % is reached, the film becomes colourless, defining the "range of colour change" from 55 to 75 % of RH.

These results also indicate a reversible response of the film in which blue films can recover the transparency/whitish colour at room temperature, confirming the reversible thermochromism, which is explained by an abrupt change in the chemical structure as indicated in section 3.5.3 [65].

Further, when the RH increases, keeping the temperature constant (**Figure 6.10b**), the film remains completely blue. When a RH of 40% is achieved, the film starts to change its colour to a lighter blue (similarly to the first test at room temperature). Finally, when a RH of 55 % is reached, the film becomes colourless, defining the range of colour change from 40 to 55 % RH. Thus, temperature has a strong influence on the range of colour change, a decrease from 55% to 40 % of RH being observed for the beginning of the colour change when the tests are performed at constant temperature of 25 ºC or 45 ºC, respectively.

When the temperature is maintained at 10 ºC (**Figure 6.10c**), a similar result is obtained. However, in this case, the film has not turned completely colourless at the end of the experiment, remaining slightly blue. In addition, the colour change begins at higher RH, around 65 % of RH, than in the previous test indicating that the water absorption (hydration of $[Bmim]_2[NiCl_4]$) is slower than when temperature is 25 ºC or 45 ºC. Thus, the variation on the moisture absorption capacity by the ILs with temperature and RH is confirmed [66]. The ILs structure (cation and anion type or cation alkyl chain length) and external factors (relative humidity, temperature or impurities) have an influence on the hydration of ILs [67] demonstrating that is a process sensitive to and stimulated by temperature [68].

Figure 6.10d show that the colourless sample does not undergo any change during the heating process under the defined test conditions (temperature variation from 25 ºC to 75 ºC under constant RH of 60 %). Thus, when there is enough humidity, the temperature has not influence for the colouring process.

Finally, as shown in **Figure 6.10e** of the supporting information, when the temperature reaches 65 ºC, the film begins to undergo a colour change. This result indicates that the water evaporation occurs when temperature reaches the mentioned value and, as a result, a

hydrothermochromatic coordination reaction occurs (from the colourless octahedral complex to the blue tetrahedral). Thus, when humidity is lower than 55 %, temperature induces water evaporation and, therefore, substitution of water molecules by Cl$^-$ atoms in the Ni (II) complex [69].

Thus, it is shown that the chromic phenomenon is humidity governed as at each temperature the humidity sets the colour change (directly dependence on the humidity of the system), and is thermally activated as the humidity limit value for the colour change depends on the temperature of the system. Thus, these humidity hybrid sensing materials present a temperature limit of 10 ºC below which colour change is not clearly observed. At room temperature, colour change occurs at 55 % of RH, setting this value as limit for thermochromic effect upon temperature variation.

6.3.5.3. Colour change mechanism

The colour changes observed by both the UV-Vis (**Figures 6.8 and 6.9**) and the climate chamber assays (**Figure 6.9**), are attributed to the $[NiCl_4]^{2-}$ complex in its tetrahedral conformation [64]. Therefore, the colour change of the films is explained by the modification of the coordination reaction as reported in **Scheme 6.1a** [35].

$[Bmim]_2[NiCl_4]$ is a hygroscopic salt capable of absorbing water molecules from ambient humidity. The afore discussed experiments show that the observed colour change is attributed to an absorption/dehydration process of the IL [35]. The coordination number of Ni (II) in the IL structure undergoes a change, varying its structure form tetrahedral (blue colour) to octahedral (not colour) without change in the cationic structure (see **Scheme 6.1b**) [70]. At room temperature, the Cl$^-$ ions of the nickel complex are replaced by water molecules from ambient humidity as a result of H-bonding interactions with the IL anion $[NiCl_4]^{2-}$ [64], corroborating the DSC endothermic peak results [59] (section 3.3). Therefore, the colouring process is dependent on the environmental humidity as demonstrated in the **Scheme 6.1b**.

Therefore, the thermochromic effect of the IL/PUA composite is an effect due to the water absorption/dehydration of the $[NiCl_4]^{2-}$, i.e. a change on the coordination number of the Ni(II) from octahedral to tetrahedral depending on the hydrated ($[Ni(H_2O)_6]^{2+}$) or dehydrated ($[NiCl_4]^{2-}$) state.
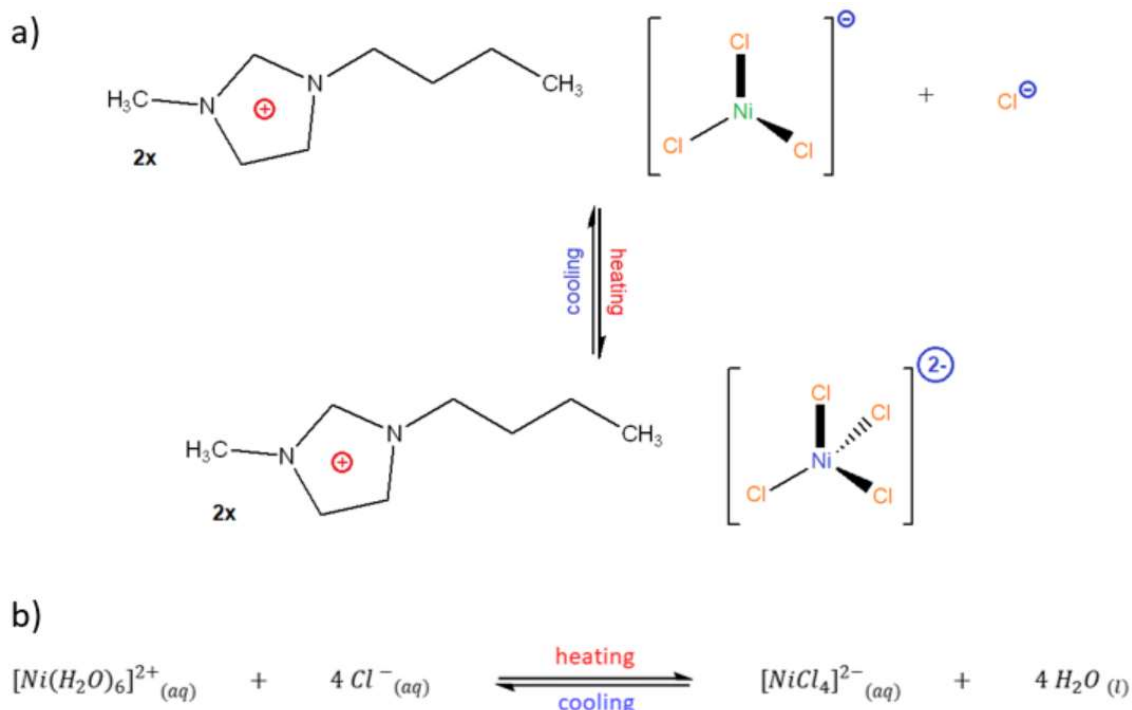
Scheme 6.1 – Chemical modifications occurring during the heating and cooling process of the [Bmim]2[NiCl4] ionic liquid (a) and changes in the coordination number of Ni(II) from octahedral to tetrahedral structure (b). Reproduced with permission [35]. Copyright 2019.

6.4. Conclusions

Flexible electronic devices and smart and multifunctional coatings are one of the cornerstones of the current technological advances. In this work, a flexible and cost-effective thermally activated humidity sensor and/or coating material has been successfully developed. After the incorporation of ionic liquid in a UV-curable polymer matrix, a porous network structure is obtained without relevant chemical changes neither in the IL or in the polymer matrix. In addition, the incorporation of the IL slightly influences the UV curing process of the polymer obtaining in all cases a polymer curing conversion of 88% or above. Further, the inclusion of the IL influences the electrical and mechanical properties of the samples for the higher IL contents obtaining an increase on the electrical conductivity and a decrease on the Young modulus.

Thermochromic effect was observed even at low IL loads. It was observed that humidity has a strong influence in the thermochromic effect up to 55% RH and that this process is thermally influenced. This effect is due to the water absorption/dehydration of $[NiCl_4]^{2-}$,

which is related to a change on the coordination number of the Ni(II) from octahedral to tetrahedral depending the hydrated ($[Ni(H_2O)_6]^{2+}$) or dehydrated ($[NiCl_4]^{2-}$) state.

Thus, the present work demonstrated the suitability of UV curable hybrid materials for smart and multifunctional coatings processable by additive manufacturing technologies, paving the way to cost-effective sensing coatings with a low carbon footprint due to it solvent-less process.

6.5. References

[1]   H. Wu, W.P. Fahy, S. Kim, H. Kim, N. Zhao, L. Pilato, A. Kafi, S. Bateman, J.H. Koo, Recent developments in polymers/polymer nanocomposites for additive manufacturing, Prog. Mater. Sci. 111 (2020). doi:10.1016/j.pmatsci.2020.100638.

[2]   J.Y. Lee, J. An, C.K. Chua, Fundamentals and applications of 3D printing for novel materials, Appl. Mater. Today. 7 (2017) 120–133. doi:10.1016/j.apmt.2017.02.004.

[3]   A. Endruweit, M.S. Johnson, A.C. Long, Curing of Composite Components by Ultraviolet Radiation: A Review, Polym. Compos. 27 (2006) 119–128. doi:10.1002/pc.20166.

[4]   P. Xiao, J. Zhang, F. Dumur, M.A. Tehfe, F. Morlet-Savary, B. Graff, D. Gigmes, J.P. Fouassier, J. Lalevée, Visible light sensitive photoinitiating systems: Recent progress in cationic and radical photopolymerization reactions under soft conditions, Prog. Polym. Sci. 41 (2015) 32–66. doi:10.1016/j.progpolymsci.2014.09.001.

[5]   C. Mendes-Felipe, J. Oliveira, I. Etxebarria, J.L. Vilas-Vilela, S. Lanceros-Mendez, State-of-the-Art and Future Challenges of UV Curable Polymer-Based Smart Materials for Printing Technologies, Adv. Mater. Technol. 4 (2019) 1–16. doi:10.1002/admt.201800618.

[6]   I. Gibson, D. Rosen, B. Stucker, Additive Manufacturing Technologies: 3D Printing, Rapid Prototyping, and Direct Digital Manufacturing, Second Edi, Springer, 2015. doi:10.2495/SDP-V9-N5-658-668.

[7]   H. Lasi, P. Fettke, H.G. Kemper, T. Feld, M. Hoffmann, Industry 4.0, Bus. Inf. Syst. Eng. 6 (2014) 239–242. doi:10.1007/s12599-014-0334-4.

[8]   E. Oztemel, S. Gursev, Literature review of Industry 4.0 and related technologies, J. Intell. Manuf. 31 (2020) 127–182. doi:10.1007/s10845-018-1433-8.

[9]   M.L. Kolhe, T. Shailesh, M.C. Trivedi, K.K. Mishra, Advances in Data and Information Sciences Proceedings of ICDIS 2019, Springer, 2020. doi:10.1007/978-981-15-0694-9_34.

[10]   Y. Xu, X. Wu, X. Guo, B. Kong, M. Zhang, X. Qian, S. Mi, W. Sun, The Boom in 3D-Printed Sensor Technology, China, 2017. doi:10.3390/s17051166.

[11]   S. Díaz, J.B. Stephenson, M.A. Labrador, Use of wearable sensor technology in gait, balance, and range of motion analysis, Appl. Sci. 10 (2020). doi:10.3390/app10010234.

[12]   L.T. Ng, J.T. Guthrie, Y.J. Yuan, H. Zhao, UV-cured natural polymer-based membrane for biosensor application, J. Appl. Polym. Sci. 79 (2001) 466–472. doi:10.1002/1097-4628(20010118)79:3<466::AID-APP90>3.0.CO;2-F.

[13]   C. Mendes-Felipe, J. Oliveira, P. Costa, L. Ruiz-Rubio, A. Iregui, A. González, J.L. Vilas, S. Lanceros-Mendez, Stimuli responsive UV cured polyurethane acrylated/carbon nanotube composites for piezoresistive sensing, Eur. Polym. J. 120 (2019) 109226. doi:10.1016/j.eurpolymj.2019.109226.

[14]   O. Jifei, D. Gershon, C. Chin-Yi, H. Felix, W. Karl, H. Ishii, Cilllia - 3D Printed Micro-Pillar Structures for Surface Texture, Actuation and Sensing, Des. New Mater. Manuf. Tech. (2016) 5753–5764. doi:10.2307/j.ctt1n7qkg7.29.

[15]   D.I. Woodward, C.P. Purssell, D.R. Billson, D.A. Hutchins, S.J. Leigh, Additively-manufactured piezoelectric devices, Phys. Status Solidi Appl. Mater. Sci. 212 (2015) 2107–2113. doi:10.1002/pssa.201532272.

[16]   P. Maillard, A. Heinrich, 3D printed freeform optical sensors for metrology application, Opt. Syst. Des. 2015 Opt. Fabr. Testing, Metrol. V. 9628 (2015) 96281J. doi:10.1117/12.2191280.

[17]   A. Wickberg, J.B. Mueller, Y.J. Mange, J. Fischer, T. Nann, M. Wegener, Three-dimensional micro-printing of temperature sensors based on up-conversion luminescence, Appl. Phys. Lett. 106 (2015) 1–5. doi:10.1063/1.4916222.

[18]   M.E. Staymates, W.A. MacCrehan, J.L. Staymates, R.R. Kunz, T. Mendum, T.H. Ong, G. Geurtsen, G.J. Gillen, B.A. Craven, Biomimetic Sniffing Improves the Detection Performance of a 3D Printed Nose of a Dog and a Commercial Trace Vapor Detector, Sci. Rep. 6 (2016) 1–10. doi:10.1038/srep36876.

[19]   C.C. Okpala, Nanocomposites – An Overview, 8 (2013) 17–23.

[20]   X. Wang, M. Jiang, Z. Zhou, J. Gou, D. Hui, 3D printing of polymer matrix composites: A review and prospective, Compos. Part B Eng. 110 (2017) 442–458.

doi:10.1016/j.compositesb.2016.11.034.

[21]   J.W. Stansbury, M.J. Idacavage, 3D printing with polymers: Challenges among expanding options and opportunities, Dent. Mater. 32 (2016) 54–64. doi:10.1016/j.dental.2015.09.018.

[22]   J. Saroia, Y. Wang, Q. Wei, M. Lei, X. Li, Y. Guo, K. Zhang, A review on 3D printed matrix polymer composites: its potential and future challenges, Int. J. Adv. Manuf. Technol. 106 (2020) 1695–1721. doi:10.1007/s00170-019-04534-z.

[23]   J.Z. Manapat, Q. Chen, P. Ye, R.C. Advincula, 3D Printing of Polymer Nanocomposites via Stereolithography, Macromol. Mater. Eng. 302 (2017) 1–13. doi:10.1002/mame.201600553.

[24]   T.A. Campbell, O.S. Ivanova, 3D printing of multifunctional nanocomposites, Nano Today. 8 (2013) 119–120. doi:10.1016/j.nantod.2012.12.002.

[25]   D.M. Correia, L.C. Fernandes, P.M. Martins, C. García-Astrain, C.M. Costa, J. Reguera, S. Lanceros-Méndez, Ionic Liquid–Polymer Composites: A New Platform for Multifunctional Applications, Adv. Funct. Mater. 30 (2020) 1–43. doi:10.1002/adfm.201909736.

[26]   Z. Lei, B. Chen, Y.M. Koo, D.R. Macfarlane, Introduction: Ionic Liquids, Chem. Rev. 117 (2017) 6633–6635. doi:10.1021/acs.chemrev.7b00246.

[27]   S. Zhang, Q. Zhang, Y. Zhang, Z. Chen, M. Watanabe, Y. Deng, Beyond solvents and electrolytes: Ionic liquids-based advanced functional materials, Prog. Mater. Sci. 77 (2016) 80–124. doi:10.1016/j.pmatsci.2015.10.001.

[28]   C. Guerrero-Sanchez, T. Erdmenger, T. Lara-Ceniceros, E. Jimenez-Regalado, U.S. Schubert, Chapter 10 - Smart materials based on ionic liquids: The magnetorheological fluid case, in: Ion. Liq. From Knowl. to Appl., ACS Symposium Series, 2009: pp. 147–155. doi:10.1021/bk-2009-1030.ch010.

[29]   B. Ziõłkowski, Z. Ates, S. Gallagher, R. Byrne, A. Heise, K.J. Fraser, D. Diamond, Mechanical properties and UV curing behavior of poly(N-Isopropylacrylamide) in phosphonium-based ionic liquids, Macromol. Chem. Phys. 214 (2013) 787–796. doi:10.1002/macp.201200616.

[30]   C. Gerbaldi, J.R. Nair, S. Ahmad, G. Meligrana, R. Bongiovanni, S. Bodoardo, N. Penazzi, UV-cured polymer electrolytes encompassing hydrophobic room temperature ionic liquid for lithium batteries, J. Power Sources. 195 (2010) 1706–1713. doi:10.1016/j.jpowsour.2009.09.047.

[31]   N.A. Bakhtina, U. Loeffelmann, N. MacKinnon, J.G. Korvink, Two-Photon Nanolithography Enhances the Performance of an Ionic Liquid-Polymer Composite Sensor, Adv. Funct. Mater. 25 (2015) 1683–1693. doi:10.1002/adfm.201404370.

[32]   A.R. Schultz, P.M. Lambert, N.A. Chartrain, D.M. Ruohoniemi, Z. Zhang, C. Jangu, M. Zhang, C.B. Williams, T.E. Long, 3D printing phosphonium ionic liquid networks with mask projection microstereolithography, ACS Macro Lett. 3 (2014) 1205–1209. doi:10.1021/mz5006316.

[33]   K. Chen, J. Zhou, F. Ge, R. Zhao, C. Wang, Smart UV-curable fabric coatings with self-healing ability for durable self-cleaning and intelligent oil/water separation, Colloids Surfaces A Physicochem. Eng. Asp. 565 (2019) 86–96. doi:10.1016/j.colsurfa.2019.01.003.

[34]   K. Sone, Y. Fukuda, Inorganic Thermochromism, Springer-Verlag, 1987.

[35]   L.C. Fernandes, D.M. Correia, C. García-Astrain, N. Pereira, M. Tariq, J.M.S.S. Esperança, S. Lanceros-Méndez, Ionic-Liquid-Based Printable Materials for Thermochromic and Thermoresistive Applications, ACS Appl. Mater. Interfaces. 11 (2019) 20316–20324. doi:10.1021/acsami.9b00645.

[36]   D.R. Bloomquist, R.D. Willett, Thermochromic phase transitions in transition metal salts, Coord. Chem. Rev. 47 (1982) 125–164. doi:10.1016/0010-8545(82)85012-1.

[37]   L. Yu, G.Z. Chen, Cryo-solvatochromism in ionic liquids, RSC Adv. 4 (2014) 40281–40285. doi:10.1039/c4ra08116a.

[38]   G. Perez, V.R. Allegro, M. Corroto, A. Pons, A. Guerrero, Smart reversible thermochromic mortar for improvement of energy efficiency in buildings, Constr. Build. Mater. 186 (2018) 884–891. doi:10.1016/j.conbuildmat.2018.07.246.

[39]   Y. Cui, Y. Ke, C. Liu, Z. Chen, N. Wang, L. Zhang, Y. Zhou, S. Wang, Y. Gao, Y. Long, Thermochromic VO2 for Energy-Efficient Smart Windows, Joule. 2 (2018)

1707–1746. doi:10.1016/j.joule.2018.06.018.

[40]   H. Kim, Y. Kim, K.S. Kim, H.Y. Jeong, A.R. Jang, S.H. Han, D.H. Yoon, K.S. Suh, H.S. Shin, T. Kim, W.S. Yang, Flexible thermochromic window based on hybridized VO2/graphene, ACS Nano. 7 (2013) 5769–5776. doi:10.1021/nn400358x.

[41]   W. Ning, X.G. Zhao, J. Klarbring, S. Bai, F. Ji, F. Wang, S.I. Simak, Y. Tao, X.M. Ren, L. Zhang, W. Huang, I.A. Abrikosov, F. Gao, Thermochromic Lead-Free Halide Double   Perovskites,   Adv.   Funct.   Mater.   29   (2019)   1–8. doi:10.1002/adfm.201807375.

[42]   M.G. Baron, M. Elie, Temperature sensing using reversible thermochromic polymeric films, Sensors Actuators, B Chem. 90 (2003) 271–275. doi:10.1016/S0925-4005(03)00045-5.

[43]   Y. Guan, L. Zhang, D. Wang, J.L. West, S. Fu, Preparation of thermochromic liquid crystal microcapsules for intelligent functional fiber, Mater. Des. 147 (2018) 28–34. doi:10.1016/j.matdes.2018.03.030.

[44]   X. Geng, W. Li, Y. Wang, J. Lu, J. Wang, N. Wang, J. Li, X. Zhang, Reversible thermochromic microencapsulated phase change materials for thermal energy storage application in thermal protective clothing, Appl. Energy. 217 (2018) 281–294. doi:10.1016/j.apenergy.2018.02.150.

[45]   H. zhi Chen, M. Zhang, B. Bhandari, C. hui Yang, Development of a novel colorimetric food package label for monitoring lean pork freshness, Lwt. 99 (2019) 43–49. doi:10.1016/j.lwt.2018.09.048.

[46]   L.C. Fernandes, D.M. Correia, N. Pereira, C.R. Tubio, S. Lanceros-Méndez, Highly Sensitive Humidity Sensor Based on Ionic Liquid–Polymer Composites, ACS Appl. Polym. Mater. 1 (2019) 2723–2730. doi:10.1021/acsapm.9b00675.

[47]   X. Ni, J. Luo, R. Liu, X. Liu, A novel flexible UV-cured carbon nanotube composite film for humidity sensing, Sensors Actuators, B Chem. 297 (2019). doi:10.1016/j.snb.2019.126785.

[48]   X. Lv, Y. Li, P. Li, M. Yang, A resistive-type humidity sensor based on crosslinked polyelectrolyte prepared by UV irradiation, Sensors Actuators, B Chem. 135 (2009)

581–586. doi:10.1016/j.snb.2008.10.008.

[49] N.B. Cho, T.H. Lim, Y.M. Jeon, M.S. Gong, Inkjet printing of polymeric resistance humidity sensor using UV-curable electrolyte inks, Macromol. Res. 16 (2008) 149–154. doi:10.1007/BF03218844.

[50] C. Decker, New developments in UV radiation curing of protective coatings, Surf. Coatings Int. Part B Coatings Trans. 88 (2005) 9–17. doi:10.1007/BF02699702.

[51] C. Zhong, T. Sasaki, A. Jimbo-Kobayeshi, E. Fujiwara, A. Kobayashi, M. Tada, Y. Iwasawa, Syntheses, structures, and properties of a series of metal ion-containing dialkylimidazolium ionic liquids, Bull. Chem. Soc. Jpn. 80 (2007) 2365–2374. doi:10.1246/bcsj.80.2365.

[52] M.B. Meredith, C.H. McMillen, J.T. Goodman, T.P. Hanusa, Ambient temperature imidazolium-based ionic liquids with tetrachloronickelate(II) anions, Polyhedron. 28 (2009) 2355–2358. doi:10.1016/j.poly.2009.04.037.

[53] O. Llorente, M.J. Fernández-Berridi, A. González, L. Irusta, Study of the crosslinking process of waterborne UV curable polyurethane acrylates, Prog. Org. Coatings. 99 (2016) 437–442. doi:10.1016/j.porgcoat.2016.06.020.

[54] C. Mendes-Felipe, T. Rodrigues-Marinho, J.L. Vilas, S. Lanceros-Mendez, UV curable nanocomposites with tailored dielectric response, Polymer (Guildf). 196 (2020). doi:10.1016/j.polymer.2020.122498.

[55] C. Mendes-Felipe, J.C. Barbosa, S. Gonçalves, N. Pereira, C.M. Costa, J.L. Vilas-Vilela, S. Lanceros-Mendez, High dielectric constant UV curable polyurethane acrylate/indium tin oxide composites for capacitive sensing, Compos. Sci. Technol. 199 (2020). doi:10.1016/j.compscitech.2020.108363.

[56] X. Gong, J. Zhang, S. Jiang, Ionic liquid-induced nanoporous structures of polymer films, Chem. Commun. 56 (2020) 3054–3057. doi:10.1039/c9cc08768k.

[57] P.K. Behera, K.M. Usha, P.K. Guchhait, D. Jehnichen, A. Das, B. Voit, N.K. Singha, A novel ionomeric polyurethane elastomer based on ionic liquid as crosslinker, RSC Adv. 6 (2016) 99404–99413. doi:10.1039/c6ra21650a.

[58] R. Fernández De Luis, M.K. Urtiaga, J.L. Mesa, K. Vidal, L. Lezama, T. Rojo, M.I.

Arriortua, Short-Range and long-range magnetic ordering, in third generation brannerite type inorganic-organic vanadates: [{Mn(Bpy)}(VO3) 2]≈(H2O)1.16 and [{Mn(Bpy) 0.5}(VO3)2]≈(H2O)0.62, Chem. Mater. 22 (2010) 5543–5553. doi:10.1021/cm1015433.

[59] R. Fernández De Luis, J. Orive, E.S. Larrea, M.K. Urtiaga, M.I. Arriortua, Reversible solid-state transformation in {Ni2(H 2O)2(Bpa)2}(V6O17) proved by synchrotron radiation: Color and magnetic properties change, Cryst. Growth Des. 14 (2014) 658–670. doi:10.1021/cg401540s.

[60] L. Liu, Z. Zheng, C. Gu, X. Wang, The poly(urethane-ionic liquid)/multi-walled carbon nanotubes composites, Compos. Sci. Technol. 70 (2010) 1697–1703. doi:10.1016/j.compscitech.2010.06.007.

[61] D.M. Correia, J.C. Barbosa, C.M. Costa, P.M. Reis, J.M.S.S. Esperança, V. De Zea Bermudez, S. Lanceros-Méndez, Ionic Liquid Cation Size-Dependent Electromechanical Response of Ionic Liquid/Poly(vinylidene fluoride)-Based Soft Actuators, J. Phys. Chem. C. 123 (2019) 12744–12752. doi:10.1021/acs.jpcc.9b00868.

[62] A. Reizabal, R. Gonçalves, A. Fidalgo-Marijuan, C.M. Costa, L. Pérez, J.L. Vilas, S. Lanceros-Mendez, Tailoring silk fibroin separator membranes pore size for improving performance of lithium ion batteries, J. Memb. Sci. 598 (2020). doi:10.1016/j.memsci.2019.117678.

[63] J.C. Dias, M.S. Martins, S. Ribeiro, M.M. Silva, J.M.S.S. Esperança, C. Ribeiro, G. Botelho, C.M. Costa, S. Lanceros-Mendez, Electromechanical actuators based on poly(vinylidene fluoride) with [N1 1 1 2(OH)][NTf2] and [C2mim] [C2SO4], J. Mater. Sci. 51 (2016) 9490–9503. doi:10.1007/s10853-016-0193-0.

[64] X. Wei, L. Yu, D. Wang, X. Jin, G.Z. Chen, Thermo-solvatochromism of chloro-nickel complexes in 1-hydroxyalkyl-3-methyl-imidazolium cation based ionic liquids, Green Chem. 10 (2008) 296–30. doi:10.1039/b715763k.

[65] K. Sone, Y. Fukuda, Chapter F - Thermochromism of Transition Metal Complexes in the Solid State, in: Inorg. Thermochromism, Springer-Verlag, 1987: pp. 104–131. doi:10.1007/978-3-642-51017-5_6.

[66] Y. Chen, X. Gao, X. Liu, G. Ji, L. Fu, Y. Yang, Q. Yu, W. Zhang, X. Xue, Water collection from air by ionic liquids for efficient visible-light-driven hydrogen evolution by metal-free conjugated polymer photocatalysts, Renew. Energy. 147 (2020) 594–601. doi:10.1016/j.renene.2019.09.029.

[67] Y. Cao, Y. Chen, X. Sun, Z. Zhang, T. Mu, Water sorption in ionic liquids: Kinetics, mechanisms and hydrophilicity, Phys. Chem. Chem. Phys. 14 (2012) 12252–12262. doi:10.1039/c2cp41798g.

[68] M.G. Freire, C.M.S.S. Neves, I.M. Marrucho, J.A.P. Coutinho, A.M. Fernandes, Hydrolysis of tetrafluoroborate and hexafluorophosphate counter ions in imidazolium-based ionic liquids, J. Phys. Chem. A. 114 (2010) 3744–3749. doi:10.1021/jp903292n.

[69] L. Cammarata, S.G. Kazarian, P.A. Salter, T. Welton, Molecular states of water in room temperature ionic liquids, Phys. Chem. Chem. Phys. 3 (2001) 5192–5200. doi:10.1039/b106900d.

[70] X. Wei, L. Yu, X. Jin, D. Wang, G.Z. Chen, Solar-thermochromism of pseudocrystalline nanodroplets of ionic liquid-NiII complexes immobilized inside translucent microporous PVDF films, Adv. Mater. 21 (2009) 776–780. doi:10.1002/adma.200801816.

Chapter 7

Conclusions and Future Trends

The general conclusions and considerations are outlined with reference to the initial objectives of the work. Further, possible future work in the field are suggested.

7.1. Conclusions

As a conclusion, the main goal of this thesis has been fulfilled since different multifunctional photopolymerizable materials have been prepared and tested for specific applications. Different UV curable polymer composites have been obtained and characterized according to their photopolymerization capability and physico-chemical properties. Also, depending on the material, different functional characterizations have been carried out, including piezoresistivity, dielectric response, magnetic properties, thermochromism and humidity sensing.

The inks developed in the present work include the mixture of polyurethane acrylated (PUA) with multi-walled carbon nanotubes (MWCNT) for improved piezoresistive response, PUA with barium titanate ($BaTiO_3$) for dielectric materials with tailored dielectric response or PUA with indium tin oxide (ITO) for dielectric materials with improved dielectric constant and optical transparency. Further, PUA was mixed with magnetite (Fe_3O_4), cobalt ferrite (CFO) and neodymium iron boron (NdFeB) to obtain magnetic inks with tailored magnetic properties and, finally, PUA was mixed with ionic liquid (IL) to obtain thermally activated chromic humidity sensors.

As a general conclusion, the addition of fillers into the photopolymerizable material induces a decay on the polymerization process whenever the added fillers present UV light absorption. Other intrinsic properties of the fillers, such as size or shape, influence the viscosity of the photocurable inks and, therefore, the polymerization process. Further, the increasing filler content also hinders the photopolymerization process.

In this sense, particles with larger aspect ratio and/or higher UV light absorbance, such as MWCNT, Fe_3O_4 or cobalt ferrite CFO, have been added in a very small amount, up to 0.6 wt.%, 6wt.% and 10 wt.%, respectively, while particles with smaller aspect ratio and lower UV light absorbance, such as barium titanate $BaTiO_3$, can be added a higher content, up to 65 wt.%.

Regarding to physico-chemical properties of the photocured polymer composites, different effects have been observed depending on the nature of the filler. Common to all composites, no intermolecular interactions between the fillers and the polymer have been observed, however, attending to thermal properties, specifically to the glass transition temperature (T_g) of the material, different behaviour is obtained depending on the filler type and content.

Thus, MWCNT induce a significant decrease of the T_g of PUA, while $BaTiO_3$, Fe_3O_4, CFO and NdFeB just caused a slightly decrease of T_g. In the case of indium tin oxide (ITO) and IL based materials, the inclusion of different filler contents has not significantly affected the T_g of PUA.

Attending to the mechanical properties, the inclusion of fillers induces an increase on the Young modulus (E) without significant effect on the maximum elongation (ε_b) of each sample for lower filler contents independently on the filler type. This effect is associated to the reinforcement effect of the inorganic fillers. In contrast, the addition of small amounts of IL does not influence the mechanical properties of PUA. When higher filler contents are added, filler agglomeration occurs in all cases and these agglomerates act as breaking points due to stress accumulation, decreasing the ε_b.

With respect to the electrical response, the d.c. electrical conductivity and the dielectric constant of the composites have been evaluated. It has been observed that the inclusion of fillers increases the d.c. electrical conductivity, typically low for pure PUA due to its insulating characteristic. Three different effects cause this increase. First, several of the use particles show higher electrical conductivity than the PUA matrix and therefore, per mass unit, higher electrical conductivity is obtained for composite materials than for the pure polymer. Second, the inclusion of fillers induces an increase on the charges in the particle-polymer interfaces increasing the total electrical conductivity of the material. Third, the ionic conductivity contributions of the polymer matrix associated to the different degree of curing depending on the filler content and type increases the electrical conductivity of each composite material.

With respect to the dielectric constant, it increases with the addition of $BaTiO_3$ and ITO. This increase is associated to the higher dielectric constant of the fillers added and to an increase of the interface polarization effects (Maxwell–Wagner–Sillars effect) in which the filler-polymer interfaces hinder carrier transport, increasing charge trapping at the interfaces and local ionic conductivity. This dielectric constant can be tailored depending on the type and size of the fillers.

Finally, multifunctional materials are obtained depending on the filler. The electrical percolation threshold of the MWCNT/PUA composites is between 0.1 wt.% to 0.4 wt.% MWCNT content and for samples with higher MWCNT content good electrical conductivity

is obtained. Composites with 0.3 wt.% and 0.5 wt.% MWCNT content show piezoresistive response characterized by GF values between 0.8 and 2.6 that stabilizes after around 100 stress-strains cycles. Thus, MWCNT inclusion allows the fabrication of piezoresistive photocurable materials with suitable GF values for sensing applications.

Further, $BaTiO_3$ and ITO combined with PUA polymer enable the fabrication of dielectric materials with different optical properties and high dielectric constant that can be applied on flexible printing of electronic applications. When $BaTiO_3$ is used, dielectric constant variations between 7.5 to 25 can be obtained depending on the filler size and content, while ITO allows dielectric constants up to 33 together with an optical transparency which decreases with increasing content.

The use of Fe_3O_4, CFO and NdFeB particles demonstrate the ability to prepare magnetic composites with tailored magnetic properties (from hard to soft magnetic ones) depending on filler type and content. Fe_3O_4/PUA materials show a saturation magnetization up to 3.70 emu/g, remanence of 0.27 emu/g and no coercivity; while samples with CFO show saturation magnetization up to 6.50 emu/g, remanence of 1.69 emu/g and coercivity of 2000 Oe. NdFeB/PUA composites show a hard magnetic material behaviour with saturation magnetization up to 63.86 emu/g, remanence of 44.95 emu/ g and coercivity of 7000 Oe. All these develop magnetic materials are processable by additive manufacturing and tailored magnetic response for specific application requirements has been achieved.

Finally, by adding IL, PUA can be used as temperature activated thermochromic humidity sensor with a colour change from blue to colourless. This thermochromic effect has been observed even at low IL loads. Humidity has a strong influence in the thermochromic effect up to 55% relative humidity (RH). Further, the humidity sensing capability is thermally activated. Thus, the suitability of UV curable hybrid materials for smart and multifunctional coatings processable by additive manufacturing technologies has been demonstrated, paving the way to cost-effective sensing coatings with a low carbon footprint due to it solvent-less process.

7.2. Future work

In this thesis, new UV curable multifunctional materials have been developed. Nevertheless, new materials with improved properties or new functionalities can be further explored.

For instance, materials with even higher electrical conductivity can be further improved or tailored for specific applications, eventually by employing other conductive fillers such as graphene or metallic wires, through polymer curing can be an issue for some filler concentrations. The same can be started with increasing electromechanical response.

Also, the dielectric constant can be further improved/tailored as well as the optical transparency. In this area, higher aspect ratio dielectric fillers can be used.

With respect to magnetic properties, materials allowing higher magnetization and anisotropic fillers should be considered, for anisotropic magnetic response.
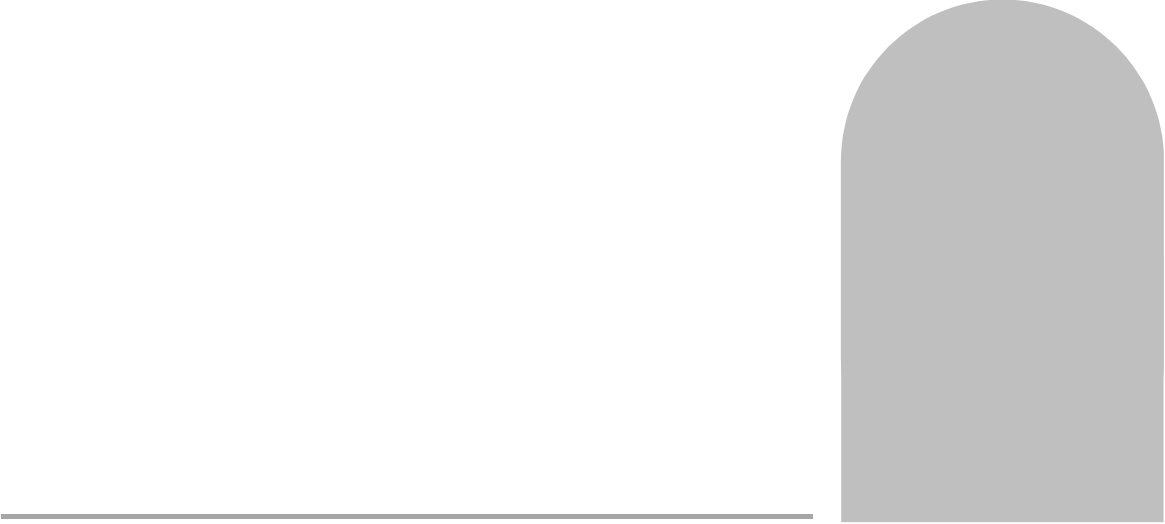
Further, new functionalities could be added to photocurable PUA materials by the use of titanium dioxide (TiO_2), and/or silver nanoparticles that induces photocatalytic, self-cleaning and antimicrobial properties to the photocurable films. In a similar way, the rich variety of stimuli IL can be further explored for integration into the UV curable matrix.

In order to improve filler integration into UV curable matrices, the polymer matrix can be tailored for specific fillers with UV curing at specific wavelengths or with tailored polymer/filler compatibility. Also, it would be interesting the integration of the developed materials in printed electronic complex components and evaluate integration, performance and reliability in real application scenarios.

In addition, all obtained multifunctional materials could be processed by additive manufacturing in order to prepare 3D printed functional materials or devices. In this sense, time responsive 3D printed structures can be fabricated that can change one or more of their properties over time. Thus, piezoresistive 3D printed sensor could be printed using MWCNT/PUA composites, 3D humidity sensor with IL/PUA hybrid materials or also polymer-bonded 3D printed magnets using NdFeB/PUA composites.

Finally, taking into consideration the green deal approach of European Commission, circular economy approaches must be integrated in order to improve sustainability. Circular economy (CE) emerges to promote sustainable development being therefore transversal in all human activities, but particularly relevant in the industrial production and consumer sectors. In this sense, a new horizon emerges related to the synthesis of new photocurable polymers and composites more environmental friendly using more sustainable precursors obtained from natural sources such as soybean oils, castor oils or biodegradable lignin.

Thus, despite the interesting results obtained in the present work, different interesting research paths must still be followed.

Curriculum Vitae and Contributions

Jesus Cristian Mendes Felipe

BCMaterials – Basque Center for Materials, Applications and Nanostructures

Edificio Martina Casiano, Planta 3

Parque Científico UPV/EHU

Barrio Sarriena, s/n, 48940 Leioa, Bizkaia

email: cristian.mendes@bcmaterials.net

PERSONAL INFORMATION

Gender: Male

Date of Birth: January 1st, 1994

Language skills: English, Spanish

RESEARCH TOPICS

Photopolymerization, UV curing, polymer composites, smart materials, 3D printing, stereolithography and digital light processing

Polymer synthesis, DSC, TGA, FTIR, DMA, mechanical tests, sensors.

EDUCATION

PhD	University of the Basque Country – UPV/EHU (2017-Present)
Thesis Title	Multifunctional photocurable advanced materials for electronics and sensing applications
Advisors	Prof. José Luis Vilas Vilela (UPV/EHU)
	Prof. Senen Lanceros Mendez (BCMaterials)
M.Sc. New Materials	University of the Basque Country – UPV/EHU (2016)
B.Sc Chemistry	University of the Basque Country – UPV/EHU (2012)

FELLOWSHIPS OR SCHOLARSHIPS

Recipient of BCMaterials Predoctoral Fellowship, 2017

> Advisor: Senen Lanceros Mendez

Recipient of Basque Government B.Sc. Scholarships, 2012 to 2017

RESEARCH STAYS ABROAD

Universidade do Minho, Braga, Portugal (one month)

> Advisor: Dr. Vanessa Fernandes Cardoso

Facultad de Farmacia y Bioquímica, Universidad de Buenos Aires, Argentina (three months)

> Advisor: Dr. Guillermo Javier Copello

SCIENTIFIC PUBLICATIONS

Part of the thesis:

1) C. Mendes-Felipe, JC Barbosa, Sérgio Gonçalves, Nelson Pereira, CM Costa, J. L. Vilas-Vilela, S. Lanceros-Mendez. High dielectric constant UV curable polyurethane acrylate/indium tin oxide composites for capacitive sensing. Compos. Sci. Technol. 2020; 199, 108363.

2) C. Mendes-Felipe, T. Rodrigues-Marinho, J. L. Vilas-Vilea, S. Lanceros-Mendez. UV curable nanocomposites with tailored dielectric response. Polymer 2020; 196, 122498.

3) C. Mendes-Felipe, J. Oliveira, P. Costa, L. Ruiz-Rubio, A. Iregui, A. González, J. L. Vilas-Vilela, S. Lanceros-Mendez. Stimuli responsive UV cured polyurethane acrylated/carbon nanotube composites for piezoresistive sensing. Eur. Polym. J. 2019; 120, 109226.

4) C. Mendes-Felipe, J. Oliveira, I. Etxebarria, J. L. Vilas-Vilela, S. Lanceros-Mendez. State-of-the-art and future challenges of UV curable polymer-based smart materials for printing technologies. Adv. Mater. Technol. 2019; 4, 1800618.

Other article:

1) C. Mendes-Felipe, L. Ruiz-Rubio, J. L. Vilas-Vilela. Biomaterials obtained by photopolymerization: from UV to two photon. Emerg. Mater. 2020; 3, 453-468.

2) C. Mendes-Felipe, B. Artetxe, L. Ruiz-Rubio, J. L. Vilas-Vilela. Polimeroetan oinarritutako fabrikazio gehigarria eta 3D inprimaketa: etorkizuneko teknologia gaur egungo gizartean. Ekaia, Zientzia eta Teknologia aldizkaria 2019; N. Extra 2019, 101-119.

3) C. Mendes-Felipe, D. Patrocinio, J. M. Laza, L. Ruiz-Rubio, J. L. Vilas-Vilela. Evaluation of postcuring process on the thermal and mechanical properties of the Clear02™ resin used in stereolithography. Polym. Test. 2018; 72, 115-121.

CONTRIBUTIONS TO MEETINGS

1) **C. Mendes-Felipe**, A. García-Díez, D. Salazar, J. L. Vilas-Vilela, S. Lanceros-Méndez. Neodymium-Iron-Boron/polyurethane acrylate (NFB/PUA) magnetic composite films obtained by photopolymerization. *"Nanomagnetism: Permanent Magnets, Applications and Sustainability" Mini-colloquia at International "CDMGEFES2020" congress*, Online (Madrid, Spain), 2020. Oral Presentation.

2) **C. Mendes-Felipe**, T. Rodrigues-Marinho, J. L. Vilas-Vilela, S. Lanceros-Mendez. UV curable nanocomposites with tailored dielectric response. *2020 #RSCPoster Twitter Conference*, Online via Twitter, 2020. Poster Contribution.

3) **C. Mendes-Felipe**, G. Ventosa, L. Ruiz-Rubio, J. L. Vilas, S. Lanceros-Méndez. A new generation of UV curable polyurethane hydrogels as new 3D printable materials for biomedical applications. *3rd Biennial Young Researchers Workshop on Biomaterials and Applications (BioMAPP2019)*, Leioa (Spain), 2019. Poster and Oral Contribution.

4) C. Mendes-Felipe, **L. Ruiz-Rubio**, J. L. Vilas, S. Lanceros-Méndez. Influence of the alcohol-terminated acrylates on the mechanical properties of a new series of UV curable polyurethane acrylated resins. *VII International Baekeland Symposium (Baekeland2019)*, Tarragona (Spain), 2019. Oral Contribution.

5) **C. Mendes-Felipe**, J. L. Vilas-Vilela, S. Lanceros-Mendez. Imprimiendo el futuro. *II Jornadas doctorales de la UPV/EHU*, Bilbao (Spain), 2019. Oral Contribution.

6) **C. Mendes-Felipe**, P. Costa, J. L. Vilas-Vilela, S. Lanceros-Mendez. Filler size and concentration dependence of the dielectric response of UV curable BaTiO$_3$ based nanocomposites. *European Materials Research Society Congress – Spring Meeting (E-MRS Spring Meeting 2019)*, Nize (France), 2019. Oral Contribution.

7) **C. Mendes-Felipe**, J. Oliveira, J. L. Vilas-Vilela, S. Lanceros-Mendez. Electro-mechanical properties of UV-curable piezoresistive composites for sensor applications. *11th International conference on Advanced Nano Materials (ANM2018)*, Aveiro (Portugal), 2018. Oral Contribution.

8) **C. Mendes-Felipe**, J. M. Laza, J. L. Vilas. A brief history of 3D printing polymers: the future technology to obtain smart and multifunctional materials. *Tejiendo redes multidisciplinares: VI Jornadas de Investigación de la Facultad de Ciencia y Tecnología*, Leioa (Spain), 2018. Oral Contribution.

AWARDS, MENTIONS AND DISTINCTIONS

1) Award winner of "**TOP downloaded paper 2018-2019**" by the John Wiley & Sons Editorial of New Jersey (EEUU) for the publication "State-of-the-art and future challenges of UV curable polymer-based smart materials for printing technologies", 2019.

2) Award winner of "**VIII Concurso de Fotografía Científica de SGIKER**" for the picture: "Volcán piezoresistivo", Universidad del País Vasco, Leioa (Spain), 2018.

3) **BCMaterials prize for the best poster flash presentation** at New Materials for a Better Life! Workshop, BCMaterials – Basque Center for Material, Applications and Nanostructures, Leioa (Spain), 2018.